



Developing Tools For Probing Stellar Interiors With Asteroseismology

Yaguang Li

This thesis is presented as part of the requirements for the conferral of the degree:

Doctor of Philosophy (PhD)

The University of Sydney
School of Physics

2023

Statement of Originality

I, Yaguang Li, declare that all work presented in this thesis has been conducted during my PhD candidature from Oct 2019 to Feb 2023, except where noted below. None of this thesis has been submitted for any degree or other purposes, except where noted below. The content of this thesis is based on collaborative efforts and I have stated clearly in each case the contributions from me and others. A complete acknowledgement of author contributions is stated in the beginning of each chapter.

- Chapter 2 is a reproduction of [Li, Yaguang et al. \(2020b\)](#). The extraction of oscillation parameters was conducted and presented under visiting programs to the University of Sydney in 2017–2019, during my Master of Science candidature in Beijing Normal University. The text writing and most follow-up analysis was conducted at University of Sydney during my PhD candidature in 2019. I led the work and wrote the paper with advice from co-authors.
- Chapter 3 presents a manuscript in preparation. I led the work and wrote the paper with advice from co-authors.
- Chapter 4 is a reproduction of [Li, Yaguang et al. \(2021\)](#). I led the work and wrote the paper with advice from co-authors.
- Chapter 5 was submitted to a peer-review journal and is under the second review. The preprint version is [Li, Yaguang et al. \(2022b\)](#). I led the work and wrote the paper with advice from co-authors.
- Chapter 6 presents a manuscript to be submitted to a peer-review journal. I led the work and wrote the paper with advice from co-authors.
- Chapter 7 is a reproduction of [Li, Yaguang et al. \(2022c\)](#). I led the work and wrote the paper with advice from co-authors.

The following co-authored contributions have partially benefited from the work presented here: [Li, Tanda et al. \(2020a\)](#), [Zhang et al. \(2020b\)](#), [Zhang et al. \(2020a\)](#), [Bedding et al. \(2020\)](#), [Yan et al. \(2021\)](#), [Zhang et al. \(2021\)](#), [Vrard et al. \(2021\)](#), [Zhou et al. \(2021a\)](#), [Li, Tanda et al. \(2022a\)](#), [Murphy et al. \(2022\)](#) and [Hatt et al. \(2023\)](#).

In addition to the statements above, in cases where I am not the corresponding author of a published item, permission to include the published material has been granted by the corresponding author.

Sydney, Feb 2023
Yaguang Li

As supervisor for the candidature upon which this thesis is based, I can confirm that the authorship attribution statements above are correct.

Sydney, Feb 2023
Timothy R. Bedding

Abstract

Asteroseismology is the study of stellar oscillations. Recent space missions, such as *CoRoT*, *Kepler*, and *TESS*, are rapidly revolutionising the field by collecting vast amounts of data. These data have enabled accurate characterisation of stellar oscillations for a wide range of stars, leading to improved understanding of stellar physics and knowledge of Galactic and planetary populations. This thesis builds on existing tools and develops new techniques to advance our understanding of stars using their oscillations.

Firstly, we investigate 36 subgiants observed by *Kepler*, measuring their oscillation parameters and extracting their frequencies, amplitudes and linewidths. They are used as modelling input to derive accurate stellar parameters.

Secondly, we measure the core and envelope rotation rates for these subgiants, and study them as a function of stellar properties. We find near solid-body rotation in early subgiants and differential rotation in later stages.

Thirdly, we evaluate the intrinsic scatter of the asteroseismic scaling relations, using the sharpness of population-level features that are naturally formed by stars. We constrain the intrinsic scatter to be a few percent.

Fourthly, we propose a new method to correct the stellar surface effect, which involves prescribing the surface effect as a function of stellar surface parameters. This method reduces the scatter of model-derived stellar properties and provides a revised correction for the $\Delta \nu$ scaling relation.

Fifthly, we test the ν_{\max} scaling relation by comparing observed ν_{\max} with model-inferred scaling ν_{\max} constrained by individual frequencies. We conclude no noticeable deviation of the ν_{\max} scaling relation and a lack of metallicity dependency.

Lastly, we construct a mass-radius diagram for red clump stars, leading to the discovery of two new types of post-mass-transfer stars. The new finding offers exciting opportunities to study binary evolution using asteroseismology.

Acknowledgements

First and foremost, I would like to thank my primary supervisor Tim Bedding for a truly amazing PhD journey, for which I will be forever grateful. I still remember my first visit to Sydney in a summer research project: all the little things that you were excited, and how you taught students unreservedly and wholeheartedly. I was amazed by how science could be done in so many clever ways! The thesis is the best testament for my belief in you. None of this would happen if not for your encouragement, enthusiasm, and guidance.

Thank you my associate supervisors, Dennis Stello (honorary mention) and Simon Murphy, for teaching me all the attention to details. I hope I can never forget how to properly use articles and the British spelling, which is the correct way. You all are the best supervisors anyone could ever ask for.

Thank you, Courtney, May, Dan Huber, Tim W, Fil, everyone in the Sydney asteroseismology group. Thank you, Marc Hon, Ben, Claudia, Guillaume in the UNSW group. You are amazing and I am sure I will see you soon! I blame Covid for not meeting all of you sooner.

Thank you to all of my collaborators! These papers won't be there without you. Thank you my mentors, for those guidance to keep me on the right track during the stressful job season, Jørgen, Jen, Dan Huber, Tim B, David, Scott and Marc Pinsonneault.

Thank you my office mates, Isabel, Dan Hey, Gang, Vic, Smrithi, Sreenivas and Ali, my roommate Di, my next-door friends Kai, Alair, for all the company and interesting conversations over the past few years. Thank you everyone in SifA who I ever have the pleasure to meet and everyone who I get to work with as Physics or Business tutors! There are too many to mention. It was a really great time.

Thank you my supervisors in Beijing, Shaolan and Xianfei, for your kindness and unwavering support. You are the nicest people I know and you always wish the best for me.

I would like to express my gratitude to the Faculty of Science Dean's International Postgraduate Scholarship, the Australian government RTP scholarship, and Postgraduate Research Support Scheme, for the financial support. Thank you the taxpayers, so that I can push the boundary of human knowledge without breaking the bank.

Thank you so much my dear friend Song, for keeping me sane in various turmoils. Thank you my parents, mom and dad, my grandma and grandpa, and my aunt, for always believing in me and supporting me in pursuing what I love.

To you, my friend, I extend a warm welcome to my thesis. It is the best summary of my past four years of life, but also a reflection of me in the past 27 years. Here it presents itself. I hope you will enjoy reading it.

Contents

Statement of Originality	iii
Abstract	v
Acknowledgements	vi
1 Introduction	1
1.1 Motivation	1
1.2 Evolution of low and intermediate mass stars	2
1.3 Solar-like oscillations	5
1.3.1 p modes	8
1.3.2 g modes	10
1.3.3 Mixed modes	11
1.4 Observational techniques	13
1.4.1 Data collection	13
1.4.2 Data processing	16
1.5 Modelling techniques	16
1.5.1 Software tools	16
1.5.2 Uncertainties of input stellar physics	18
1.6 Thesis overview	20
2 Oscillation properties of subgiant stars	23
2.1 Introduction	24
2.2 Observations	25
2.3 Parameter estimation	26
2.3.1 Mode identification	26
2.3.2 Power spectrum model	27
2.3.3 Fitting method	27
2.3.4 Fitting details	28
2.3.5 Fitting results	28
2.4 Mode frequencies	29
2.5 The p-g diagram	31
2.6 Mode linewidths	33
2.7 Mode amplitudes	35
2.8 Conclusions	36

3	Core and envelope rotation rates of subgiant stars	49
3.1	Introduction	50
3.2	Data analysis	51
3.2.1	Sample selection	51
3.2.2	Observations	51
3.2.3	Stellar models	51
3.2.4	Measuring the core and envelope rotation rates	52
3.3	Results and discussions	52
3.3.1	Core and envelope rotation rates	52
3.3.2	Implications on gyrochronology	53
3.3.3	Timescales of the angular momentum transport	53
3.4	Conclusions	54
4	Testing the intrinsic scatter of the asteroseismic scaling relations	57
4.1	Introduction	58
4.2	Sample selection	59
4.3	The RGB bump	60
4.3.1	Modelling method	60
4.3.2	Results	62
4.4	The ZAHeB edge	62
4.4.1	Modelling method	63
4.4.2	Results	63
4.5	Discussions	63
4.5.1	Assessing uncertainties	63
4.5.2	The intrinsic scatter of the scaling relations	65
4.5.3	Correcting the scaling relations with theoretical models	65
4.5.4	The intrinsic scatter of the scaling relations as a function of mass and metallicity	66
4.6	Conclusions	66
5	A prescription for the asteroseismic surface effect	69
5.1	Introduction	70
5.2	Prescribing the surface correction	71
5.3	Data analysis	72
5.3.1	Observational sample	72
5.3.2	Stellar models	72
5.3.3	Fitting method	73
5.3.4	Fitting results	73
5.4	Improvements on parameter estimations	75
5.5	Correction to the p-mode large separation from stellar models	76
5.5.1	Results	77
5.5.2	Comparisons to Gaia radii	78
5.5.3	Comparisons to eclipsing binaries	78
5.6	Conclusions	78

6	Testing the ν_{\max} scaling relation with individual frequency modelling	83
6.1	Introduction	84
6.2	Data analysis	84
6.2.1	Observations	84
6.2.2	Stellar models	85
6.2.3	Model fitting	85
6.3	Results and discussions	85
6.3.1	Degeneracies between the model-inferred scaling ν_{\max} and the mixing length	85
6.3.2	Testing the scaling relation	86
6.3.3	Implications on fundamental stellar properties	87
6.4	Conclusions	88
7	Discovery of post-mass-transfer helium-burning red giant stars	91
7.1	Main	92
7.2	Methods	94
7.2.1	Sample selection and stellar parameters	94
7.2.2	Stellar evolutionary models	95
7.2.3	Identification of the underluminous stars	95
7.2.4	Identification of the very low-mass stars	95
7.2.5	Modelling of a very low-mass star	95
7.2.6	Rates of binary interactions	96
7.2.7	Variations of RVs	96
8	Conclusions and outlook	105
8.1	Conclusions	105
8.2	Outlook	105
	Bibliography	109

1 Introduction

1.1 Motivation

Dating back to prehistory, humans were fascinated with stars and attempted to predict the future from their motions. They would not have imagined that one day, future generations would be able to understand stars in so many intricate details, far beyond just their motions. Today, we can analyze various characteristics of stars, including their sizes, ages, masses, spectral features, distances, and so on. The study of stellar oscillations, asteroseismology, even allows us to delve beneath the surface and understand what’s happening inside stars. It is fascinating that all of this knowledge is obtained by simply observing stars through telescopes.

The continuous advancement of science and technology has driven this increased understanding of stars. As the precision improves, new discoveries are revealed because everything is “seen” better. One such example is the Hertzsprung–Russell diagram (H–R) diagram, which has been studied for a century. The recent remaking of this diagram with higher precision by ESA’s *Gaia* space telescope has led to new and exciting discoveries, such as the dual sequence of white dwarfs that previously went unnoticed ([Gaia Collaboration et al., 2018](#)).

In recent years, a revolution has taken place in the field of asteroseismology for similar reasons, which is the focus of this thesis. The NASA’s *Kepler* spacecraft collected high-precision, high-cadence data from 2009 to 2014, and significantly advanced the study of asteroseismology. These data produced promising results, especially for FGK main-sequence dwarfs and red giants. The detection of numerous oscillation modes allows for a critical evaluation of current theories of stellar evolution by comparing predicted and observed oscillation properties.

The impact is mainly two-fold. It leads to a deeper understanding of the internal structure of stars, including the study of internal rotation, core and envelope properties. This reveals discrepancies in current star modelling techniques, such as the surface effect. The ability to observe oscillations in a wide range of stars enables critical examinations of these phenomena on a population level, rather than on a star-by-star basis. The wealth of data also results in precise determinations of stellar properties, such as mass, radius, and age, which would be very difficult to obtain by other means. These stellar properties have significant implications for a range of scientific fields, including planetary and Galactic studies.

We begin by reviewing basic concepts relevant to the study of stellar oscillations in Chapter 1. Section 1.2 presents a basic introduction of standard stellar structure and evolutionary theory. Section 1.3 explains how oscillations can refine our knowledge of these topics. Section 1.4 provides an overview of the observing techniques that are

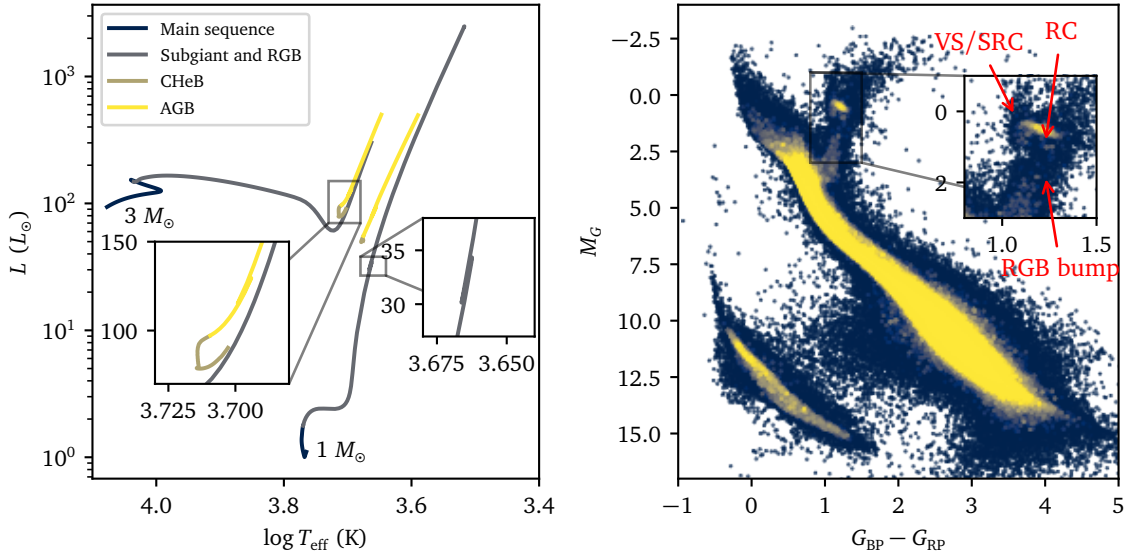


Figure 1.1: Theoretical H-R diagram showing luminosity vs. T_{eff} on the left, and observational colour-magnitude diagram showing M_G vs. $G_{\text{BP}} - G_{\text{RP}}$. The left panel shows theoretical evolutionary tracks of $1 M_\odot$ and $3 M_\odot$ stars calculated with MESA. The insets highlight the RGB bump for the $1 M_\odot$ track and the helium-burning phase for the $3 M_\odot$ track. Figure inspired by [Hekker & Christensen-Dalsgaard \(2017\)](#). The right panel shows stars observed by *Gaia* in the solar neighbourhood (within 200 pc). The inset highlights red giants, where many features such as the red clump and the secondary red clump can be seen. Figure inspired by [Gaia Collaboration et al. \(2018\)](#).

utilised in asteroseismology. Finally, Section 1.5 discusses the modelling techniques used to analyse and interpret observations.

1.2 Evolution of low and intermediate mass stars

This thesis focuses on stars in the mass range $0.5 < M/M_\odot < 3.0$. We begin with an overview of their evolution and basic properties relevant to our work. There are many comprehensive reviews and textbooks on this topic, for example, [Kippenhahn & Weigert \(1990\)](#), [Aerts et al. \(2010\)](#), [Hekker & Christensen-Dalsgaard \(2017\)](#), and [Girardi \(2016\)](#).

Single stars form from contracting interstellar clouds. They initiate nuclear burning, specifically hydrogen burning, when the centre of the cloud reaches a high enough temperature. The star stops contracting because the thermal pressure is able to balance gravity. This core hydrogen burning phase is called the main sequence, which comprises the majority of a star's lifetime. The length of the main sequence depends on the stellar mass, with more massive stars having a shorter lifespan. Low-mass stars ($M < 1.2 M_\odot$) fuse hydrogen into helium through the proton-proton reaction, while more massive stars ($M > 1.2 M_\odot$) with higher core temperatures undergo more rapid hydrogen burning through the CNO cycle, which uses carbon, nitrogen and oxygen as catalysts to speed up the fusion process. During the main sequence, stars undergo only relatively slight changes in their luminosities and effective temperatures, as shown in Fig 1.1.

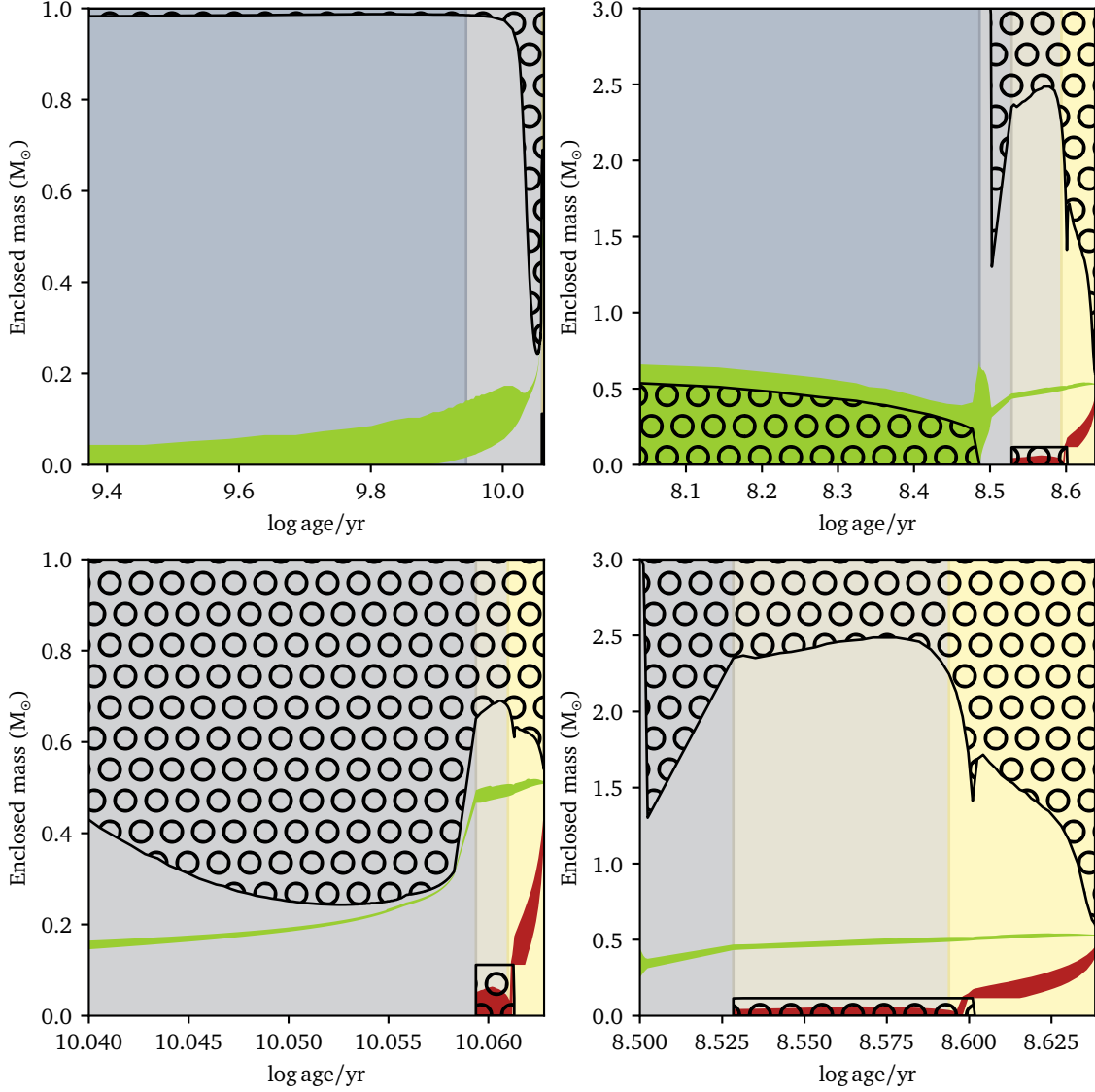


Figure 1.2: Kippenhahn diagrams showing the structural evolution of the $1\text{-}M_{\odot}$ star (left) and the $3\text{-}M_{\odot}$ star (right) described in Fig. 1.1. The bottom rows zoom in on the post-main-sequence evolution. The bubble-filled regions indicate convection zones. The green (or light grey, if viewing in greyscale) and red (dark grey) filled areas indicate hydrogen and helium burning regions, respectively. The background colours indicate the evolutionary stages as specified in the left panel of Fig. 1.1.

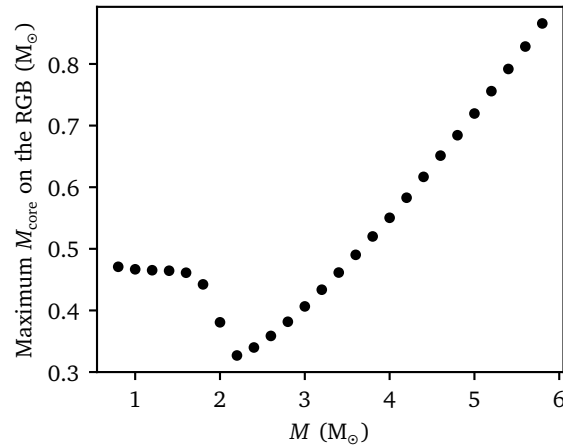


Figure 1.3: Helium core mass as a function of total mass at RGB tip (see also [Montalbán et al., 2013](#); [Hekker & Christensen-Dalsgaard, 2017](#)). The models are from MIST ([Choi et al., 2016](#)).

There are two primary ways to transport energy in stellar interiors: radiation and convection. The convective instability is decided by the Schwarzschild criterion, which compares the radiative and adiabatic temperature gradients:

$$\nabla_{\text{rad}} > \nabla_{\text{ad}}. \quad (1.1)$$

The means of energy transport has a significant impact on stellar evolution and oscillation properties, as discussed in Section 1.3. Fig. 1.2 illustrates the evolutionary picture of stellar structures for the two stars shown in Fig. 1.1. On the main-sequence, low-mass stars ($M < 1.2 M_{\odot}$) develop a radiative core and a convective envelope, while the intermediate-mass stars ($M > 1.2 M_{\odot}$) develop a convective core and a radiative envelope.

The exhaustion of central hydrogen (completion of the conversion to helium) marks the end of a star’s main-sequence phase. After this, the star enters into the subgiant phases, which is characterised by its decreasing T_{eff} . Then follows the red giant branch (RGB) phase, during which the luminosity increases. However, the boundary between these two phases is not well-defined. During the subgiant and RGB phases, hydrogen burns in a shell surrounding the inert helium core, which grows in size until reaching the tip of RGB.

During the subgiant and RGB phases, both low-mass and intermediate-mass stars have convective envelopes and radiative cores. In particular, the convective envelopes can extend to the region where fusion occurred during the main-sequence phase. This phenomenon is known as the first dredge-up. Since convection is very efficient at mixing chemical elements, the surface abundance ratios $^{12}\text{C}/^{13}\text{C}$ and C/N may be lowered due to the mixing with core materials. The dredge-up also leaves a chemical discontinuity at the bottom of the convective envelope when it is deepest.

On the RGB, the increasing luminosity is associated with an increase in the mean molecular weight μ . However, when the hydrogen-burning shell crosses the composition discontinuity created during the dredge-up, there is a sudden decrease in μ , changing opacities and hence luminosities ([Refsdal & Weigert, 1970](#); [Christensen-Dalsgaard, 2015](#); [Khan et al., 2018](#)). Thus, as the star climbs up the RGB, there is a

temporary drop in luminosity before increasing again. This leads to the RGB bump (the inset of Fig. 1.1), which can be observed as an overdensity of RGB stars at this luminosity.

It is worth noting that the properties of the helium core developed on the RGB depend on the star's mass. For stars below $1.8 M_{\odot}$, the inert helium core is supported by electron degeneracy pressure, preventing it from collapsing. At the RGB tip, where the core temperatures are high enough to burn helium, the helium is ignited in an explosive process known as the helium flash. The formed helium core has a mass around $0.5 M_{\odot}$. For stars above $1.8 M_{\odot}$ on the RGB, the radiative pressure in the core is strong enough to support against gravity. For these stars, the masses of helium core formed at the RGB tip could be deduced from the Schönberg–Chandrasekhar limit (Schönberg & Chandrasekhar, 1942), which states that the helium core mass is approximately a fixed fraction of the total mass. Fig. 1.3 shows this relationship. Interestingly, a $2.2 M_{\odot}$ star will have a smaller helium core than a $1.0 M_{\odot}$ star.

When helium is ignited, the star will contract and reduce to a lower luminosity than at the RGB tip. This is called the core-helium-burning phase (cHeB; see Fig. 1.1). The core helium is converted into carbon through the triple alpha reaction. The T_{eff} of cHeB and RGB are very similar, so it is difficult to distinguish the two groups of stars based on their positions on the H–R diagram. However, their internal structures are different: the cHeB stars have a convective core while the RGB stars have a radiative core (see Fig. 1.2). The cHeB phase is relatively long compared to the RGB, resulting in an overdensity of stars on the H–R diagram, a feature known as the red clump (RC), mainly formed by $M < 1.8 M_{\odot}$ stars. Stars with $M > 1.8 M_{\odot}$ are more vertically aligned on the H–R diagram, a feature known as the vertical structure (VS) or the secondary red clump (SRC).

Once the core helium is exhausted, the star will ascend in luminosity again on the asymptotic-giant branch (AGB). The energy sources of AGB stars are helium and hydrogen burning shells surrounding the carbon core. The AGB bump, a temporary drop in luminosity, similar to the RGB bump, occurs during the ascending phase (Dréau et al., 2022).

1.3 Solar-like oscillations

Fig. 1.4 illustrates how stars pulsate across different regions of the H–R diagram. This thesis focuses on solar-type stars (below $1.2 M_{\odot}$ on the main-sequence) and red giants (below $5 M_{\odot}$). They are located on the right part of the H–R diagram (below 6500 K), and host thick convective envelopes. These stars exhibit *solar-like oscillations*, which are driven by near-surface turbulent convection and were first discovered in the Sun (Balmforth, 1992; Goldreich et al., 1994). For a comprehensive review of the excitation and damping mechanisms (non-adiabatic effects) of oscillations, we refer to Samadi et al. (2015) and Houdek & Dupret (2015). In this section, we review some basic properties of solar-like oscillations (see also Chaplin & Miglio, 2013; Bedding, 2014; Basu & Chaplin, 2017; Basu & Hekker, 2020; Aerts, 2021; Kurtz, 2022).

The oscillations studied here are standing waves within stars, whose restoring forces are either the pressure gradient (pressure, or p modes) or the buoyancy (gravity, or g modes). Mixed modes also arise in evolved stars, resulting from a coupling of p and

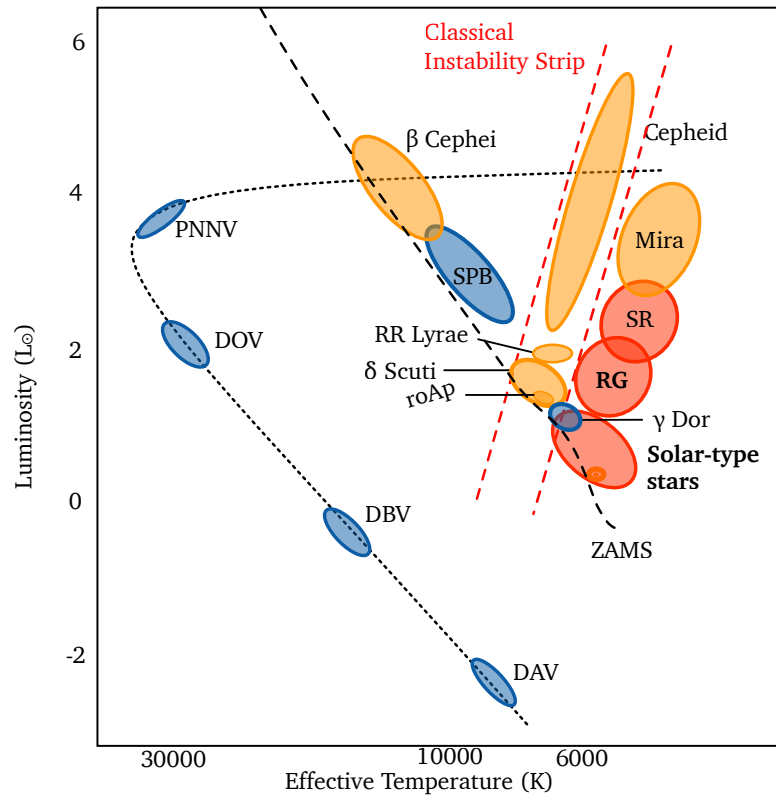


Figure 1.4: Some types of pulsating stars on the H–R diagram. Figure inspired by [Aerts et al. \(2010\)](#) and adapted from [Hey \(2021\)](#). This thesis focuses on solar-type stars and red giants, which show solar-like oscillations.

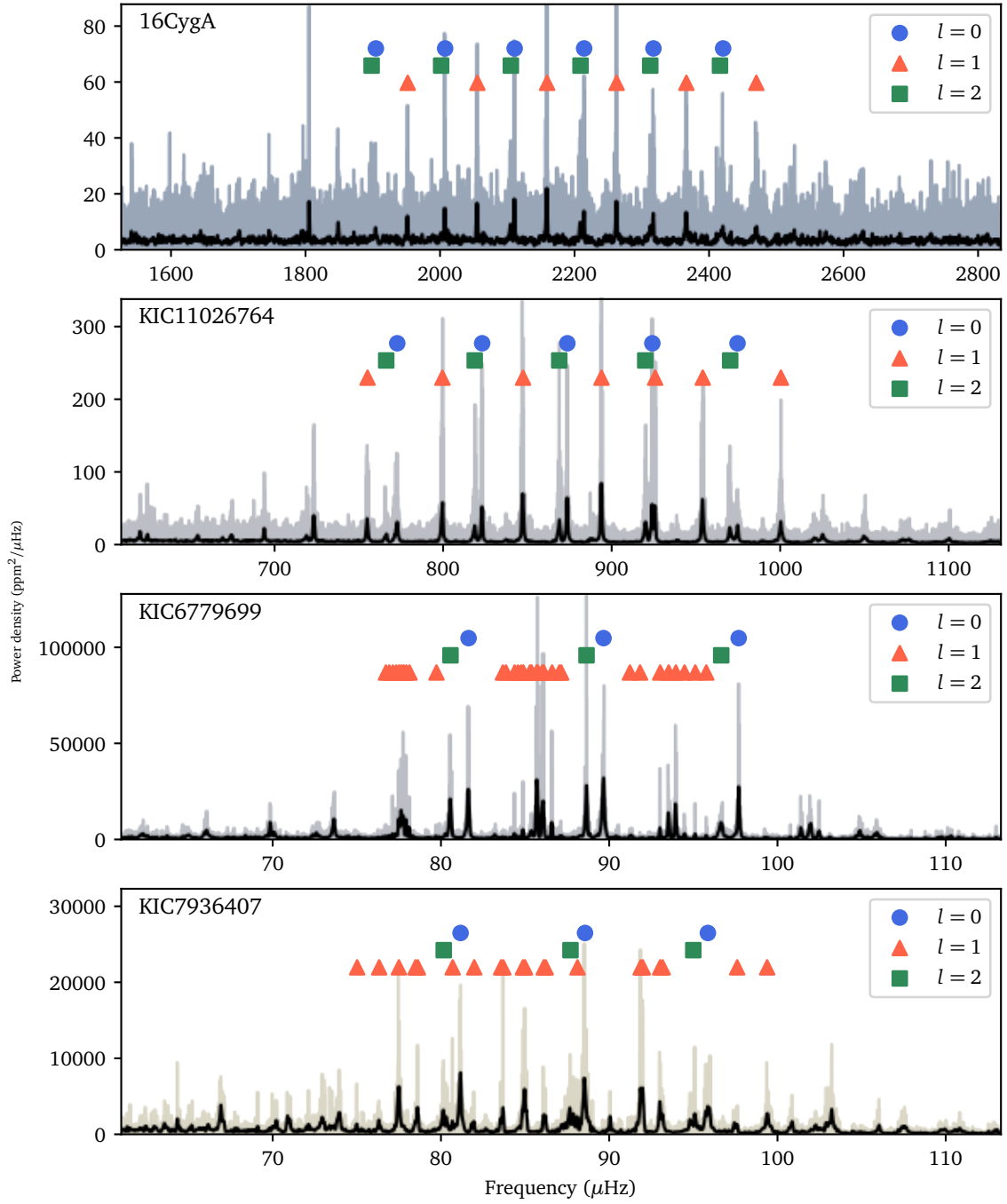


Figure 1.5: Power spectra of four representative stars. From top to bottom: 16 Cyg A (main-sequence star), KIC 11026764 (subgiant), KIC 6779699 (RGB), KIC 7936407 (CHeB). The radial ($l = 0$), dipole ($l = 1$), and quadrupole ($l = 2$) modes are marked by circles, squares, and triangles, respectively.

g modes, so the modes are oscillating like p modes in the envelope and like g modes in the core. Each mode is characterised by three quantum numbers: the radial order n , the spherical degree l , and the azimuthal degree m . We only consider m when non-axis-symmetric effect such as rotation are concerned.

The distinctive signal of solar-like oscillations is a series of peaks in the oscillation power spectrum, obtained by Fourier-transforming the photometric light curves or radial velocities. The amplitudes of these peaks are modulated by a Gaussian-like envelope centred around a frequency known as ν_{\max} . Fig. 1.5 presents the power spectra of four stars observed by *Kepler*: a main sequence star (16 Cyg A), a subgiant (KIC 11026764), a red-giant-branch star (KIC 6779699), and a core helium-burning star (KIC 7936407).

Note their oscillation frequencies, which are in a range around ν_{\max} , are significantly different from star to star. Brown et al. (1991) hypothesised that ν_{\max} is proportional to the acoustic cutoff frequency, ν_{ac} , which is an upper limit of oscillation frequency. Standing waves cannot form above ν_{ac} , as they are not reflected in the atmosphere. The acoustic cutoff frequency is given by

$$\nu_{\text{ac}} = \frac{c}{4\pi H} \left(1 - 2 \frac{dH}{dr} \right)^{1/2}, \quad (1.2)$$

where c and H are the sound speed and the density scale height in the stellar atmosphere. Hence, following a scaling law and some approximations, it suggests (Brown et al., 1991; Kjeldsen & Bedding, 1995),

$$\nu_{\max} \propto \nu_{\text{ac}} \propto \frac{c}{H} \propto g / \sqrt{T_{\text{eff}}} \propto MR^{-2} T_{\text{eff}}^{-1/2}, \quad (1.3)$$

where g , T_{eff} , M , and R are the surface gravity, effective temperature, mass, and radius, respectively. Despite being based on a fairly crude assumption, the relation has shown to have great precision, and is widely used to derive stellar properties (e.g. Pinsonneault et al., 2018). From the above equation, it can be seen that ν_{\max} mainly depends on surface gravity. Therefore, solar-type main-sequence stars have larger ν_{\max} (the ν_{\max} of the Sun is $3090 \mu\text{Hz}$), red giants have smaller ν_{\max} (below $400 \mu\text{Hz}$), and subgiants are somewhere in between. This is illustrated in Fig. 1.5.

1.3.1 p modes

Upon closer examination of Fig. 1.5, a discernible regular pattern emerges in the oscillation frequencies. High radial order (n) p modes can be described by an asymptotic expression (Tassoul, 1980; Gough, 1986):

$$\nu_{nl} = \Delta \nu \left(n + \frac{l}{2} + \epsilon_p \right) - \delta \nu_{nl}, \quad (1.4)$$

where $\Delta \nu$ is the p-mode large separation, ϵ_p is the dimensionless phase offset, and $\delta \nu_{nl}$ is the small separation that specifies the distances between radial and non-radial modes (which is small compared to $\Delta \nu$). The large separation is related to the inverse of sound travel time across the star and can be expressed as

$$\Delta \nu = \left(2 \int_0^R \frac{dr}{c} \right)^{-1}, \quad (1.5)$$

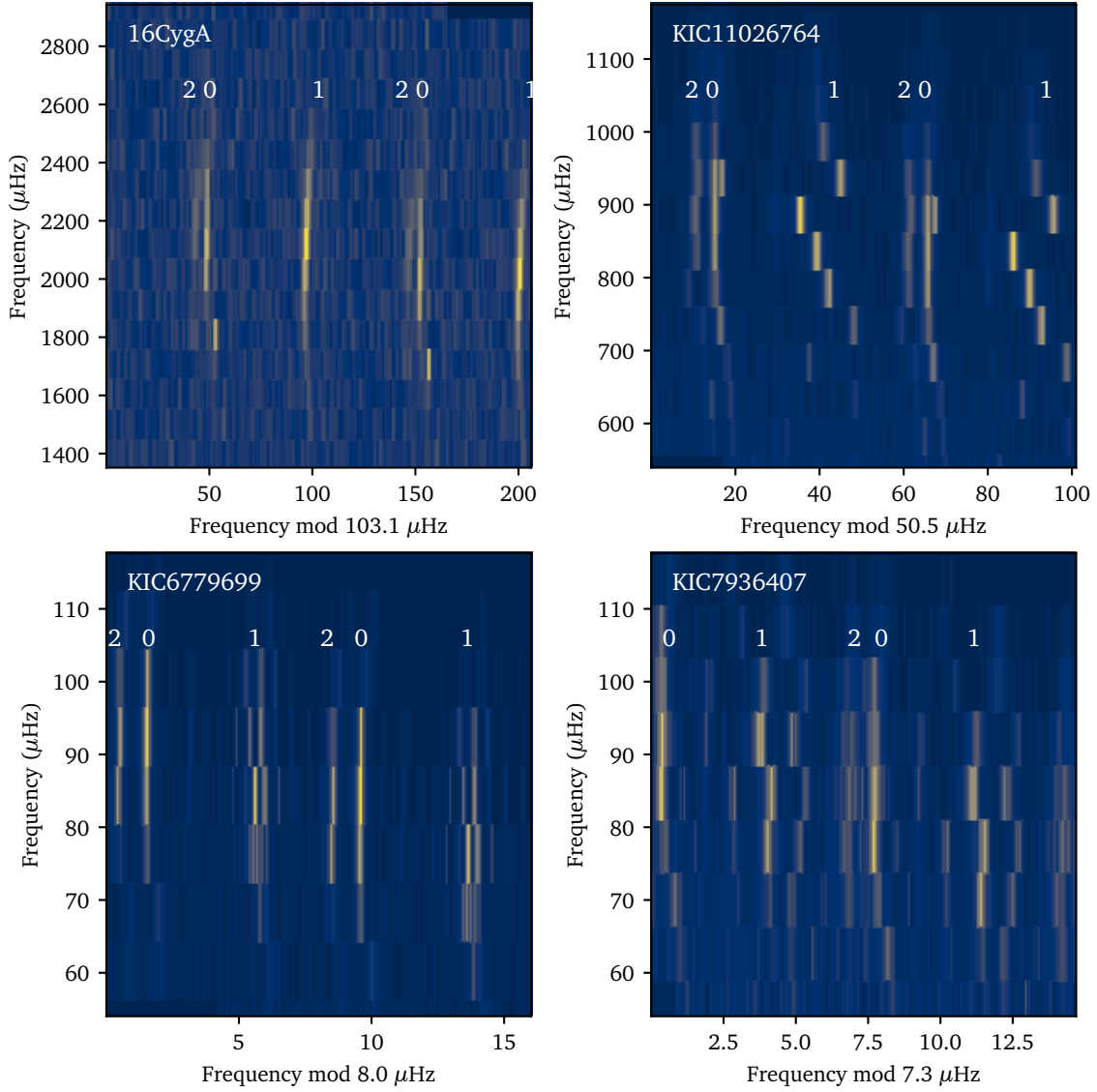


Figure 1.6: Power spectra of the four stars in Fig. 1.5 shown in the échelle format. Note the same spectrum is plotted twice to avoid edge effect.

where c is the sound speed, and R is the stellar radius. Under simple approximations, $\Delta\nu$ is related to the mean stellar density $\bar{\rho}$ (Ulrich, 1986; Kjeldsen & Bedding, 1995):

$$\Delta\nu \propto \sqrt{\bar{\rho}} \propto M^{1/2}R^{-3/2}. \quad (1.6)$$

This is another very useful scaling relation to derive stellar properties. According to Eq. 1.4, modes of the same spherical degree l but with consecutive orders n are equally spaced by $\Delta\nu$. This can be observed from Fig. 1.5, particularly in 16 Cyg A, whose oscillations are all high-order p modes.

The regular spacings in the oscillation frequencies can be conveniently displayed using the échelle diagram, where the power spectrum is sliced into equal segments of length $\Delta\nu$ and each segments are stacked vertically. Fig. 1.6 shows the power spectra in the échelle format for the stars in Fig. 1.5. The color scale now represents the power of oscillations. For main-sequence stars like 16 Cyg A, which exhibit high radial-order

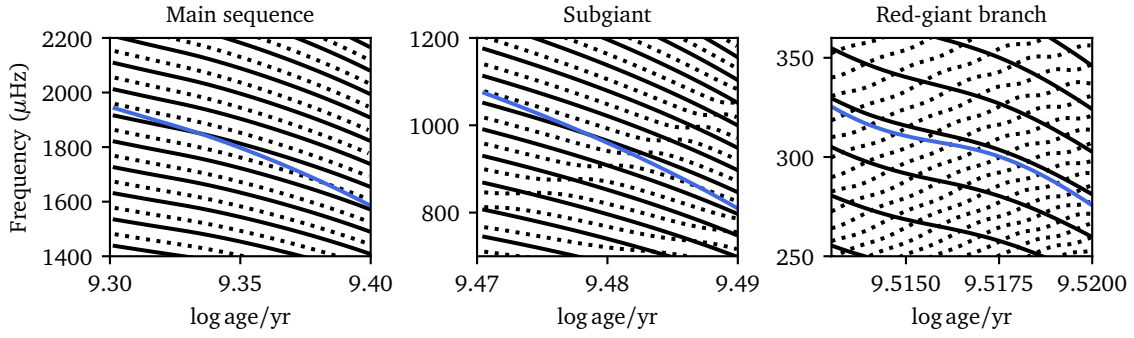


Figure 1.7: Evolution of mode frequencies in $1\text{-}M_{\odot}$ stellar models calculated with MESA. The solid and the dotted black lines indicate $l = 0$ and $l = 1$ modes, respectively. The blue lines in the middle trace the evolution of ν_{\max} .

p modes, modes with the same l degrees align vertically on this diagram and form three ridges, since they are equally spaced by $\Delta\nu$.

It is also easy to identify the value of ϵ_p and small separations $\delta\nu_{nl}$ in this diagram. According to Eq. 1.4, for radial modes, we have

$$\nu_{n,l=0} = \Delta\nu(n + \epsilon_p). \quad (1.7)$$

Hence, the distance of the $l = 0$ ridge from the left edge of the échelle is $\Delta\nu \cdot \epsilon_p$ (or $\Delta\nu \cdot (\epsilon_p - 1)$, since ϵ_p could be larger than 1 but smaller than 2, according to theoretical models). For dipole and quadrupole modes, we have

$$\nu_{n,l=1} = \Delta\nu(n + 1/2 + \epsilon_p) - \delta\nu_{n,l=1}, \quad (1.8)$$

and

$$\nu_{n,l=2} = \Delta\nu(n + 1 + \epsilon_p) - \delta\nu_{n,l=2}. \quad (1.9)$$

Thus, the 02 small separation $\delta\nu_{n,l=2} = \nu_{n+1,l=0} - \nu_{n,l=2}$ is the horizontal distance between the 0 and 2 ridges on the échelle. The 01 small separation $\delta\nu_{n,l=1} = (\nu_{n+1,l=0} + \nu_{n,l=0})/2 - \nu_{n,l=1}$ is the offset of the $l = 1$ ridge from the midpoint of the two copies of $l = 0$ ridges.

1.3.2 g modes

As a star evolves from the main sequence to the RGB, its surface gravity g decreases, resulting a decrease in ν_{\max} . The value of $\Delta\nu$, which is related to the mean density, also decreases. According to Eq. 1.4, the frequency for each individual mode also decreases. In Fig. 1.7, the evolution of mode frequencies are shown in three evolutionary stages. An interesting phenomenon occurs during the subgiant phase. Although the $l = 0$ modes remain equally spaced by $\Delta\nu$, the $l = 1$ modes depart from this pattern. This is known as mode bumping. These $l = 1$ modes in subgiants are mixed modes, resulting from the coupling of p modes, which mainly propagates in the outer convective envelope, and g modes, which only propagate in the inner radiative zone. The frequencies of gravity modes are very low on the main sequence and gradually increase as stars evolve.

According to asymptotic theories, high order g modes are equally spaced in period, whereas high order p modes are equally spaced in frequency. The periods of g modes can be written as

$$\Pi_{nl} = \nu_{nl}^{-1} = \Delta\Pi_l(n + \epsilon_g), \quad (1.10)$$

where ϵ_g is the dimensionless phase offset for g modes. The period spacing $\Delta\Pi_l$ is related to the buoyancy frequency N (or Brunt-Väisälä frequency), which is given by

$$\Delta\Pi_1 = \frac{2\pi^2}{\sqrt{l(l+1)}} \left(\int_{r_1}^{r_2} N \frac{dr}{r} \right)^{-1}, \quad (1.11)$$

and

$$N^2 = g \left(\frac{1}{\Gamma_1} \frac{d \ln p}{dr} - \frac{d \ln \rho}{dr} \right), \quad (1.12)$$

where $N > 0$, Γ_1 is the first adiabatic component, and the region for g mode propagation is defined by (r_1, r_2) .

1.3.3 Mixed modes

To understand the nature of p and g modes, it is helpful to consider the equation that describes stellar oscillations. By neglecting some terms (for a full derivation see [Aerts et al. 2010](#)) and using the Cowling approximation, that is, neglecting gravitational perturbations in the oscillation equations (shown in Section 1.5), it can be shown that the oscillations can be described by a second order differential equation:

$$\frac{d^2 \xi_r}{dr^2} = -K(r) \xi_r = -\frac{\omega^2}{c^2} \left(\frac{N^2}{\omega^2} - 1 \right) \left(\frac{S_l^2}{\omega^2} - 1 \right) \xi_r, \quad (1.13)$$

where ξ_r is the radial displacement of the oscillation at distance r from the stellar centre, ω is the angular oscillation frequency, and S_l is the Lamb frequency defined by

$$S_l^2 = \frac{l(l+1)c^2}{r^2}. \quad (1.14)$$

The condition for oscillatory solutions is $K(r) > 0$, which corresponds to two scenarios: (1) $|\omega| > |N|$ and $|\omega| > S_l$, and (2) $|\omega| < |N|$ and $|\omega| < S_l$. Scenario (1) forms p modes, and scenario (2) forms g modes. The so-called propagation diagrams for three evolutionary stages are shown in Fig. 1.8, highlighting the propagation regions of p and g modes according to the above criteria. On the main sequence, only p modes are relevant near ν_{\max} . However, in the subgiant phase, modes near ν_{\max} behave as g modes in the inner g-mode cavity and as p modes in the outer p-mode cavity, creating p-g mixed modes. Mixed modes only exist as non-radial modes ($l \geq 1$), because there are no radial g modes. In red giants, the buoyancy frequency increases while ν_{\max} decreases, allowing more g modes to couple with p modes, resulting in many mixed modes per radial order, as shown in Fig. 1.7. In Fig. 1.6, the multiple $l = 1$ peaks present in subgiants and red giants are mixed modes resulting from p and g mode coupling. The coupling also happens for $l = 2$ modes, but they have a weaker coupling so only p-like $l = 2$ modes are seen.

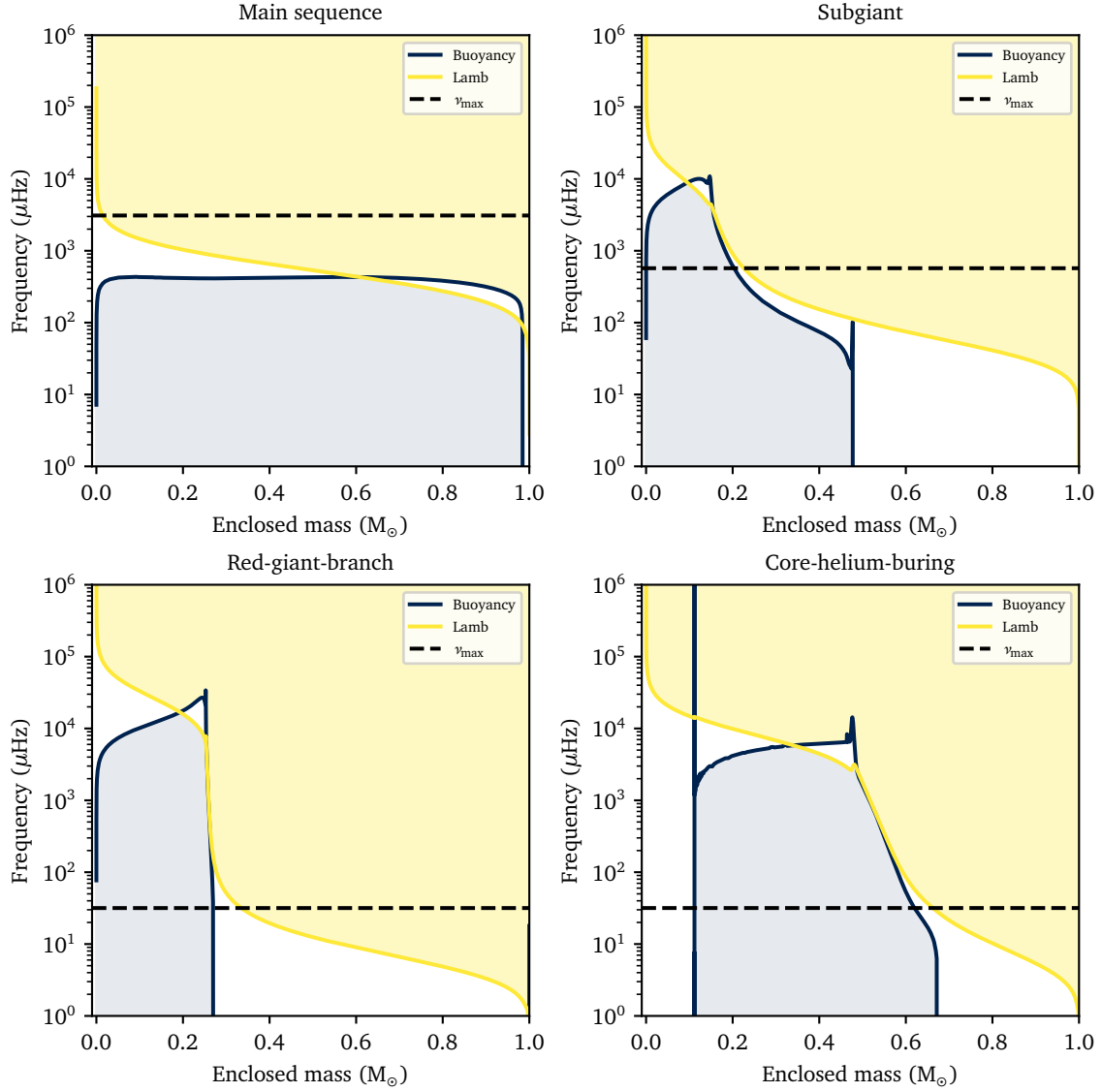


Figure 1.8: Propagation diagrams in four models at different evolutionary stages calculated with MESA. The blue and yellow regions show the g mode and p mode propagation areas, respectively, which are characterised by the buoyancy frequencies and lamb frequencies. Only modes near ν_{max} (dashed lines) are excited.

Mixed modes are not equally spaced in either period or frequency. Rather, they can be described by an asymptotic expression (Unno et al., 1989; Mosser et al., 2018):

$$\tan \theta_p = q \tan \theta_g, \quad (1.15)$$

$$\theta_p = \pi \frac{\nu - \nu_p}{\Delta \nu}, \quad (1.16)$$

and

$$\theta_g = \pi \frac{1}{\Delta \Pi_l} \left(\frac{1}{\nu} - \frac{1}{\nu_g} \right), \quad (1.17)$$

where q is the coupling factor ranging from 0 to 1, ν is the mixed mode frequency, and ν_p and ν_g are the pure p and g mode frequencies calculated from Eqs. 1.4 and 1.10. Based on the observed mixed mode frequencies and $\Delta \nu$ inferred from radial modes, it is possible to derive the true g mode period spacings for dipole modes (e.g. Vrad et al., 2016). It has been shown that HeB stars have $\Delta \Pi_1 \sim 300$ s, while $\Delta \Pi_1$ of RGB stars are much lower. This is mainly because HeB stars have convective cores ($N < 0$ so g modes do not exist), which affects the g mode propagation regions (Fig. 1.8). This in turn affects the upper and lower boundary for the integration in Eq. 1.11, resulting in larger $\Delta \Pi_1$. This fact has been used to distinguish HeB and RGB stars (Dupret et al., 2009; Bedding et al., 2011; Mosser et al., 2012a).

From Eq. 1.15, it is not straightforward to see how mixed mode frequencies are spaced. However, in red giants, it is informative to consider the mixed mode periods to be equally spaced (g mode period spacing $\Delta \Pi_1$) but with a departure function p to be determined, i.e. $P = n_m \Delta \Pi_1 + p$ (n_m is the order of mixed modes). Substituting this prescription to the derivative of Eq. 1.15 with respect to n_m , Mosser et al. (2015) showed that the period spacings of mixed modes ΔP link to $\Delta \Pi_1$ by a function ζ :

$$\frac{\Delta P}{\Delta \Pi_1} = \zeta(\nu) = \left(1 + \frac{q}{\Delta \nu / (\nu^2 \Delta \Pi_1)} \frac{1}{q^2 \cos^2 \theta_p + \sin^2 \theta_p} \right)^{-1}. \quad (1.18)$$

Furthermore, ζ can be shown to be the ratio of mode inertia in the core to the total mode inertia (Goupil et al., 2013):

$$\zeta = I_{\text{core}} / I, \quad (1.19)$$

which can be evaluated from models. Fig. 1.9 shows the mode inertia I , the function ζ , and the mixed mode period spacings for an RGB model, revealing the close connection between these quantities. Specifically, the g-like $l = 1$ modes, close to the $l = 0$ mode frequencies, are more likely to be equally spaced in periods, while the p-like $l = 1$ modes, close to the midpoint of consecutive $l = 0$ modes, are shifted away from the regular period spacing.

1.4 Observational techniques

1.4.1 Data collection

Observing oscillations in stars can be done using two main methods (see reviews by Bedding, 2014). The first method is to measure brightness fluctuations using photometry. However, ground-based observations of solar-type stars are challenging due to

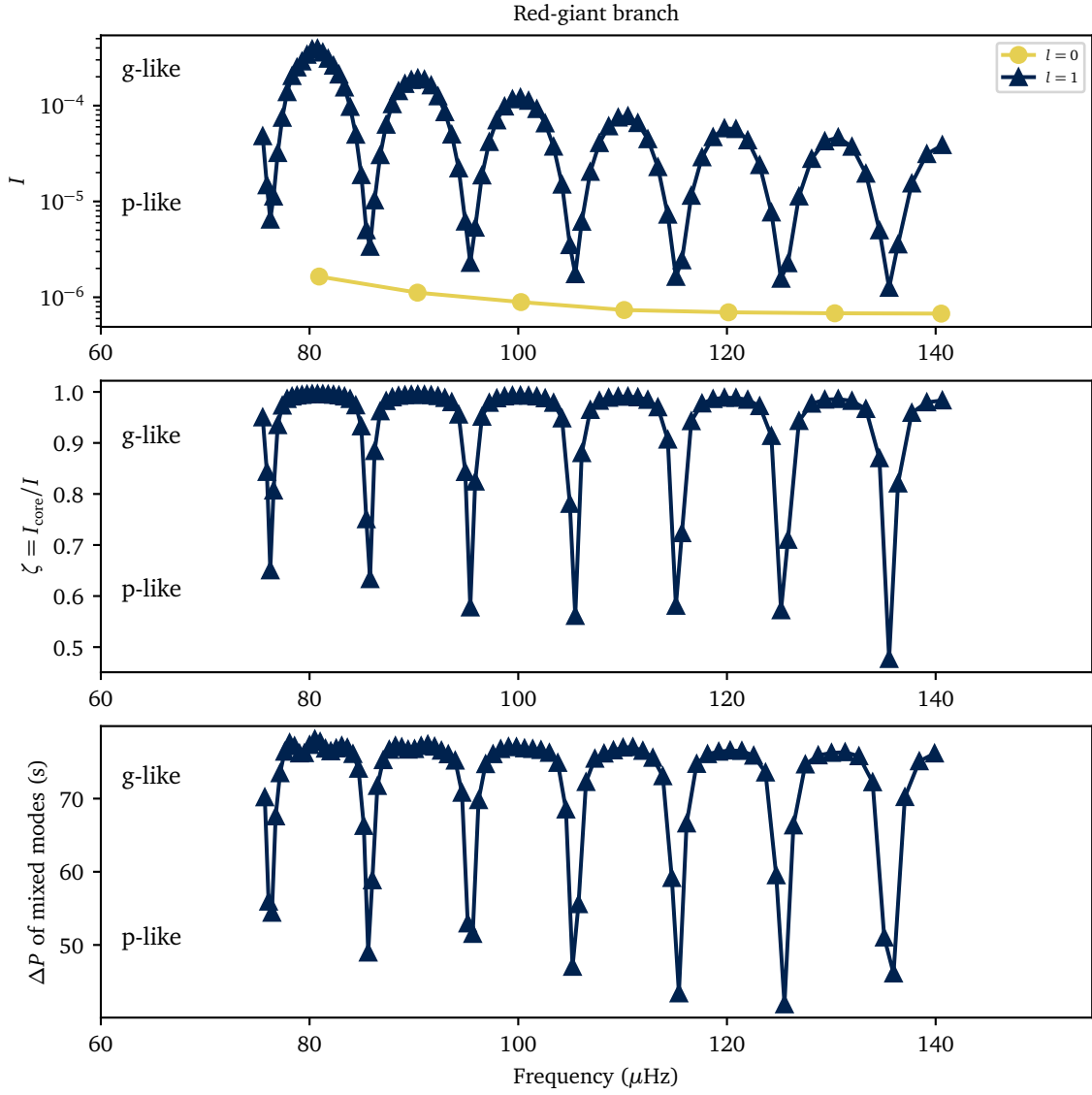


Figure 1.9: Mode inertia, ζ functions and consecutive period spacings vs. frequencies, shown for a $1\text{-}M_{\odot}$ RGB stellar model calculated with MESA.

atmospheric scintillation. Spaced-based observations, such as those from *MOST* and *CoRoT*, and then *Kepler* and *TESS* played a significant role in obtaining photometric data for these stars. These space missions are able to provide high-precision photometry for a large number of stars at the same time. The revolution of studying solar-like oscillations begins with *CoRoT* for red giants (De Ridder et al., 2009; Mosser et al., 2011) and then really took off with *Kepler*, a 0.95-m space telescope funded by NASA and launched in 2009. The majority of this thesis is enabled by the data collected by this mission. The telescope operates in a earth-trailing orbit, and have a fixed field-of-view of 115 square degrees pointed at the constellations Cynus, Lyra and Draco, for a continuous time of four years. The combined differential photometric precision of *Kepler* is 30 ppm for a 12th magnitude star over 6.5 hr (Gilliland et al., 2011). During its primary mission, *Kepler* observed oscillations of $\sim 20,000$ red giants in a 30-min long-cadence mode, and ~ 700 main-sequence stars and subgiants in a 1-min short-cadence mode (e.g. Hekker et al., 2011a; Huber et al., 2011; Chaplin et al., 2014; Huber et al., 2013; Stello et al., 2013; Huber et al., 2014; Mathur et al., 2016; Yu et al., 2016, 2018; Mathur et al., 2022). Additionally, there are four open clusters observed in the *Kepler* field, and three of them have high-quality oscillation data in red giants (Hekker et al., 2011b; Stello et al., 2011; Corsaro et al., 2012; Colman et al., 2022). In 2013, following the failure of two out of four reaction wheels, the spacecraft was unable to sustain stable pointing. It began a drifting mode, debuted as the K2 mission, that observes different fields near the ecliptic every few months, expanding the mission's capability to observe a wider range of stars.

The second method for observing stellar oscillations is to utilise Doppler shifts in radial velocities. The technique has been widely used in ground-based observations since the 1980s. See Bedding (2014) for a review on the history of ground-based observations. The first detections of solar-like oscillations in stars other than the Sun were in the F star Procyon (Brown et al., 1991) and the subgiant η Boo (Kjeldsen et al., 1995), although the detection in η Boo also utilised oscillations in Balmer line equivalent widths. However, single-site ground-based observations suffer from Fourier aliases, which can greatly hamper the interpretation of oscillation spectra, especially when searching for regular spacings. To overcome this limitation, the Stellar Oscillations Network Group (SONG; Grundahl et al., 2008) will be established as a global network of one-metre telescopes with high precision radial velocity spectrographs. SONG has successfully detected oscillations in stars including the subgiant μ Her (Grundahl et al., 2017), the red giant 46 LMi (Frandsen et al., 2018), and ϵ Tau (Arentoft et al., 2019). The use of radial velocities (RV) to detect oscillations still has very important advantages: (1) simultaneous RV and photometric measurements provide amplitude ratios and phase offsets, putting extra constraints on stellar atmosphere and pulsation theories (Houdek, 2006; Zhou et al., 2021b); (2) RV power spectra have lower granulation noise, making it easier to observe oscillations in K dwarfs; (3) ground-based RV campaigns can target nearby benchmark stars or exoplanet hosts, the oscillations of which provide valuable information on stellar interiors and stellar properties.

1.4.2 Data processing

Once we collected data (brightness or radial velocities) in the time domain, the common approach is to model their oscillation behaviour in the frequency domain using a Fourier transform. However, it should be noted that approaches that directly model data in the time domain also exist, such as Gaussian processes (e.g. [Foreman-Mackey et al., 2017](#)). The basis to transform a continuous function $x(t)$ to a Fourier spectrum $X(\omega)$ is,

$$X(\omega) = \frac{1}{\sqrt{2\pi}} \int_{-\infty}^{+\infty} x(t) \exp(-i\omega t) dt. \quad (1.20)$$

For a time series x_j , the discrete transform X_k is

$$X_k = \frac{1}{\sqrt{N}} \sum_{j=0}^{N-1} x_j \exp(-i2\pi k j / N), \quad (1.21)$$

Then the power spectrum is defined as $P_k = |X_k|^2$. However, for a time series with gaps and irregular cadence defined by pairs of $\{t_n, x_n\}$, we can use the Lomb-Scargle method to calculate the power spectrum at any frequency f :

$$P(f) = \frac{1}{N} \left| \sum_{n=1}^N x_n \exp(-i2\pi f t_n) \right|^2. \quad (1.22)$$

This is equivalent to fitting sines and cosines to the time series.

The signal in the power spectrum has multiple stellar astrophysics origins, including rotation, granulation, and oscillation. Oscillations in solar-like stars can be thought of damped oscillators with a typical damping timescale (the so-called mode lifetime τ), which are stochastically re-excited. If the observing time is much longer than the mode lifetime, then the oscillation has a Lorentzian profile on the power spectrum:

$$P(\nu) = \frac{H}{1 + [(\nu - \nu_0)/(\Gamma/2)]^2}, \quad (1.23)$$

where H is the mode height, ν_0 is the mode frequency, and Γ is the full-width at half-maximum, which relates to the mode lifetime through $\Gamma = 1/(\pi\tau)$. If the observing time is shorter than the mode lifetime, then the oscillation appears as a coherent signal.

The normally distributed noise in the time domain will generate a power spectrum that follows the χ^2 distribution with two degrees of freedom (d.o.f.). To estimate parameters in the power spectrum, one can fit the power spectrum using superimposition of Lorentzian profiles. More details regarding fitting techniques can be found in ([Basu & Chaplin, 2017](#)).

1.5 Modelling techniques

1.5.1 Software tools

To compare observations with theoretical models and study the internal structure and evolution of stars, we need software tools to model stars. In this work, we use Modules

for Experiments in Stellar Astrophysics (MESA; Paxton et al., 2011, 2013, 2015, 2018, 2019), a set of open-source, robust and modular software tools to model stellar structure and evolution. Another tool is GYRE (Townsend & Teitler, 2013), an open-source stellar oscillation code that solves oscillation modes based on the stellar structure output from MESA. These software tools have become widely used and have revolutionized asteroseismology in the computational aspect. We provide a brief overview of the equations that govern the computations here. A more detailed derivation can be found in textbooks such as Aerts et al. (2010) and Basu & Chaplin (2017).

One-dimensional modelling codes assume spherically symmetric, non-rotating, and non-magnetic stellar structure, and solve a set of equations derived from the conservation of mass, momentum and energy:

$$\frac{\partial p}{\partial m} = -\frac{g}{4\pi r^2} = -\frac{Gm}{4\pi r^4}, \quad (1.24)$$

$$\frac{\partial r}{\partial m} = \frac{1}{4\pi r^2 \rho}, \quad (1.25)$$

$$\frac{\partial L}{\partial m} = \epsilon - \epsilon_\nu - \epsilon_g \quad (1.26)$$

$$\frac{\partial T}{\partial m} = -\frac{GmT}{4\pi r^4 p} \nabla, \quad \nabla = \begin{cases} \nabla_{\text{rad}} = (3\kappa p L)/(16\pi a \tilde{c} G T^4 m) & , \text{ in radiative regions} \\ \nabla_{\text{conv}} & , \text{ in convective regions} \end{cases} \quad (1.27)$$

and the equation that governs the evolution of chemical abundance X_k :

$$\frac{\partial X_k}{\partial t} = R_k + \frac{\partial}{\partial m} \left(D_k \frac{\partial X_k}{\partial m} \right) + \frac{\partial}{\partial m} (V_k X_k). \quad (1.28)$$

In these equations, t is the time, p the pressure, m the mass within r , g the gravity at r , ρ the density, L the luminosity within r , ϵ the rate of energy generation per unit mass, ϵ_ν the rate of energy lost per unit mass through neutrino cooling, ϵ_g the rate of energy released through gravitational contraction or expansion, a the radiation density constant, \tilde{c} the speed of light, G the Gravitational constant, κ the opacity, R_k the rate of change of X_k due to nuclear reactions, D_k the diffusion coefficients, and V_k the settling coefficients. The convective instability is decided by the Schwarzschild criterion. In radiative regions, the temperature gradient ∇ is obtained via the diffusion approximation. In convective region, this quantity is usually obtained through the mixing length theory (e.g. Böhm-Vitense, 1958; Henyey et al., 1965; Cox & Giuli, 1968), which involves at least one free parameter. Once supplied with necessary atmospheric boundary conditions, as well as configurations to microphysics (the equation of state, opacities, nuclear reaction rates, diffusion coefficients) and macrophysics (mixing length, convective overshoot), MESA is able to evolve stars from a protostar to a white dwarf, and to save the equilibrium structure and stellar properties at each step.

To obtain the fundamental oscillation modes for a stellar structure, a linear and first-order perturbation approach can be used to analyze all physical quantities. For example, pressure, density, and gravitation potential can be rewritten as $p + p'$, $\rho + \rho'$,

and $\Phi + \Phi'$. Using the separation of variables, the displacement vector of a gas blob can be expressed as

$$\delta r = \sqrt{4\pi} \operatorname{Re} \left\{ \left[\xi_r(r) Y_l^m(\theta, \phi) a_r + \xi_h(r) \left(\frac{\partial Y_l^m}{\partial \theta} a_\theta + \frac{1}{\sin \theta} \frac{\partial Y_l^m}{\partial \phi} a_\phi \right) \right] \exp(-i\omega t) \right\}, \quad (1.29)$$

where (r, θ, ϕ) , (a_r, a_θ, a_ϕ) , ξ_r , ξ_h , and Y_l^m represent the spherical coordinates, the base vectors, the radial displacement, the horizontal displacement, and the spherical harmonics, respectively. Using these perturbative quantities, the structure equations can be reformulated by neglecting higher-order terms and subtracting the original equilibrium equations. This exercise can lead to the oscillation equations to be solved. In the case of adiabatic oscillations, where no energy is injection or dissipated, the obtained equations are

$$\frac{d\xi_r}{dr} = - \left(\frac{2}{r} + \frac{1}{\Gamma_1 p} \frac{dp}{dr} \right) \xi_r + \frac{1}{\rho c^2} \left(\frac{S_l^2}{\omega^2} - 1 \right) p' + \frac{l(l+1)}{\omega^2 r^2} \Phi', \quad (1.30)$$

$$\frac{dp'}{dr} = \rho(\omega^2 - N^2) \xi_r + \frac{1}{\Gamma_1 p} \frac{dp}{dr} p' - p \frac{d\Phi'}{dr}, \quad (1.31)$$

and

$$\frac{1}{r^2} \frac{d}{dr} \left(r^2 \frac{d\Phi'}{dr} \right) = 4\pi G \left(\frac{p'}{c^2} + \frac{\rho \xi_r}{g} N^2 \right) + \frac{l(l+1)}{r^2} \Phi'. \quad (1.32)$$

They form a complete set of ordinary differential equations with ξ_r , p' , Φ' , and $d\Phi'/dr$ being the dependent variables. Their eigenfunctions together with eigenvalues ω can be solved by applying appropriate boundary conditions. Although GYRE uses a slightly different format for writing the oscillation equations, the fundamental idea remains the same.

1.5.2 Uncertainties of input stellar physics

Understanding model and code dependencies are crucial, since they modify predicted oscillation behaviours (see e.g. [Monteiro, 2009](#); [Silva Aguirre et al., 2020](#); [Christensen-Dalsgaard et al., 2020](#); [Cunha et al., 2021](#)). In this section, we provide a brief overview of several key physical ingredients involved in stellar modelling that are pertinent to this thesis.

Initial helium abundance. To simulate the evolution of a star, it is essential to specify not only the input physics but also the initial chemical composition, which include helium and metal abundances. Unlike metal abundances, direct measurement of helium abundances through spectroscopy is challenging due to the absence of helium lines in the atmospheres of cool stars. Hence, the initial helium abundance (Y_{init}) remains rather uncertain, as neither the initial nor the current helium abundance of the star can be precisely determined.

In stellar modelling, there is a known degeneracy between Y_{init} and stellar mass ([Lebreton & Goupil, 2014](#); [Verma et al., 2022](#)). Given a set of observational constraints such as luminosity and radius, a range of (Y_{init}, M) values can satisfy these conditions. This poses a serious limitations on the precision of mass derived from stellar modelling ([Nsamba et al., 2021](#)). Additionally, a low value of Y_{init} may result in the development

of a convective core for low-mass stellar models, significantly altering their evolutionary paths (Basu & Chaplin, 2017). Due to the lack of reliable ground truth for helium abundance, this parameter Y_{init} is often treated as a free parameter, as has been done in this thesis.

Helium abundances in the stellar envelope could be measured directly from seismology. The ionization of hydrogen and helium results in a local dip in the first adiabatic index, $\Gamma_1(r)$, which affects all acoustic waves passing through this region. This effect introduces a characteristic oscillatory modulation in mode frequencies as a function of n , in addition to the regular spacing predicted by Eq. 1.4. This principle has been successfully applied to the Sun, allowing for precise solar envelope helium abundance determined using intermediate-degree oscillation modes (Basu et al., 2004). For other stars, only low-degree modes can be observed, but this technique still remains feasible if uncertainties of frequencies are small (Mazumdar et al., 2014; Verma & Silva Aguirre, 2019; Farnir et al., 2023). This presents a promising approach for constraining Y_{init} in a select group of benchmark stars.

Alternatively, helium abundances can influence the shape of evolutionary tracks (or isochrones). Therefore, when several stars in a stellar cluster are used collectively, Y_{init} can be more precisely constrained (e.g. McKeever et al., 2019). The method can be extended to a broader range of samples.

Convection. One-dimensional stellar models employ the mixing-length theory to determine the temperature gradient in convective regions (as illustrated in Eq. 1.27). This theory depends on the mixing length parameter (α_{MLT}), which defines the distance of a convective parcel that travels before dispersing into its surroundings. Essentially, it serves as an indicator of convective efficiency within superadiabatic regions, such as the surfaces of cool stars ($T_{\text{eff}} < 6500$ K). There are a number of problems associated with this theory. For a thorough review on this subject, see Joyce & Tayar (2023).

To model a star using 1D models, the value of α_{MLT} must be specified. Traditionally, this parameter is calibrated using solar observational data (by matching L , R , age, abundances, and seismology), and then applied to non-solar targets. However, it is unclear whether this parameter has the same value for all stars and throughout all evolutionary phases (Tayar et al., 2017; Joyce & Chaboyer, 2018; Li et al., 2018; Viani et al., 2018; Valle et al., 2019). Calibrations of this parameter using 3D hydrodynamic simulations of stellar surfaces suggest slightly different values than those obtained from 1D stellar models (Trampedach et al., 2014; Magic et al., 2015), indicating 1D-calibrated α_{MLT} may be incompatible with 3D calibrations, since it also carries deficiencies that may stem from other poorly described model physics.

The uncertainty of α_{MLT} represents another significant source of uncertainty in stellar modelling, in addition to Y_{init} . It is crucial to understand and properly calibrate this parameter such that observational properties of stars can be properly described.

Angular momentum transport. Rotation and angular momentum (AM) transport are physical processes not accounted for in traditional 1D stellar models, making it an emerging and exciting research field. Observations of p-g mixed modes have advanced our understanding of AM transport within stars by probing both the core and envelope rotation rates for evolved stars. Early subgiants have been observed to exhibit near solid-body rotation (Deheuvels et al., 2020). On the RGB, the core rotates rapidly,

with periods between 10 and 20 days, whereas the surface rotates much more slowly (Beck et al., 2012; Deheuvels et al., 2014; Ceillier et al., 2017; Triana et al., 2017; Gehan et al., 2018; Fellay et al., 2021). During the HeB phase, the core experiences spin-down and rotates in the range of 30–200 days (Deheuvels et al., 2015; Mosser et al., 2012b; Tayar et al., 2019), suggesting that efficient AM transport mechanisms are at play. Various candidates for AM transport mechanisms have been proposed, including shear instabilities, meridional circulation, (Marques et al., 2013; Eggenberger et al., 2012; Ceillier et al., 2013), internal gravity waves (Fuller et al., 2014; Pinçon et al., 2016), mixed modes (Belkacem et al., 2015a,b), and magnetic fields (Cantiello et al., 2014; Eggenberger et al., 2019; den Hartogh et al., 2019; Eggenberger et al., 2022; Moyano et al., 2023). However, none of these mechanisms can fully explain the observed rotation rates across all evolutionary phases. See Aerts (2021) for a review on this topic.

Mass loss. The amount of mass loss due to radiation and pulsation is another crucial aspect of stellar evolution. In this thesis, it is particularly important to examine mass loss on the RGB, since it directly impacts the mass of zero-age helium-burning stars. Recent studies have focused on comparing mass differences between coeval RGB and RC stars within the same stellar clusters. Although the RGB and RC stars have different initial masses, that difference is relatively small compared to the amount of mass loss they experience. It can be concluded that the mass loss at the RGB tip range from $0.1 M_{\odot}$ to $0.2 M_{\odot}$ depending on the stars’ metallicities and ages (Miglio et al., 2012; Stello et al., 2016; Handberg et al., 2017; Howell et al., 2022; McDonald & Zijlstra, 2015). Substantial efforts are still required to map mass loss as a function of mass, metallicity and luminosity, and to establish connections with mass-loss prescriptions implemented in stellar models (Reimers, 1975; Schröder & Cuntz, 2005).

Mass transfer. An additional source of mass loss on the RGB is mass transfer due to binary interactions. When a star ascends the RGB and is within a binary system, its envelope could potentially fill its Roche lobe. Binary interactions can lead to stable Roche lobe overflow and also to unstable Roche lobe overflow that can include common-envelope ejection and merger (Han et al., 2020). If a red giant’s envelope is completely stripped, the star could form a subdwarf B star or a low-mass white dwarf, depending on the system’s properties (Heber, 2016; Byrne et al., 2021; Lynas-Gray, 2021). However, if only part of the envelope is removed, the result is still a red giant, seemingly indistinguishable from a regular red giant. Recent advancements in asteroseismology offer a way forward to identify such objects through their anomalous stellar properties, such as core size, radius, mass, and rotation period, which deviate from expectations for regular stars (Rui & Fuller, 2021; Deheuvels et al., 2021; Li et al., 2022c; Tayar et al., 2022b; Matteuzzi et al., 2023).

1.6 Thesis overview

The purpose of this thesis is to build upon current knowledge and further advance the techniques used to study stellar oscillations. The fundamental methodology is based on the comparison between observations and models, which enables us to address, constrain, and improve any discrepancies that may arise. The rest of the thesis is organised as follows.

Chapter 2–3 focus on *Kepler* subgiants. In Chapter 2, we extract their oscillation properties and use them as modelling inputs. In Chapter 3, we further analyse their core and envelope rotation rates to constrain the timescales of angular momentum transport.

Chapter 4–6 investigate the validity of the $\Delta\nu$ and ν_{\max} scaling relations, which are widely used for deriving stellar mass and radius. Chapter 4 tests the intrinsic scatter of the scaling relations, utilising the sharpness of population-level features that are naturally formed in stars. Chapter 5 provides a new correction for the $\Delta\nu$ scaling relation, taking into account that the surface correction for the first time. Chapter 6 evaluates the systematic offsets of the ν_{\max} relation, by comparing observed ν_{\max} with model-inferred scaling ν_{\max} constrained by individual frequencies.

Chapter 5 presents a new method for correcting the stellar surface effect, which is a well-known model deficiency that often overestimates the modelled oscillation frequencies. Traditional approaches use functions involving free parameters to correct it. We impose those parameters to relate with stellar surface parameters.

Chapter 7 constructs a mass–radius diagram for red clump stars. Thanks to the remarkable precision provided by asteroseismology, we found two types of stars that do not conform to single stellar evolution and we explained their existence using dramatic mass loss due to binary evolution.

2 Oscillation properties of subgiant stars

The paper produced in this chapter is published as [Li, Yaguang et al. \(2020b\)](#). The work is a collaborative effort. I created the pipeline and extracted the oscillation parameters. Tim Bedding, Tanda Li, and Shaolan Bi provided the initial idea. Dennis Stello, Yixiao Zhou and Timothy R. White contributed to the interpretation of the results. I wrote the paper, and all authors (especially Tim Bedding) commented on the manuscript. The result of this paper has been used as modelling input in the companion study: [Li, Tanda et al. \(2020a\)](#).

Asteroseismology of 36 *Kepler* subgiants – I. Oscillation frequencies, linewidths, and amplitudes

Yaguang Li¹,^{2,3} Timothy R. Bedding^{2,3} Tanda Li^{2,3} Shaolan Bi,¹★
Dennis Stello,^{2,3,4} Yixiao Zhou⁵ and Timothy R. White^{2,3}

¹Department of Astronomy, Beijing Normal University, Beijing 100875, China

²Sydney Institute for Astronomy (SIfA), School of Physics, University of Sydney, Sydney, NSW 2006, Australia

³Stellar Astrophysics Centre, Department of Physics and Astronomy, Aarhus University, Ny Munkegade 120, DK-8000 Aarhus C, Denmark

⁴School of Physics, University of New South Wales, Kensington, NSW 2052, Australia

⁵Research School of Astronomy and Astrophysics, Australian National University, Canberra, ACT 2611, Australia

Accepted 2020 May 7. Received 2020 May 7; in original form 2019 December 20

ABSTRACT

The presence of mixed modes makes subgiants excellent targets for asteroseismology, providing a probe for the internal structure of stars. Here we study 36 *Kepler* subgiants with solar-like oscillations and report their oscillation mode parameters. We performed a so-called peakbagging exercise, i.e. estimating oscillation mode frequencies, linewidths, and amplitudes with a power spectrum model, fitted in the Bayesian framework and sampled with a Markov chain Monte Carlo algorithm. The uncertainties of the mode frequencies have a median value of 0.180 μHz . We obtained seismic parameters from the peakbagging, analysed their correlation with stellar parameters, and examined against scaling relations. The behaviour of seismic parameters (e.g. $\Delta\nu$, ν_{max} , ϵ_p) is in general consistent with theoretical predictions. We presented the observational p – g diagrams, namely γ_1 – $\Delta\nu$ for early subgiants and $\Delta\Pi_1$ – $\Delta\nu$ for late subgiants, and demonstrate their capability to estimate stellar mass. We also found a $\log g$ dependence on the linewidths and a mass dependence on the oscillation amplitudes and the widths of oscillation excess. This sample will be valuable constraints for modelling stars and studying mode physics such as excitation and damping.

Key words: stars: low-mass – stars: solar-type – stars: oscillations.

1 INTRODUCTION

Some of the first detections of solar-like oscillations, using ground-based spectroscopy, were in subgiant stars such as η Boo (Christensen-Dalsgaard, Bedding & Kjeldsen 1995; Kjeldsen et al. 1995, 2003; Guenther & Demarque 1996; Di Mauro et al. 2003a; Guenther 2004; Carrier, Eggenberger & Bouchy 2005), β Hyi (Bedding et al. 2001, 2007; Carrier et al. 2001; Fernandes & Monteiro 2003; Di Mauro, Christensen-Dalsgaard & Paternò 2003b; Brandão et al. 2011), ν Ind (Bedding et al. 2006; Carrier et al. 2007), and μ Her (Bonanno et al. 2008; Pinheiro & Fernandes 2010; Grundahl et al. 2017). Observations by the space telescopes *CoRoT* and *Kepler* enabled high-quality photometry with high duty cycle. These include subgiants such as HD 49385 (Deheuvels & Michel 2010; Paxton et al. 2013), HD 169392A (Mathur et al. 2013), KIC 11026764 (‘Gemma’; Metcalfe et al. 2010), KIC 11395018 (‘Boogie’; Mathur et al. 2011), KIC 10920273 and KIC 10273246

(‘Scully’ and ‘Mulder’; Campante et al. 2011), the α -enhanced star KIC 7976303 (Ge et al. 2015), and the binary twin system KIC 7107778 (Li et al. 2018).

Beginning with η Boo, it was realized that subgiants show mixed modes (Christensen-Dalsgaard et al. 1995), which are now recognized as a feature in all evolved stars. Main-sequence (MS) dwarfs with solar-like oscillations host a convective envelope, which excites and propagates pressure (p) modes. In subgiants, the so-called mixed modes that result from coupling between the pressure mode cavity and gravity (g) mode cavity carry information from the core and have observable amplitudes on the surface.

The mixed modes have long been realized to have strong diagnostic potential because the frequencies of g modes, which we denote by γ , evolve quite rapidly (Christensen-Dalsgaard et al. 1995). Bedding (2014) suggested a new asteroseismic diagram, the p – g diagram, which plots γ versus the large separation of p modes $\Delta\nu$. By comparing observed values of γ and $\Delta\nu$ with stellar models on this diagram, a stellar mass can be estimated. Benomar et al. (2012) showed that the coupling strength (see Section 3) is a strong indicator of evolutionary stage in subgiants. These suggestions of the diagnostic power of mixed modes were confirmed with

* E-mail: yali4742@uni.sydney.edu.au (YL); tim.bedding@sydney.edu.au (TRB); bisl@bnu.edu.cn (SB)

modelling. When modelling Gemma (KIC 11026764), Metcalfe et al. (2010) showed that the asteroseismic age could be constrained to a precision of 15 percent, which was set by the choice of input physics. Li et al. (2019) modelled μ Her and demonstrated that the asteroseismic age did not significantly change as a function of the mixing-length parameter, or the initial helium abundance. In addition to global parameters, the mixed modes also shed light on the interior physics of stars, for example, constraining the buoyancy frequency profile (Li et al. 2019), internal angular momentum transport (Deheuvels et al. 2014; Eggenberger et al. 2019), and convective core overshooting (Deheuvels et al. 2016).

A complete analysis of oscillation modes has been made for *Kepler* observations of 35 planet-host stars (Davies et al. 2016) and 66 MS stars (Lund et al. 2017), the so-called LEGACY sample. However, similar analyses for subgiants have only been done on a subset of *Kepler* data (e.g. Appourchaux et al. 2012). Therefore, it is valuable to gather and analyse subgiants with the full set of *Kepler* observations, given the great promise of mixed modes. In this paper, we fit the oscillation modes and analyse the fitted frequencies, linewidths, and amplitudes from the fit. In a companion paper (Li et al. submitted, hereafter Paper II), we perform a detailed modelling to these stars with the constraints of frequencies obtained here.

2 OBSERVATIONS

We considered *Kepler* targets observed in a short-cadence mode, which samples at an integration time $\Delta t = 58.89$ s, or frequency $f_s = 1/\Delta t = 16980.8$ μHz . There are about 5000 stars observed in this mode, and we detected about 50 subgiants. In this context, we define subgiants as stars showing oscillations of mixed modes, recognized as mode bumping (see Section 3.1 for a detailed discussion), which starts around the time of hydrogen exhaustion in the core. However, we required that the density of the mixed modes should be low enough, such that $\Delta\Pi_1 > \Delta\nu/\nu^2$, where $\Delta\Pi_1$ is the period spacing of dipolar g modes. This occurs around the subgiant phase. Only subgiants with high signal-to-noise ratios (S/Ns) were selected to avoid any ambiguity of the correct assignment of the spherical degree l of each mode (see Section 3.1). Further, we required the observation duration, denoted by t_{obs} , to be at least two months. This resulted in a total of 36 subgiants that we analyse here.

The atmospheric parameters (T_{eff} and $[\text{Fe}/\text{H}]$) were adopted from the KIC DR25 release (Mathur et al. 2017). Table 1 lists the 36 stars in our sample along with t_{obs} , nicknames used in previous papers and references to any previous studies. Fig. 1 shows the targets in the $\Delta\nu - T_{\text{eff}}$ plane. They extend from the MS turn-off phase to the bottom of red giant branch (RGB). The MS stars in the *Kepler* LEGACY sample (Lund et al. 2017) are also shown.

We used light curves measured from simple aperture photometry (SAP) by the Kepler Science Center.¹ We corrected instrumental effects with the KASOC FILTER.² For a full description of this reduction procedure, see García et al. (2011) and Handberg & Lund (2014). Briefly, it constructs moving-median high-pass filters, one with $\tau_{\text{long}} = 1/2$ d, and another with $\tau_{\text{short}} = 1/24$ d. Trends longer than $1/\tau_{\text{long}} \sim 23$ μHz are removed, and any sharp feature that could produce drastically different signals for the two filters are eliminated. The light curves were converted into relative flux in ppm (parts per million) and we calculated power spectra by a Lomb–Scargle Periodogram algorithm (Lomb 1976; Scargle 1982),

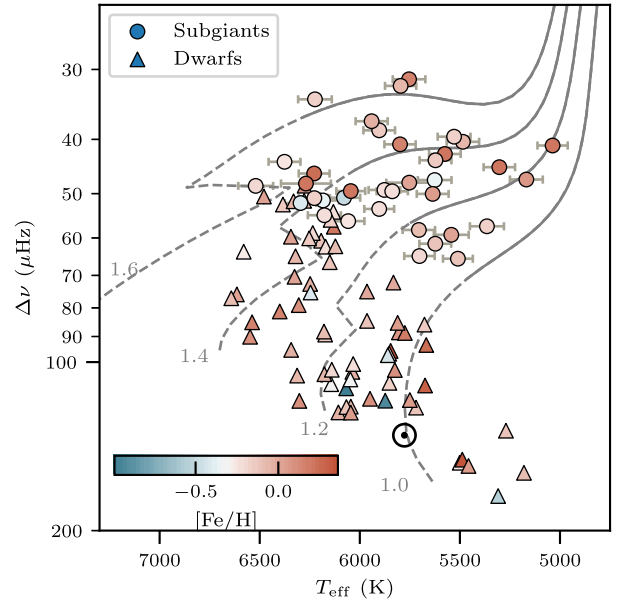


Figure 1. Asteroseismic H-R diagram showing $\Delta\nu$ versus T_{eff} for the 36 subgiants shown as black circles colour-coded by metallicity. For comparison, the LEGACY sample (Lund et al. 2017) is together shown in triangles labelled as dwarfs. The Sun is marked by the usual symbol. The theoretical evolutionary tracks with solar metallicity (Stello et al. 2013) are shown before (dashed lines) and after (solid lines) the exhaustion of central hydrogen, with each track labelled with mass in solar units.

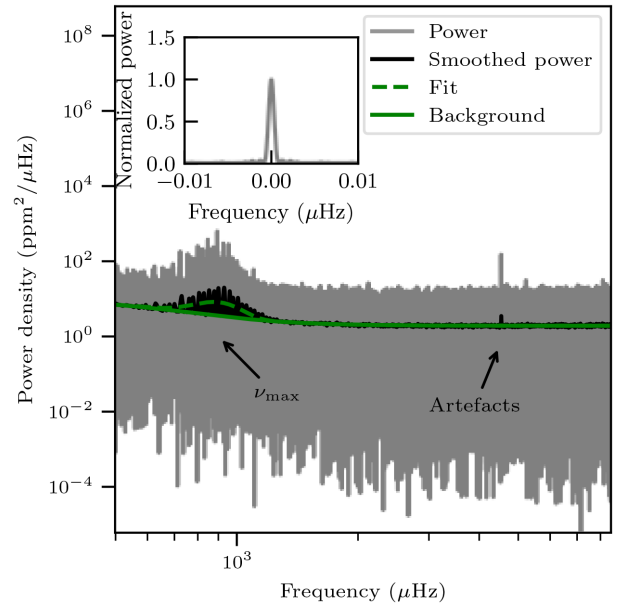


Figure 2. Power spectrum density of Gemma (KIC 11026764). The original (grey), smoothed (black), and fitted power spectra (green) are shown. The peaks around 4500 μHz are artifacts (Gilliland et al. 2010). The inset shows the normalized spectral window.

equivalent to a sine-wave fitting, as implemented in ASTROPY (Astropy Collaboration 2013, 2018). The power density spectra were constructed by multiplying the power by the total observing time (Kjeldsen & Bedding 1995). Fig. 2 uses Gemma (KIC 11026764) as an example to illustrate the power density spectrum and the spectral window. The former is comprised of a background and a group

¹<https://archive.stsci.edu/kepler/>.

²<https://github.com/tasoc/corrections>.

Table 1. Observational properties.

KIC	Nickname	t_{obs} (d)	T_{eff} (K)	$\log g$ (cgs; dex)	[Fe/H] (dex)	References
2991448	–	204	5623 ± 80	3.98 ± 0.02	-0.10 ± 0.15	–
3852594	–	540	6296 ± 78	4.02 ± 0.14	-0.40 ± 0.15	–
4346201	–	108	6058 ± 81	3.97 ± 0.01	-0.24 ± 0.17	–
5108214	–	222	5799 ± 78	3.81 ± 0.07	0.16 ± 0.15	–
5607242	–	1031	5485 ± 81	3.76 ± 0.06	-0.06 ± 0.15	a
5689820	–	506	5037 ± 76	3.76 ± 0.06	0.21 ± 0.15	b
5955122	Rhapsody	988	5877 ± 79	3.87 ± 0.01	-0.22 ± 0.15	a
6064910	–	532	6376 ± 80	3.83 ± 0.01	-0.26 ± 0.17	–
6370489	–	97	6184 ± 80	3.92 ± 0.01	-0.36 ± 0.15	–
6442183	Dougal	822	5702 ± 76	4.00 ± 0.01	-0.20 ± 0.15	c, d
6693861	–	565	5626 ± 84	3.84 ± 0.02	-0.36 ± 0.15	–
6766513	–	534	6227 ± 78	3.93 ± 0.02	-0.18 ± 0.15	–
7174707	–	1031	5168 ± 82	3.71 ± 0.12	0.07 ± 0.15	–
7199397	–	1182	5903 ± 79	3.76 ± 0.07	-0.14 ± 0.15	e
7668623	–	112	6228 ± 77	3.87 ± 0.02	0.24 ± 0.15	–
7747078	–	986	5903 ± 74	3.90 ± 0.01	-0.22 ± 0.15	a
7976303	John	962	6079 ± 81	3.89 ± 0.06	-0.48 ± 0.15	a
8026226	Gypsy	305	6224 ± 84	3.70 ± 0.06	-0.18 ± 0.17	a
8524425	Katrina	1006	5543 ± 87	3.97 ± 0.01	0.02 ± 0.17	a
8702606	–	980	5529 ± 82	3.76 ± 0.06	-0.16 ± 0.15	a, b
8738809	–	341	6045 ± 72	3.90 ± 0.01	0.20 ± 0.12	–
9512063	–	110	5838 ± 78	3.88 ± 0.02	-0.22 ± 0.15	–
10018963	Klaas	936	6177 ± 82	3.93 ± 0.01	-0.22 ± 0.17	a
10147635	–	761	5941 ± 80	3.75 ± 0.02	-0.02 ± 0.15	–
10273246	Mulder	705	6269 ± 124	4.41 ± 0.07	0.21 ± 0.15	f
10593351	–	528	5754 ± 82	3.66 ± 0.06	0.16 ± 0.15	–
10873176	–	122	6520 ± 87	3.90 ± 0.01	-0.20 ± 0.28	–
10920273	Scully	532	5365 ± 85	3.78 ± 0.12	-0.16 ± 0.15	f
10972873	–	878	5705 ± 81	3.96 ± 0.02	-0.08 ± 0.15	–
11026764	Gemma	985	5636 ± 80	3.89 ± 0.06	0.04 ± 0.15	a
11137075	Zebedee	530	5510 ± 74	4.00 ± 0.01	-0.12 ± 0.12	c
11193681	–	1026	5575 ± 79	3.79 ± 0.06	0.21 ± 0.15	a
11395018	Boogie	562	5753 ± 114	3.65 ± 0.18	0.02 ± 0.15	a, g
11414712	Jingle	943	5622 ± 80	3.80 ± 0.06	-0.14 ± 0.15	a
11771760	–	1030	5796 ± 78	3.67 ± 0.06	-0.06 ± 0.17	a
12508433	–	999	5303 ± 78	3.83 ± 0.06	0.20 ± 0.15	a, b

References. (a) Appourchaux et al. (2012); (b) Deheuvels et al. (2014); (c) Tian et al. (2015); (d) Appourchaux et al. (2014); (e) Davies et al. (2016); (f) Campante et al. (2011); (g) Mathur et al. (2011).

of peaks with a Gaussian-like envelope centred on ν_{max} . Although there are small gaps in the original data, they have a negligible influence on the shape of oscillation modes. This can be seen from the fact that the spectral window has sidelobes with very low power.

3 PARAMETER ESTIMATION

3.1 Mode identification

Each oscillation mode is associated with three quantum numbers (n, l, m). The first step in mode identification is to assign an l -degree to each peak. In the asymptotic regime ($n \gg l$) of p modes (Tassoul 1980; Gough 1986), this is straightforward because modes follow regular patterns. The frequencies are approximately equally spaced by $\Delta\nu$:

$$\nu_p(n_p, l) \approx \Delta\nu \left(n_p + \frac{l}{2} + \epsilon_p \right) - \delta\nu_{0l}, \quad (1)$$

where $\Delta\nu$ is the separation between adjacent radial modes, ϵ_p is the offset of the pattern, and the small separation $\delta\nu_{0l}$ defines the

frequency differences between $l = 0$ and l . The g modes, which we do not observe directly, are approximately equally spaced in period in the asymptotic regime:

$$\Pi_g(n_g, l) = \nu_g^{-1}(n_g, l) \approx \Delta\Pi_l (n_g + \epsilon_g), \quad (2)$$

where $\Delta\Pi_l$ and ϵ_g are the period spacing and offset for g modes, respectively. Shibahashi (1979) derived an asymptotic spacing for mixed modes. Specifically, for dipolar modes ($l = 1$), the mixed-mode frequencies ν_m satisfy

$$\tan\theta_p = q \tan\theta_g, \quad (3)$$

where

$$\theta_p = \frac{\pi}{\Delta\nu} (\nu_m - \nu_p), \quad (4)$$

$$\theta_g = \frac{\pi}{\Delta\Pi_1} \left(\frac{1}{\nu_m} - \frac{1}{\nu_g} \right), \quad (5)$$

and q is a coupling factor determined by the width of the evanescent zone (Mosser et al. 2015). Less-evolved subgiants have large period spacings, with one g mode often coupling with several p modes. The coupled modes can be bumped very far away from their regular p-mode spacings. By replicating echelle diagrams

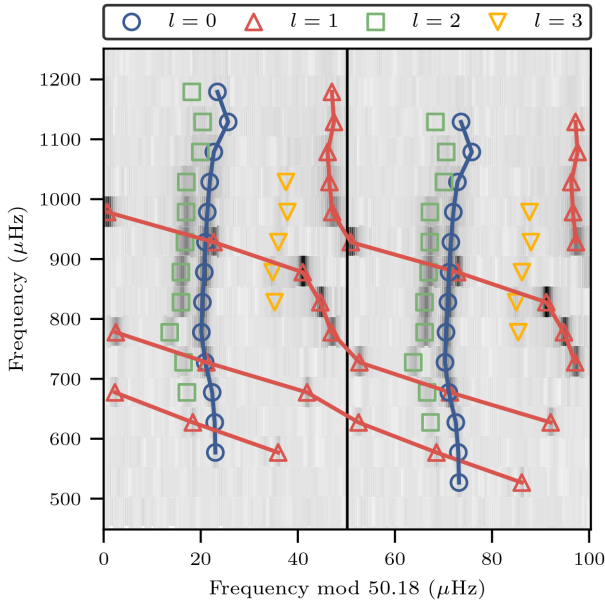


Figure 3. Replicated echelle diagram for Gemma (KIC 11026764). By shifting one $\Delta\nu$ downwards for the right replicate, the dipolar modes can be traced by a single line with one mode per horizontal row. The grey scale denotes the square root of S/N to enhance contrast. The symbols represent extracted frequencies.

horizontally, a line can trace all mixed modes, which helps mode identification (Bedding 2012; Benomar et al. 2012). See Fig. 3 for an illustration. Using this method, we were able to make unambiguous identifications for mixed dipolar modes, which still have a detectable amplitude even when they are bumped by a large amount. However, that is not the case for quadrupolar ($l = 2$) modes due to their weaker couplings. Therefore, in most cases, we only expect to detect one mixed quadrupolar mode in each order, even though sometimes two should be present. The same is true for octupolar ($l = 3$) modes. To sum up, the dipolar mixed modes follow equation (3) closely, and the radial, quadrupolar and octupolar modes are distributed regularly, approximately, as described by equation (1).

We first obtained a crude estimate of $\Delta\nu$ by tuning the horizontal width of the echelle diagram such that the ridge of radial modes was vertical. To identify modes in each star, we smoothed the power spectrum and folded by $\Delta\nu$ to create a collapsed power spectrum. This was cross-correlated with a template spectrum comprising three peaks, two narrower ($l = 0$ and 2) and one wider ($l = 1$), to simulate the ridges. The value of ϵ_p , which defines the location of $l = 0$, could be correctly identified according to the lag at which the correlation coefficient was the largest. The modes satisfying $(\nu/\Delta\nu \bmod 1) \in [\epsilon_p - 0.04, \epsilon_p + 0.04]$, $[\epsilon_p - 0.12, \epsilon_p - 0.04]$, and $[\epsilon_p + 0.31, \epsilon_p + 0.39]$ were labelled as $l = 0, 2$, and 3, respectively. These ranges were first empirically chosen. The reason is that $\delta\nu_{0l}$ approximately follows a linear trend with $\Delta\nu$ and the slope is consistent with the ranges defined by those numbers (see Section 4). All other modes were provisionally assigned as $l = 1$, noting that some $l = 0, 2$, and 3 modes could actually be $l = 1$. We used the relative height ($l = 1$ modes are typically higher) and the regularity of those modes (equation 1) to help resolve the ambiguity. All labels were further confirmed in echelle diagrams using the method mentioned above. We identified all modes within $\pm 8\Delta\nu$ around ν_{\max} . The identified peaks were used as inputs for the peakbagging.

3.2 Power spectrum model

We now describe the model used to fit the power spectrum. First, we consider the background caused by granulation, modelled as a sum of Lorentzian profiles:

$$B(\nu) = \sum_{i=1}^n \frac{2\sqrt{2}}{\pi} \frac{a_i^2/b_i}{1 + (\nu/b_i)^{c_i}}. \quad (6)$$

The number of power profiles was set to be $n = 1$ or 2 (Harvey 1985; Kallinger et al. 2014), subject to the goodness of fit, which is sufficient to account for the background near ν_{\max} . Secondly, we describe the signal of oscillations. For a mode with quantum number (n, l, m), we adopted a power spectrum model

$$L_{nlm}(\nu) = \frac{\mathcal{E}_{lm}(i^*) 2A_{nl}^2 / (\pi\Gamma_{nl})}{1 + 4(\nu - \nu_{nl} + m\nu_{s,nl})^2 / \Gamma_{nl}^2} \quad (7)$$

to account for oscillations, where the frequency ν_{nl} , linewidth Γ_{nl} , amplitude A_{nl} , and rotational splitting $\nu_{s,nl}$ varies with n and l (Anderson, Duvall & Jefferies 1990). The relative height within a multiplet depends on the inclination angle i^* of the star and is modulated by a visibility function:

$$\mathcal{E}_{lm}(i^*) = \frac{(l - |m|)!}{(l + |m|)!} \left[P_l^{|m|}(\cos i^*) \right]^2, \quad (8)$$

where $P_l^{|m|}$ are Legendre functions (Gizon & Solanki 2003). The final model to fit the whole power spectrum was

$$M(\nu) = \eta^2(\nu) \left[\sum_{n=n_{\min}}^{n_{\max}} \sum_{l=0}^3 \sum_{m=-l}^l L_{nlm}(\nu) + B(\nu) \right] + W. \quad (9)$$

We used a frequency-independent constant W to account for white/photon noise. The apodization of the signal due to the integration time $\Delta t = 58.89$ s was

$$\eta^2(\nu) = \frac{\sin^2(\pi\nu\Delta t)}{(\pi\nu\Delta t)^2}. \quad (10)$$

The free parameters to fit the power spectrum were $\theta = \{\nu_{nl}, A_{nl}, \Gamma_{nl}, \nu_{s,nl}, i^*, a_i, b_i, c_i, W\}$.

3.3 Fitting method

We estimated the model parameters in the Bayesian framework (Handberg & Campante 2011). Given data D , model M , and prior information I , the parameters θ were estimated via posterior probability using Bayes' theorem:

$$p(\theta|D, M, I) = \frac{p(\theta|M, I)p(D|\theta, M, I)}{p(D|M, I)}. \quad (11)$$

The posterior probability can be seen as a product of the prior and the likelihood function, divided by the Bayesian evidence, which is the marginalization of that product over all parameter space.

We utilized three kinds of prior functions. The first was a uniform prior, which sets the prior probability as a constant over a parameter range:

$$p(\theta|M, I) = \begin{cases} \frac{1}{\theta_{\max} - \theta_{\min}}, & \theta_{\min} < \theta < \theta_{\max} \\ 0, & \text{otherwise} \end{cases}. \quad (12)$$

We used uniform priors for most parameters. For example, the priors on the frequencies, ν_{nl} , were set to be 3- μ Hz ranges centred around their initial guessed values. The inclination angle was assigned a uniform prior across $[-\pi/2, \pi]$ and folded to $[0, \pi/2]$ after sampling. We also tested an isotropic prior for the inclination, but found no

significant bias on mode parameters. The second is a modified Jeffreys prior, which was set for the linewidths and amplitudes:

$$p(\theta|M, I) = \begin{cases} \frac{1}{\theta + \theta_{\text{uni}}} \frac{1}{\log((\theta_{\text{uni}} + \theta_{\text{max}})/\theta_{\text{uni}})}, & 0 < \theta < \theta_{\text{max}} \\ 0, & \text{otherwise} \end{cases} \quad (13)$$

We tested the impact of adopting uniform priors for these two particular parameters. The amplitudes do not present obvious bias while the linewidths are typically overestimated using the uniform priors. Despite the present bias, more than 95 per cent modes in our sample agree within 1σ . For the splitting frequency, $\nu_{s, nl}$, we used the third prior, a flat prior with a half-Gaussian:

$$p(\theta|M, I) = \begin{cases} 0, & \theta < S \\ C, & S \leq \theta < U \\ C \cdot \exp\left[-\frac{(\theta - U)^2}{2\sigma^2}\right], & \theta \geq U \end{cases}, \quad (14)$$

where $C = (U - S + \sqrt{\pi/2}\sigma)^{-1}$. We applied this prior to $\nu_{s, nl}$ with $S = 0$, $U = 1$, and $\sigma = 0.5 \mu\text{Hz}$ (Deheuvels et al. 2014).

Gaussian noise in the time domain translates into a χ^2 distribution with 2 degrees of freedom in the frequency domain (in power). Assuming all frequency bins, indexed by i in the power spectrum, are statistically independent, the logarithm of the likelihood function is

$$\ln p(D|\theta, M, I) = -\sum_i \left[\ln M_i(\theta) + \frac{D_i}{M_i(\theta)} \right]. \quad (15)$$

We used an H1 (odds ratio) approach to test whether a frequency range contains a mode (Appourchaux et al. 2012; Corsaro & De Ridder 2014; Davies et al. 2016). H1 is the hypothesis that a range of a power spectrum contains the mode, while H0 is the null hypothesis. In short, we computed the Bayes factor $\ln K = \ln p(D|M_1, I) - \ln p(D|M_0, I)$ and assessed it based on the Kass & Raftery (1995) scale:

$$\ln K = \begin{cases} < 0 & \text{favours H0} \\ 0-1 & \text{not worth more than a bare mention} \\ 1-3 & \text{positive} \\ 3-5 & \text{strong} \\ > 5 & \text{very strong} \end{cases}. \quad (16)$$

3.4 Fitting details

Based on the methods mentioned in the previous sections, we fitted the data as follows:

- (i) The power spectrum was initially fitted with equation (9) but the sum of Lorentzians was replaced by a single Gaussian profile centred around ν_{max} (see Fig. 2). The background spectrum was determined from this fit. By dividing the signal by the background, we obtained the S/N spectrum, which fluctuates around 1.
- (ii) We selected seven modes with the highest amplitudes to fit simultaneously and to determine the inclination angle by maximizing the posterior probability.
- (iii) The power spectrum was divided into segments and modes were fitted in each segment separately with a fixed inclination determined in step (ii). The sizes of the segments were based on the proximity of consecutive mode frequencies. Any two modes closer than $10 \mu\text{Hz}$ were grouped into the same segment. There was a minimum of one and a maximum of five modes per segment.

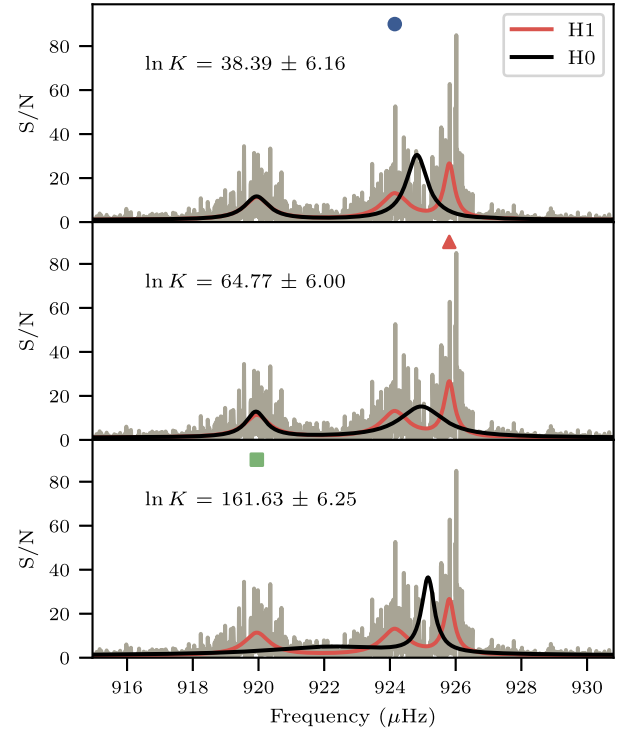


Figure 4. Significance tests for three modes of Gemma (KIC 11026764). Each panel presents the fits of the mode marked by the symbol, under H1 and H0 hypotheses separately. All three modes show very strong detections according to the Kass & Raftery (1995) scale.

The estimation of each parameter was obtained by marginalizing the posterior probability and calculating median and 68 per cent credible limit values.

(iv) The Bayes factor was calculated for each mode to evaluate its significance, by comparing the Bayesian evidence with or without that mode in the model. Fig. 4 shows the fit of the three modes in a segment. All of them have very strong detections.

We developed PYTHON software called SOLARLIKEPEAKBAGGING,³ providing a wrapper for the Markov chain Monte Carlo (MCMC) sampling algorithm implemented in EMCEE (Goodman & Weare 2010; Foreman-Mackey et al. 2013), also featuring customizable Bayesian statistics, models, and other fitting algorithms. For the above fits, the sampler was chosen either to be an affine-invariant ensemble sampler (step ii) or a parallel-tempering sampler with 20 temperatures (step iii), depending on whether the Bayes factor was calculated. We initialized 500 walkers with values adopted from a least-squares fit, then burned-in for 1000 steps and iterated for 2000 steps. After each run, we checked convergence and the goodness of sampling by several metrics, including auto-correlation time, acceptance fraction, the evolution of model parameters, and the shapes of the marginal probability distributions.

3.5 Fitting results

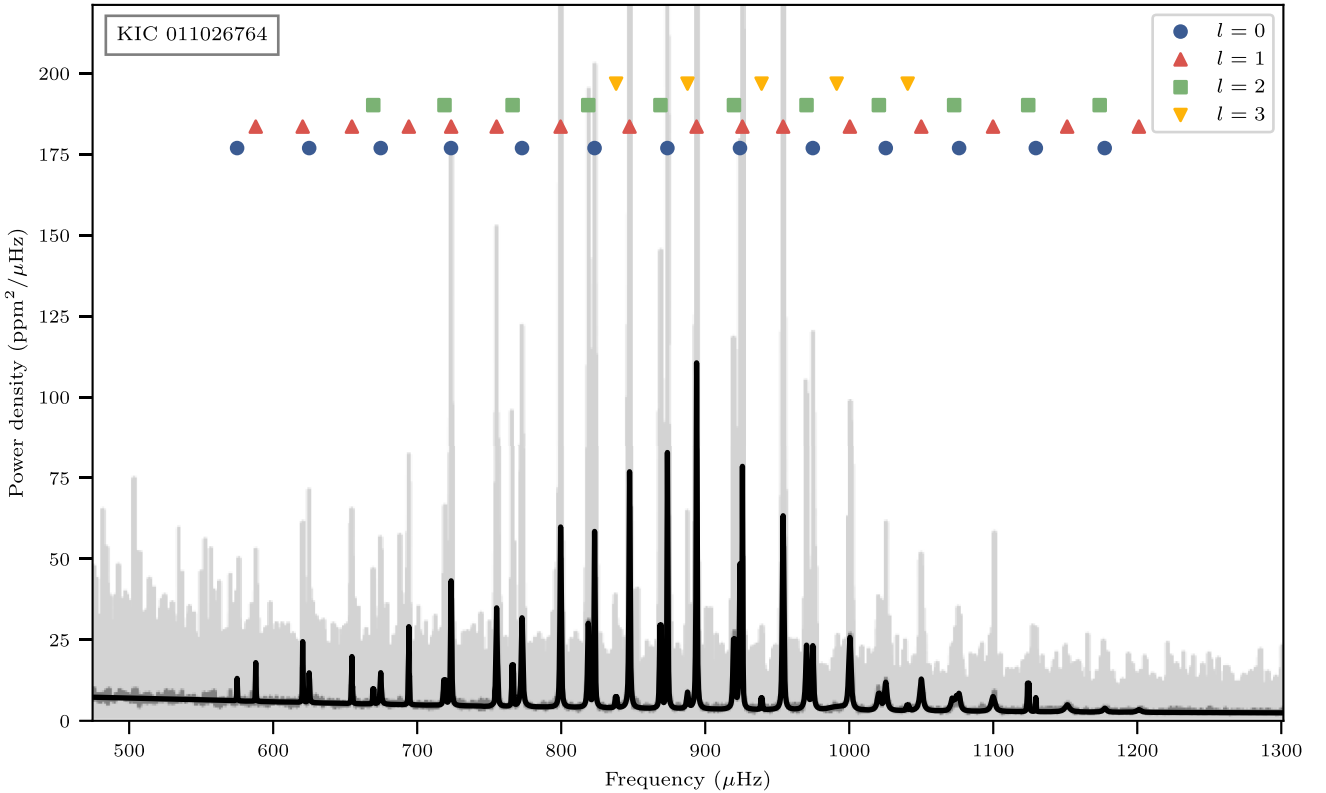
We present mode frequencies, amplitudes, and linewidths for $m = 0$ modes in Table 2. The rotational splittings will be comprehensively studied in a future paper. Fig. 5 shows the power spectrum of Gemma

³<https://github.com/parallelpro/SolarlikePeakbagging>.

Table 2. Mode parameters obtained from the peakbagging.

KIC	l	ν_{nl} (μHz)	Γ_{nl} (μHz)	A_{nl} (ppm)	$\ln K$
2991448	0	889.34 ± 0.312	0.79 ± 0.96	5.72 ± 1.53	2.16 ± 0.75
2991448	0	949.46 ± 1.111	8.02 ± 2.37	12.95 ± 1.61	3.61 ± 0.98
2991448	0	1011.17 ± 0.202	1.15 ± 0.46	9.47 ± 1.23	20.49 ± 4.32
2991448	0	1072.78 ± 0.099	0.76 ± 0.24	14.78 ± 1.49	39.42 ± 2.54
2991448	0	1134.18 ± 0.113	0.89 ± 0.28	14.21 ± 1.38	47.86 ± 2.81
2991448	0	1195.89 ± 0.547	3.29 ± 1.72	13.37 ± 2.38	5.40 ± 2.13
2991448	0	1257.81 ± 0.969	3.53 ± 2.63	10.04 ± 2.96	2.68 ± 1.52
2991448	0	1319.52 ± 1.294	3.00 ± 3.56	5.09 ± 3.29	0.18 ± 1.20
2991448	1	857.88 ± 0.384	0.97 ± 0.79	5.88 ± 1.62	-0.21 ± 0.69
2991448	1	915.60 ± 0.153	0.81 ± 0.32	9.62 ± 1.27	19.19 ± 1.16

Notes. These are $m = 0$ modes. Only the first 10 rows are shown. The full table is available online.

**Figure 5.** Power spectrum of Gemma (KIC 11026764). The fitted power spectrum (black) is overlaid on the original power spectrum (light grey).

(KIC 11026764) with fitted mode frequencies overlaid. We present the plots of the other stars in Appendix A.

In Fig. 6, we show the histograms of uncertainties. The median value of frequency uncertainties is $0.180 \mu\text{Hz}$. As expected, the uncertainty is a function of S/N. The typical uncertainty is $0.1 \mu\text{Hz}$ for $S/N = 3$. The median uncertainties of linewidths are 31.7 per cent and amplitudes are 10.1 per cent.

As a check, we can consider the classical maximum likelihood estimator (MLE; Libbrecht 1992; Toutain & Appourchaux 1994; Ballot et al. 2008). This calculates uncertainties by inverting the Hessian matrix whose elements are the second derivatives of the likelihood function to the parameters. The Cramér–Rao bound states that an unbiased MLE reaches the lowest variance bound, so any other unbiased estimators are expected to obtain a larger variance. Libbrecht (1992) derived an analytical form of the uncertainty. We

found the estimated uncertainties derived from the MCMC-based posterior distributions were typically larger than those obtained from the above analytical forms, by factors of 1.15 (frequency), 1.18 (linewidth), and 1.41 (height), respectively. Thus, the uncertainties are safe to use for modelling.

4 MODE FREQUENCIES

We fitted the radial mode frequencies with equation (1) to estimate $\Delta\nu$ and ϵ_p . The errors were considered within the Bayesian framework; thus, they were propagated from the priors and likelihoods. The likelihood function was selected to reflect the residuals between data and the models, weighted by uncorrelated uncertainties from both dependent and independent variables, as normal distributions.

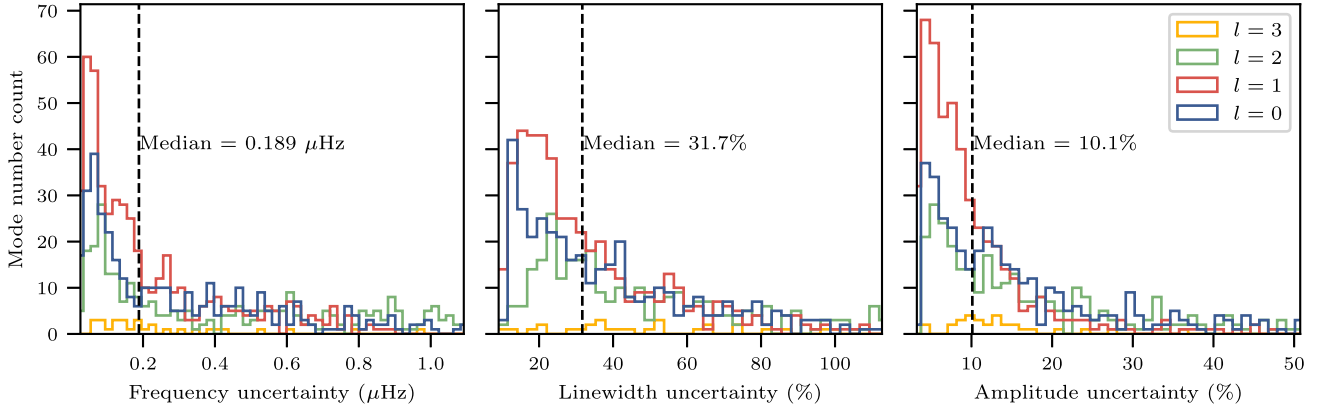


Figure 6. Histograms of the uncertainties for measured mode frequencies (left-hand panel), linewidths (middle panel), and amplitudes (right-hand panel). The linewidths and amplitudes are shown in relative uncertainty.

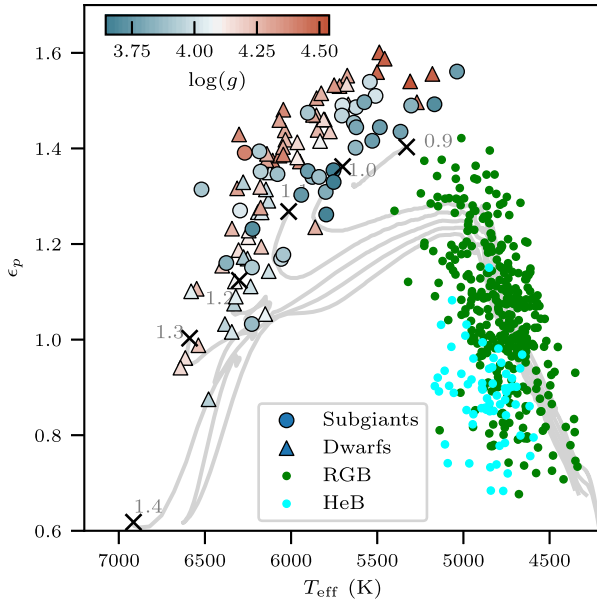


Figure 7. ϵ_p versus T_{eff} with colour-coded $\log g$. The measurement of red giants were adopted from Huber et al. (2010). The theoretical evolutionary tracks (White et al. 2011b) are labelled with mass in solar units. The crosses mark the zero-age MS.

The p-mode offset ϵ_p is sensitive to the lower and upper turning points of a mode (e.g. Gough 1986). It has been demonstrated to vary with T_{eff} and $\Delta\nu$ (White et al. 2011b; Hon, Stello & Yu 2018), and was used to resolve ambiguous mode identification problems found in F-type dwarfs (White et al. 2012) and to discriminate between RGB and helium-core-burning (HeB) stars (Kallinger et al. 2012). The upper turning point lies at the surface, where T_{eff} and $\log g$ are relevant quantities, so it may be conjectured that ϵ_p is related to both of them. In Fig. 7, we present ϵ_p as a function of T_{eff} . As Ong & Basu (2019) pointed out, ϵ_p depends on the method of measurement, so we recalculated the ϵ_p of the MS dwarfs from Lund et al. (2017) using our approach. As the figure shows, the general trend of ϵ_p in subgiants follows a similar pattern as for dwarfs. We also identify a dependence on $\log g$: stars with similar T_{eff} but smaller $\log g$ have lower ϵ_p . The dwarf stars, which have higher $\log g$, sit above the subgiants on the $\epsilon_p - T_{\text{eff}}$ diagram. In the bottom panel of Fig. 8, we present ϵ_p as a function of $\Delta\nu$. The obvious offset between

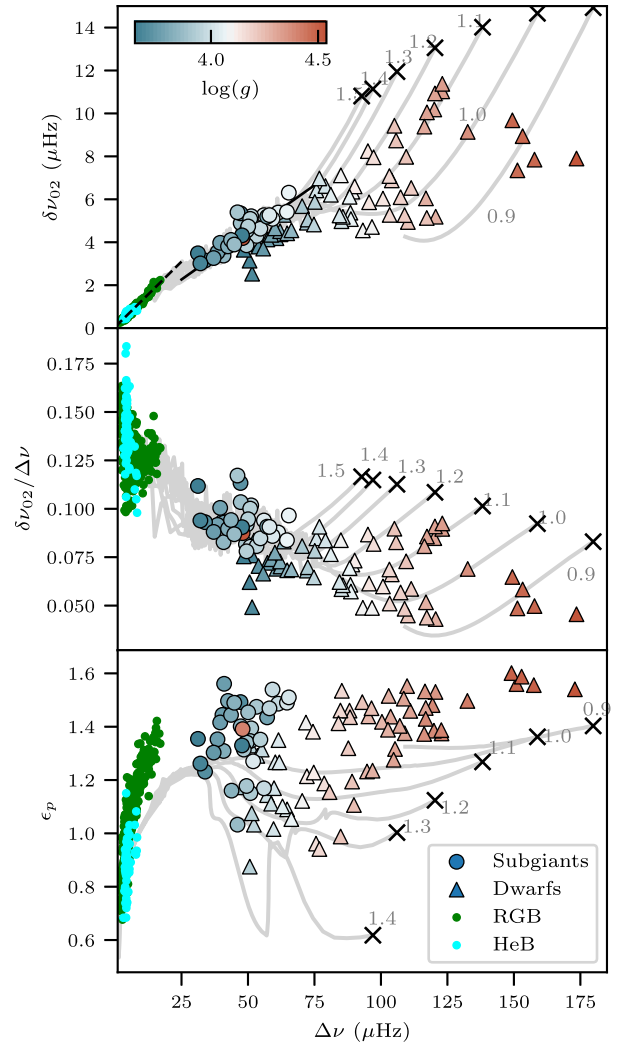


Figure 8. Top and middle panels: C–D diagrams, which show the small separation $\delta\nu_{02}$ as a function of $\Delta\nu$, with colour-coded $\log g$. The solid line is a linear fit to the subgiants, and the dashed line is a similar fit to low-luminosity red giants (Bedding et al. 2010). Bottom panel: ϵ_p versus $\Delta\nu$. The measurement of dwarfs and red giants were adopted from Lund et al. (2017) and Huber et al. (2010), respectively. The theoretical evolutionary tracks (White et al. 2011b) are labelled with mass in solar units with crosses marking the zero-age MS.

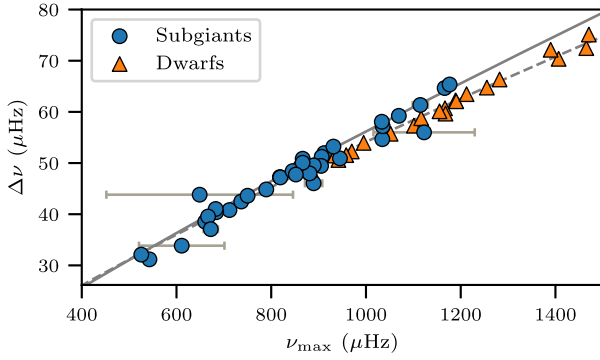


Figure 9. $\Delta\nu$ – ν_{\max} diagram. The solid line is the best-fitting curve for subgiants. The dashed line is a similar fit, but obtained from a sample of MS dwarfs and red giants (Huber et al. 2011). The measurement of dwarfs were adopted from Lund et al. (2017).

observations and stellar models stems from the improper modelling of near-surface layers (Christensen-Dalsgaard, Dappen & Lebreton 1988).

We show the small separations $\delta\nu_{02}$ versus $\Delta\nu$ in Fig. 8, the so-called C–D diagram (Christensen-Dalsgaard 1984; Mazumdar 2005). The evolutionary tracks with different masses are well separated on the MS. By comparing to models, the diagram is useful for estimating mass and age when $\delta\nu_{02}$ and $\Delta\nu$ are known. We note that the ϵ_p – $\Delta\nu$ diagram could be used for a similar purpose, provided the surface effect is well accounted for. However, the tracks become more degenerate in the subgiant phase (White et al. 2011a, b). We performed a linear fit to the subgiants:

$$\delta\nu_{02} = (0.088 \pm 0.001)\Delta\nu + (0.070 \pm 0.059) \mu\text{Hz}. \quad (17)$$

We point out that some obvious outliers from the fitted line are present. They are affected by bumped $l = 2$ modes, which lift the average distance of a quadrupolar mode to a radial mode. Bedding et al. (2010) fitted the same relation to a sample of red giants, which have a steeper slope (as shown by the dashed line in Fig. 8). This difference is also visible from the calculation of stellar models. Similarly, we fitted $\delta\nu_{03}$ using ten stars that have detected $l = 3$ modes:

$$\delta\nu_{03} = (0.152 \pm 0.002)\Delta\nu + (2.578 \pm 0.102) \mu\text{Hz}. \quad (18)$$

Finally, we use the radial modes to determine ν_{\max} because they are purely acoustic, since there are no radial g modes for them to couple with. By fitting the amplitudes versus frequencies of radial modes with a Gaussian function, ν_{\max} was obtained as the Gaussian’s centre. The height of the Gaussian, A_{\max} , together with the width, are analysed in Section 7. We fitted the well-established $\Delta\nu$ – ν_{\max} relation (e.g. Stello et al. 2009; Huber et al. 2009) to our subgiants,

$$\Delta\nu = a(\nu_{\max}/\mu\text{Hz})^b \mu\text{Hz}, \quad (19)$$

and determined the best-fitting parameters as $a = 0.158 \pm 0.036$ and $b = 0.847 \pm 0.034$. Huber et al. (2011) determined $a = 0.22$ and $b = 0.797$ from a sample consisting of both MS stars and red giants. We plot the two relations in Fig. 9. The most noticeable effect is that the subgiants lie above the dwarfs, which can be understood from simple scaling arguments. The asteroseismic scaling relations (Brown et al. 1991; Kjeldsen & Bedding 1995) state that $\Delta\nu \propto \sqrt{\rho} \propto M^{1/2}R^{-3/2}$, and $\nu_{\max} \propto g/\sqrt{T_{\text{eff}}} \propto MR^{-2}T_{\text{eff}}^{-1/2}$. Dividing the two relations, we obtain $\Delta\nu/\nu_{\max} \propto M^{-1/2}R^{1/2}T_{\text{eff}}^{-1/2}$. The subgiants and dwarfs have similar M and T_{eff} , but subgiants are

more inflated, which ultimately leads to higher $\Delta\nu/\nu_{\max}$. Indeed, this spread is the signal upon which the widely used scaling relations for mass and radius are based (Stello et al. 2008; Kallinger et al. 2010).

5 THE P–G DIAGRAM

We now focus on the frequencies of the underlying g modes, which we denote by γ (Aizenman, Smeyers & Weigert 1977). Adjusting the model parameters to fit the observed frequencies can be difficult and time-consuming. As pointed out by Bedding (2014), the information contained in the mixed modes can be used more elegantly, by considering the frequencies of the avoided crossings themselves. The suggestion was that, before fitting models to the observed mixed modes, one can first consider the underlying g modes. These are not directly detected but their frequencies can be inferred from the locations of the avoided crossings.

This discussion suggests a new asteroseismic diagram (Bedding 2014), inspired by the classical C–D diagram, in which the frequencies of the avoided crossings γ are plotted against the large separation of the p modes. This p–g diagram, so named because it plots g-mode frequencies versus p-mode frequencies, could prove to be an instructive way to display results of many stars and to make a first comparison with theoretical models (Campante et al. 2011; Bedding 2014).

For example, the echelle diagram in Fig. 3 shows three avoided crossings of dipole modes, at about 950, 750, and 650 μHz . We recognize these as the frequencies of the γ modes, that is, the pure g modes that would exist in the core cavity if there was no coupling to the p modes in the envelope (Aizenman et al. 1977). Much of the diagnostic information contained in the mixed modes can be captured in this way. This is because the overall pattern of the mixed modes is determined by the mode bumping at each avoided crossing, and these patterns are determined by the g modes trapped in the core. For related discussion on this point, see Deheuvels & Michel (2010) and Benomar et al. (2013).

We determined the g-mode frequencies, γ , from fitting $l = 1$ mixed-mode frequencies $\nu_{n,l=1}$. Specifically, Lorentzian profiles were fitted to $\nu_{n+1,l=1} - \nu_{n,l=1}$ versus $(\nu_{n+1,l=1} + \nu_{n,l=1})/2$. A dip is present wherever there is an avoided crossing. This is because the presence of mixed modes makes two adjacent modes closer in frequency. We identified the centres of the Lorentzian profiles as the g-mode frequencies, γ . The errors were estimated following a Monte Carlo procedure by adding Gaussian errors to mode frequencies, repeating the fitting for 1000 times, and adopting the standard deviation of γ from the distribution. If multiple avoided crossings (at least three) are present, we further estimated $\Delta\Pi_1$ by calculating the average differences between $1/\gamma$. The results are shown in Table 3. Some stars do not have reported γ_1 or $\Delta\Pi_1$ because they tend to have uncertain identifications of the first g mode, and they also present a small number of avoided crossings.

For less-evolved subgiants in which the first ($n_g = 1$) g-mode frequency, γ_1 , is present, we made the γ_1 – $\Delta\nu$ diagram in Fig. 10. This provides an indicative measurement of stellar mass when evolutionary tracks are simultaneously plotted, unlike the C–D diagram where stellar tracks are degenerate. The stars evolve diagonally, so γ_1 and $\Delta\nu$ can determine not only mass, but age as well.

Another important diagnostic diagram is to plot the period spacings of g-mode $\Delta\Pi_1$ in equation (2) versus $\Delta\nu$ (another p–

6 MODE LINEWIDTHS

6.1 Linewidths as a function of frequency

The modes of solar-like oscillations are damped by convection. For these observations, the modes have lifetimes much shorter than the length of time series, which results in a broadened Lorentzian shape in the power spectrum. The modes are hence ‘resolved’. The linewidth [full width at half-maximum (FWHM)] of that shape can be translated to the lifetime through $\tau = (\pi\Gamma)^{-1}$, or damping rate $\eta = \pi\Gamma$. This is important to constrain the physics of the superadiabatic layers near the surface, including the mechanism of how the kinetic energy of oscillations is dissipated into turbulent convection. The answer requires a detailed treatment of convection, but it is difficult to formulate with current convection theories (Gough 1980; Balmforth 1992a; Gabriel 1996; Houdek et al. 1999; Grigahcène et al. 2005; Xiong, Deng & Zhang 2015). However, the theories are able to reproduce the frequency dependence of the linewidths seen in the observations, provided the free parameters in the modelling are carefully calibrated, in red giants (Aarslev et al. 2018) and in MS stars (Houdek et al. 2019). 3D hydrodynamical convection simulations may offer a promising path, by eliminating the degrees of freedom in the theory and provide a numerical solution (e.g. Belkacem et al. 2019; Zhou, Asplund & Collet 2019).

Appourchaux et al. (2014) first parametrized the Γ – ν relation in a given star and Lund et al. (2017) improved the fitting details. Here, we followed the definition in Lund et al. (2017) to fit the linewidths of radial modes, as follows:

$$\ln \Gamma(\nu; \theta) = \alpha \ln(\nu/\nu_{\max}) + \ln \Gamma_{\alpha} + \frac{\ln \Delta \Gamma_{\text{dip}}}{1 + \left[\frac{2 \ln(\nu/\nu_{\text{dip}})}{\ln(W_{\text{dip}}/\nu_{\max})} \right]^2}, \quad (20)$$

where the free parameters are $\theta = (\alpha, \Gamma_{\alpha}, \Delta \Gamma_{\text{dip}}, \nu_{\text{dip}}, W_{\text{dip}})$. This Γ – ν relation follows a power-law but saturates near ν_{\max} to form a plateau (or a dip) centred on ν_{dip} , with width W_{dip} and height $\Delta \Gamma_{\text{dip}}$. The dip could originate from a resonance of the thermal time-scale in the superadiabatic layer and mode frequency (Balmforth 1992a; Belkacem et al. 2011). To fit the parameters, we optimized the likelihood function:

$$\ln L \propto \sum_i [\ln \Gamma_i - \ln \Gamma(\nu_i; \theta)]^2 / \sigma_{\ln \Gamma_i}^2. \quad (21)$$

The modes used in this fit were radial modes satisfying Bayes factors $\ln K > 1$. The priors of $\Delta \Gamma_{\text{dip}}$ and W_{dip} deserve a further mention. As suggested by Lund et al. (2017), the values of $\Delta \Gamma_{\text{dip}}$ were bound to be between 0 and 1 to reduce correlations between the parameters. W_{dip} can have two solutions: one larger than ν_{\max} , and one smaller. We kept the convention from Lund et al. (2017) to use the larger one. We estimated the FWHM of the dip through $\text{FWHM} = \nu_{\text{dip}} \left| \sqrt{W_{\text{dip}}/\nu_{\max}} - \sqrt{\nu_{\max}/W_{\text{dip}}} \right|$ (Appourchaux et al. 2016), and the amplitude of the dip as $A_{\text{dip}} = \exp |\ln \Delta \Gamma_{\text{dip}}|$ (Lund et al. 2017). Fig. 12 shows the fit for Gemma (KIC 11026764), which shows a dip around ν_{\max} . Note that some stars do not present the evidence of a dip. Their linewidths increase monotonically with frequencies. We only fitted those stars with the first two terms of equation (20). Fig. 12 also shows an example, KIC 9512063, where the large random errors obscure the presence of either a dip or a plateau. Table 4 lists the fitted parameters for all stars.

The dipole modes have a more complicated Γ – ν relation. The dipole modes with more g-mode characteristics have larger inertia and are less affected by damping from the surface than are radial modes, hence resulting in smaller linewidths. Benomar et al. (2014) suggested using linewidths to measure mode inertias, which could also be obtained from the asymptotic formalism of mixed

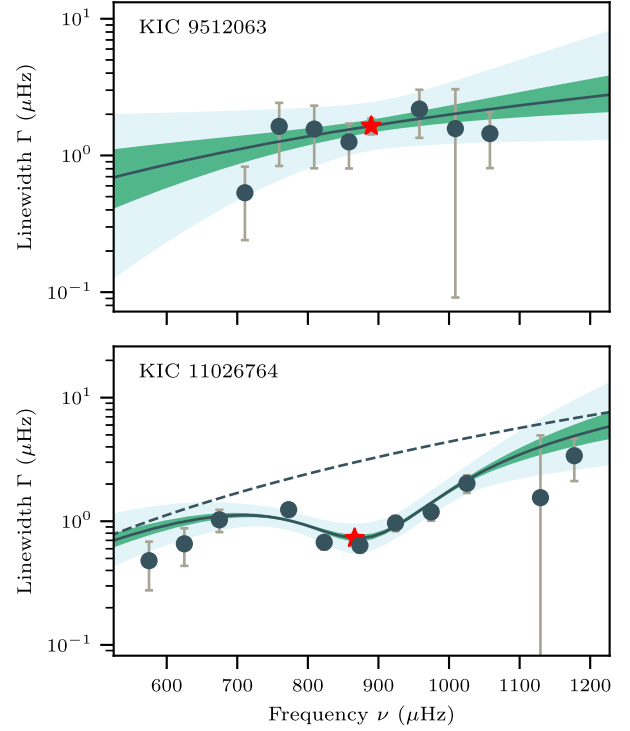


Figure 12. Linewidths as a function of frequencies for KIC 9512063 (top panel) and Gemma (KIC 11026764, bottom panel), denoted by the filled circles. The solid lines are the fits of equation (20), with KIC 9512063 using the first two terms (the power law), and Gemma using the full terms. The dashed line is the power-law component in Gemma’s fit. The shaded green regions show 1σ and 3σ credible intervals for the fit. The red star symbols around 900 μHz are the estimations of linewidth at ν_{\max} , obtained from the MCMC samples.

modes (Shibahashi 1979; Goupil et al. 2013). Mosser et al. (2018) introduced a stretch function ζ , which is the degree of mode trapping characterized by the ratio of mode inertia inside the g-mode cavity to that throughout the star. The linewidths of mixed modes, Γ_1 , relate to those of radial modes, Γ_0 , as follows (Mosser et al. 2011, 2015, 2018; Vrad et al. 2016; Hekker & Christensen-Dalsgaard 2017):

$$\Gamma_1 = \Gamma_0(1 - \zeta), \quad (22)$$

where

$$\zeta(\nu) = \left[1 + \frac{q}{N(\nu)} \frac{1}{q^2 \cos^2 \theta_p(\nu) + \sin^2 \theta_p(\nu)} \right]^{-1}, \quad (23)$$

$$N(\nu) = \frac{\Delta \nu}{\nu^2 \Delta \Pi_1}, \quad (24)$$

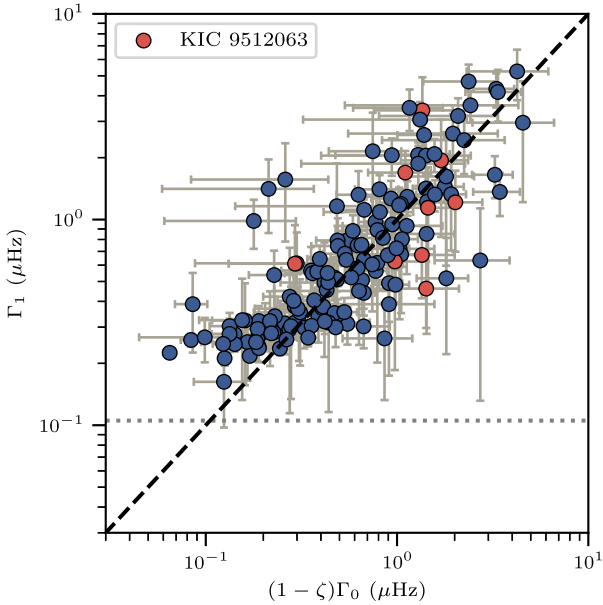
and

$$\theta_p(\nu) = \pi \left\{ \frac{\nu}{\Delta \nu} - \left[n_p + \frac{l}{2} + \epsilon_p - d_{0l} + \frac{\alpha_p}{2} \left(n_p - \frac{\nu_{\max}}{\Delta \nu} \right)^2 \right] \right\}, \quad (25)$$

Using the above definition of θ_p , together with equations (3) and 5, we fitted the asymptotic parameters $\{\epsilon_p, \alpha_p, d_{0l}, \Delta \nu, \Delta \Pi_1, \epsilon_g\}$ to the dipole mode frequencies estimated from the peakbagging. The value of ζ was then straightforwardly obtained. In Fig. 13, we compare Γ_1 with $\Gamma_0(1 - \zeta)$ and find good agreement. That is, the widths of the dipole modes are smaller than those of the radial modes, as expected. This suggests that the asymptotic theory agrees well with the observation.

Table 4. Fit parameters of the Γ - ν relation.

KIC	$\Gamma(\nu_{\max})$	α	Γ_{α} (μHz)	$\Delta\Gamma_{\text{dip}}$ (μHz)	ν_{dip} (μHz)	W_{dip} (μHz)	FWHM (μHz)	A_{dip} (μHz^{-1})
2991448	0.73 ± 0.22	1.35 ± 1.38	56.96 ± 55.33	0.01 ± 0.01	1100 ± 11	1477 ± 93	311 ± 72	80 ± 87
3852594	4.42 ± 1.18	1.35 ± 0.64	5.95 ± 0.40	—	—	—	—	—
5607242	0.43 ± 0.16	4.24 ± 0.71	2.35 ± 1.17	0.12 ± 0.04	698 ± 7	898 ± 76	191 ± 60	8 ± 3
5689820	0.13 ± 0.05	1.71 ± 1.65	12.70 ± 30.15	0.01 ± 0.05	731 ± 67	2534 ± 1580	1029 ± 565	69 ± 233
5955122	1.67 ± 0.41	3.17 ± 0.94	11.83 ± 28.40	0.10 ± 0.12	874 ± 37	1729 ± 554	621 ± 298	10 ± 12
6064910	5.13 ± 1.33	0.16 ± 0.17	6.59 ± 0.38	—	—	—	—	—
6442183	0.64 ± 0.13	2.93 ± 0.41	2.79 ± 1.44	0.20 ± 0.07	1166 ± 12	1572 ± 181	350 ± 136	5 ± 2
6693861	0.59 ± 0.46	5.39 ± 2.75	42.11 ± 58.02	0.01 ± 0.03	838 ± 39	1529 ± 337	532 ± 195	71 ± 174
7174707	0.42 ± 0.22	1.70 ± 1.41	18.61 ± 39.44	0.02 ± 0.07	806 ± 27	1723 ± 473	613 ± 238	54 ± 211
7199397	1.15 ± 0.26	2.23 ± 0.34	1.41 ± 0.07	—	—	—	—	—
7747078	1.04 ± 0.16	3.15 ± 1.56	10.96 ± 34.76	0.09 ± 0.18	958 ± 66	2006 ± 751	753 ± 389	11 ± 20
7976303	1.76 ± 0.26	2.11 ± 1.09	8.63 ± 34.46	0.18 ± 0.28	933 ± 121	2790 ± 2583	1155 ± 1027	6 ± 9
8524425	0.60 ± 0.65	4.64 ± 1.13	2.97 ± 3.81	0.21 ± 0.13	1096 ± 35	1603 ± 284	447 ± 199	5 ± 3
8702606	0.31 ± 0.09	3.14 ± 0.95	12.17 ± 32.95	0.04 ± 0.10	660 ± 26	1547 ± 512	572 ± 239	23 ± 55
9512063	1.21 ± 0.63	1.75 ± 0.92	1.48 ± 0.18	—	—	—	—	—
10018963	2.37 ± 0.42	2.60 ± 0.22	2.37 ± 0.09	—	—	—	—	—
10147635	2.79 ± 0.73	3.71 ± 0.43	2.43 ± 0.16	—	—	—	—	—
10273246	1.68 ± 0.46	5.07 ± 1.08	8.51 ± 21.03	0.23 ± 0.31	1359 ± 695	5690 ± 2432	2919 ± 1719	4 ± 6
10593351	2.03 ± 0.64	3.04 ± 0.44	2.29 ± 0.17	—	—	—	—	—
10873176	3.26 ± 1.59	3.67 ± 2.10	3.42 ± 0.76	—	—	—	—	—
10920273	0.57 ± 0.25	8.48 ± 3.66	21.88 ± 44.10	0.03 ± 0.07	1082 ± 35	1577 ± 443	459 ± 311	33 ± 81
10972873	0.67 ± 0.14	3.69 ± 1.40	13.36 ± 38.59	0.05 ± 0.14	1062 ± 52	2204 ± 932	823 ± 483	18 ± 46
11026764	0.73 ± 0.17	2.17 ± 0.43	1.99 ± 0.36	0.31 ± 0.06	882 ± 10	1065 ± 51	183 ± 43	3 ± 1
11137075	0.53 ± 0.22	10.02 ± 1.98	49.24 ± 55.66	0.01 ± 0.01	1224 ± 25	1912 ± 173	601 ± 115	110 ± 173
11193681	0.86 ± 0.22	3.06 ± 0.37	1.20 ± 0.06	—	—	—	—	—
11395018	0.67 ± 0.15	1.72 ± 1.56	35.73 ± 51.69	0.02 ± 0.03	822 ± 21	1497 ± 200	469 ± 115	45 ± 70
11414712	0.69 ± 0.16	2.66 ± 0.26	0.94 ± 0.04	—	—	—	—	—
11771760	0.63 ± 0.17	0.79 ± 0.52	1.05 ± 0.07	—	—	—	—	—
12508433	0.27 ± 0.06	3.92 ± 1.66	26.15 ± 44.41	0.01 ± 0.03	796 ± 56	2294 ± 556	890 ± 230	73 ± 154


Figure 13. Linewidths of dipole mixed modes versus those of radial modes modified with the stretch function ζ . The dashed line indicates the 1:1 relation. The horizontal dotted line denotes the nominal frequency resolution, $1/t_{\text{obs}}$, of KIC 9512063, which is around 0.1 μHz , the largest among the sample.

6.2 Scaling relations for linewidths

Scaling relations for linewidths were studied only recently, focusing on the linewidths around ν_{\max} , denoted by $\Gamma(\nu_{\max})$. Chaplin et al. (2009) used non-adiabatic pulsation computations and ground-based observations to study the linewidths across different stages of evolution. They showed that the linewidths scale with fundamental stellar parameters, primarily T_{eff} . This dependence on surface properties is expected because damping mainly happens in the superadiabatic regions near the surface (Goldreich & Kumar 1991). The studies of *CoRoT* and *Kepler* targets also suggested that $\Gamma(\nu_{\max})$ correlates mainly with T_{eff} , but only weakly depends on $\log g$ (Baudin et al. 2011; Appourchaux et al. 2014; Vrad et al. 2018).

To estimate $\Gamma(\nu_{\max})$, we used the MCMC samples from the fit of the $\Gamma - \nu$ relation (Section 6.1) to draw the probability distribution of Γ at ν_{\max} . This method assumes that $\Gamma - \nu$ follows the power-law model (or the power law with a dip). Fig. 12 shows an estimation for Gemma (KIC 11026764), marked by a red star around 700 μHz .

In Fig. 14, we show $\Gamma(\nu_{\max})$ for our subgiant sample, together with MS stars from Lund et al. (2017), and RGB and HeB stars from Vrad et al. (2018). Note that Vrad et al. (2018) calculated $\Gamma(\nu_{\max})$ for the giants differently to how it was done for subgiants and MS stars by averaging linewidths using three modes near ν_{\max} . Fig. 14 shows that $\Gamma(\nu_{\max})$ mainly depends on T_{eff} , and weakly correlates with $\log g$. To parametrize this relation, we fitted $\Gamma(\nu_{\max})$ using

$$\log(\Gamma/\Gamma_0) = c_1 \log(T_{\text{eff}}/5777 \text{ K}) + c_2 \log(g/274 \text{ ms}^{-1}). \quad (26)$$

We optimized the likelihood function:

$$\ln L \propto [\ln \Gamma_i - \ln \Gamma(T_i, g_i; \theta)]^2 / (2\sigma_{\ln \Gamma_i}^2). \quad (27)$$

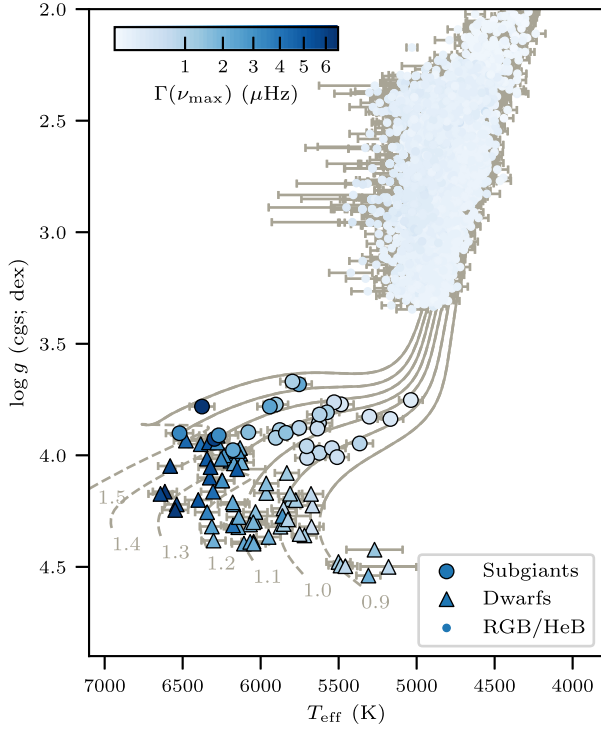


Figure 14. Kiel diagram with colour-coded $\Gamma(\nu_{\max})$. The measurements of dwarfs and red giants are adopted from Lund et al. (2017) and Vrad et al. (2018), respectively. The theoretical evolutionary tracks (Choi et al. 2016) before and after the MS turn-off are shown in the dashed and solid lines, respectively, with each track labelled with mass in solar units.

Table 5. Fit parameters of the $\Gamma(\nu_{\max})$ scaling relation.

Phase	Γ_0	c_1	c_2
MS	1.10 ± 0.01	13.41 ± 0.10	0.05 ± 0.02
Subgiants	0.50 ± 0.04	13.71 ± 0.19	-0.65 ± 0.06
RGB	0.25 ± 0.00	2.78 ± 0.09	0.09 ± 0.00
HeB	0.47 ± 0.02	1.70 ± 0.13	0.19 ± 0.01

Some previous works (Belkacem et al. 2012; Samadi, Belkacem & Sonoi 2015) pointed out that $\Gamma(\nu_{\max})$ depends on T_{eff} and $\log g$ differently in each evolutionary stage, which motivates us to fit them separately as well.

The fitted parameters are shown in Table 5. From the table, we conclude that $\Gamma(\nu_{\max})$ primarily depends on T_{eff} but with significantly different power-law indices (c_1) for red giants and non-red giants. This could be attributed to different dominant damping mechanisms, as some works suggested (e.g. Baudin et al. 2011). However, it could also be an artefact while selecting modes to compute $\Gamma(\nu_{\max})$ for red giants (Belkacem et al. 2012). The power-law index for $\log g$ (c_2) in subgiants has a reversed sign compared to MS stars and red giants. This effect could be slightly spotted in Fig. 14.

7 MODE AMPLITUDES

7.1 Amplitudes as a function of frequency

The amplitudes of radial modes follow a roughly Gaussian distribution centred on ν_{\max} , as we analysed in Section 4. The dipole mixed modes have an added dependence on mode inertia, but are

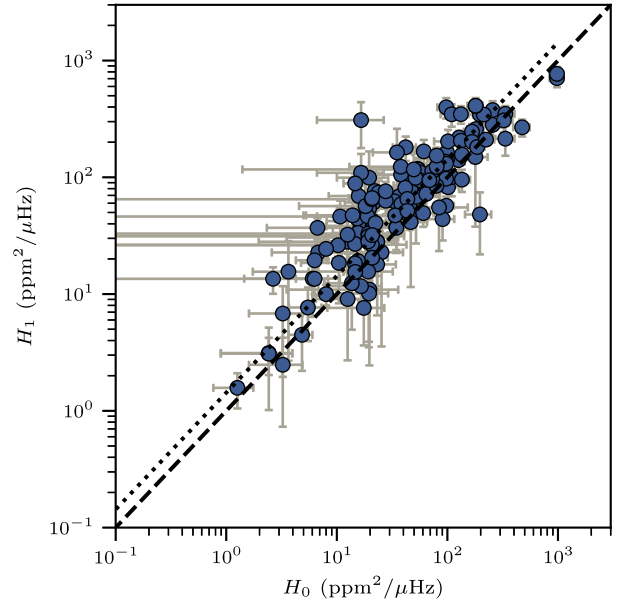


Figure 15. Height of dipole mixed modes H_1 versus those of radial modes H_0 . The dashed line indicate the 1:1 relation, and the dotted line shows 1.5:1 relation. The factor of 1.5 shows the median value of our observed H_1/H_0 , which stems from a geometric effect.

still predictable using the stretch function: $A_1^2 = (1 - \zeta)A_0^2$, with A_0 being the radial-mode amplitudes (Benomar et al. 2014; Belkacem et al. 2015; Mosser et al. 2018). Considering $\Gamma_1 = (1 - \zeta)\Gamma_0$, we obtained $H_1 = H_0$, suggesting similar mode heights. In Fig. 15, we show H_1 against H_0 . The points deviate from the 1:1 relation because the height of dipole modes are influenced by a geometric effect. Dividing H_1 by H_0 , we get the visibility factor V_1^2 with a median value equal to 1.5, similar to the one calculated using stellar atmosphere models (Ballot, Barban & van't Veer-Menneret 2011), which is also around 1.5.

7.2 Scaling relations for amplitudes

Kjeldsen & Bedding (1995) first proposed a scaling relation for the amplitudes of solar-like oscillations to scale from the Sun to other stars, relating both radial velocity and photometric amplitude to fundamental parameters L , M and T_{eff} . It received numerous application, e.g. for optimizing target selections (Chaplin et al. 2011b; Schofield et al. 2019), and understanding how modes are excited with different treatment for convection and excitation processes (e.g. Goldreich & Keeley 1977; Balmforth 1992b; Samadi & Goupil 2001; Chaplin et al. 2005; Zhou et al. 2019). As we mentioned in Section 4, while estimating ν_{\max} , we also measured the maximum photometric amplitude expressed by A_{\max} and the width of the Gaussian-like envelopes. To compare A_{\max} with scaling relations, we used two results from Huber et al. (2011):

$$\frac{A_{\max}}{A_{\text{bol},\odot}} = c_K \left(\frac{L}{L_\odot} \right)^{0.838} \left(\frac{M}{M_\odot} \right)^{-1.32} \left(\frac{T_{\text{eff}}}{T_{\text{eff},\odot}} \right)^{-1}, \quad (28)$$

and Corsaro et al. (2013):

$$\frac{A_{\max}}{A_{\text{bol},\odot}} = 1.38c_K \left(\frac{\nu_{\max}}{\nu_{\max,\odot}} \right)^{-2.314} \left(\frac{\Delta\nu}{\Delta\nu_\odot} \right)^{2.088} \left(\frac{T_{\text{eff}}}{T_{\text{eff},\odot}} \right)^{0.365}, \quad (29)$$

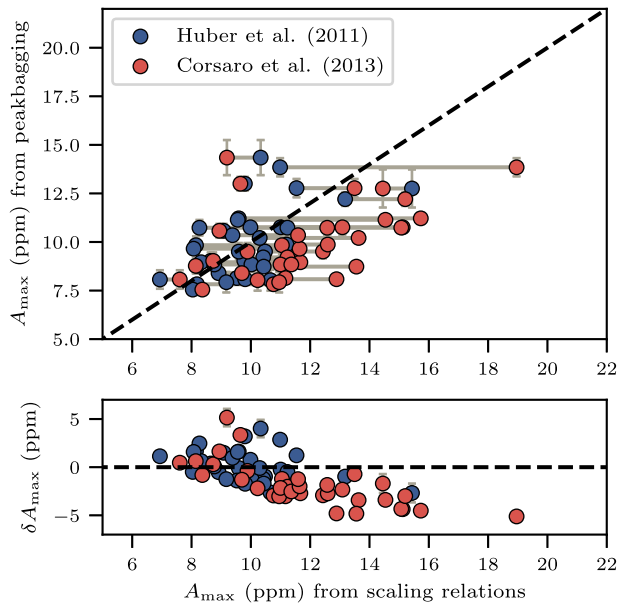


Figure 16. Top panel: A_{\max} estimated using the radial mode amplitudes versus A_{\max} from the scaling relations. The dashed line indicates the 1:1 relation. Bottom panel: the absolute differences in the top panel.

where $A_{\text{bol}, \odot} = 3.6 \pm 0.11$ ppm and $c_K = (T_{\text{eff}}/5934 \text{ K})^{0.8}$ (Huber et al. 2011). There has been some discussions concerning the exponent of each term (e.g. Houdek et al. 1999; Houdek 2006; Samadi et al. 2007), and the above two papers set the exponents free and calibrated with observations (see also e.g. Stello et al. 2011). Fig. 16 shows the comparison. In the regime of subgiants, Huber et al.’s (2011) relation seems to fit better, with a correlation coefficient of 0.55 against 0.49 from Corsaro et al. (2013). However, both relations overestimate the amplitudes, by factors of 9 and 24 percent, respectively. The scatter of the data points could be caused by activity (Chaplin et al. 2011a) or an unaccounted metallicity effect (Yu et al. 2018). We also verified that the suppression effect of non-radial modes seen in red giants (Mosser et al. 2012a; Stello et al. 2016) does not affect the subgiants in our sample (García et al. 2014; Fuller et al. 2015).

In Fig. 17, we plot both A_{\max} and the width against ν_{\max} . The values of A_{\max} increase and the widths decrease with decreasing ν_{\max} , indicating that the Gaussian envelope becomes higher and narrower as the star evolves. The points in Fig. 17 are also colour-coded with mass, and we identify a weak correlation: at a given ν_{\max} , A_{\max} is smaller in higher mass stars, with the width being larger. This phenomenon is also seen in the *Kepler* red giant sample (e.g. Yu et al. 2018). We also analysed the effect of metallicity on mode amplitude but due to the small size of our sample, we were not able to draw any conclusions.

8 CONCLUSIONS

In this paper, we presented oscillation frequencies, linewidths and amplitudes for 36 subgiants observed by the 4-yr *Kepler* mission. We derived those parameters with uncertainties from MCMC fitting, using an open-source software package SOLARLIKEPEAKBAGGING. Significance tests and visual inspections were applied to ensure a robust identification. Our main results are summarized as follows:

(i) With the long baseline of *Kepler* observations, the median value for the frequency uncertainties of the subgiants is 0.180

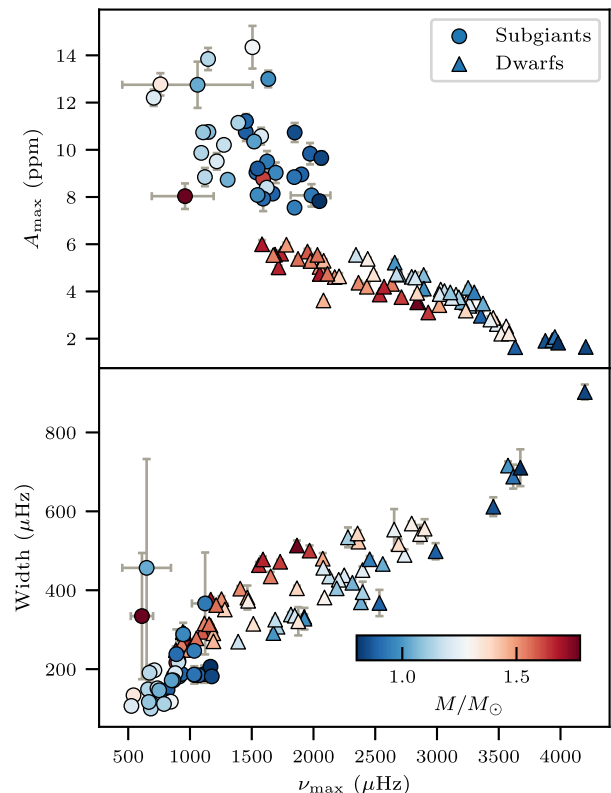


Figure 17. A_{\max} and width of the Gaussian envelope against ν_{\max} . The colour denotes stellar mass.

μHz . For modes with $S/N = 3$, the typical uncertainty is 0.1 μHz , providing strong constraint on stellar models with these data.

(ii) The asymptotic parameters ϵ_p , $\Delta\nu$, ν_{\max} , and $\delta\nu_{0l}$ were derived using the mode parameters. We identified a T_{eff} and $\log g$ dependence for ϵ_p . We also revisited the C–D diagram and the $\Delta\nu - \nu_{\max}$ diagram with a focus on subgiants. The subgiants deviate slightly from the general trend, but could be explained using simple scaling arguments or stellar models.

(iii) We presented two p–g diagrams, the $\gamma_1 - \Delta\nu$ diagram for less-evolved subgiants, and the $\Delta\P_1 - \Delta\nu$ diagram for more evolved subgiants. Both diagrams were populated with *Kepler* observations and can be used as a first simple estimation of stellar mass.

(iv) The linewidths of radial modes were analysed as functions of frequencies, and the linewidths of dipolar mixed modes agree well with asymptotic predictions. We verified the dependence of $\Gamma(\nu_{\max})$ on T_{eff} and also observed a weak $\log g$ effect.

(v) The amplitudes of dipolar mixed modes also agree with asymptotic predictions. The mass dependence of A_{\max} and the width is present both in subgiants and MS stars.

The unprecedented quality of asteroseismic data presented by this sample is valuable for the study of stellar physics. The mode frequencies are further used as modelling input in Paper II. The linewidths and amplitudes derived in this work can be used to study mode excitation and damping. In the observation data, one missing piece that remains unexplored in this work is the rotational splitting, which provides a golden opportunity to study the angular momentum transport in subgiants. We will continue to study this topic in this series of papers.

ACKNOWLEDGEMENTS

We thank Mikkel Lund and Jørgen Christensen-Dalsgaard for very helpful discussions. We also appreciate efforts from the referee to improve the quality of this paper, especially during a pandemic outbreak. The *Kepler* Discovery mission is funded by NASA's Science Mission Directorate. We acknowledge the Joint Research Fund in Astronomy (U1631236) under cooperative agreement between the National Natural Science Foundation of China (NSFC) and Chinese Academy of Sciences (CAS) (NSFC 11273007 and 10933002), and the Fundamental Research Funds for the Central Universities. We also acknowledge funding from the Australian Research Council.

REFERENCES

- Aarslev M. J., Houdek G., Handberg R., Christensen-Dalsgaard J., 2018, *MNRAS*, 478, 69
- Aizenman M., Smeyers P., Weigert A., 1977, *A&A*, 58, 41
- Anderson E. R., Duvall, Thomas L. J., Jefferies S. M., 1990, *ApJ*, 364, 699
- Appourchaux T. et al., 2012, *A&A*, 543, A54
- Appourchaux T. et al., 2014, *A&A*, 566, A20
- Appourchaux T. et al., 2016, *A&A*, 595, C2
- Astropy Collaboration, 2013, *A&A*, 558, A33
- Astropy Collaboration, 2018, *ApJ*, 156, 123
- Ballot J., Appourchaux T., Toutain T., Guittet M., 2008, *A&A*, 486, 867
- Ballot J., Barban C., van't Veer-Menneret C., 2011, *A&A*, 531, A124
- Balmforth N. J., 1992a, *MNRAS*, 255, 603
- Balmforth N. J., 1992b, *MNRAS*, 255, 639
- Baudin F. et al., 2011, *A&A*, 529, A84
- Bedding T. R., 2012, in Shibahashi H., Takata M., Lynas-Gray A. E., eds, ASP Conf. Ser. Vol. 462, Progress in Solar/Stellar Physics with Helio- and Asteroseismology. Astron. Soc. Pac., San Francisco, p. 195
- Bedding T. R., 2014, Asteroseismology. Cambridge Univ. Press, Cambridge
- Bedding T. R. et al., 2001, *ApJ*, 549, L105
- Bedding T. R. et al., 2006, *ApJ*, 647, 558
- Bedding T. R. et al., 2007, *ApJ*, 663, 1315
- Bedding T. R. et al., 2010, *ApJ*, 713, L176
- Bedding T. R. et al., 2011, *Nature*, 471, 608
- Belkacem K., Goupil M. J., Dupret M. A., Samadi R., Baudin F., Noels A., Mosser B., 2011, *A&A*, 530, A142
- Belkacem K., Dupret M. A., Baudin F., Appourchaux T., Marques J. P., Samadi R., 2012, *A&A*, 540, L7
- Belkacem K. et al., 2015, *A&A*, 579, A31
- Belkacem K., Kupka F., Samadi R., Grimm-Strele H., 2019, *A&A*, 625, A20
- Benomar O., Bedding T. R., Stello D., Deheuvels S., White T. R., Christensen-Dalsgaard J., 2012, *ApJ*, 745, L33
- Benomar O. et al., 2013, *ApJ*, 767, 158
- Benomar O. et al., 2014, *ApJ*, 781, L29
- Bonanno A., Benatti S., Claudi R., Desidera S., Gratton R., Leccia S., Paternò L., 2008, *ApJ*, 676, 1248
- Brandão I. M. et al., 2011, *A&A*, 527, A37
- Brown T. M., Gilliland R. L., Noyes R. W., Ramsey L. W., 1991, *ApJ*, 368, 599
- Campante T. L. et al., 2011, *A&A*, 534, A6
- Carrier F. et al., 2001, *A&A*, 378, 142
- Carrier F., Eggenberger P., Bouchy F., 2005, *A&A*, 434, 1085
- Carrier F. et al., 2007, *A&A*, 470, 1059
- Chaplin W. J., Houdek G., Elsworth Y., Gough D. O., Isaak G. R., New R., 2005, *MNRAS*, 360, 859
- Chaplin W. J., Houdek G., Karoff C., Elsworth Y., New R., 2009, *A&A*, 500, L21
- Chaplin W. J. et al., 2011a, *ApJ*, 732, L5
- Chaplin W. J. et al., 2011b, *ApJ*, 732, 54
- Choi J., Dotter A., Conroy C., Cantiello M., Paxton B., Johnson B. D., 2016, *ApJ*, 823, 102
- Christensen-Dalsgaard J., 1984, in Mangeney A., Praderie F., eds, Space Research in Stellar Activity and Variability. Observatoire de Paris, Meudon, France
- Christensen-Dalsgaard J., Dappen W., Lebreton Y., 1988, *Nature*, 336, 634
- Christensen-Dalsgaard J., Bedding T. R., Kjeldsen H., 1995, *ApJ*, 443, L29
- Corsaro E., De Ridder J., 2014, *A&A*, 571, A71
- Corsaro E., Fröhlich H. E., Bonanno A., Huber D., Bedding T. R., Benomar O., De Ridder J., Stello D., 2013, *MNRAS*, 430, 2313
- Davies G. R. et al., 2016, *MNRAS*, 456, 2183
- Deheuvels S., Michel E., 2010, *Ap&SS*, 328, 259
- Deheuvels S. et al., 2014, *A&A*, 564, A27
- Deheuvels S., Brandão I., Silva Aguirre V., Ballot J., Michel E., Cunha M. S., Lebreton Y., Appourchaux T., 2016, *A&A*, 589, A93
- Di Mauro M. P., Christensen-Dalsgaard J., Kjeldsen H., Bedding T. R., Paternò L., 2003a, *A&A*, 404, 341
- Di Mauro M. P., Christensen-Dalsgaard J., Paternò L., 2003b, *Ap&SS*, 284, 229
- Eggenberger P. et al., 2019, *A&A*, 621, A66
- Fernandes J., Monteiro M. J. P. F. G., 2003, *A&A*, 399, 243
- Foreman-Mackey D., Hogg D. W., Lang D., Goodman J., 2013, *PASP*, 125, 306
- Fuller J., Cantiello M., Stello D., Garcia R. A., Bildsten L., 2015, *Science*, 350, 423
- Gabriel M., 1996, *Bull. Astron. Soc. India*, 24, 233
- Gai N., Tang Y., Yu P., Dou X., 2017, *ApJ*, 836, 3
- García R. A. et al., 2011, *MNRAS*, 414, L6
- García R. A. et al., 2014, *A&A*, 572, A34
- Ge Z. S., Bi S. L., Li T. D., Liu K., Tian Z. J., Yang W. M., Liu Z. E., Yu J., 2015, *MNRAS*, 447, 680
- Gilliland R. L. et al., 2010, *ApJ*, 713, L160
- Gizon L., Solanki S. K., 2003, *ApJ*, 589, 1009
- Goldreich P., Keeley D. A., 1977, *ApJ*, 212, 243
- Goldreich P., Kumar P., 1991, *ApJ*, 374, 366
- Goodman J., Weare J., 2010, *Commun. Appl. Math. Comput. Sci.*, 5, 65
- Gough D., 1980, *Nonradial and Nonlinear Stellar Pulsation*. Springer-Verlag, Berlin
- Gough D. O., 1986, in Osaki Y., ed., Hydrodynamic and Magnetodynamic Problems in the Sun and Stars. Tokyo Univ., Tokyo
- Goupil M. J., Mosser B., Marques J. P., Ouazzani R. M., Belkacem K., Lebreton Y., Samadi R., 2013, *A&A*, 549, A75
- Grigahcène A., Dupret M.-A., Gabriel M., Garrido R., Scuflaire R., 2005, *A&A*, 434, 1055
- Grundahl F. et al., 2017, *ApJ*, 836, 142
- Guenther D. B., 2004, *ApJ*, 612, 454
- Guenther D. B., Demarque P., 1996, *ApJ*, 456, 798
- Handberg R., Campante T. L., 2011, *A&A*, 527, A56
- Handberg R., Lund M. N., 2014, *MNRAS*, 445, 2698
- Harvey J., 1985, in Rolfe E., Battrick B., eds, ESA SP-235: Future Missions in Solar, Heliospheric & Space Plasma Physics. ESA, Noordwijk, p. 199
- Hekker S., Christensen-Dalsgaard J., 2017, *A&AR*, 25, 1
- Hon M., Stello D., Yu J., 2018, *MNRAS*, 476, 3233
- Houdek G., 2006, in Fletcher K., Thompson M., eds, ESA SP-624: Beyond the Spherical Sun. ESA, Noordwijk, p. 28
- Houdek G., Balmforth N. J., Christensen-Dalsgaard J., Gough D. O., 1999, *A&A*, 351, 582
- Houdek G., Lund M. N., Trampedach R., Christensen-Dalsgaard J., Handberg R., Appourchaux T., 2019, *MNRAS*, 487, 595
- Huber D., Stello D., Bedding T. R., Chaplin W. J., Arentoft T., Quirion P. O., Kjeldsen H., 2009, *Commun. Asteroseismol.*, 160, 74
- Huber D. et al., 2010, *ApJ*, 723, 1607
- Huber D. et al., 2011, *ApJ*, 743, 143
- Kallinger T. et al., 2010, *A&A*, 509, A77
- Kallinger T. et al., 2012, *A&A*, 541, A51
- Kallinger T. et al., 2014, *A&A*, 570, A41
- Kass R. E., Raftery A. E., 1995, *J. Am. Stat. Assoc.*, 90, 773
- Kjeldsen H., Bedding T. R., 1995, *A&A*, 293, 87
- Kjeldsen H., Bedding T. R., Viskum M., Frandsen S., 1995, *AJ*, 109, 1313

- Kjeldsen H. et al., 2003, *AJ*, 126, 1483
- Li Y., Bedding T. R., Li T., Bi S., Murphy S. J., Corsaro E., Chen L., Tian Z., 2018, *MNRAS*, 476, 470
- Li T., Bedding T. R., Kjeldsen H., Stello D., Christensen-Dalsgaard J., Deng L., 2019, *MNRAS*, 483, 780
- Libbrecht K. G., 1992, *ApJ*, 387, 712
- Lomb N. R., 1976, *Ap&SS*, 39, 447
- Lund M. N. et al., 2017, *ApJ*, 835, 172
- Mathur S. et al., 2011, *ApJ*, 733, 95
- Mathur S. et al., 2013, *A&A*, 549, A12
- Mathur S. et al., 2017, *ApJS*, 229, 30
- Mazumdar A., 2005, *A&A*, 441, 1079
- Metcalfe T. S. et al., 2010, *ApJ*, 723, 1583
- Mosser B. et al., 2011, *A&A*, 525, L9
- Mosser B. et al., 2012a, *A&A*, 537, A30
- Mosser B. et al., 2012b, *A&A*, 540, A143
- Mosser B., Vrad M., Belkacem K., Deheuvels S., Goupil M. J., 2015, *A&A*, 584, A50
- Mosser B., Gehan C., Belkacem K., Samadi R., Michel E., Goupil M.-J., 2018, *A&A*, 618, A109
- Ong J. M. J., Basu S., 2019, *ApJ*, 885, 26
- Paxton B. et al., 2013, *ApJS*, 208, 4
- Pinheiro F. J. G., Fernandes J. M., 2010, *Ap&SS*, 328, 73
- Samadi R., Goupil M.-J., 2001, *A&A*, 370, 136
- Samadi R., Georgobiani D., Trampedach R., Goupil M. J., Stein R. F., Nordlund Å., 2007, *A&A*, 463, 297
- Samadi R., Belkacem K., Sonoi T., 2015, *EAS Publ. Ser.*, 73-74, 111
- Scargle J. D., 1982, *ApJ*, 263, 835
- Schofield M. et al., 2019, *ApJS*, 241, 12
- Shibahashi H., 1979, *PASJ*, 31, 87
- Stello D., Bruntt H., Preston H., Buzasi D., 2008, *ApJ*, 674, L53
- Stello D., Chaplin W. J., Basu S., Elsworth Y., Bedding T. R., 2009, *MNRAS*, 400, L80
- Stello D. et al., 2011, *ApJ*, 737, L10
- Stello D. et al., 2013, *ApJ*, 765, L41
- Stello D., Cantiello M., Fuller J., Garcia R. A., Huber D., 2016, *Publ. Astron. Soc. Aust.*, 33, e011
- Tassoul M., 1980, *ApJS*, 43, 469
- Tian Z., Bi S., Bedding T. R., Yang W., 2015, *A&A*, 580, A44
- Toutain T., Appourchaux T., 1994, *A&A*, 289, 649
- Vrad M., Mosser B., Samadi R., 2016, *A&A*, 588, A87
- Vrad M., Kallinger T., Mosser B., Barban C., Baudin F., Belkacem K., Cunha M. S., 2018, *A&A*, 616, A94
- White T. R. et al., 2011a, *ApJ*, 742, L3
- White T. R., Bedding T. R., Stello D., Christensen-Dalsgaard J., Huber D., Kjeldsen H., 2011b, *ApJ*, 743, 161
- White T. R. et al., 2012, *ApJ*, 751, L36
- Xiong D. R., Deng L., Zhang C., 2015, *MNRAS*, 451, 3354
- Yu J., Huber D., Bedding T. R., Stello D., Hon M., Murphy S. J., Khanna S., 2018, *ApJS*, 236, 42
- Zhou Y., Asplund M., Collet R., 2019, *ApJ*, 880, 13

SUPPORTING INFORMATION

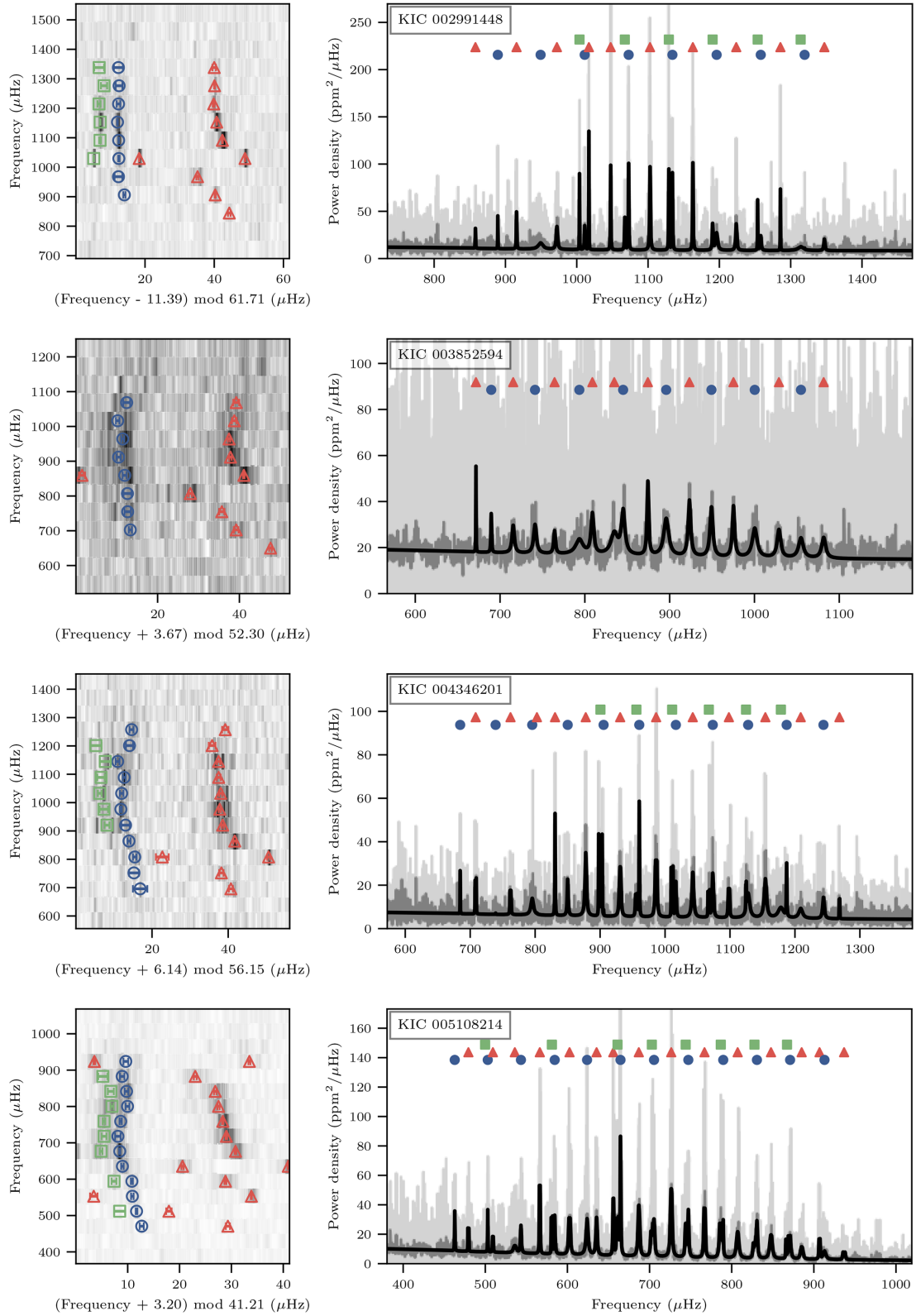
Supplementary data are available at [MNRAS](https://academic.oup.com/mnras/article/495/2/2363/5840550) online.

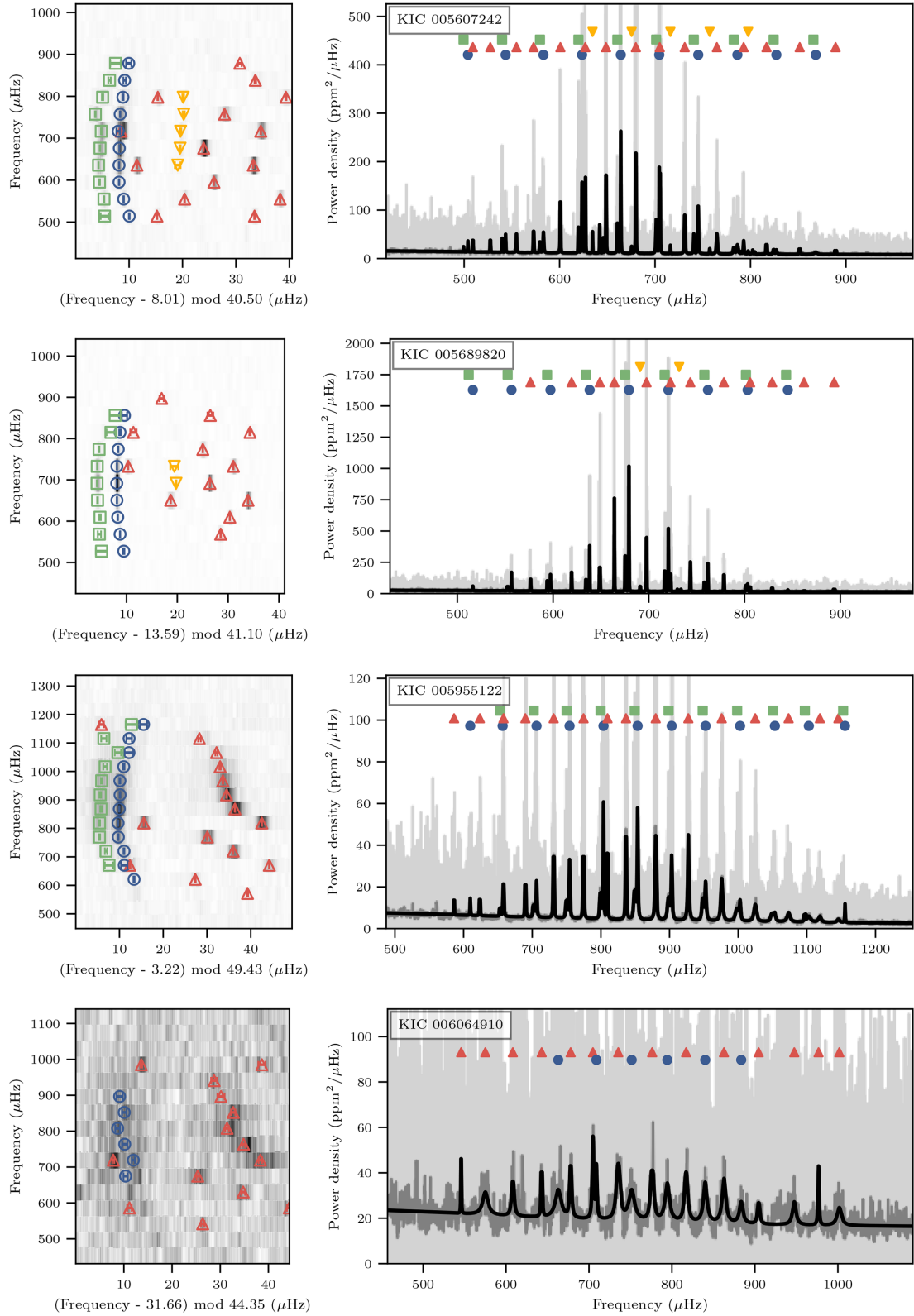
Table 2. Mode parameters obtained from the peakbagging.

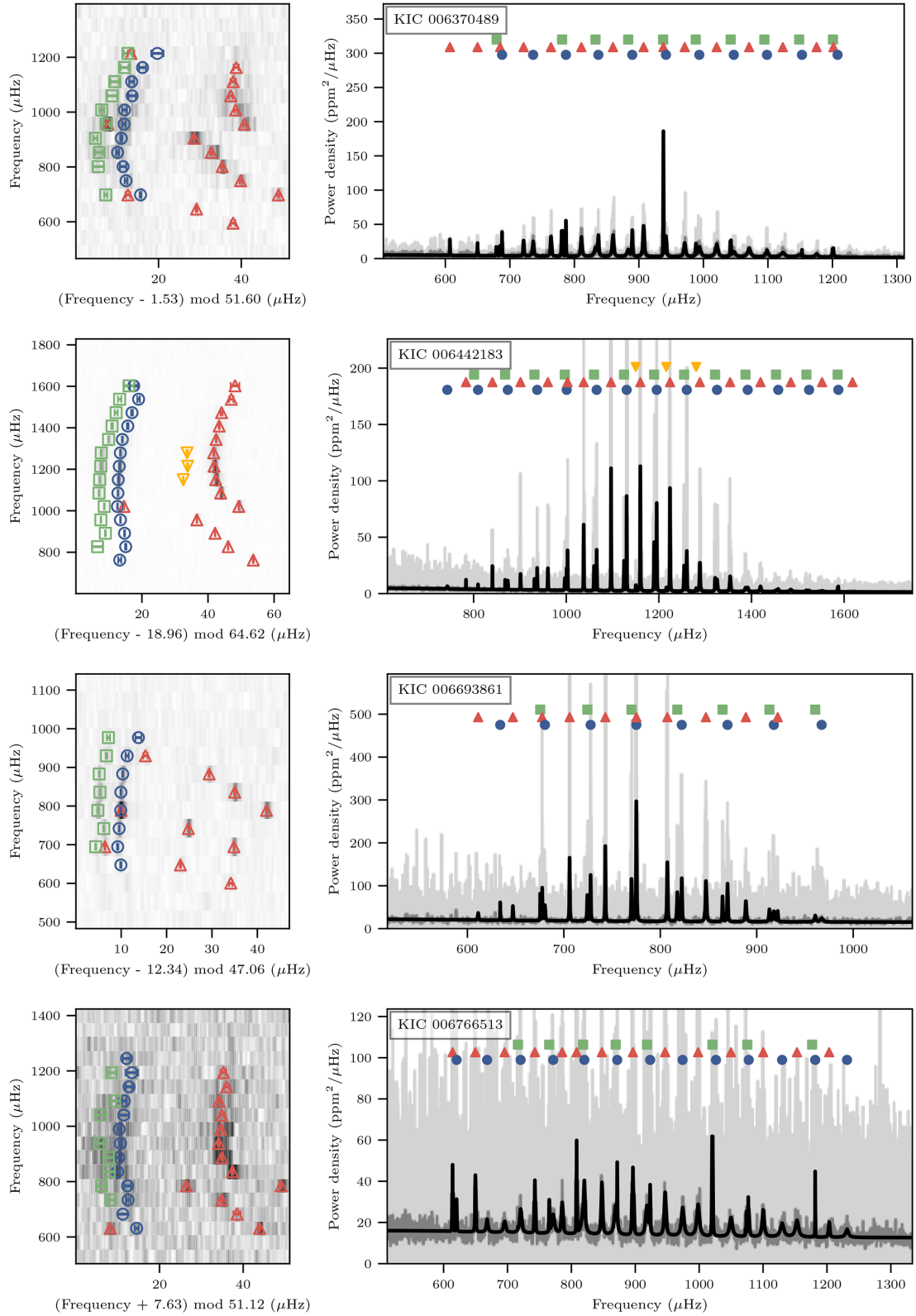
Please note: Oxford University Press is not responsible for the content or functionality of any supporting materials supplied by the authors. Any queries (other than missing material) should be directed to the corresponding author for the article.

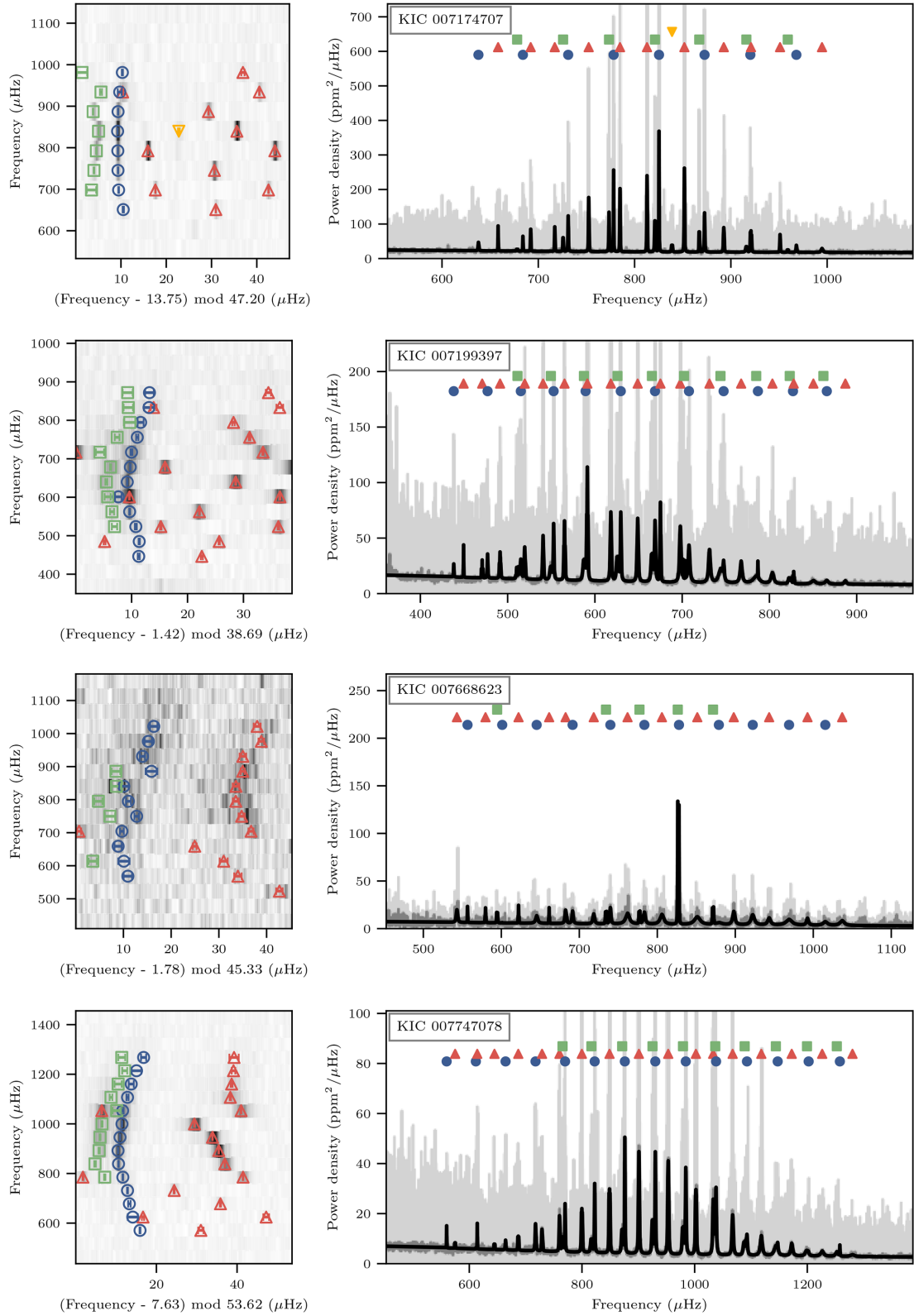
APPENDIX A: POWER SPECTRA OF 36 SUBGIANTS

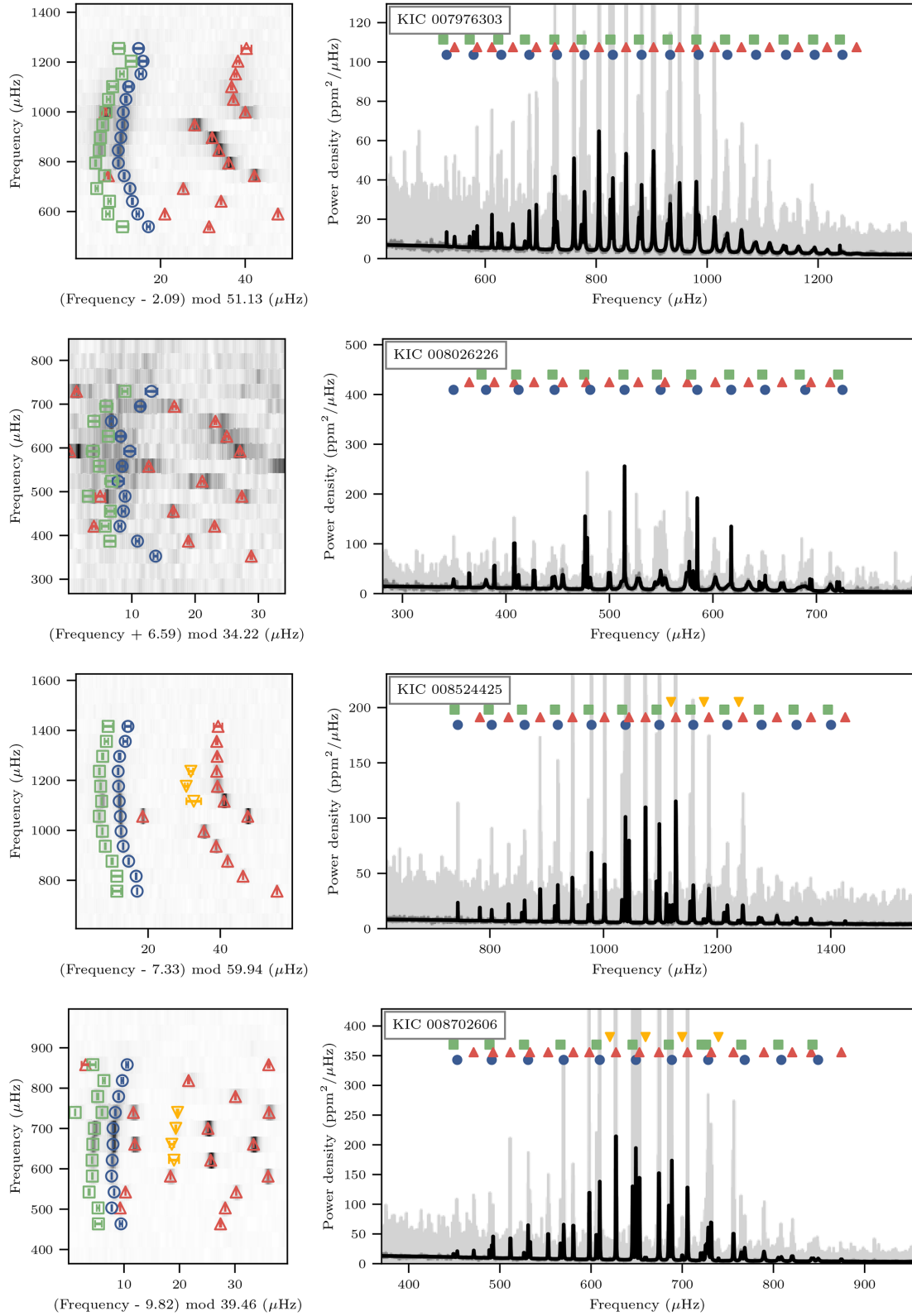
Left-hand panels: echelle diagrams. The blue circles ($l = 0$), red upward triangles ($l = 1$), green squares ($l = 2$), and purple downward triangles ($l = 3$) mark the extracted frequencies. Right-hand panels: power spectra. The fitted power spectra (black) are overlaid on the original power spectra (light grey) and the 1.0- μ Hz smoothed spectra (grey).

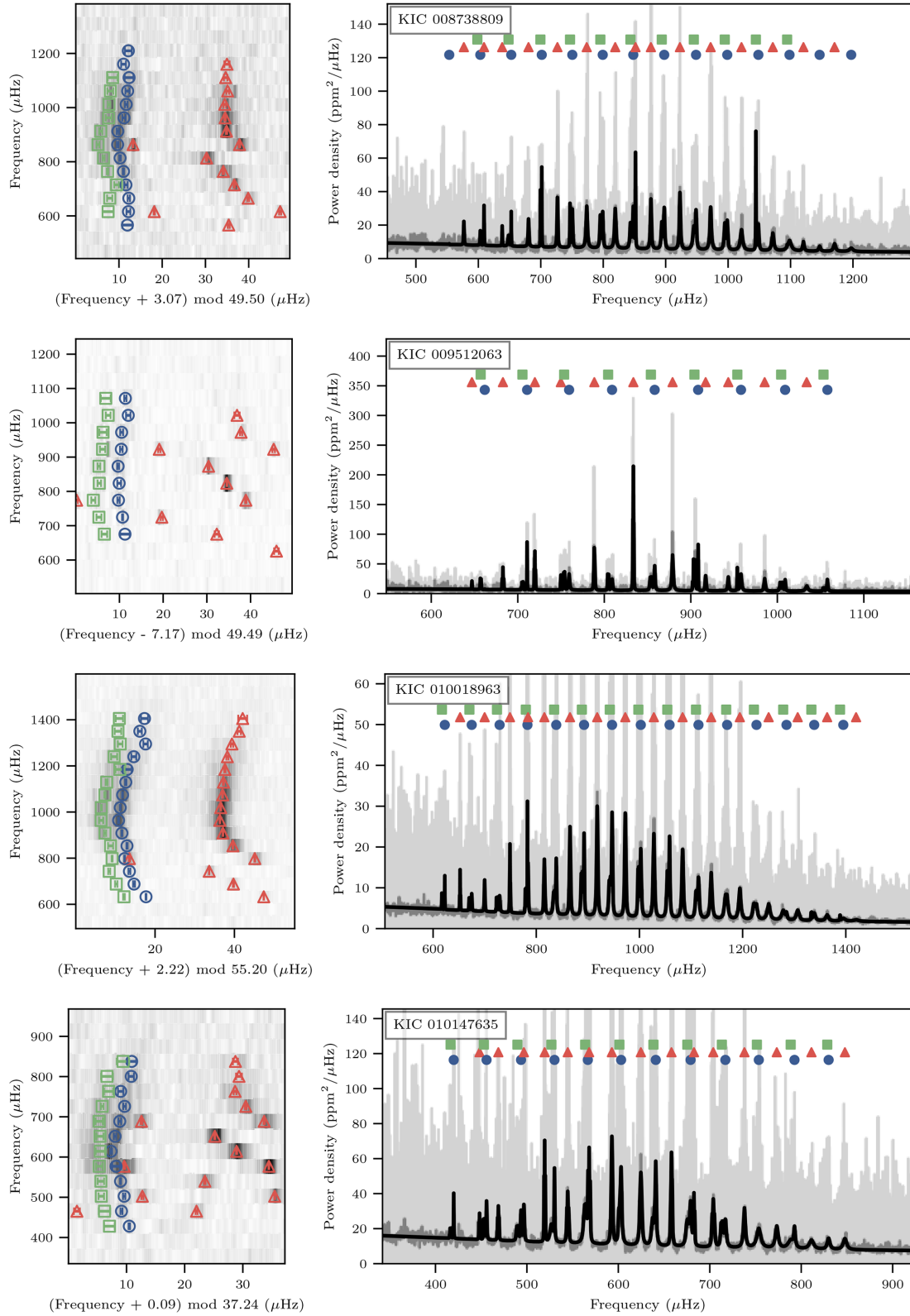


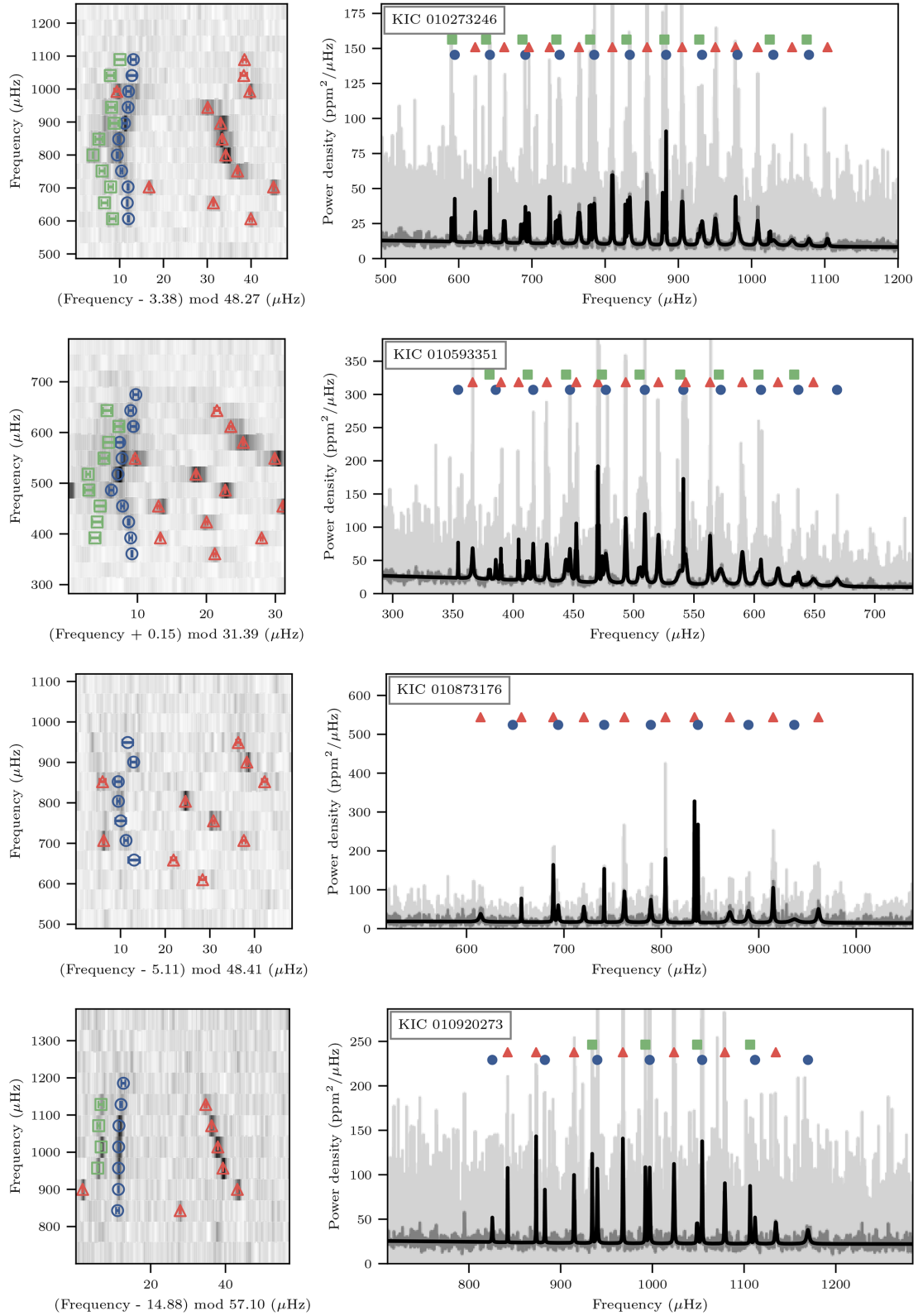


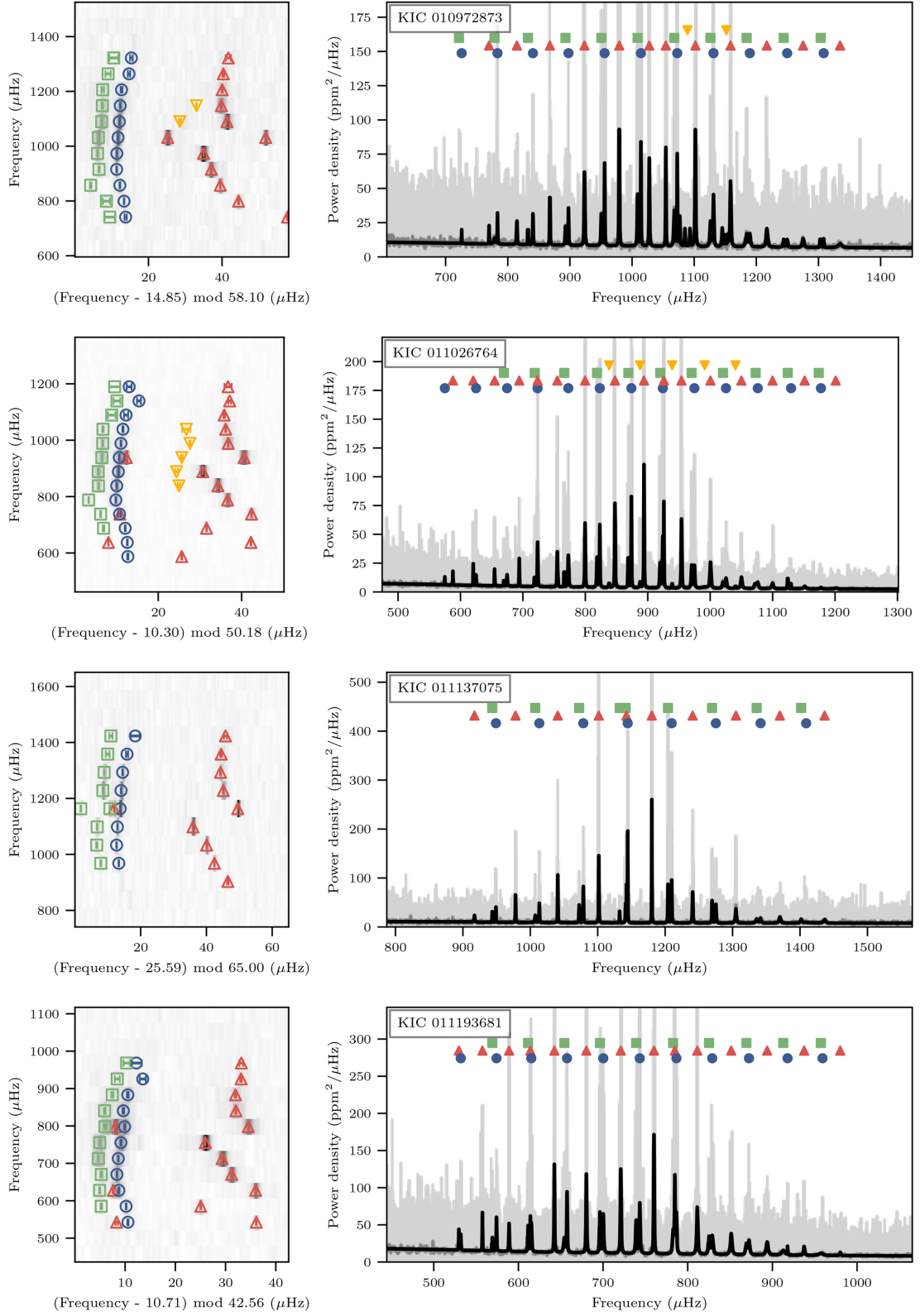


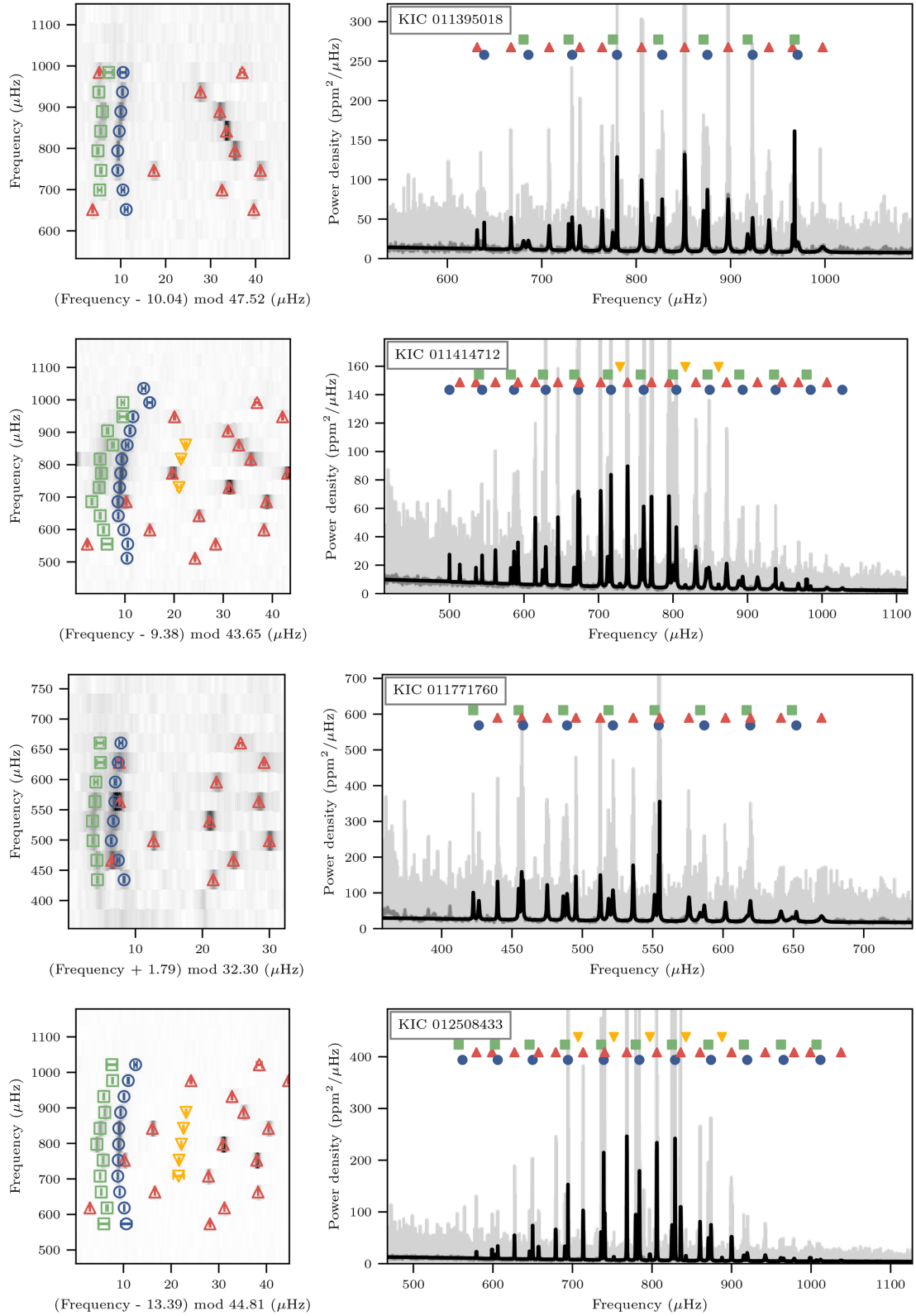













This paper has been typeset from a \LaTeX file prepared by the author.

3 Core and envelope rotation rates of subgiant stars

The paper produced in this chapter is in preparation and will be submitted to a peer-review journal. It may be expanded to use rotating stellar models to constrain the efficiency of angular momentum transport. The work is a collaborative effort. I performed the observational data analysis and stellar modelling. I and Jamie Tayar contributed to most experiments in this work. Jamie Tayar and Dennis Stello analysed the stellar models. Daniel Huber and Simon Murphy interpreted the rotation results. Sébastien Deheuvels contributed to the extraction of rotation rates. I wrote the manuscript, and the other authors have not yet commented on it.

Core and envelope rotation rates of *Kepler* subgiants probed by asteroseismology

Yaguang Li¹^{*}, Jamie Tayar,² Timothy R. Bedding,¹ Dennis Stello,³ Daniel Huber,⁴ Simon J. Murphy⁵ and Sébastien Deheuvels⁶

¹ *Sydney Institute for Astronomy (SIfA), School of Physics, University of Sydney, NSW 2006, Australia*

² *Department of Astronomy, University of Florida, Bryant Space Science Center, Stadium Road, Gainesville, FL 32611, USA*
DK-8000 Aarhus C, Denmark

³ *School of Physics, University of New South Wales, 2052, Australia*

⁴ *Institute for Astronomy, University of Hawai'i, 2680 Woodlawn Drive, Honolulu, HI 96822, USA*

⁵ *Centre for Astrophysics, University of Southern Queensland, Toowoomba, QLD 4350, Australia*

⁶ *IRAP, Université de Toulouse, CNRS, CNES, UPS, 14 avenue Edouard Belin, 31400 Toulouse, France*

Accepted XXX. Received YYY; in original form ZZZ

ABSTRACT

The angular momentum transport inside stars is a complex process that is not fully understood. Subgiants provide an excellent opportunity to test different mechanisms, because stars in this phase begin to deviate from near solid-body rotation. In this study, we measured the core and envelope rotation rates for 17 subgiants observed by *Kepler*, more than twice than previously measured stars. We used stellar models to determine the contribution of core and envelope to the rotational splittings of mixed modes, and then we fitted the splittings in the power spectrum. Firstly, we found that early subgiants exhibit similar core and envelope rotation periods, which fall within the range of 10 to 30 days. These rotation periods support the weakened magnetic braking theory on the main sequence. Secondly, we observed that strong differential rotation occurs around 800 Myr after the main sequence for stars with a mass lower than $1.2 M_{\odot}$, and approximately 300 Myr for higher-mass stars. The variation in the core rotation rates is not highly correlated with other stellar properties, while the envelopes slow down significantly towards the red-giant branch. These findings provide insight on the complex dynamics of angular momentum transport inside stars.

Key words: stars: rotation – stars: oscillations – stars: low-mass.

1 INTRODUCTION

Despite the significant progress that asteroseismology has made in measuring rotation rates in stars at various evolutionary stages, there remains a substantial knowledge gap in understanding angular momentum (AM) transport in stellar physics (Aerts 2021). Proposed processes for AM transport have yet to account for these observations.

At birth, stars have different initial rotation rates. Magnetic braking causes main-sequence stars with a mass below $1.2 M_{\odot}$ to have synchronised rotation rates with age, resulting in a well-defined rotation-mass-age relationship (Meibom et al. 2011; Barnes et al. 2016; Gruner & Barnes 2020). However, a weakened magnetic braking disrupts this relationship during the late main-sequence (Angus et al. 2015; van Saders et al. 2016; Metcalfe & Egeland 2019; Metcalfe et al. 2020; Hall et al. 2021). The envelope rotation rates in solar-like main-sequence stars, as traced by p-mode splittings, are consistent with surface rotation rates measured through spectro-

scopic linewidths or light curve spot modulations (Benomar et al. 2015; Nielsen et al. 2017; Hall et al. 2021). This suggests near solid-body rotation in the convective envelope during the main-sequence phase. In stars with a mass larger than $1.2 M_{\odot}$, which do not exhibit convective envelopes, rotation rates largely depend on the initial conditions when the stars were born. Near-core rotation rates inferred from g mode period spacing patterns generally agree with surface rotation rates measured by p mode splittings, Zeeman splittings, or spot modulations (Kurtz et al. 2014; Donati & Landstreet 2009; Van Reeth et al. 2018; Li et al. 2020a). These observations again support the notion of near solid-body rotation on the main-sequence, for most intrinsically slow rotators.

Our understanding of how angular momentum (AM) is transported inside evolved stars has been dramatically improved by the use of p-g mixed modes, which allows to probe both the core and envelope rotation rates. Early subgiants have been observed to exhibit near solid-body rotation (Deheuvels et al. 2020). On the red-giant branch (RGB), the core rotates rapidly with a range of values between 10 and 20 days, whereas the surface rotates much more slowly (Beck

* E-mail: yaguang.li@sydney.edu.au

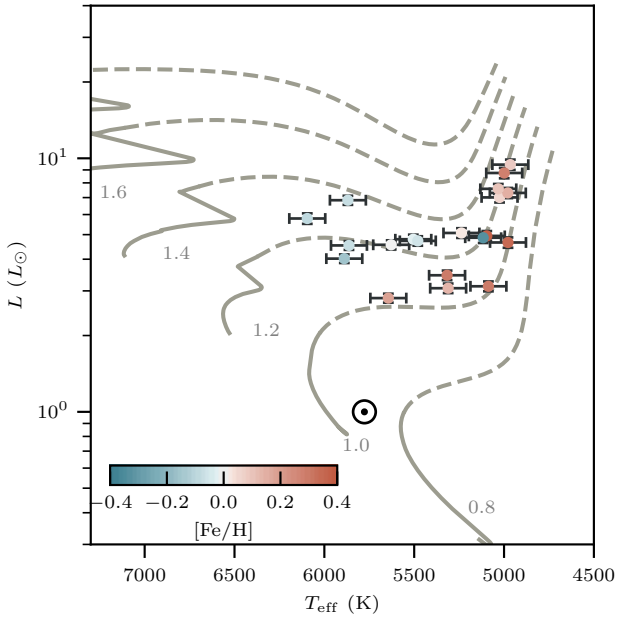


Figure 1. H–R diagram showing L vs. T_{eff} for the subgiant stars studied in this work, shown as circles colour-coded by metallicity. The Sun is marked by the usual symbol. The theoretical evolutionary models, calculated with MESA using $Y_{\text{init}} = 0.29$, $Z_{\text{init}} = 0.015$, and $\alpha_{\text{MLT}} = 2.0$, are shown in solid (main-sequence) and dashed (post-main-sequence) lines, labelled with mass in solar units.

et al. 2012; Deheuvels et al. 2014; Ceillier et al. 2017; Triana et al. 2017; Gehan et al. 2018; Fellay et al. 2021). During the helium-burning phase (HeB), the core undergoes spin down and rotates in the range of 30–200 days (Deheuvels et al. 2015; Mosser et al. 2012), with a gradual decrease over surface gravity (Tayar et al. 2019).

Shear instabilities and meridional circulation have been proposed as mechanisms for AM transport, but they have not been able to account for the observed rotation rates in stars (Marques et al. 2013; Eggenberger et al. 2012; Ceillier et al. 2013). Other candidates including internal gravity waves (Fuller et al. 2014; Pinçon et al. 2016), mixed modes (Belkacem et al. 2015a,b), and magnetic fields (Cantiello et al. 2014; Eggenberger et al. 2019; den Hartogh et al. 2019; Eggenberger et al. 2022; Moyano et al. 2023) have been proposed to explain the observations. During the evolution from early subgiant to the RGB phases, stars undergo significant structural changes: the core contracts and the envelope expands. Precise age measurements using mixed modes (Benomar et al. 2012; Li et al. 2020c) offer an opportunity to precisely constrain the timescales for AM transport. However, the rotation rates of only a few subgiants have been measured (Deheuvels et al. 2014, 2020). To bridge this knowledge gap, we extend the work of Li et al. (2020b) and present new measurements of the rotation rates of *Kepler* subgiants in this study.

2 DATA ANALYSIS

2.1 Sample selection

We collected the early subgiant sample (defined by the mixed-mode density smaller than 1) with mode frequencies extracted by Li et al. (2020b). To expand beyond early subgiants, we also examined the sample of Mathur et al. (2022). Combined with the 9 early subgiants from Li et al. (2020b), our sample now consists of 17 stars with a minimum ν_{max} value of 300 μHz . The Hertzsprung–Russell diagram for our sample is presented in Fig. 1.

2.2 Observations

In order to obtain a reference model for each star, we need the observed mode frequencies ν_{nl} to constrain models. We extracted the frequencies with the “peakbagging” approach (Handberg & Campante 2011; Davies et al. 2016; Lund et al. 2017), using the same method as illustrated in Li et al. (2020b). In brief, we fitted the power spectrum of a mode associated with orders (n, l, m) with a Lorentzian profile:

$$L_{nlm}(\nu) = \frac{\mathcal{E}_{lm}(i) 2A_{nl}^2 / (\pi \Gamma_{nl})}{1 + 4(\nu - \nu_{nl} + m\nu_{s,nl})^2 / \Gamma_{nl}^2}, \quad (1)$$

where ν_{nl} is the mode frequency, A_{nl} the mode amplitude, Γ_{nl} the mode linewidth, and $\nu_{s,nl}$ the splitting frequency, which varies with n and l . The visibility function $\mathcal{E}_{lm}(i)$ depends on the inclination i and is given by

$$\mathcal{E}_{lm}(i) = \frac{(l - |m|)!}{(l + |m|)!} \left[P_l^{|m|}(\cos i^*) \right]^2, \quad (2)$$

where $P_l^{|m|}$ are the Legendre functions (Gizon & Solanki 2003). At this step, we treated the rotational splittings $\nu_{s,nl}$ included in the fit as completely free parameters, without considering the connections between each mode. This is to avoid any potential bias on mode frequencies ν_{nl} and their associated uncertainties.

We derived the atmospheric parameters T_{eff} and $[\text{Fe}/\text{H}]$ for the sample through spectroscopy using the Keck HIRES spectrograph (Vogt et al. 1994) at the Keck-I 10-m telescope on Maunakea observatory, Hawai‘i (Furlan et al. 2018). The spectra were obtained and reduced by the California Planet Search queue (CPS, Howard et al. 2010). We used the C5 decker and obtained spectra with a S/N per pixel of 80 at $\sim 600 \text{ nm}$ and a spectral resolving power of $R \sim 60000$. To measure the metallicities, we utilized Specmatch-synth (Petigura 2015), which fits a synthetic grid of model atmospheres and has been thoroughly validated through the California Kepler Survey (Petigura et al. 2017; Johnson et al. 2017).

With *Gaia* DR3 (Gaia Collaboration et al. 2016, 2020), we determined their luminosities, L , by combining the parallaxes with the 2MASS K -band magnitudes. We used the “direct” method implemented in the software ISOCCLASSIFY (Huber et al. 2017; Berger et al. 2020), combining with the Green et al. (2019) dust map and the bolometric corrections from MIST models (Choi et al. 2016).

2.3 Stellar models

We constructed a grid of stellar models with MESA (version r15140; Paxton et al. 2011, 2013, 2015, 2018, 2019) and

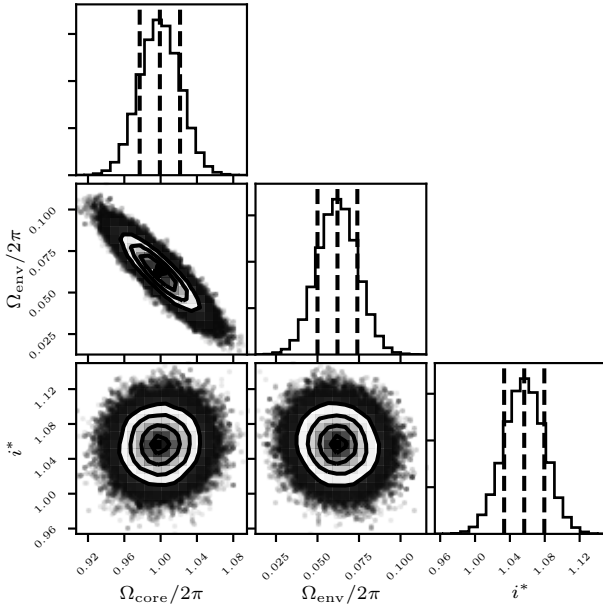


Figure 2. Probability distributions of the core rotation rate Ω_{core} , the envelope rotation rate Ω_{env} , and the inclination angle i , for KIC 3429205.

GRYE (version 6.0.1; [Townsend & Teitler 2013](#)). We refer to [Li et al. \(2022\)](#) for a full description of the adopted input physics. The grid spans a range of input parameters, including stellar mass $M \in (0.7, 1.8) M_{\odot}$, initial helium abundance $Y_{\text{init}} \in (0.22, 0.32)$, metallicity $[M/H] \in (-0.5, 0.5)$, the mixing-length parameter $\alpha_{\text{MLT}} \in (1.3, 2.7)$, and core overshoot $f_{\text{core}} \in (0., 0.02)$. We uniformly sampled these five parameters using a quasi-random Sobol sequence with a total number of 16384 points ([Bellinger et al. 2016](#)). Each set of parameters defines a distinct evolutionary track. At each time step, we saved the stellar structure and solved for the radial and dipole modes based on the adiabatic oscillation equations. The surface effect was corrected based on the methods outlined in [Ball & Gizon \(2014\)](#); [Li et al. \(2022\)](#).

To determine the best-fitting model for each stars, we utilised classical observables $q = \{T_{\text{eff}}, [\text{Fe}/H], L\}$, and the frequencies of radial ($l = 0$) and dipole ($l = 1$) modes. Our approach involved minimising the χ^2 function given by

$$\chi^2 = \sum_q \frac{(q_{\text{obs}} - q_{\text{mod}})^2}{\sigma_q^2} + \sum_{\nu_{nl}} \frac{(\nu_{nl, \text{obs}} - \nu_{nl, \text{mod}})^2}{\sigma_{\nu_{nl}}^2}. \quad (3)$$

2.4 Measuring the core and envelope rotation rates

The rotational splitting of a mode could be described by the following expression ([Ledoux 1951](#); [Unno et al. 1989](#); [Christensen-Dalsgaard & Berthomieu 1991](#); [Goupil et al. 2013](#)):

$$\nu_s = \frac{1}{2\pi} \int_0^1 K(x) \Omega(x) dx, \quad (4)$$

where $x = r/R$ is the normalised radius, $\Omega(x)$ is the radial rotational profile in angular frequency. $K(x)$ is the rotational

kernel defined as

$$K(x) = \frac{1}{I} \left(z_1^2 + z_2^2 - \frac{2}{\sqrt{l(l+1)}} z_1 z_2 - \frac{1}{l(l+1)} z_2^2 \right) \frac{1}{x}, \quad (5)$$

$$z_1 = (3\rho/\bar{\rho})^{1/2} x^{3/2} \xi_r/R, \quad (6)$$

and

$$z_2 = \sqrt{l(l+1)} (3\rho/\bar{\rho})^{1/2} x^{3/2} \xi_h/R, \quad (7)$$

where I is the mode inertia, ρ is the density, $\bar{\rho}$ is the stellar mean density, and ξ_r and ξ_h represents radial and horizontal displacement eigenfunctions, respectively.

Furthermore, we can express Eq. 4 as a sum of two terms corresponding to the rotational kernels in the core and envelope regions, respectively, with characteristic rotation rates, Ω_{core} and Ω_{env} :

$$\nu_s = \beta_{\text{core}} \Omega_{\text{core}} + \beta_{\text{env}} \Omega_{\text{env}}, \quad (8)$$

where

$$\beta_{\text{core}} = \int_0^{x_{\text{core}}} K(x) dx, \quad (9)$$

$$\beta_{\text{env}} = \int_{x_{\text{core}}}^1 K(x) dx, \quad (10)$$

and

$$\Omega_{\text{core}} = \frac{\int_0^{x_{\text{core}}} \Omega(x') K(x') dx'}{\int_0^{x_{\text{core}}} K(x') dx'}, \quad (11)$$

$$\Omega_{\text{env}} = \frac{\int_{x_{\text{core}}}^1 \Omega(x') K(x') dx'}{\int_{x_{\text{core}}}^1 K(x') dx'}. \quad (12)$$

Here, $x_{\text{core}} = r_{\text{core}}/R$ is the upper turning point of the g mode cavity.

Based on the reference model we obtained in Section 2.3, we calculated β_{core} and β_{env} for all $l = 1$ modes. To obtain estimates of Ω_{core} and Ω_{env} , we substituted Eq. 8 as the expression for $\nu_{s, nl}$ in Eq. 1, and then re-fitted the power spectra. Fig. 2 shows an example of well-constrained posterior distributions of Ω_{core} , Ω_{env} and the inclination i .

3 RESULTS AND DISCUSSIONS

3.1 Core and envelope rotation rates

Fig. 3 presents the core and envelope rotation periods as a function of radius or $\log g$, with stellar mass indicated by colour. The envelope rotation periods for main-sequence stars probed by p mode splittings ([Hall et al. 2021](#)) and the core rotation periods for RGB stars probed by p-g mixed mode splittings ([Gehan et al. 2018](#)) are also shown for comparison. As the star evolve from the main sequence to the RGB, their core rotation rates exhibit a wide range of values, typically within 10 to 30 days. The envelopes slow down significantly in this process.

Our sample spans the subgiant phase and reveals a clear development of differential rotation in this evolutionary phase. To highlight this effect, we calculated the ratio of the core and envelope rotation rates $\Omega_{\text{core}}/\Omega_{\text{env}}$ as a function of mixed mode density N , defined as $\Delta\nu/\nu_{\text{max}}^2/\Delta\Pi_1$, where $\Delta\nu$, ν_{max}

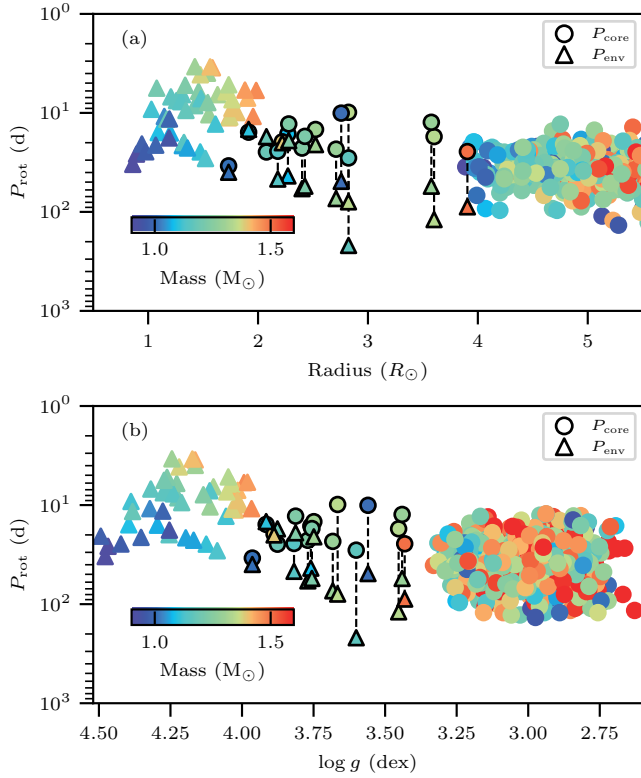


Figure 3. Core and envelope rotation periods vs. radius (panel a) and $\log g$ (panel b), colour-coded by stellar mass. The symbols with black edges show the stars measured in this work. The rest stars are measured by Hall et al. (2021) for main-sequence stars and Gehan et al. (2018) for RGB stars.

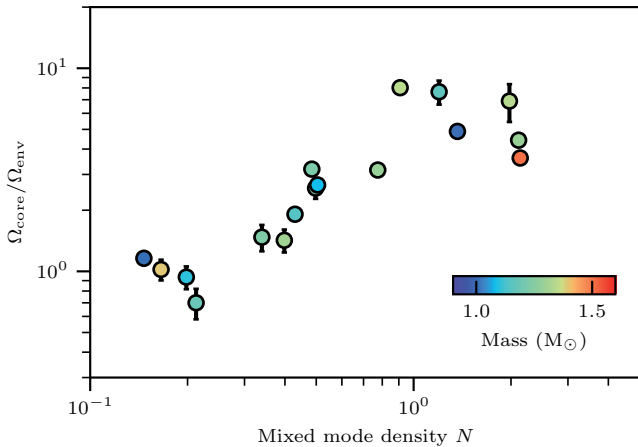


Figure 4. Ratio of the core and envelope rotation rates vs. mixed mode density as a proxy of evolutionary stage.

and $\Delta\Pi_1$ are the p-mode large separation, the frequency of maximum power, and the g-mode period spacing, respectively. Fig. 4 illustrates this relationship.

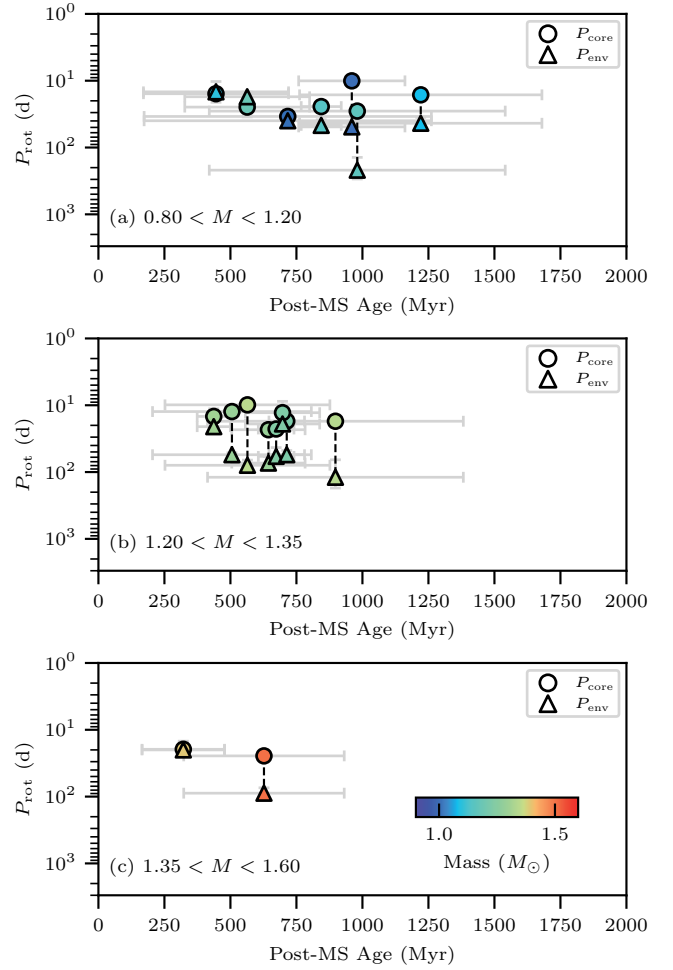


Figure 5. Core and envelope rotation periods versus post-main-sequence age in three separate mass bins.

3.2 Implications on gyrochronology

Early subgiants with $R \sim 2 R_{\odot}$ or $\log g \sim 3.9$, display similar rotation rates across the core and envelope, with rotation periods ranging from 10 to 30 days. Interestingly, these rotation periods are in a similar range of old main-sequence asteroseismic targets (Angus et al. 2015; Hall et al. 2021). This suggests that the rotation rates of early subgiants can further support the scenario of weakened magnetic braking during the intermediate main-sequence (van Saders et al. 2016; Metcalfe et al. 2020). This finding also supports the idea that the core-envelope decoupling in subgiants is driven by the development of radial differential rotation.

3.3 Timescales of the angular momentum transport

To investigate the time evolution of differential rotation, we present the rotation periods as a function of post-main-sequence age in Fig. 5, where we further divide the sample into three mass bins. We define the termination of the main sequence when the mass fraction of central hydrogen drops below 10^{-5} .

During the subgiant phase, the core contracts and the envelope expands. If there were no AM transport within stars,

we would expect the core spin up and the envelope to slow down, resulting in a growing contrast between the core and envelope rotation rates. However, this is not observed in early subgiants, indicating that there must be an efficient transport mechanism taking place. Nevertheless, even though the AM transport mechanisms at work are rather efficient, they are not able to fully counteract the structural changes that lead to the development of differential rotation.

For stars with masses below $1.2 M_{\odot}$, differential rotation typically develops around 800 Myr after the main-sequence turn-off point. For intermediate-mass stars with $1.2 < M < 1.6 M_{\odot}$, differential rotation takes place earlier, at around 300 Myr after the turn-off point. By comparing our results with rotating stellar models, we could obtain valuable constraints on the timescales of AM transport in subgiants.

4 CONCLUSIONS

In this paper, we present an analysis of core and envelope rotation rates for 17 subgiants observed by *Kepler*. Our results provide important insights into the AM transport at work inside stars. We summarise our findings as follows:

- (i) Early subgiants have similar rotation rates in their cores and envelopes, suggesting efficient transport of AM within these stars.
- (ii) Our measurements of rotation periods for early subgiants support the idea of weakened magnetic braking during the main sequence.
- (iii) As subgiants evolve towards the RGB, we observed a range of rotation rates in the core (10 to 30 days), and a significant slowdown in the envelope.
- (iv) We found that differential rotation takes place in subgiants at around 800 Myr after the main-sequence turn-off point for $M < 1.2 M_{\odot}$ stars, and around 300 Myr for $M > 1.2 M_{\odot}$ stars.

ACKNOWLEDGEMENTS

This work is made possible by the following open-source Python software: Numpy (van der Walt et al. 2011), Scipy (Virtanen et al. 2020), Matplotlib (Hunter 2007), Corner (Foreman-Mackey 2016), and ISOCCLASSIFY (Huber et al. 2017; Berger et al. 2020).

REFERENCES

Aerts C., 2021, *Reviews of Modern Physics*, 93, 015001
 Angus R., Aigrain S., Foreman-Mackey D., McQuillan A., 2015, *MNRAS*, 450, 1787
 Ball W. H., Gizon L., 2014, *A&A*, 568, A123
 Barnes S. A., Weingrill J., Fritzewski D., Strassmeier K. G., Platais I., 2016, *ApJ*, 823, 16
 Beck P. G., et al., 2012, *Nature*, 481, 55
 Belkacem K., et al., 2015a, *A&A*, 579, A30
 Belkacem K., et al., 2015b, *A&A*, 579, A31
 Bellinger E. P., Angelou G. C., Hekker S., Basu S., Ball W. H., Guggenberger E., 2016, *ApJ*, 830, 31
 Benomar O., Bedding T. R., Stello D., Deheuvels S., White T. R., Christensen-Dalsgaard J., 2012, *ApJ*, 745, L33

Benomar O., Takata M., Shibahashi H., Ceillier T., García R. A., 2015, *MNRAS*, 452, 2654
 Berger T. A., Huber D., van Saders J. L., Gaidos E., Tayar J., Kraus A. L., 2020, *AJ*, 159, 280
 Cantiello M., Mankovich C., Bildsten L., Christensen-Dalsgaard J., Paxton B., 2014, *ApJ*, 788, 93
 Ceillier T., Eggenberger P., García R. A., Mathis S., 2013, *A&A*, 555, A54
 Ceillier T., et al., 2017, *A&A*, 605, A111
 Choi J., Dotter A., Conroy C., Cantiello M., Paxton B., Johnson B. D., 2016, *ApJ*, 823, 102
 Christensen-Dalsgaard J., Berthomieu G., 1991, in , *Solar Interior and Atmosphere*. pp 401–478
 Davies G. R., et al., 2016, *MNRAS*, 456, 2183
 Deheuvels S., et al., 2014, *A&A*, 564, A27
 Deheuvels S., Ballot J., Beck P. G., Mosser B., Østensen R., García R. A., Goupil M. J., 2015, *A&A*, 580, A96
 Deheuvels S., Ballot J., Eggenberger P., Spada F., Noll A., den Hartogh J. W., 2020, arXiv e-prints, p. arXiv:2007.02585
 Donati J. F., Landstreet J. D., 2009, *ARA&A*, 47, 333
 Eggenberger P., Montalbán J., Miglio A., 2012, *A&A*, 544, L4
 Eggenberger P., den Hartogh J. W., Buldgen G., Meynet G., Salmon S. J. A. J., Deheuvels S., 2019, *A&A*, 631, L6
 Eggenberger P., Moyano F. D., den Hartogh J. W., 2022, *A&A*, 664, L16
 Fellay L., Buldgen G., Eggenberger P., Khan S., Salmon S. J. A. J., Miglio A., Montalbán J., 2021, *A&A*, 654, A133
 Foreman-Mackey D., 2016, *The Journal of Open Source Software*, 24
 Fuller J., Lecoanet D., Cantiello M., Brown B., 2014, *ApJ*, 796, 17
 Furlan E., et al., 2018, *ApJ*, 861, 149
 Gaia Collaboration et al., 2016, *A&A*, 595, A1
 Gaia Collaboration Brown A. G. A., Vallenari A., Prusti T., de Bruijne J. H. J., Babusiaux C., Biermann M., 2020, arXiv e-prints, p. arXiv:2012.01533
 Gehan C., Mosser B., Michel E., Samadi R., Kallinger T., 2018, *A&A*, 616, A24
 Gizon L., Solanki S. K., 2003, *ApJ*, 589, 1009
 Goupil M. J., Mosser B., Marques J. P., Ouazzani R. M., Belkacem K., Lebreton Y., Samadi R., 2013, *A&A*, 549, A75
 Green G. M., Schlafly E., Zucker C., Speagle J. S., Finkbeiner D., 2019, *ApJ*, 887, 93
 Gruner D., Barnes S. A., 2020, *A&A*, 644, A16
 Hall O. J., et al., 2021, *Nature Astronomy*, 5, 707
 Handberg R., Campante T. L., 2011, *A&A*, 527, A56
 Howard A. W., et al., 2010, *ApJ*, 721, 1467
 Huber D., et al., 2017, *ApJ*, 844, 102
 Hunter J. D., 2007, *Computing in Science & Engineering*, 9, 90
 Johnson J. A., et al., 2017, *AJ*, 154, 108
 Kurtz D. W., Saio H., Takata M., Shibahashi H., Murphy S. J., Sekii T., 2014, *MNRAS*, 444, 102
 Ledoux P., 1951, *ApJ*, 114, 373
 Li G., Van Reeth T., Bedding T. R., Murphy S. J., Antoci V., Ouazzani R.-M., Barbara N. H., 2020a, *MNRAS*, 491, 3586
 Li Y., Bedding T. R., Li T., Bi S., Stello D., Zhou Y., White T. R., 2020b, *MNRAS*, 495, 2363
 Li T., Bedding T. R., Christensen-Dalsgaard J., Stello D., Li Y., Keen M. A., 2020c, *MNRAS*, 495, 3431
 Li Y., et al., 2022, arXiv e-prints, p. arXiv:2208.01176
 Lund M. N., et al., 2017, *ApJ*, 835, 172
 Marques J. P., et al., 2013, *A&A*, 549, A74
 Mathur S., et al., 2022, *A&A*, 657, A31
 Meibom S., et al., 2011, *ApJ*, 733, L9
 Metcalfe T. S., Egeland R., 2019, *ApJ*, 871, 39
 Metcalfe T. S., et al., 2020, arXiv e-prints, p. arXiv:2007.12755
 Mosser B., et al., 2012, *A&A*, 548, A10
 Moyano F. D., Eggenberger P., Mosser B., Spada F., 2023, arXiv e-prints, p. arXiv:2302.07811

- Nielsen M. B., Schunker H., Gizon L., Schou J., Ball W. H., 2017, *A&A*, **603**, [A6](#)
- Paxton B., Bildsten L., Dotter A., Herwig F., Lesaffre P., Timmes F., 2011, *ApJS*, **192**, [3](#)
- Paxton B., et al., 2013, *ApJS*, **208**, [4](#)
- Paxton B., et al., 2015, *ApJS*, **220**, [15](#)
- Paxton B., et al., 2018, *ApJS*, **234**, [34](#)
- Paxton B., et al., 2019, *ApJS*, **243**, [10](#)
- Petigura E. A., 2015, PhD thesis, University of California, Berkeley
- Petigura E. A., et al., 2017, *AJ*, **154**, [107](#)
- Pinçon C., Belkacem K., Goupil M. J., 2016, *A&A*, **588**, [A122](#)
- Tayar J., Beck P. G., Pinsonneault M. H., García R. A., Mathur S., 2019, *ApJ*, **887**, [203](#)
- Townsend R. H. D., Teitler S. A., 2013, *MNRAS*, **435**, [3406](#)
- Triana S. A., Corsaro E., De Ridder J., Bonanno A., Pérez Hernández F., García R. A., 2017, *A&A*, **602**, [A62](#)
- Unno W., Osaki Y., Ando H., Saio H., Shibahashi H., 1989, Non-radial oscillations of stars
- Van Reeth T., et al., 2018, *A&A*, **618**, [A24](#)
- Virtanen P., et al., 2020, *Nature Methods*, **17**, [261](#)
- Vogt S. S., et al., 1994, in Crawford D. L., Craine E. R., eds, Society of Photo-Optical Instrumentation Engineers (SPIE) Conference Series Vol. 2198, Instrumentation in Astronomy VIII. p. 362, [doi:10.1117/12.176725](#)
- den Hartogh J. W., Eggenberger P., Hirschi R., 2019, *A&A*, **622**, [A187](#)
- van Saders J. L., Ceillier T., Metcalfe T. S., Silva Aguirre V., Pinsonneault M. H., García R. A., Mathur S., Davies G. R., 2016, *Nature*, **529**, [181](#)
- van der Walt S., Colbert S. C., Varoquaux G., 2011, *Computing in Science Engineering*, **13**, [22](#)

This paper has been typeset from a \TeX / \LaTeX file prepared by the author.

4 Testing the intrinsic scatter of the astero-seismic scaling relations

The paper produced in this chapter is published as [Li, Yaguang et al. \(2021\)](#). The work is a collaborative effort. I performed the data analysis and compared the distributions of stellar populations between *Galaxia* and *Kepler*. Tim Bedding provided the initial idea. I and Tim Bedding contributed to most experiments in this paper. Sanjib Sharma generated the *Galaxia* synthetic sample. Dennis Stello, Daniel Huber, and Simon Murphy contributed to the interpretation of the results. I wrote the paper, and all authors (especially Tim Bedding and Dennis Stello) commented on the manuscript.



Testing the intrinsic scatter of the asteroseismic scaling relations with *Kepler* red giants

Yaguang Li^{1,2,★}, Timothy R. Bedding^{1,2}, Dennis Stello^{1,2,3}, Sanjib Sharma¹, Daniel Huber^{1,4}
and Simon J. Murphy^{1,2}

¹Sydney Institute for Astronomy (SfA), School of Physics, University of Sydney, NSW 2006, Australia

²Stellar Astrophysics Centre, Department of Physics and Astronomy, Aarhus University, Ny Munkegade 120, DK-8000 Aarhus C, Denmark

³School of Physics, University of New South Wales, NSW 2052, Australia

⁴Institute for Astronomy, University of Hawai‘i, 2680 Woodlawn Drive, Honolulu, HI 96822, USA

Accepted 2020 December 15. Received 2020 December 10; in original form 2020 October 27

ABSTRACT

Asteroseismic scaling relations are often used to derive stellar masses and radii, particularly for stellar, exoplanet, and Galactic studies. It is therefore important that their precisions are known. Here we measure the intrinsic scatter of the underlying seismic scaling relations for $\Delta\nu$ and ν_{\max} , using two sharp features that are formed in the H–R diagram (or related diagrams) by the red giant populations. These features are the edge near the zero-age core-helium-burning phase, and the strong clustering of stars at the so-called red giant branch bump. The broadening of those features is determined by factors including the intrinsic scatter of the scaling relations themselves, and therefore it is capable of imposing constraints on them. We modelled *Kepler* stars with a *Galaxia* synthetic population, upon which we applied the intrinsic scatter of the scaling relations to match the degree of sharpness seen in the observation. We found that the random errors from measuring $\Delta\nu$ and ν_{\max} provide the dominating scatter that blurs the features. As a consequence, we conclude that the scaling relations have intrinsic scatter of ~ 0.5 ($\Delta\nu$), ~ 1.1 (ν_{\max}), ~ 1.7 (M), and ~ 0.4 per cent (R), for the SYD pipeline measured $\Delta\nu$ and ν_{\max} . This confirms that the scaling relations are very powerful tools. In addition, we show that standard evolution models fail to predict some of the structures in the observed population of both the HeB and RGB stars. Further stellar model improvements are needed to reproduce the exact distributions.

Key words: stars: low-mass – stars: oscillations – stars: solar-type.

1 INTRODUCTION

The asteroseismic scaling relations for red giants have so far proved to be an extremely useful tool to obtain stellar masses and radii. A critical issue associated with the scaling relations is that their limits are poorly understood (Hekker 2020). The intrinsic scatter of the scaling relations, originating from potential hidden dependencies not accounted for in the current relations, can cause a seemingly random fluctuation. Testing the intrinsic scatter of these relations is the aim of this paper.

The scaling relations rely on two characteristic frequencies in the power spectra of solar-like oscillations. The first one is $\Delta\nu$, the large separation of p modes, approximately proportional to the square root of mean density (Ulrich 1986):

$$\frac{\Delta\nu}{\Delta\nu_{\odot}} \approx \left(\frac{M}{M_{\odot}}\right)^{1/2} \left(\frac{R}{R_{\odot}}\right)^{-3/2}. \quad (1)$$

The second is ν_{\max} , which is the frequency where the power of the oscillations is strongest. It relates to the surface properties $g/\sqrt{T_{\text{eff}}}$

(Brown et al. 1991; Kjeldsen & Bedding 1995):

$$\frac{\nu_{\max}}{\nu_{\max,\odot}} \approx \left(\frac{M}{M_{\odot}}\right) \left(\frac{R}{R_{\odot}}\right)^{-2} \left(\frac{T_{\text{eff}}}{T_{\text{eff},\odot}}\right)^{-1/2}. \quad (2)$$

Using these, the mass and radius can be determined if the effective temperature is known (Stello et al. 2008; Kallinger et al. 2010a):

$$\frac{M}{M_{\odot}} \approx \left(\frac{\nu_{\max}}{\nu_{\max,\odot}}\right)^3 \left(\frac{\Delta\nu}{\Delta\nu_{\odot}}\right)^{-4} \left(\frac{T_{\text{eff}}}{T_{\text{eff},\odot}}\right)^{3/2}, \quad (3)$$

$$\frac{R}{R_{\odot}} \approx \left(\frac{\nu_{\max}}{\nu_{\max,\odot}}\right) \left(\frac{\Delta\nu}{\Delta\nu_{\odot}}\right)^{-2} \left(\frac{T_{\text{eff}}}{T_{\text{eff},\odot}}\right)^{1/2}. \quad (4)$$

From a theoretical point of view, a more accurate value for $\Delta\nu$ can be calculated from oscillation frequencies, given a stellar model; thus, it is possible to map the departure of equation (1), as a function of $[M/H]$, M , T_{eff} and evolutionary state (White et al. 2011; Guggenberger et al. 2016; Sharma et al. 2016; Rodrigues et al. 2017; Serenelli et al. 2017; Pinsonneault et al. 2018). Improvements are seen when adopting this revised theoretical $\Delta\nu$ over the standard density scaling (e.g. Brogaard et al. 2018). However, there are some degrees of uncertainty. Christensen-Dalsgaard et al. (2020) found a 0.2 per cent spread in the theoretical departure stemming from implementing the calculation with different codes, and the degree of model dependence on physical processes has not been explored extensively.

* E-mail: yali4742@uni.sydney.edu.au

The ν_{\max} scaling relation is much harder to assess theoretically because calculating ν_{\max} would require a detailed treatment of non-adiabatic processes, via either 1D or 3D stellar models (e.g. Balmforth 1992; Houdek et al. 1999; Belkacem et al. 2019; Zhou, Asplund & Collet 2019). Some works concluded a possible departure could correlate with, for example, the Mach number (Belkacem et al. 2011), magnetic activity (Jiménez, García & Pallé 2011) and mean molecular weight (Jiménez et al. 2015; Yıldız, Çelik Orhan & Kayhan 2016; Viani et al. 2017). In general, it is still impossible to accurately predict ν_{\max} from theory.

Another way to test the scaling relations is by comparing with fundamental data from independent observations. This requires masses and radii obtained by other means, such as astrometric surveys, where radii are deduced using the Stefan–Boltzmann law, eclipsing binaries, where masses and radii are derived from dynamic modelling. So far, the radii tests based on parallaxes suggest agreement within 4 per cent for stars smaller than $30 R_{\odot}$ (Silva Aguirre et al. 2012; Huber et al. 2017; Sahlholdt & Silva Aguirre 2018; Hall et al. 2019; Khan et al. 2019; Zinn et al. 2019). With 16 eclipsing binaries, Gaulme et al. (2016) found the asteroseismic masses and radii are systematically overestimated, by factors of 15 and 5 per cent, respectively. This result is in disagreement with *Gaia* radii, possibly because the binary temperature is affected by blending (Huber et al. 2017; Zinn et al. 2019). Subsequent analyses indicate that the main source of departure could come from the $\Delta\nu$ scaling relation (Brogaard et al. 2018; Sharma et al. 2019).

As we noted earlier, the random departures of the scaling relations can be associated with unaccounted factors, for example, metallicity, rotation, and magnetism, some of which are known to have a wide-ranging distribution among red giants (e.g. Mosser et al. 2012; Stello et al. 2016; Ceillier et al. 2017). They could be responsible for some intrinsic scatter in these rather simple relations.

We propose a new approach to investigate the intrinsic scatter, based on two sharp features in the H–R diagram observed among the red giant population. The first feature is the accumulation of stars at the bump of red giant branch (RGB). The second feature is the sharp edge formed by the zero-age sequence of core-helium-burning (HeB) stars. These features were known before seismic observations became available.

The RGB bump is an evolutionary stage where a star ascending the RGB temporarily drops in luminosity before again ascending towards the tip of the RGB, causing a hump in the luminosity distribution. This feature is prominent in colour–magnitude diagrams of stellar clusters (Iben 1968; King, Da Costa & Demarque 1985). The luminosity drop takes place after the first dredge-up and is caused by a change in the composition profile near the hydrogen-burning shell, leading to a decrease in mean molecular weight outside the composition discontinuity point (Refsdal & Weigert 1970; Christensen-Dalsgaard 2015). *Kepler* data show that this bump is also present in the distributions of $\Delta\nu$ and ν_{\max} (Kallinger et al. 2010b; Khan et al. 2018).

After reaching the tip of RGB, stars strongly decrease in luminosity and commence core helium burning, forming the red clump, also commonly recognized as the horizontal branch in metal-poor clusters (Cannon 1970; Girardi, Rubele & Kerber 2010). The low-luminosity edge defines the beginning of the red clump and secondary clump phase, which we will refer to as the zero-age HeB (ZAHeB) phase. This feature is also imprinted on seismic observables (Huber et al. 2010; Mosser et al. 2010; Kallinger et al. 2010b; Yu et al. 2018).

The fact that the seismic parameters ($\Delta\nu$ and ν_{\max}) preserve these sharp features indicates that the seismic parameters must be tightly related to the fundamental stellar parameters. Put another way, if there

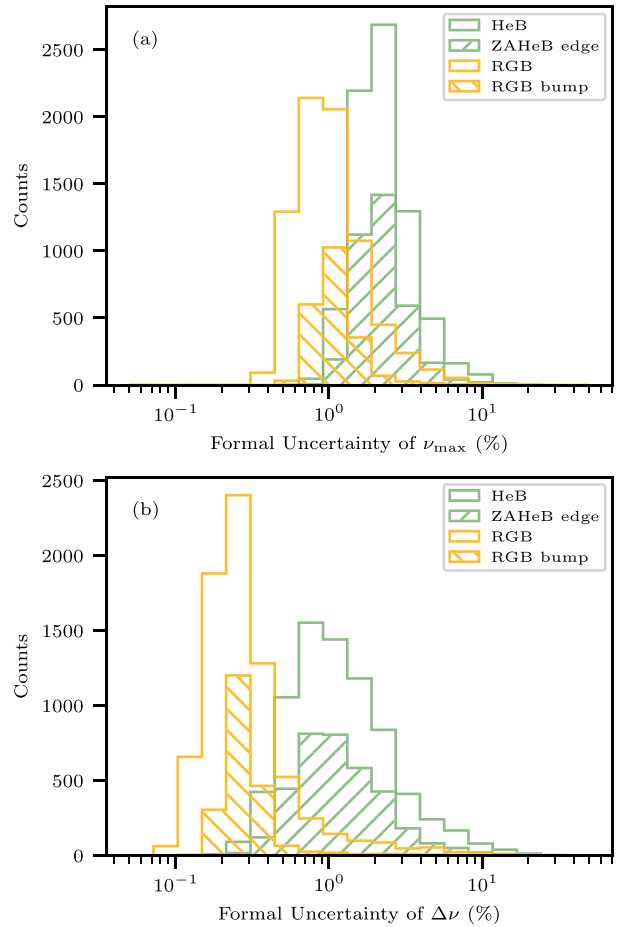


Figure 1. Distributions of the SYD18 formal uncertainties of the ν_{\max} and $\Delta\nu$ measurements.

were a large intrinsic scatter in the scaling relations, the features in the seismic diagrams would not be as sharp. Using this principle, we can quantify the limits on the intrinsic scatter in the scaling relations. That is the aim of this paper.

2 SAMPLE SELECTION

To create our sample, we used the red giants observed by *Kepler*, with $\Delta\nu$ and ν_{\max} measured by the SYD pipeline (Huber et al. 2009; Yu et al. 2018), and classifications of evolutionary stage (RGB/HeB) from Hon, Stello & Yu (2017). We denote this sample as SYD18, including 7543 HeB stars and 7534 RGB stars. A subset of 2531 HeB and 3308 RGB stars with T_{eff} and $[M/H]$ from the APOKASC-2 catalogue (Pinsonneault et al. 2018) was also used, denoted as APK18. In Fig. 1, we show the distributions of the formal uncertainties of ν_{\max} and $\Delta\nu$ measured by SYD18. The SYD18 sample reports a typical formal uncertainty of 2.1 per cent on ν_{\max} and 1.0 per cent on $\Delta\nu$ in HeB stars, and 0.95 per cent on ν_{\max} and 0.3 per cent on $\Delta\nu$ in RGB stars.

To model the observed population, we used a synthetic sample produced by Sharma et al. (2019) with a Galactic model, *Galaxia* (Sharma et al. 2011). Compared to a previous synthetic sample in Sharma et al. (2016), the synthetic sample we used in this work adds a metal-rich thick disc, which improves the overall match with the *Kepler* observation (Sharma et al. 2019). Here we denote this sample

as G19. The G19 simulated sample is about 10 times larger than the SYD18 sample. Each star in the simulated sample is associated with an initial mass, an age, and a metallicity, sampled from a Galactic distribution function and passed through a selection function tied to the *Kepler* mission. Other fundamental stellar parameters (e.g. M , R , and T_{eff}) were estimated via two different sets of theoretical isochrones: PARSEC (Marigo et al. 2017) and MIST (Choi et al. 2016). Both sets of isochrones include some mass-loss along the RGB, using the Reimers (1975) prescription with an efficiency of $\eta_R = 0.2$ (PARSEC) and 0.1 (MIST), consistent with the asteroseismology of open clusters (Miglio et al. 2012). The seismic parameters, $\Delta\nu$ and ν_{max} , were calculated through the scaling relations (equations 1 and 2) without any corrections. By examining the sharpness of the two features discussed above, and comparing the *Galaxia* simulation with the observations, we are able to draw conclusions about the intrinsic scatter of the scaling relations.

3 THE RGB BUMP

In this section, we look at the RGB bump. In a traditional H–R diagram, the bump is tilted so that the luminosity L of the bump is a function of T_{eff} and its shape can be parametrized by stellar mass M , using $L = L(M)$ and $T_{\text{eff}} = T_{\text{eff}}(M)$. By introducing the ν_{max} scaling relation, we can obtain $\nu_{\text{max}} \propto ML^{-1}T_{\text{eff}}^{7/2}$. Therefore, a narrow bump in the L – T_{eff} plane will also show a bump due to this M dependence in the ν_{max} – T_{eff} plane. If the ν_{max} scaling relation has some intrinsic scatter due to other dependences, such as metallicity, then the observed bump in the ν_{max} – T_{eff} plane could be wider.

For $\Delta\nu$, the argument is similar. Fig. 2 shows the RGB bump for both *Kepler* and *Galaxia* samples. Here we wish to model the width of the RGB bump. We will start by investigating the features in the $\Delta\nu$ – T_{eff} and ν_{max} – T_{eff} diagrams, and then in the M – R diagram.

We further note that the width of RGB bump strongly depends on how the physical processes are modelled in the isochrones. This is illustrated in Fig. 3, where the shapes of the RGB bump predicted by the two sets of isochrones are inconsistent. The PARSEC models predict that the stellar radii at the RGB bump should decrease with masses for masses larger than $\sim 1.2 M_{\odot}$. However, the opposite is observed in the *Kepler* samples, and this behaviour is correctly described by the MIST models. It implies that the RGB bump may not serve as a useful diagnostic for the scaling relations. We will examine this caveat more extensively in Section 5.1.1. Nevertheless, here we still use the RGB bump to introduce our method and we analyse the G19 samples with the two sets of isochrones separately.

3.1 Modelling method

We used a forward-modelling approach by constructing synthetic samples based on the G19 sample, and setting the intrinsic scatter of the scaling relations, σ , as a free parameter. The width of the bump was evaluated by measuring the distances of model samples to the centre of the bump, and fitting their distributions to the APK18 sample.

The first step was to define the locations of the RGB bump in the APK18 and G19 samples with straight lines in the ν_{max} – T_{eff} and $\Delta\nu$ – T_{eff} diagrams, shown in Fig. 2.

We generated a synthetic population by adding random scatter to the G19 sample. Each physical quantity x (one of $\Delta\nu$, ν_{max} , M , or R) for the i th star in the sample was

$$x_i = x_{\text{Galaxia},i}(1 + \sigma_{\text{total},i}). \quad (5)$$

The quantity $x_{\text{Galaxia},i}$ is the physical value without any perturbation. For M and R , they were directly estimated from isochrones. Note that M is the actual mass rather than the initial mass. Values for $\Delta\nu$ and ν_{max} were determined via scaling relations (equations 1 and 2) and further corrected using oscillation frequencies ($\Delta\nu$ in particular; see Section 3.2). We modelled the total scatter needed to reproduce the width of the RGB bump, $\sigma_{\text{total},i}$, which was drawn from a normal distribution with a standard deviation σ_{total} .

To account for the scatter induced by the formal uncertainties of the $\Delta\nu$ and ν_{max} measurements, we modelled each quantity x with

$$x_i = x_{\text{Galaxia},i}(1 + \sigma_{x,i} + \sigma_{\text{SR},i}), \quad (6)$$

where $\sigma_{x,i}$ represents the fractional uncertainty of $x_{\text{Galaxia},i}$, and was drawn randomly from the APK18 formal uncertainty distribution of RGB bump stars. The intrinsic scatter in the scaling relation was modelled via $\sigma_{\text{SR},i}$, drawn from a normal distribution with a standard deviation σ_{SR} .

We then calculated the distributions of distances to bump lines. The bump lines, shown in Fig. 2, were picked so that the distances to the line have the smallest standard deviation. For $\Delta\nu$ and ν_{max} , we calculated the vertical distances in the $\Delta\nu$ – T_{eff} and ν_{max} – T_{eff} diagrams, respectively. For M and R , we used the horizontal and vertical distances in the M – R diagram. This procedure allowed us to investigate the scatter in each relation separately because perturbing the horizontal value will not change the vertical value, and vice versa. In Fig. 4, we plot the distributions of those distances with two representative choices for σ_{total} . A larger value for σ_{total} flattens the hump, demonstrating the width of the bump itself provides a measure of the intrinsic scatter in the scaling relations.

Next, we introduce our fitting strategy to enable the comparison, which is to match the counts in each bin of the histograms. We first identified a central region in the histograms of the APK18 sample by fitting a Gaussian profile plus a sloping straight line, illustrated by the dashed curves in Fig. 4. The central region was defined to be a range centred around the Gaussian, with a width of six times the Gaussian standard deviation. In Fig. 4, they are shown in grey-shaded areas. In our fit described below, we matched the distributions in the central regions only.

Because the G19 sample is larger than the APK18 sample, we re-scaled the number of model samples by normalising according to the APK18 sample in the central region. We also added a constant c as a free parameter to the distance of the model samples, in order to compensate for a possible offset of maxima, which could originate from a bias in identifying the bump.

We optimized the likelihood function, assuming the distribution of counts in each bin is set by Poisson statistics:

$$\ln L = \sum_{m_j \neq 0} [d_j \ln m_j - m_j - \ln(d_j!)], \quad (7)$$

where d_j and m_j are counts in the j th bins of the *Kepler* and model distributions. This fitting method is commonly used in population studies to constrain the star formation history, initial mass function and binary properties (e.g. Dolphin 2002; Geha et al. 2013; El-Badry et al. 2019). The posterior distributions of parameters c and σ were sampled with uninformative flat priors, using a Markov chain Monte Carlo (MCMC) method. We used 200 white walkers, burned in for 500 steps to reach convergence, and then iterated for another 1000 steps. The medians and 68 per cent credible uncertainties of the parameters were estimated from the posteriors directly.

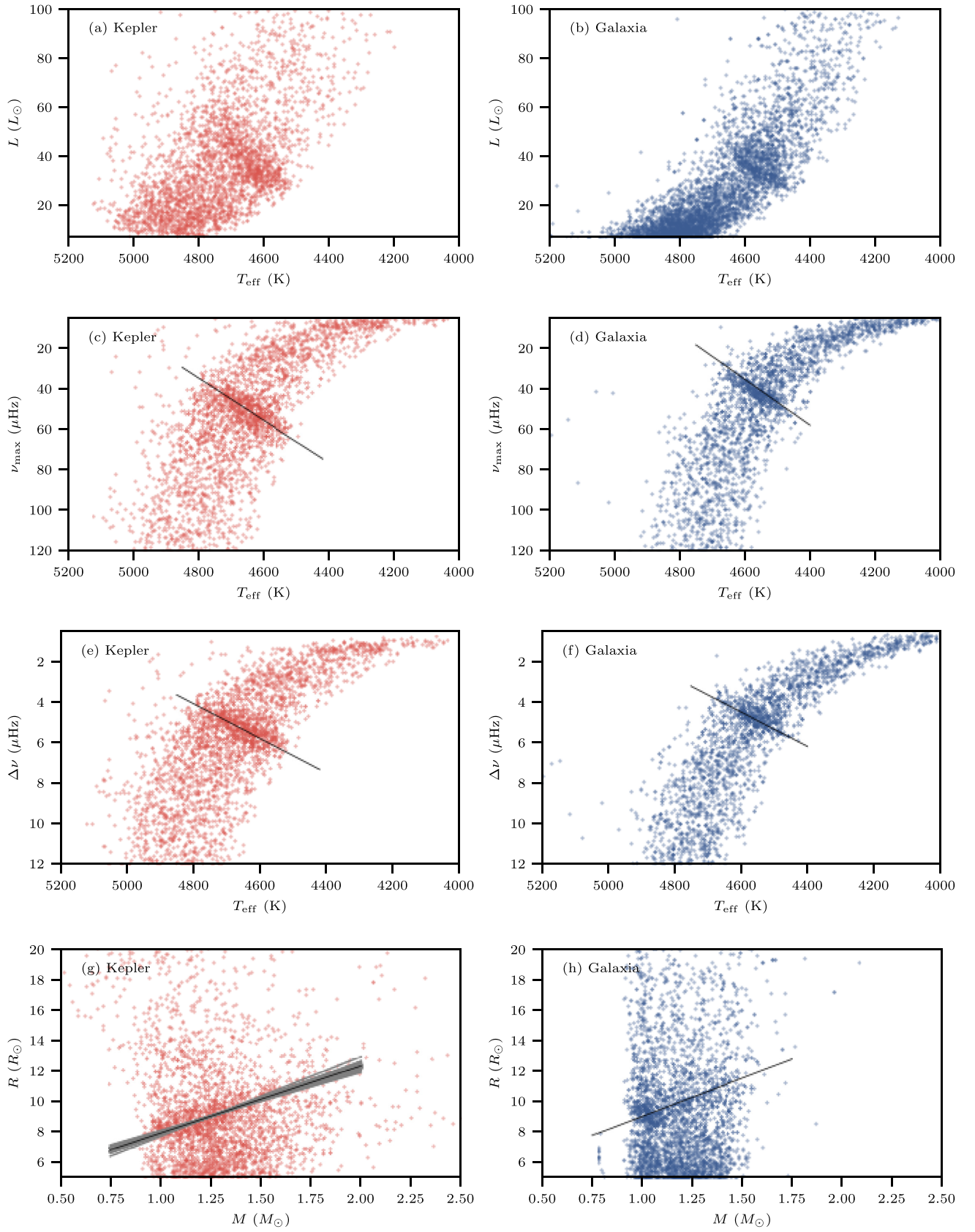


Figure 2. L versus T_{eff} (panels a–b), ν_{max} versus T_{eff} (panels c–d), $\Delta\nu$ versus T_{eff} (panels e–f), and R versus M (bottom g–h) for RGB stars in the APK18 sample (red) and the G19 sample (blue). The RGB bumps were defined using the black straight fiducial lines. The grey-shaded areas denote the uncertainty of identifying the bump (see Section 5.1.2).

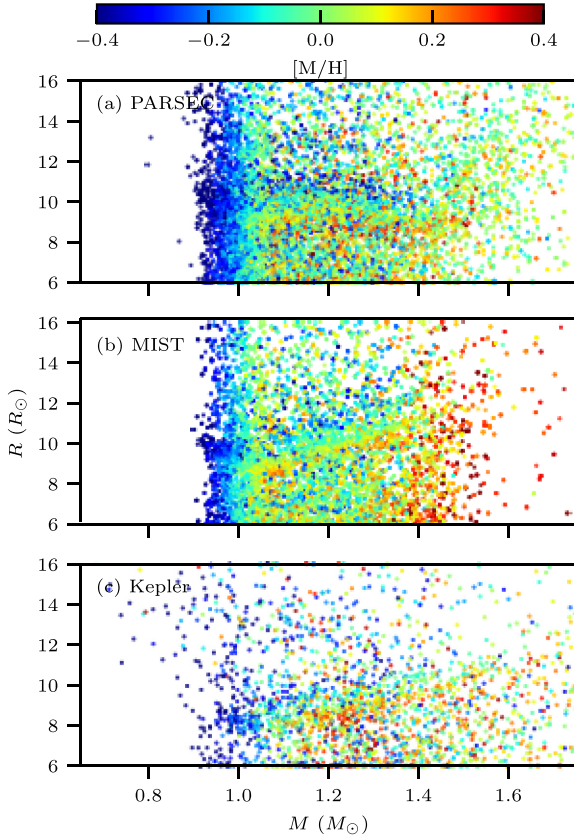


Figure 3. Radius versus mass for RGB stars near the RGB bump, colour-coded by metallicity. The PARSEC and MIST isochrones predict different outcomes on the shape of the RGB bump.

3.2 Results

Our first step is to derive the total scatter responsible for the width of the RGB bump, σ_{total} , in equation (5). We obtained 0.61 ($\Delta\nu$), 2.89 (ν_{max}), 4.05 (M), and 0.90 per cent (R), with PARSEC, and 5.74 per cent \pm 0.80 per cent ($\Delta\nu$), 9.80 per cent \pm 0.90 per cent (ν_{max}), 1.79 per cent \pm 1.34 per cent (M), and 2.75 per cent \pm 0.88 per cent (R) with MIST.

Next we took the formal uncertainties of the $\Delta\nu$ and ν_{max} measurements into account and obtained the limits on the intrinsic scatter of the scaling relations, σ_{SR} , in equation (6). With PARSEC, we obtained 0.88 ($\Delta\nu$), 2.00 (ν_{max}), 2.26 (M), and 0.60 per cent (R). With MIST, we obtained 5.97 ($\Delta\nu$), 9.76 (ν_{max}), 1.89 (M), and 0.56 per cent (R). These numbers are plotted in Fig. 5. There is a huge difference between MIST and PARSEC. We will discuss it in Section 5.1.1.

4 THE ZAHEB EDGE

Similar to the RGB bump, the zero-age sequence of HeB stars (ZAHeB) also forms a well-defined feature in the H–R diagram (Girardi et al. 2010; Girardi 2016). We note that the transition from the red clump (low-mass stars that ignite helium in a fully degenerate core) to the secondary red clump (higher-mass stars that ignite helium in a partly or non-degenerate core) is smooth and continuous (Girardi 2016). Given the scaling relations, there should exist a close correlation between $\Delta\nu$ and ν_{max} for the ZAHeB.

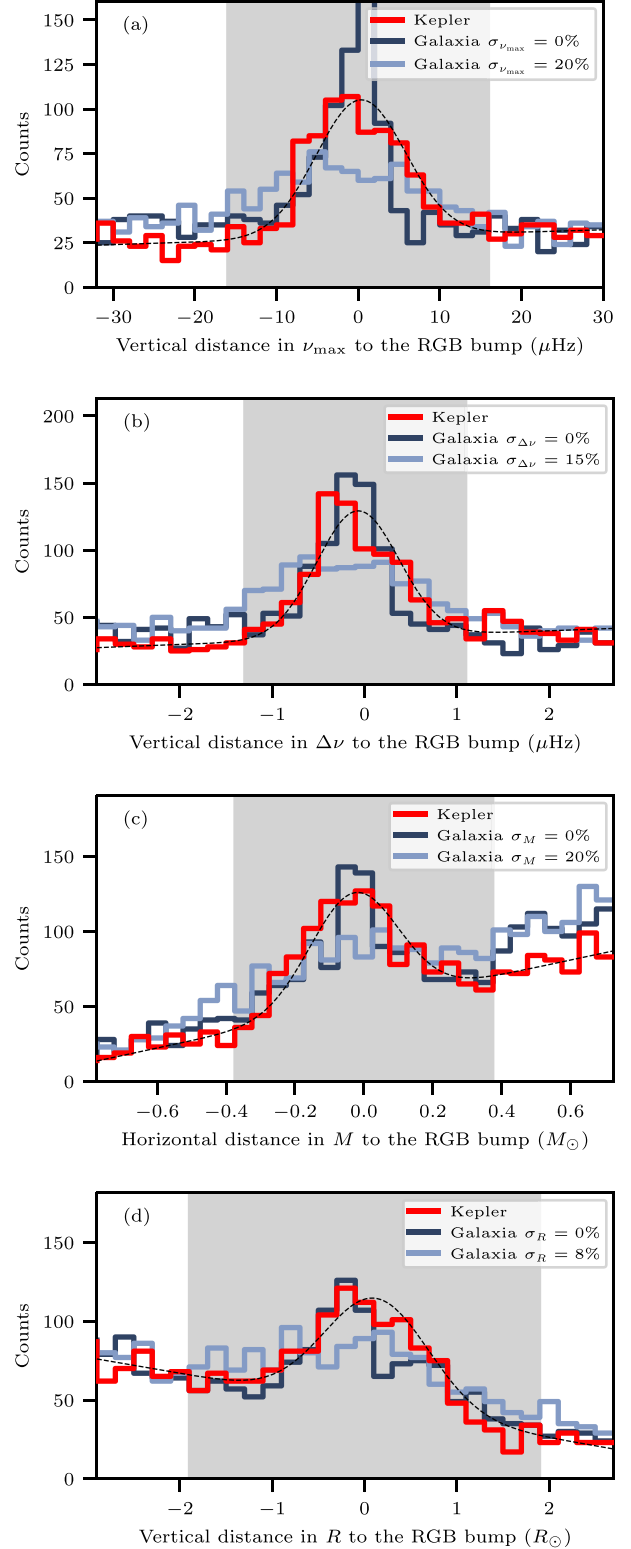


Figure 4. Distributions of distances to the bump features. The top two panels are measured in the $T_{\text{eff}}-\nu_{\text{max}}$ and $T_{\text{eff}}-\Delta\nu$ diagrams, and the bottom two panels are measured in the $M-R$ diagram. The *Kepler* (APK18) distributions are shown in red, fitted with a Gaussian model, denoted by the black dashed lines. The synthetic G19 samples are shown in blue. The grey-shaded areas denote the range used to compare the data.

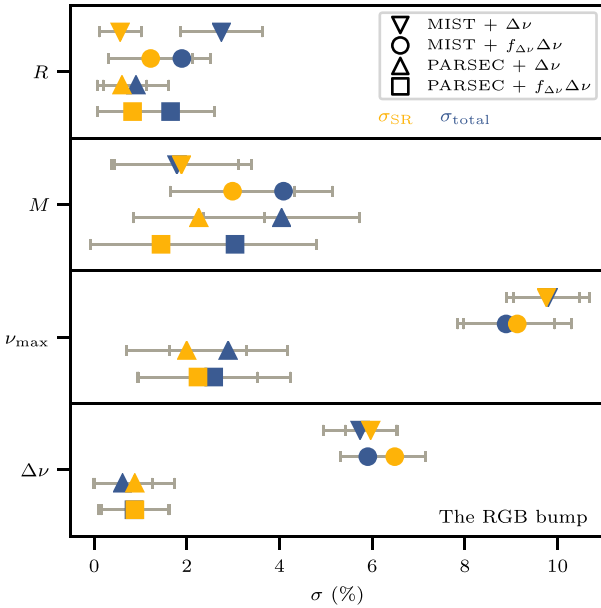


Figure 5. Intrinsic scatter of the scaling relations σ_{SR} (yellow) and total scatter σ_{total} (blue), derived using the width of the RGB bump.

In Fig. 6, we show the HeB stars in the $\Delta\nu$ – ν_{max} and M – R diagrams. The ZAHeB appears as a very sharp feature: All HeB stars are located at only one side of the ZAHeB, forming a remarkably sharp edge.¹ Now we use the sharpness of this edge to quantify the intrinsic scatter of the scaling relations.

4.1 Modelling method

To measure the sharpness of the ZAHeB edge, we used a modelling method similar to that for the RGB bump in Section 3.1, but with three important differences.

The first difference is related to defining the location of the feature. For RGB stars, we used straight lines to denote the location of the bump. For HeB stars, we used splines in the $\Delta\nu$ – ν_{max} and M – R diagrams to define the ZAHeB edges. This is illustrated in Fig. 6, where the edges are shown as black lines.

The second difference is how we calculated the horizontal and vertical distances to the ZAHeB edge. In the $\Delta\nu$ – ν_{max} diagram, the stars below the lowest point of the edge do not have a meaningful horizontal distance. We therefore excluded them for the horizontal distance calculation. The same strategy was also applied to all stars that lie on the left of the leftmost point of the defined ZAHeB edge when calculating vertical distances. Similarly, in the M – R diagram, the stars above the highest point of the ZAHeB edge were not considered in calculating horizontal distances. In Fig. 7, we plot the distributions of those distances with two σ_{total} . As for the RGB bump, we see that a larger scatter σ_{total} smooths the hump.

The third difference is that, in order to choose regions near each edge to compare, we fitted a profile to the distributions for the SYD18 sample. The profiles, shown as the dashed lines in Fig. 7, consisted of a half-Gaussian (left-hand panel) and a half-Lorentzian (right-hand panel). The histogram region that we fitted was a range centred at the

¹ It has not escaped our attention that Fig. 6(a) bears a strong resemblance to the logo of a major footwear manufacturer. We plan to investigate sponsorship opportunities.

Gaussian’s centre, with a width of six times the Gaussian’s standard deviation. These regions are shown as grey-shaded areas.

4.2 Results

We measured the total scatter σ_{total} that contributes to the broadening of the edges in the ν_{max} – $\Delta\nu$ and M – R diagrams: 1.25 per cent \pm 0.05 per cent ($\Delta\nu$), 2.23 per cent \pm 0.12 per cent (ν_{max}), 9.10 per cent \pm 0.50 per cent (M), and 2.01 per cent \pm 0.05 per cent (R) using the PARSEC models, and 1.56 per cent \pm 0.04 per cent ($\Delta\nu$), 2.99 per cent \pm 0.19 per cent (ν_{max}), 7.00 per cent \pm 0.54 per cent (M), and 2.29 per cent \pm 0.07 per cent (R) using the MIST models. These numbers are in general agreement with the formal uncertainties of $\Delta\nu$ and ν_{max} reported by SYD18 for HeB stars (Fig. 1), suggesting a main contribution to the broadening of the ZAHeB edge.

Next, we tested whether we needed to add intrinsic scaling relation scatter to the SYD18 measurement uncertainties in order to reproduce the sharpness of the ZAHeB edge. We derived σ_{SR} with the PARSEC models: 0.13 per cent \pm 0.18 per cent ($\Delta\nu$), 0.72 per cent \pm 0.24 per cent (ν_{max}), 2.34 per cent \pm 1.38 per cent (M), and 0.22 per cent \pm 0.12 per cent (R). And with the MIST models we obtained 0.89 per cent \pm 0.11 per cent ($\Delta\nu$), 1.52 per cent \pm 0.09 per cent (ν_{max}), 0.28 per cent \pm 0.32 per cent (M), and 0.08 per cent \pm 0.14 per cent (R). These numbers are plotted in Fig. 8.

5 DISCUSSION

5.1 Assessing uncertainties

5.1.1 The uncertainty of modelling the stellar population

Figs 5 and 8 present the total scatter σ_{total} and the limits on the intrinsic scatter of the scaling relations σ_{SR} derived under various assumptions. A feature become immediately obvious: The results depend on how the synthetic stars are modelled.

We first discuss its impact on the RGB bump. The input physics has significantly influenced the width of the RGB bump. As we already illustrated in Fig. 3, the shapes of the RGB bump predicted by the two isochrones are inconsistent. Furthermore, the PARSEC models predict a wider bump than the observation, even when the quantities were not perturbed with any scatter. In contrast, the MIST models present a much narrower bump, and so a much larger scatter needs to be added to match the observed width.

For some cases in Fig. 5, σ_{total} exceeds σ_{SR} , which is also a signature that the shape of RGB bump predicted by models cannot properly match the observation. For example, the G19 synthetic samples overestimate the number of low-mass stars near $\sim 1 M_{\odot}$, which can be seen from the panel h of Fig. 2. The mismatch was first discussed by Sharma et al. (2016), and Sharma et al. (2019) used a metal-rich thick disc to ease the tension, but the inconsistency still exists.

The RGB bump is an important diagnostic for stellar physics. Christensen-Dalsgaard (2015) linked the width of the RGB bump with the magnitude of the hydrogen abundance discontinuity in the vicinity of the hydrogen-burning shell, which depends on the evolution history. The modelling of convection (e.g. mixing length and overshoot) can also have an impact on the location of the bump (see Khan et al. 2018 and references therein).

From the above discussion, we conclude that the RGB bump is not useful for our purpose, unless an initial calibration of stellar

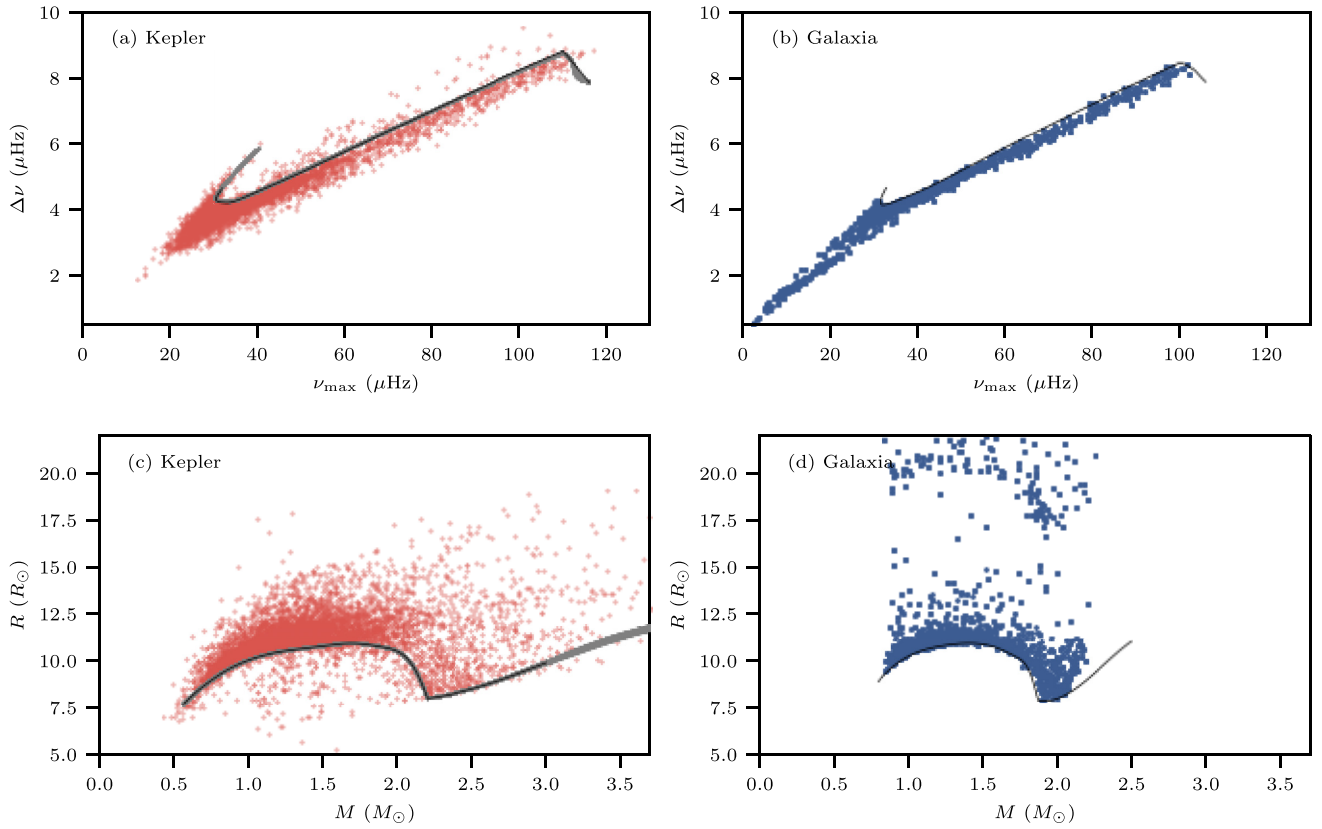


Figure 6. ν_{\max} - $\Delta\nu$ diagram (panels a–b) and M - R diagram (panels c–d) for HeB stars in the SYD18 sample (red) and the G19 sample (blue). The ZAHHeB edges were defined using splines, shown as the black lines. The grey-shaded areas denote the uncertainty of identifying the edges (see Section 5.1.2). The stars around $20 R_{\odot}$ in the G19 sample are at the asymptotic giant branch phase.

models is properly done. The calibration can be achieved by matching luminosity distributions using benchmark data, and then the feature can be compared in the seismic diagrams. This is beyond the scope of this paper, and we defer it for future work.

Turning into the ZAHHeB edge, we noticed the shape of the edges is also model-dependent. A noticeable feature in Fig. 6 is that the mass limit of the helium flash in models does not match with the observation. The mass limit has been shown to be dependent on the treatment of overshooting (Girardi 2016), which is often considered as a free parameter in stellar modelling. Fig. 6 also shows a lack of low-mass HeB stars in the G19 sample, likely because the synthetic sample does not incorporate enough mass-loss.

Despite these model uncertainties, we found they are less sensitive to the values of σ_{SR} that we are interested in. This means that using the ZAHHeB edge to put a limit on the intrinsic scatter of the scaling relations is a realistic approach in this work.

5.1.2 The uncertainty of identifying the features

The chosen ZAHHeB edges and RGB bumps in the *Kepler* samples might deviate from their real positions. Here we test its influence on the inferred σ_{SR} by shifting the locations in the observation samples. We perturbed the points used to define the splines (ZAHHeB edge) and the straight lines (RGB bump) with an amount of s/\sqrt{N} . We took s as the standard deviation of the Gaussian profiles fitted in Figs 4 and 7, and N as the number of samples. This perturbation is similar to the standard deviation of the sample mean, and should provide a good approximation to the uncertainty of choosing the

centre of those features. In Figs 2 and 6, the grey-shaded areas show the amount of uncertainty. We found the resulting σ_{SR} agrees with the reported values within 0.06 per cent for $\Delta\nu$, 0.1 per cent for ν_{\max} , 1.8 per cent for M , and 0.7 per cent for R . This result indicates that the uncertainty of identifying the features is much smaller than σ_{total} , but is on a similar level of σ_{SR} .

In addition, we note that there is a selection effect (will be shown in Section 5.4 and Fig. 10) due to excluding HeB stars near the ZAHHeB edge when there were no horizontal or vertical distances. For example, the obtained values for the mass relation are only applicable to stars in the range of 0.8 – $1.1 M_{\odot}$, so the derived numbers for σ_{total} and σ_{SR} are the averages for those specific subsamples, making the numbers between each relations not directly comparable.

5.1.3 The uncertainty of measuring $\Delta\nu$ and ν_{\max}

The limits we obtained for σ_{SR} depend on how well the values for $\Delta\nu$ and ν_{\max} are measured. Up to now we focused our discussion using the SYD pipeline, which measures $\Delta\nu$ and ν_{\max} from a global fitting of the power spectrum (Huber et al. 2009; Yu et al. 2018). Although the global fitting method is more common, an alternative approach is to only use the radial mode frequencies and avoid the effect from mixed modes. An example is the CAN pipeline (Kallinger et al. 2010b), which obtained a more precise measurements on $\Delta\nu$ and ν_{\max} . For stars near the ZAHHeB edge, their typical formal uncertainties are 0.6 per cent for ν_{\max} , and 0.3 per cent for $\Delta\nu$ (Pinsonneault et al. 2018). Using their reported uncertainties, we show in Fig. 8, that the values for σ_{SR} in the $\Delta\nu$ and ν_{\max} relations

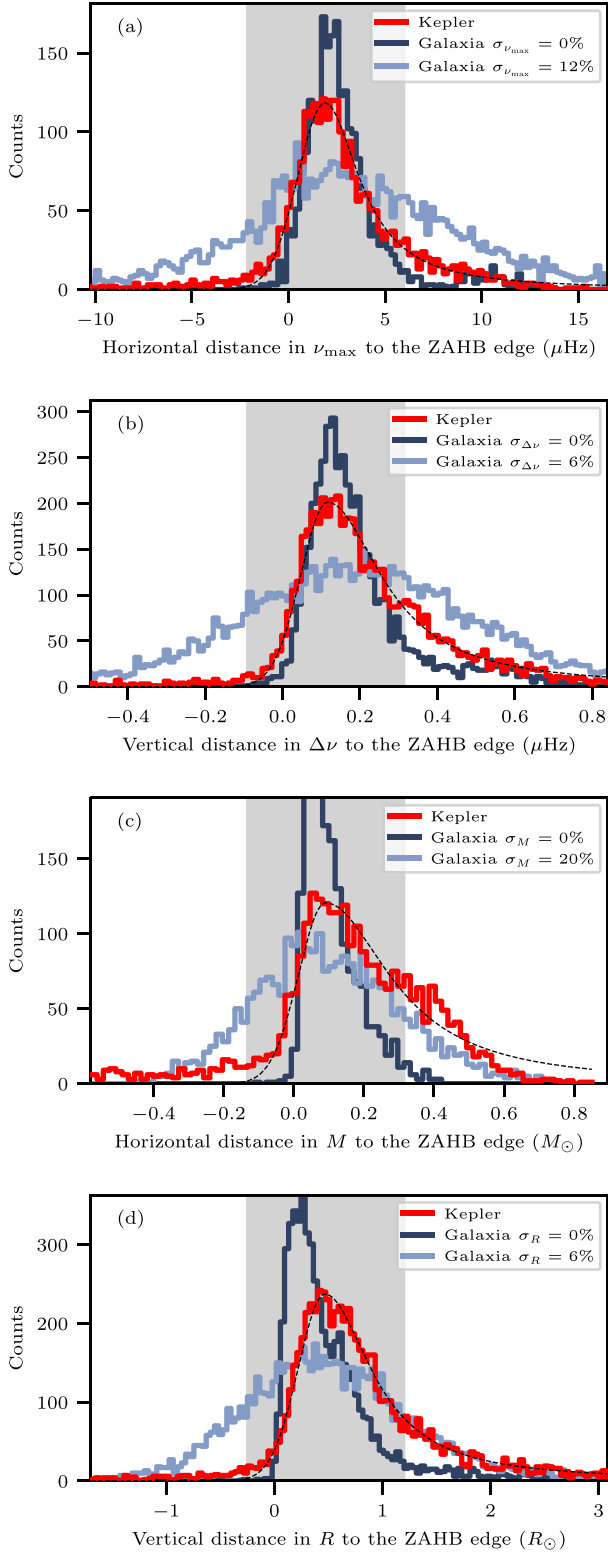


Figure 7. Distributions of distances to the ZAHB edges. The top two panels are measured in the ν_{\max} – $\Delta\nu$ diagram, and the bottom two panels are measured in the M – R diagram. The *Kepler* (SYD18) distributions are shown in red, fitted with a half-Gaussian, half-Lorentzian model, denoted by the black dashed lines. The synthetic G19 samples are shown in blue. The grey-shaded areas denote the range used to compare the data.

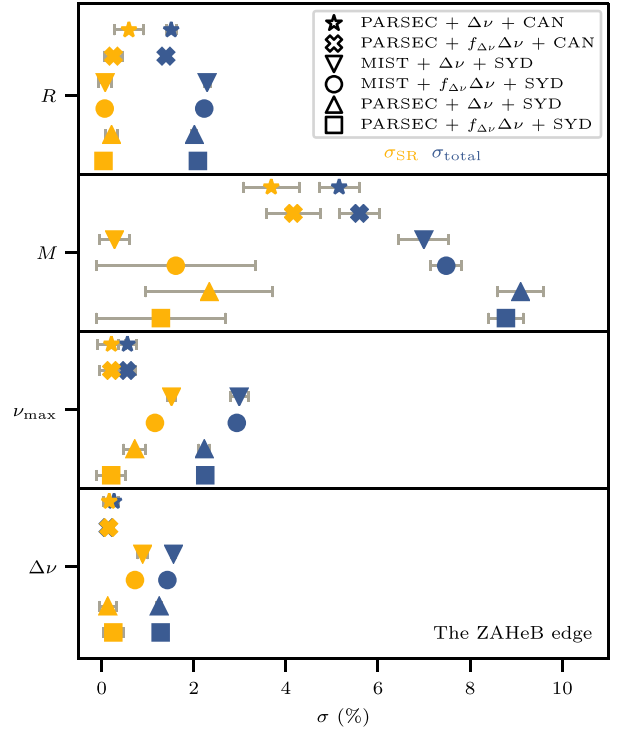


Figure 8. Intrinsic scatter of the scaling relations σ_{SR} (yellow) and total scatter σ_{total} (blue), derived using the sharpness of the ZAHB edge.

can greatly decrease. If the values for $\Delta\nu$ and ν_{\max} are measured in this way, the scaling relations can have much smaller intrinsic scatter in principle. However, we also found the intrinsic scatter in the M and R scaling relations does not decrease accordingly because the uncertainty of T_{eff} still dominates. In the rest of this paper, we continue our discussion using the SYD pipeline values.

5.2 The intrinsic scatter of the scaling relations

Based on the discussion in Section 5.1, we estimate the final values of the intrinsic scatter of the scaling relations, σ_{SR} , by averaging them from both RGB and HeB stars for the M and R relations, but only HeB stars for the $\Delta\nu$ and ν_{\max} relations because these values tend to show less severe dependences on isochrones. We conclude that the intrinsic scatter of the scaling relations have values of ~ 0.5 ($\Delta\nu$), ~ 1.1 (ν_{\max}), ~ 1.7 (M), and ~ 0.4 per cent (R), for the SYD pipeline, keeping in mind that the systematic uncertainty of our method is on a similar level. The values of σ_{SR} are small in general, suggesting the observational uncertainty typically exceeds the intrinsic scatter of the scaling relations even with 4 yr of *Kepler* data for the SYD pipeline.

In our study, we separately located the ZAHB edges in the *Kepler* and *Galaxia* samples. This means that any systematic offset in the scaling relations (for example, using a different set of solar reference values) would not be reflected in σ_{SR} . The intrinsic scatter in the scaling relation can still be small compared to any systematic offset in the scaling relations.

5.3 Correcting the scaling relations with theoretical models

It is interesting to test whether the common model-based correction of $\Delta\nu$ proposed by Sharma et al. (2016) can reduce the scatter in the scaling relations. We calculated the departure of the $\Delta\nu$ scaling

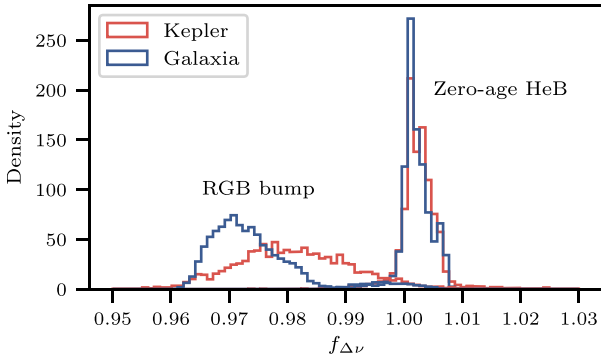


Figure 9. Distributions of the correction factor $f_{\Delta\nu}$ for stars near the RGB bump and stars near the ZAHHeB edge (grey-shaded area in Fig. 4 and 7) in both *Kepler* (red) and *Galaxia* (blue) samples.

relation, $f_{\Delta\nu}$, for each star in both samples. We implemented the corrected mass $M' = f_{\Delta\nu}^4 M$ and radius $R' = f_{\Delta\nu}^2 R$ in the *Kepler* sample, and the corrected p-mode separation $\Delta\nu' = f_{\Delta\nu} \Delta\nu$ in the synthetic sample.

These $\Delta\nu$ corrections made little difference to our results, for both RGB stars (Fig. 5) and HeB stars (Fig. 8). The likely explanation is that $f_{\Delta\nu}$ mainly corrects the systematic offsets in the scaling relations, which affect the location of the RGB bump and ZAHHeB edge, but has a negligible influence on the intrinsic scatter of the scaling relations (Fig. 9). The standard deviation of $f_{\Delta\nu}$ for stars near the ZAHHeB edge is below 0.5 per cent, and that for stars near the RGB bump is about 1.0 per cent.

5.4 The intrinsic scatter of the scaling relations as a function of mass and metallicity

We expect the intrinsic scatter in the scaling relations to be a function of stellar mass and metallicity, as we see in $f_{\Delta\nu}$. To test whether this dependence can be seen in our sample, we used HeB stars and divided both the *Kepler* and *Galaxia* samples into bins with equal widths in M and $[M/H]$, and repeated the exercise in each bin. We note that for $\Delta\nu$, ν_{\max} , and M , we could only test a limited range in mass, because some points do not have vertical or horizontal distances. To study the dependence on $[M/H]$, we used the APK18 sample instead of the SYD18 sample because the APK18 metallicities were derived from a single instrument.

In Figs 10 and 11, we show σ_{total} (dark blue regions) and σ_{SR} (dashed lines) as functions of M and $[M/H]$, respectively. We find no obvious change in the spread of points for $\Delta\nu$, ν_{\max} , and M , possibly due to a direct consequence of the method uncertainty we claimed in Section 5.1.2. The data also suggest that a higher mass and higher metallicity may result in a larger intrinsic scatter for the radius scaling relation. Whether this is a true statement can be found by populating more stars in the high-mass and high-metallicity region with upcoming space missions.

6 CONCLUSIONS

In this paper, we used a forward-modelling approach to match the width of the RGB bump and the sharpness of the edge formed by ZAHHeB stars. Matching the broadening of those features between the *Kepler* and *Galaxia* samples allowed us to constrain the intrinsic scatter of the asteroseismic scaling relations.

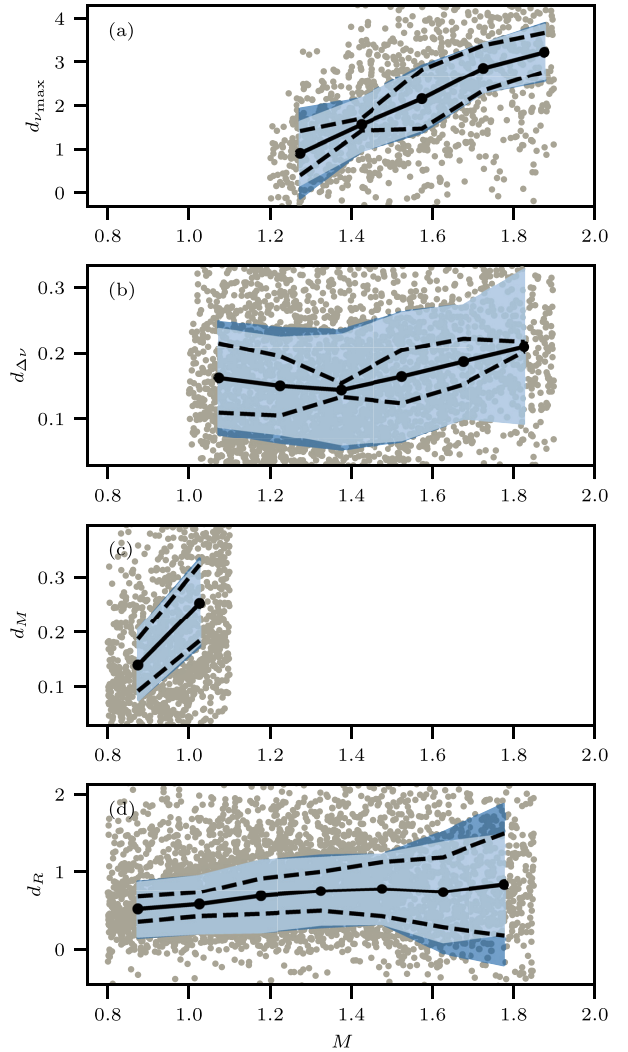


Figure 10. Distances to the ZAHHeB edge as a function of stellar mass for the SYD18 sample (grey points). The solid black line traces the median values of the distances in each mass bin. The light blue show the formal uncertainties of $\Delta\nu$ and ν_{\max} reported by the SYD pipeline, and the dark blue regions show the intrinsic scatter of the scaling relations σ_{SR} . The dashed black lines show the total scatter σ_{total} .

The main results are summarized in Figs 5 and 8. We found that the observed broadening arises primarily from the measurement uncertainties of $\Delta\nu$ and ν_{\max} . By taking into account the uncertainty reported by the SYD pipeline, the scaling relations have intrinsic scatter have values of ~ 0.5 ($\Delta\nu$), ~ 1.1 (ν_{\max}), ~ 1.7 (M), and ~ 0.4 per cent (R). This confirms the remarkable constraining power of the scaling relations. The above numbers are approximate because the systematic uncertainties of our method arising from identifying the features is on a similar level. Although this result was obtained using stars in a limited parameter space, we expect they are applicable to a broader population spanning most low-mass red giants, provided they have similar surface properties.

Moreover, we demonstrate that using the theoretically corrected $\Delta\nu$ does not reduce the scatter by a large amount. We also found a marginal dependence of the intrinsic scatter of the radius scaling relation on mass and metallicity. However, these interpretations are limited by the systematic uncertainties of our method.

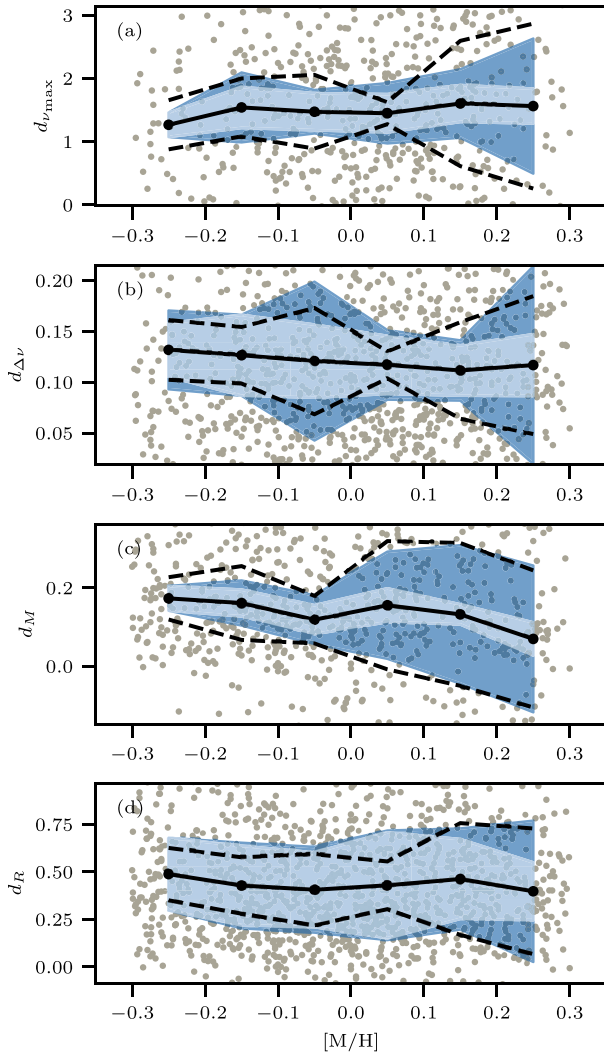


Figure 11. Similar to Fig. 10 but shown as a function of metallicity, and restricted to the APK18 sample.

Future work could include using more data from both asteroseismology and spectroscopy to allow tests in more mass and metallicity bins, especially improving the constraints for secondary clump stars. Additionally, by considering the position of those features and matching the exact distributions of stellar parameters (instead of simply the distances to the edge), one could provide constraints on physical processes such as convection and mass-loss, and potentially on the offset of the scaling relations.

ACKNOWLEDGEMENTS

We thank the *Kepler* Discovery mission funded by NASA's Science Mission Directorate for the incredible quality of data. We acknowledge funding from the Australian Research Council, and the Joint Research Fund in Astronomy (U2031203) under cooperative agreement between the National Natural Science Foundation of China (NSFC) and Chinese Academy of Sciences (CAS). This work is made possible by the following open-source PYTHON softwares: NUMPY (van der Walt, Colbert & Varoquaux 2011), SCIPY (Virtanen et al. 2020), MATPLOTLIB (Hunter 2007), CORNER (Foreman-

Mackey 2016), EMCEE (Foreman-Mackey et al. 2013), and SEABORN (Waskom & the seaborn development team 2020).

DATA AVAILABILITY

The code repository for this work is available on Github.² The data sets will be shared on request to the corresponding author.

REFERENCES

- Balmforth N. J., 1992, *MNRAS*, 255, 603
 Belkacem K., Goupil M. J., Dupret M. A., Samadi R., Baudin F., Noels A., Mosser B., 2011, *A&A*, 530, A142
 Belkacem K., Kupka F., Samadi R., Grimm-Strele H., 2019, *A&A*, 625, A20
 Brogaard K. et al., 2018, *MNRAS*, 476, 3729
 Brown T. M., Gilliland R. L., Noyes R. W., Ramsey L. W., 1991, *ApJ*, 368, 599
 Cannon R. D., 1970, *MNRAS*, 150, 111
 Ceillier T. et al., 2017, *A&A*, 605, A111
 Choi J., Dotter A., Conroy C., Cantiello M., Paxton B., Johnson B. D., 2016, *ApJ*, 823, 102
 Christensen-Dalsgaard J., 2015, *MNRAS*, 453, 666
 Christensen-Dalsgaard J. et al., 2020, *A&A*, 635, A165
 Dolphin A. E., 2002, *MNRAS*, 332, 91
 El-Badry K., Rix H.-W., Tian H., Duchêne G., Moe M., 2019, *MNRAS*, 489, 5822
 Foreman-Mackey D., 2016, *J. Open Source Softw.*, 1, 24
 Foreman-Mackey D., Hogg D. W., Lang D., Goodman J., 2013, *PASP*, 125, 306
 Gaulme P. et al., 2016, *ApJ*, 832, 121
 Geha M. et al., 2013, *ApJ*, 771, 29
 Girardi L., 2016, *ARA&A*, 54, 95
 Girardi L., Rubele S., Kerber L., 2010, in de Grijs R., Lépine J. R. D., eds, Proc. IAU Symp. 266, Star Clusters: Basic Galactic Building Blocks Throughout Time and Space. Kluwer, Dordrecht, p. 320
 Guggenberger E., Hekker S., Basu S., Bellinger E., 2016, *MNRAS*, 460, 4277
 Hall O. J. et al., 2019, *MNRAS*, 486, 3569
 Hekker S., 2020, *Frontiers Astron. Space Sci.*, 7, 3
 Hon M., Stello D., Yu J., 2017, *MNRAS*, 469, 4578
 Houdek G., Balmforth N. J., Christensen-Dalsgaard J., Gough D. O., 1999, *A&A*, 351, 582
 Huber D., Stello D., Bedding T. R., Chaplin W. J., Arentoft T., Quirion P. O., Kjeldsen H., 2009, *Commun. Asteroseismol.*, 160, 74
 Huber D. et al., 2010, *ApJ*, 723, 1607
 Huber D. et al., 2017, *ApJ*, 844, 102
 Hunter J. D., 2007, *Comput. Sci. Eng.*, 9, 90
 Iben I., 1968, *Nature*, 220, 143
 Jiménez A., García R. A., Pallé P. L., 2011, *ApJ*, 743, 99
 Jiménez A., García R. A., Pérez Hernández F., Mathur S., 2015, *A&A*, 583, A74
 Kallinger T. et al., 2010a, *A&A*, 509, A77
 Kallinger T. et al., 2010b, *A&A*, 522, A1
 Khan S., Hall O. J., Miglio A., Davies G. R., Mosser B., Girardi L., Montalbán J., 2018, *ApJ*, 859, 156
 Khan S. et al., 2019, *A&A*, 628, A35
 King C. R., Da Costa G. S., Demarque P., 1985, *ApJ*, 299, 674
 Kjeldsen H., Bedding T. R., 1995, *A&A*, 293, 87
 Marigo P. et al., 2017, *ApJ*, 835, 77
 Miglio A. et al., 2012, *MNRAS*, 419, 2077
 Mosser B. et al., 2010, *A&A*, 517, A22
 Mosser B. et al., 2012, *A&A*, 548, A10
 Pinsonneault M. H. et al., 2018, *ApJS*, 239, 32
 Refsdal S., Weigert A., 1970, *A&A*, 6, 426

²<https://github.com/parallpro/nike>.















- Reimers D., 1975, *Mem. Soc. R. Sci. Liege*, 8, 369
- Rodrigues T. S. et al., 2017, *MNRAS*, 467, 1433
- Sahlholdt C. L., Silva Aguirre V., 2018, *MNRAS*, 481, L125
- Serenelli A. et al., 2017, *ApJS*, 233, 23
- Sharma S., Bland-Hawthorn J., Johnston K. V., Binney J., 2011, *ApJ*, 730, 3
- Sharma S., Stello D., Bland-Hawthorn J., Huber D., Bedding T. R., 2016, *ApJ*, 822, 15
- Sharma S. et al., 2019, *MNRAS*, 490, 5335
- Silva Aguirre V. et al., 2012, *ApJ*, 757, 99
- Stello D., Bruntt H., Preston H., Buzasi D., 2008, *ApJ*, 674, L53
- Stello D., Cantiello M., Fuller J., Garcia R. A., Huber D., 2016, *PASA*, 33, e011
- Ulrich R. K., 1986, *ApJ*, 306, L37
- van der Walt S., Colbert S. C., Varoquaux G., 2011, *Comput. Sci. Eng.*, 13, 22
- Viani L. S., Basu S., Chaplin W. J., Davies G. R., Elsworth Y., 2017, *ApJ*, 843, 11
- Virtanen P. et al., 2020, *Nat. Methods*, 17, 261
- Waskom M., the seaborn development team, 2020, *mwaskom/seaborn*, Zenodo, Available at: <https://doi.org/10.5281/zenodo.592845>
- White T. R., Bedding T. R., Stello D., Christensen-Dalsgaard J., Huber D., Kjeldsen H., 2011, *ApJ*, 743, 161
- Yıldız M., Çelik Orhan Z., Kayhan C., 2016, *MNRAS*, 462, 1577
- Yu J., Huber D., Bedding T. R., Stello D., Hon M., Murphy S. J., Khanna S., 2018, *ApJS*, 236, 42
- Zhou Y., Asplund M., Collet R., 2019, *ApJ*, 880, 13
- Zinn J. C., Pinsonneault M. H., Huber D., Stello D., Stassun K., Serenelli A., 2019, *ApJ*, 885, 166

This paper has been typeset from a $\text{\TeX}/\text{\LaTeX}$ file prepared by the author.

5 A prescription for the asteroseismic surface effect

The paper produced in this chapter is submitted to Monthly Notices of the Royal Astronomical Society, and it is currently under the second review. The preprint version is available as [Li, Yaguang et al. \(2022b\)](#). The work is a collaborative effort. I performed the observational data analysis and stellar modelling. I and Tim Bedding contributed to most experiments in this paper. Dennis Stello, Meridith Joyce, and Tanda Li contributed to the calculation of stellar models. Daniel Huber, Andrew Howard, and Howard Isaacson scheduled the spectroscopic observations with Keck HIRES. Marc Hon compared the interferometric radii with the seismic radii. This analysis is not presented in the final paper because most stars in the common sample have uncertain evolutionary phases (AGB/RGB), which limits the interpretation. Jean Perkins extracted the oscillation frequencies for NGC 6791. Tim White helped calculate the f_{Δ} correction factors. Joel Zinn computed the *Gaia* radii. Daniel Hey helped optimise the modelling code. Hans Kjeldsen contributed to the interpretation of the results. I wrote the paper, and all authors (especially Tim Bedding) commented on the manuscript.

A prescription for the asteroseismic surface correction

Yaguang Li (李亚光)¹  ^{*} Timothy R. Bedding¹  [†] Dennis Stello²  ² Daniel Huber³  ³
 Marc Hon³  ³, Meridith Joyce⁴  ⁴, Tanda Li (李坦达)⁵  ⁵, Jean Perkins⁶  ⁶, Timothy R. White¹  ¹,
 Joel C. Zinn⁷  ⁷, Andrew W. Howard⁸  ⁸, Howard Isaacson⁹  ⁹, Daniel R. Hey³  ³ and Hans Kjeldsen¹⁰  ¹⁰

¹*Sydney Institute for Astronomy (SIfA), School of Physics, University of Sydney, NSW 2006, Australia*

²*School of Physics, University of New South Wales, 2052, Australia*

³*Institute for Astronomy, University of Hawai'i, 2680 Woodlawn Drive, Honolulu, HI 96822, USA*

⁴*Space Telescope Science Institute, 3700 San Martin Dr, Baltimore, MD 21218, USA*

⁵*Department of Astronomy, Beijing Normal University, Haidian District, Beijing 100875, China*

⁶*Monterey Institute for Research in Astronomy, 200 8th St, Marina, CA 93933*

⁷*Department of Astrophysics, American Museum of Natural History, Central Park West at 79th Street, New York, NY 10024, USA*

⁸*Division of Physics, Mathematics and Astronomy, Caltech, 1200 E California Blvd, Pasadena CA 91125, USA*

⁹*Department of Astronomy, University of California at Berkeley, 501 Campbell Hall, Berkeley, CA 94720-3411, USA*

¹⁰*Stellar Astrophysics Centre, Department of Physics and Astronomy, Aarhus University, 8000 Aarhus C, Denmark*

Accepted XXX. Received YYY; in original form ZZZ

ABSTRACT

In asteroseismology, the surface effect refers to a disparity between the observed and the modelled frequencies in stars with solar-like oscillations. It originates from improper modelling of the surface layers. Correcting the surface effect usually requires using functions with free parameters, which are conventionally fitted to the observed frequencies. On the basis that the correction should vary smoothly across the H–R diagram, we parameterize it as a simple function of surface gravity, effective temperature, and metallicity. We determine this function by fitting a wide range of stars. The absolute amount of the surface correction decreases with luminosity, but the ratio between it and ν_{\max} increases, suggesting the surface effect is more important for red giants than dwarfs. Applying the prescription can eliminate unrealistic surface correction, which improves parameter estimations with stellar modelling. Using two open clusters, we found a reduction of scatter in the model-derived ages for each star in the same cluster. As an important application, we provide a new revision for the $\Delta\nu$ scaling relation that, for the first time, accounts for the surface correction. The values of the correction factor, $f_{\Delta\nu}$, are up to 2% smaller than those determined without the surface effect considered, suggesting decreases of up to 4% in radii and up to 8% in masses when using the asteroseismic scaling relations. This revision brings the asteroseismic properties into an agreement with those determined from eclipsing binaries. The new correction factor and the stellar models with the corrected frequencies are available at <https://www.github.com/parallelpro/surface>.

Key words: stars: solar-type – stars: oscillations (including pulsations) – stars: low-mass

1 INTRODUCTION

Correcting the asteroseismic surface effect has so far been a troublesome procedure. Convection affects pulsation properties through turbulent pressure, opacity variations, and convective energy flux (Houdek et al. 2017). Small-scale magnetic fields can form layers that affect the propagation of pulsations (Li et al. 2021b). All these processes are poorly modelled in the near-surface convective atmosphere in most 1D stellar models (Christensen-Dalsgaard et al. 1988; Dziembowski et al. 1988). Improvements have been seen with the surface

layers replaced by 3D averaged atmospheric models, producing more realistic equilibrium structures (Rosenthal et al. 1999; Magic & Weiss 2016; Jørgensen et al. 2017; Trampedach et al. 2017; Jørgensen et al. 2018, 2019; Mosumgaard et al. 2020), or with time-dependent 1D convection models, accounting for the coupling between oscillation and convection (Balmforth 1992; Grigahcène et al. 2012; Christensen-Dalsgaard 2012; Houdek et al. 2017, 2019; Belkacem et al. 2021; Philidet et al. 2021).

In practice, the surface effect is usually corrected empirically with simple functions of frequency. Christensen-Dalsgaard et al. (1989) provided a justification, based on a perturbation to an asymptotic formalism of acoustic modes.

* yaguang.li@sydney.edu.au

† tim.bedding@sydney.edu.au

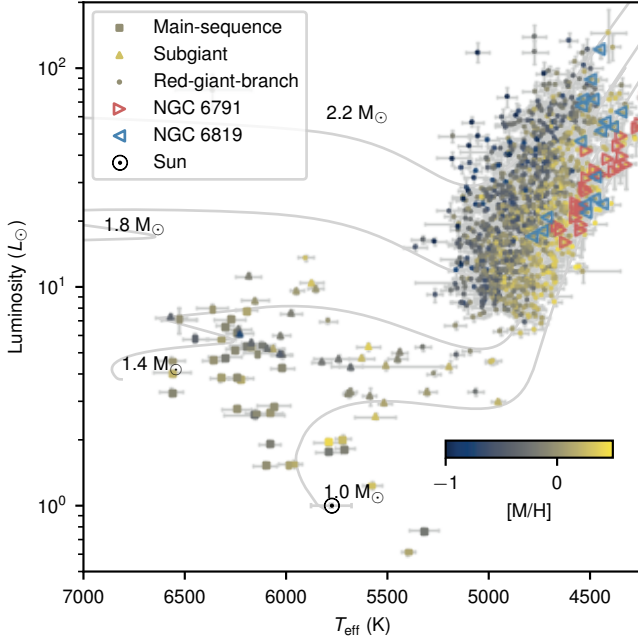


Figure 1. H–R diagram showing the studied sample in this work. The evolutionary tracks for four masses with $Y_{\text{init}} = 0.29$, $[M/H] = 0.0$, $\alpha_{\text{MLT}} = 1.7$ are shown in grey lines. Note these model parameters are approximate, not exact, since the tracks were generated pseudo-randomly (see Sec. 3.2).

By rescaling the frequency correction obtained from the solar standard model, [Silva Aguirre et al. \(2015\)](#) and [Houdek et al. \(2019\)](#) applied it to other main-sequence stars. Several other correction formula were also put forward (e.g. [Kjeldsen et al. 2008](#); [Sonoi et al. 2015](#)). In particular, [Gough \(1990\)](#) suggested that the corrections are proportional to the cubic and the inverse of frequencies scaled by mode inertia:

$$\delta\nu = [a_3(\nu/\nu_{\text{max}})^3 + a_{-1}(\nu/\nu_{\text{max}})^{-1}] / I, \quad (1)$$

where a_3 and a_{-1} are the free parameters to be determined. The frequency of maximum power, ν_{max} , is evaluated via the scaling relation ([Brown et al. 1991](#); [Kjeldsen & Bedding 1995](#)):

$$\frac{\nu_{\text{max}}}{\nu_{\text{max},\odot}} \approx \frac{g}{g_{\odot}} \left(\frac{T_{\text{eff}}}{T_{\text{eff},\odot}} \right)^{-1/2}, \quad (2)$$

where we adopt $g_{\odot} = 274 \text{ m/s}^2$, $T_{\text{eff},\odot} = 5777 \text{ K}$, and $\nu_{\text{max},\odot} = 3090 \mu\text{Hz}$ throughout this work. Since the cubic term usually dominates the frequency correction, another correction form is written as

$$\delta\nu = a_3(\nu/\nu_{\text{max}})^3 / I, \quad (3)$$

where a_3 is the free parameter.

These two functional forms have shown to match observations quite well. [Ball & Gizon \(2014, 2017\)](#) showed that they work well for radial modes on the Sun and red-giant-branch stars, albeit with some caveats for mixed modes ([Ong et al. 2021a,b](#)). Many works concluded the inverse-cubic form could obtain an overall good fit ([Schmitt & Basu 2015](#); [Compton et al. 2018](#); [Nsamba et al. 2018](#); [Jørgensen et al. 2020](#)) and correctly recover the dynamical stellar properties of binary systems ([Jørgensen et al. 2020](#)).

The correction usually works as follows. Given a star with a set of observational frequencies and a stellar model with a set of theoretical frequencies, one can calculate the difference between the two frequency sets. This difference is then fitted to the right-hand-side of the frequency correction function (Eq. 1 or 3) to determine the free parameters. The amount of frequency correction is then calculated with the best-fitting values and added to the theoretical frequencies.

One problem with this method is that the surface correction can only be determined with a fit to observed frequencies. It does not allow us to estimate the surface terms for any theoretical model without being close to the observed star. More seriously, it can lead to a model with an unphysically large (or small) surface correction that fits the data well but is a poor representation of the star. In this paper, we tackle these problems through a simple prescription for the surface effect, assuming that it varies smoothly with stellar parameters (Sec. 2). This variation is then constrained by an ensemble fit to a wide range of stars (Sec. 3). Adopting this prescription improves parameter estimations with stellar modelling (Sec. 4). It further enables an improved correction to the commonly-used $\Delta\nu$ scaling relation (Sec. 5).

2 PRESCRIBING THE SURFACE CORRECTION

Since the surface effect originates from the model atmosphere, it is reasonable to assume it is a smooth function of surface parameters, i.e. surface gravity g , effective temperature T_{eff} , and metallicity $[M/H]$. This assumption is supported by 3D atmospheric simulations ([Sonoi et al. 2015](#); [Manchon et al. 2018](#)) and 1D non-adiabatic convection models ([Houdek et al. 2019](#)). These works suggested that the surface correction at ν_{max} , denoted by $\delta\nu_{\text{m}}$, varies from star to star as a function of T_{eff} and g . Hence, we propose a prescription for $\delta\nu_{\text{m}}$ as follows:

$$\delta\nu_{\text{m}} = a \cdot (g/g_{\odot})^b \cdot (T_{\text{eff}}/T_{\text{eff},\odot})^c \cdot (d \cdot [M/H] + 1), \quad (4)$$

where the free parameters to be determined are $\theta_s = \{a, b, c, d\}$. By construction, the parameter a is the amount of surface correction at ν_{max} for a solar model. If we adopt the cubic formula, for each star we can directly use Eq. 4 to solve the surface term a_3 in Eq. 3 with ν equal to ν_{max} . To obtain the mode inertia I on the RHS of Eq. 3, we interpolated ν^3/I to the frequency ν_{max} .

If we adopt the inverse-cubic formula to correct model frequencies, another equation is needed since there are two surface terms, a_{-1} and a_3 . We propose that the surface correction at s times of ν_{max} , denoted by $\delta\nu'_{\text{m}}$, also varies with the surface parameters:

$$\delta\nu'_{\text{m}} = a' \cdot (g/g_{\odot})^{b'} \cdot (T_{\text{eff}}/T_{\text{eff},\odot})^{c'} \cdot (d' \cdot [M/H] + 1). \quad (5)$$

Together with Eq. 4, the free parameters in this prescription are $\theta_s = \{a, b, c, d, a', b', c', d'\}$. By varying the value of s , we found no obvious changes to the solutions of those free parameters. Hence, we fixed s at 1.1, so that $\delta\nu'_{\text{m}}$ represents the amount of surface correction at $1.1\nu_{\text{max}}$. For each star, we then used Eq. 4 and Eq. 5 to solve a_{-1} and a_3 in Eq. 1 with $\nu = \nu_{\text{max}}$ and $\nu = 1.1\nu_{\text{max}}$, respectively. To calculate the RHS of Eq. 1, we interpolated ν^3/I and ν^{-1}/I to the frequency ν_{max} .

Table 1. Stellar parameters of the studied sample.

Star	L	σ_L	Ref(L)	T_{eff}	$\sigma_{T_{\text{eff}}}$	Ref(T_{eff})	[M/H]	$\sigma_{[\text{M}/\text{H}]}$	Ref([M/H])
Sun	1.0	0.02	—	5777	100	—	0.0	0.05	—
μ Her	2.54	0.08	2	5560	100	3	0.28	0.05	3
KIC10000547	12.68	0.51	0	4969	36	1	-0.26	0.05	6
KIC10001440	39.77	3.8	0	4773	42	1	-0.65	0.05	6
KIC10004825	42.35	3.34	0	4611	55	1	0.21	0.05	6
KIC10014893	68.69	4.67	0	4579	26	1	-0.13	0.05	6
KIC10014959	9.29	0.33	0	4813	29	1	0.11	0.05	6
KIC10018442	37.7	1.89	0	4781	41	1	-0.03	0.05	6
KIC10018811	27.11	1.41	0	4918	28	1	-0.29	0.05	6

Note: References for the stellar parameters: 0 (This work); 1 (Casagrande et al. 2021); 2 (Grundahl et al. 2017); 3 (Jofré et al. 2015); 4 (Furlan et al. 2018); 5 (Lund et al. 2017); 6 (Ahumada et al. 2020); 7 (Buchhave & Latham 2015). Only the first 10 lines are shown. The full table can be accessed online.

3 DATA ANALYSIS

3.1 Observational sample

In order to constrain Eqs. 4 and 5, we need a sample of stars spanning a sufficiently large parameter space. Our sample (see Fig. 1) consists of stars with measured individual frequencies: the Sun (Broomhall et al. 2009), the SONG subgiant μ Herculis (Grundahl et al. 2017), *Kepler* main-sequence dwarfs (Lund et al. 2017), *Kepler* subgiants (Li et al. 2020a) and *Kepler* red-giant-branch (RGB) stars with $\Delta\nu > 2 \mu\text{Hz}$ (Li et al. 2022). The RGB stars were distinguished from helium-burning stars by Bedding et al. (2011), Stello et al. (2013), Mosser et al. (2014), Vradar et al. (2016), Elsworth et al. (2017), and Hon et al. (2017).

We compiled metallicities [M/H] from various sources, including HIRES spectra (see below), APOGEE DR16 (Ahumada et al. 2020), Lund et al. (2017), and Buchhave & Latham (2015) (listed in the order of priority) wherever possible. We collected metallicities for 36 stars measured with HIRES spectrograph (Vogt et al. 1994) at the Keck-I 10-m telescope on Maunakea observatory, Hawai‘i by Furlan et al. (2018). We also obtained new HIRES spectra for 21 stars in this work. The spectra were obtained and reduced as part of the California Planet Search queue (CPS, Howard et al. 2010). We used the C5 decker and obtained spectra with a S/N per pixel of 80 at $\sim 600\text{nm}$ with a spectral resolving power of $R \sim 60000$. To measure the metallicities, we applied Specmatch-synth (Petigura 2015), which fits a synthetic grid of model atmospheres and has been extensively validated through the California Kepler Survey (Petigura et al. 2017; Johnson et al. 2017). All metallicity measurements were brought to the APOGEE abundance scale by adding constant offsets, determined with the [M/H] measurements of same stars. Because of the limited number of metal-poor stars, we restricted our sample to have [M/H] > -0.8 dex.

We determined the effective temperatures, T_{eff} , with *Gaia* and 2MASS photometry, using the infrared flux method (IRFM) calibrated by Casagrande et al. (2021). This T_{eff} scale was benchmarked against solar twins, *Gaia* benchmark stars, and interferometry.

We determined luminosities, L , using *Gaia* DR3 (Gaia Collaboration et al. 2016, 2021). *Gaia* parallaxes are known to have zero-point offsets, which we corrected using a model from Lindegren et al. (2021). The reported parallaxes also have underestimated uncertainties. Therefore we inflated them by a factor of 1.3, according to external calibrations

(El-Badry et al. 2021; Zinn 2021; Maíz Apellániz et al. 2021). We then calculated the luminosities by combining the parallaxes with the 2MASS K -band magnitudes and using the “direct” method in the software ISOCCLASSIFY (Huber et al. 2017; Berger et al. 2020), which implements the Green et al. (2019) dust map and the bolometric corrections from MIST models (Choi et al. 2016).

Additionally, we used RGB stars from two *Kepler* clusters as a test sample: NGC 6791 (Basu et al. 2011; McKeever et al. 2019; Brogaard et al. 2021) and NGC 6819 (Stello et al. 2010; Corsaro et al. 2012; Handberg et al. 2017). These cluster stars were not used for fitting the prescription, but for validating the result (Sec. 4). We estimated their stellar parameters following the same procedure illustrated above. Table 1 lists the stellar parameters used in modelling. Fig. 1 shows an overview of our sample on the H–R diagram.

3.2 Stellar models

We calculated a grid of stellar models using Modules for Experiments in Stellar Astrophysics (MESA, version r15140; Paxton et al. 2011, 2013, 2015, 2018, 2019) to model stellar evolution and structure, and GYRE (version 6.0.1; Townsend & Teitler 2013) to calculate adiabatic frequencies from the structure profiles computed from MESA.

Here, we summarise the input physics for the constructed models. We used the Henyey et al. (1965) description of the mixing length theory to formulate convection, with the mixing length being one of the free parameters, since a solar-calibrated mixing length can not fit stars with various stellar properties (Tayar et al. 2017; Joyce & Chaboyer 2018a). We set the convective overshoot with an exponential scheme discussed by Herwig (2000). For core overshoot, we set the efficiency parameter $f_{\text{ov,core}}$ as a function of mass, according to the calibration from eclipsing binaries (equation 2 of Claret & Torres 2018). For envelope overshoot, we set $f_{\text{ov,env}}$ as 0.006, according to a solar calibration with our adopted input physics.

We chose the current solar photospheric abundance as the reference scale for metallicity: $X_{\odot} = 0.7381$, $Y_{\odot} = 0.2485$, $Z_{\odot} = 0.0134$ (Asplund et al. 2009, the AGSS09 scale). Hence the metallicity is

$$[\text{M}/\text{H}] = \log_{10}(Z/X) - \log_{10}(Z_{\odot}/X_{\odot}). \quad (6)$$

The opacity tables were accordingly chosen based on the

AGSS09 metal mixture. MESA implements electron conduction opacities (Cassisi et al. 2007) and radiative opacities from OPAL (Iglesias & Rogers 1993, 1996), except low-temperature data (Ferguson et al. 2005) and the high-temperature Compton-scattering regime (Buchler & Yueh 1976). The equation of state adopted by MESA blends from OPAL (Rogers & Nayfonov 2002), SCVH (Saumon et al. 1995), PTEH (Pols et al. 1995), HELM (Timmes & Swesty 2000), and PC (Potekhin & Chabrier 2010). We adopted nuclear reaction rates from JINA REACLIB database. We only considered a minimal set of elements specified in `basic.net` of MESA. We did not account for atomic diffusion or gravitational settling in the models.

For the surface boundary conditions, we used the grey model atmosphere together with Eddington $T - \tau$ integration (Eddington 1926). We caution that by default, MESA does not include the atmosphere in the output structure. The resulting bias looks very similar to the surface effect, although the amount of correction is larger. To avoid this, one should specifically set `add_atmosphere_to_pulse_data` as `.true`.

The free parameters for the model grid are stellar mass $M \in (0.7, 2.3) M_{\odot}$, initial helium abundance $Y_{\text{init}} \in (0.22, 0.32)$, metallicity $[M/H] \in (-0.94, 0.56)$ (the corresponding Z_{init} ranges from 0.0016 to 0.0522), and mixing-length parameter $\alpha_{\text{MLT}} \in (1.3, 2.7)$. These four parameters were uniformly sampled in a quasi-random Sobol sequence with a total number of 8191 (Bellinger et al. 2016). Each set of parameters uniquely determines an evolutionary track. Along each evolutionary track, we saved one structure model at least every $0.3 \mu\text{Hz}$ in $\Delta\nu$ or 5 K in T_{eff} . For each structure model, we calculated radial mode frequencies with GYRE in a wide frequency range around ν_{max} . We used the 6th-order Gauss-Legendre Magnus method to solve the adiabatic oscillations. We caution that a lower-order algorithm could produce inaccurate frequencies, which differ by an amount larger than the typical observational uncertainties. Although a higher-order scheme is sensitive to abrupt changes in the structure, we examined the variables (such as density, temperature, sound speed and the first adiabatic index) in the set of oscillation equations, and found they vary smoothly near the atmospheres.

3.3 Fitting method

We now describe the fitting method to obtain the surface parameters θ_s in the prescriptions. They determine the amount of surface correction of each model $\theta_m = \{M, Y_{\text{init}}, \alpha_{\text{MLT}}, [M/H], \text{age}\}$. For each star i , we considered three classical constraints $q = \{L, T_{\text{eff}}, [M/H]\}$ (e.g. Valle et al. 2015; Joyce & Chaboyer 2018b; Duan et al. 2021; Jiang & Gizon 2021):

$$\chi_{\text{classical},i}^2 = \sum_q \frac{(q_{\text{mod},i} - q_{\text{obs},i})^2}{\sigma_{q,i}^2}. \quad (7)$$

The seismic constraints include radial mode frequencies. They are normalised by the number of observed modes N_i , in order to avoid unrealistically small error bars (Cunha et al. 2021; Aguirre Børsen-Koch et al. 2022):

$$\chi_{\text{seismic},i}^2 = \frac{1}{N_i} \sum_n \frac{(\nu_{\text{mod},n,i} + \delta\nu_{n,i} - \nu_{\text{obs},n,i})^2}{\sigma_{\text{mod}}^2 + \sigma_{\text{obs},n,i}^2}. \quad (8)$$

Normalising by the number of modes N_i in $\chi_{\text{seismic},i}^2$ is equivalent to reducing the relative weight of $\chi_{\text{seismic},i}^2$ with respect to $\chi_{\text{classical},i}^2$ and artificially inflating returned formal uncertainties. Cunha et al. (2021) noted that this is a common practice in stellar modelling, but it is not statistically valid and is sometimes unable to capture the systematic uncertainties originating from stellar physics. In the above equation, $\delta\nu_{n,i}$ is the amount of surface correction, and σ_{mod} is the systematic uncertainty of stellar model frequencies (Li et al. 2020b; Ong et al. 2021b). To evaluate σ_{mod} , we identified the best-fitting model (using the above χ_{seismic} and treating $\sigma_{\text{mod},i}$ as 0) and calculated its root-mean-square difference between the observed and corrected modelled frequencies. At this step, the amount of surface correction for each mode, $\delta\nu_{n,i}$, was determined by fitting Eq. 1 or 3 to the actual differences between the uncorrected model frequencies $\nu_{\text{mod},n,i}$ and the observed frequencies $\nu_{\text{obs},n,i}$ (i.e. the traditional star-by-star surface correction). We then fitted the root-mean-square differences as a function of ν_{max} and T_{eff} for the whole sample and used this function to describe σ_{mod} , which gave

$$\sigma_{\text{mod}}/\mu\text{Hz} = 1.65 \cdot (\nu_{\text{max}}/\nu_{\text{max},\odot})^{1.45} (T_{\text{eff}}/T_{\text{eff},\odot})^{2.30}. \quad (9)$$

The value of σ_{mod} is generally smaller than σ_{obs} in RGB stars and comparable in main-sequence stars, hence the poorly- and well-observed modes in one star are not weighted similarly. For our final fitting, $\delta\nu_{n,i}$ was calculated using the prescription described in Sec. 2.

To obtain the probability distributions of the surface parameters θ_s , we marginalised the probability over other model parameters:

$$p_i(\theta_s) = \int \exp[-(\chi_{\text{classical},i}^2 + \chi_{\text{seismic},i}^2)/2] d\theta_m. \quad (10)$$

Since θ_m is sampled on a pre-computed model grid, in practice, we approximated this integration by taking the average values of the integrated function for all eligible models. Finally, putting them together, we maximised the joint probability from all stars in the sample:

$$p(\theta_s) = \prod_i p_i(\theta_s) \quad (11)$$

We used a gradient descent algorithm written with JAX and OPJAX (Babuschkin et al. 2020) to optimise this function. We adopted the uncertainties for the fitted parameters using the diagonal elements of the covariance matrix, which was constructed with the Hessian matrix for $\log p$. Ensemble modelling to constrain uncertain stellar physics has been used to study the mixing length and helium abundance (Lyttle et al. 2021).

3.4 Fitting results

In addition to fitting the whole sample, we performed fits in two classes of stars: pre-RGB ($\nu_{\text{max}} > 283 \mu\text{Hz}$) and RGB ($\nu_{\text{max}} < 283 \mu\text{Hz}$). In Table 2, we show the best-fitting values of the surface parameters in the prescriptions. Firstly, the best-fitting parameters for the whole sample and the RGB sample are similar, since RGB stars dominate the sample. Secondly, the power indices for g , T_{eff} , and $[M/H]$ (b , c , and d) are quite different for the RGB fit compared to the pre-RGB fit. These parameters are also highly correlated, indicating that their values could be poorly constrained, rather than highly

Table 2. Best-fitting parameters in the surface correction prescriptions. The stellar models are calculated with $T - \tau$ integrated model atmospheres using the Eddington relation.

Atmosphere Model	Sample	a	b	c	d	a'	b'	c'	d'
Eddington	Cubic	All	-4.15 ± 0.13	0.95 ± 0.01	-5.48 ± 0.23	-1.10 ± 0.03	—	—	—
Eddington	Cubic	Pre-RGB	-4.19 ± 0.39	0.78 ± 0.07	-5.71 ± 0.58	-0.07 ± 0.13	—	—	—
Eddington	Cubic	RGB	-4.18 ± 0.13	0.96 ± 0.01	-5.64 ± 0.22	-1.11 ± 0.02	—	—	—
Eddington	Inverse-cubic	All	-3.74 ± 0.13	1.09 ± 0.01	-8.74 ± 0.23	-1.38 ± 0.02	-4.99 ± 0.14	1.05 ± 0.01	-8.15 ± 0.18
Eddington	Inverse-cubic	Pre-RGB	-3.72 ± 0.40	0.61 ± 0.08	-1.68 ± 0.82	-0.08 ± 0.14	-5.55 ± 0.42	0.65 ± 0.06	-1.57 ± 0.62
Eddington	Inverse-cubic	RGB	-3.84 ± 0.16	1.10 ± 0.01	-8.83 ± 0.24	-1.38 ± 0.02	-5.04 ± 0.17	1.07 ± 0.01	-8.33 ± 0.19

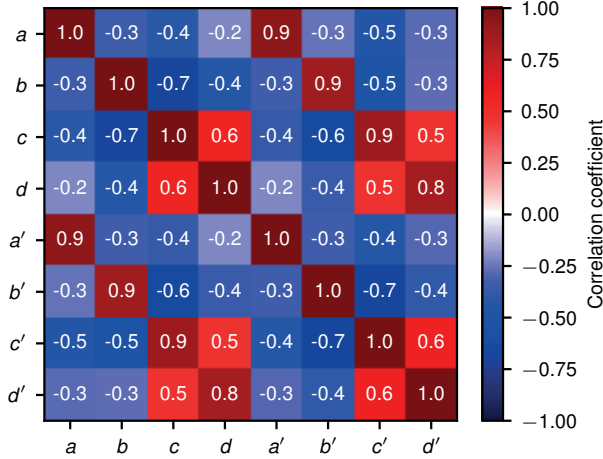


Figure 2. Correlation matrix of the fitted parameters for all sample using the inverse-cubic model.

physically different. Fig. 2 shows the correlation matrix of the fitted parameters for all sample using the inverse-cubic model. Thirdly, although the reported uncertainties are small, we observed strong correlations (correlation coefficient greater than 0.5) between b and c , b' and c' , c and d , c' and d' , a and a' , b and b' , c and c' , and d and d' . Fourthly, the inverse-cubic and the cubic models show little differences. We discuss the inverse-cubic model and the fit with the whole sample in the rest of the paper.

To visualise our fitting result, we colour-coded the values of $\delta\nu_m$ and $\delta\nu_m/\nu_{\max}$ in Fig. 3 on the $\Delta\nu$ - T_{eff} diagrams. In terms of the absolute value $\delta\nu_m$ (which is always negative), the main-sequence stars have the largest amount of surface correction. It decreases towards higher T_{eff} (hotter F-stars) and smaller $\Delta\nu$ (more luminous red giants). Concerning the relative value of $\delta\nu_m$ with respect to ν_{\max} , the trend is reversed. The main-sequences stars have smaller corrections, and the surface effect becomes increasingly significant for luminous red giants. Those trends are similar compared to those found by Trampedach et al. (2017, Fig. 5 and 6), who improved the mean atmospheric structure with 3D-averaged models (the so-called “structural effect”).

Sonoi et al. (2015, Eqs. 9 and 10) also studied the structural effect, mainly for dwarfs and subgiants, and concluded positive correlations between $\delta\nu_m$ and g or T_{eff} . Houdek et al. (2019, Fig. 5) studied the “modal effect”, which accounts for the coupling between convection and oscillation, and reported a similar correlation with their 1D time-dependent convec-

tion models. These works are qualitatively consistent with our best-fitting parameters for dwarfs and subgiants (Table 2).

We emphasise that the values reported in Table 2 may not be directly applicable to other stellar models, which could have different outer boundary conditions. For example, in Fig. 2 of Christensen-Dalsgaard et al. (1996) there are three modifications to the solar atmosphere: one with an alternative treatment of the convective flux, one with the inclusion of turbulent pressure, and one with replacement from 3D averaged models. Each one has a different value for the surface effect at ν_{\max} , ranging from 5 to 17 μHz , suggesting that an alternative atmosphere could differ by a factor of three from our fitted values for the Sun. Moreover, the differences in the model physics and even numerical treatment can change the fitted values. To test this, we applied our prescriptions to a grid of models calculated by Sharma et al. (2016). Even though they set the same Eddington atmosphere with MESA as in this work, we obtained unrealistically large corrections in their models at high radial orders. Additionally, Appendix A examines an alternative atmosphere based on the Hopf $T - \tau$ relation. We found that the fitted coefficients are drastically different from those obtained using the Eddington relation. Hence, to correctly implement our method, we recommend to either use the stellar models corrected in this work or to re-fit the prescriptions with stellar models of the user’s choice.

4 IMPROVEMENTS ON PARAMETER ESTIMATIONS

We now check whether applying our prescription introduces bias in the estimated stellar properties. In Fig. 4, we show the fractional differences of mass, radius, and age, between modelling without and with the prescription. The differences have medians fluctuating around 0, suggesting no systematic bias.

Next, we demonstrate two major improvements by using our method. Firstly, we note that adopting the prescriptions reduces outliers when inferring parameters from stellar modelling. For example, Fig. 4 shows some stars significantly away from the median values. These data points correspond to a poor fit due to the unconstrained surface correction. To confirm this, we show the differences between the modelled and observed values of $\Delta\nu$ in Fig. 5, where the former were obtained from the best-fitting model. The model $\Delta\nu$ values were determined from the slope of a linear fit to the radial frequencies versus the orders, with weights of each mode assigned by a Gaussian envelope (centred around ν_{\max} ; see White et al. 2011)

$$w = \exp \left[-\frac{(\nu - \nu_{\max})^2}{2\sigma^2} \right], \quad (12)$$

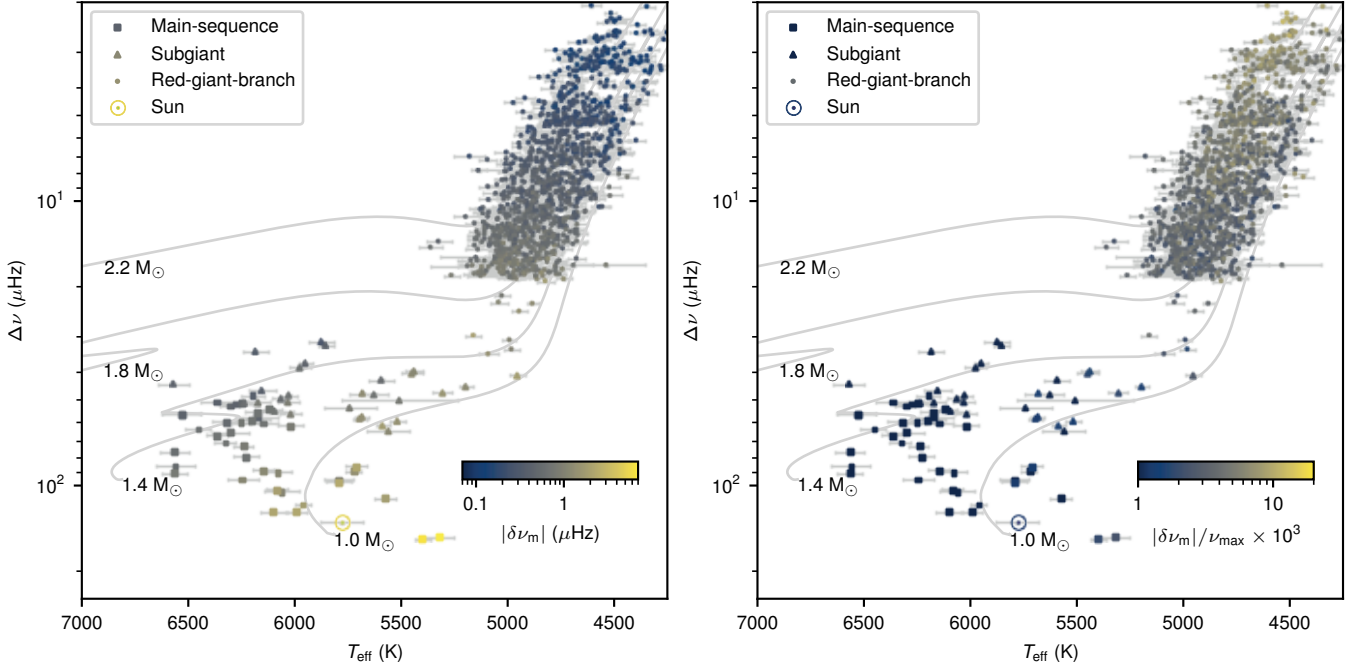


Figure 3. Surface correction at ν_{\max} , $\delta\nu_m$, determined based on the prescriptions with the inverse-cubic model, shown on the $\Delta\nu$ - T_{eff} diagrams. The left panel colour-codes the absolute value of $\delta\nu_m$ (which is negative). The right panel colour-codes the dimensionless quantity, $\delta\nu_m/\nu_{\max}$. The $M = 1.0, 1.4, 1.8$ and $2.2 M_{\odot}$ evolutionary tracks are shown in grey lines.

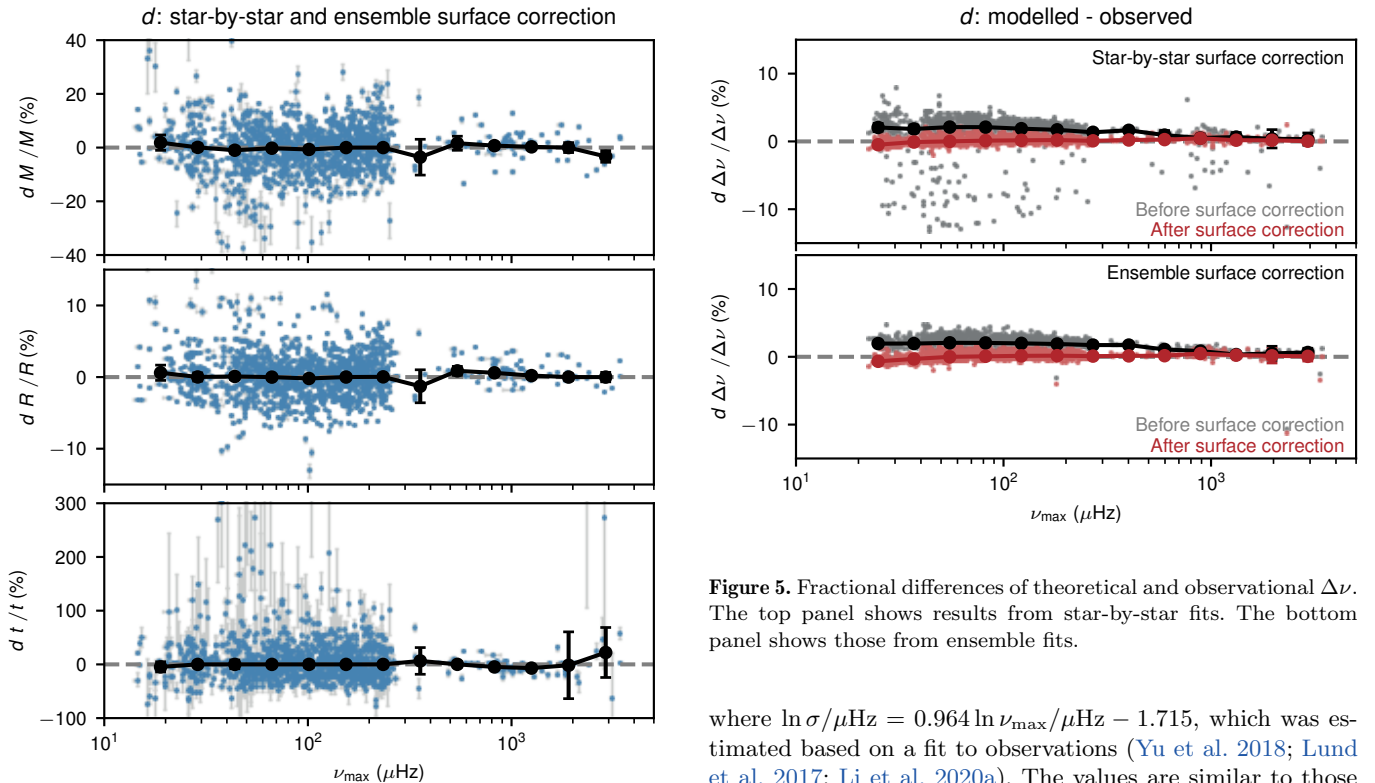


Figure 4. Fractional differences of mass, radius, and age, between modelling using star-by-star and ensemble surface correction. The medians and the associated error bars in bins of equal width in $\log \nu_{\max}$ are shown in black circles.

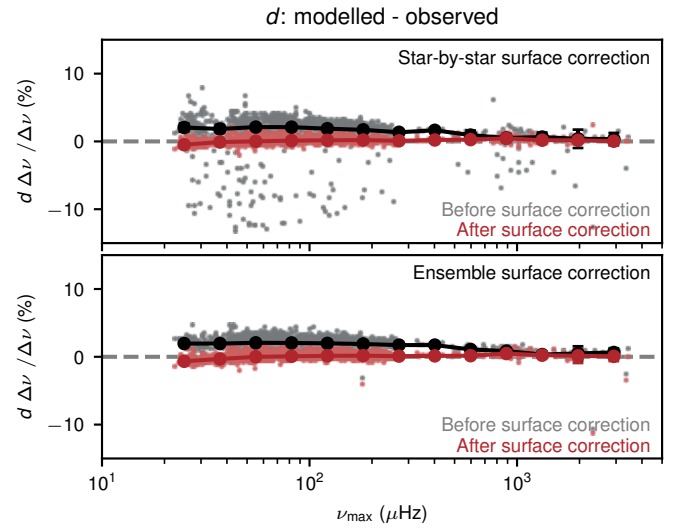


Figure 5. Fractional differences of theoretical and observational $\Delta\nu$. The top panel shows results from star-by-star fits. The bottom panel shows those from ensemble fits.

where $\ln \sigma/\mu\text{Hz} = 0.964 \ln \nu_{\max}/\mu\text{Hz} - 1.715$, which was estimated based on a fit to observations (Yu et al. 2018; Lund et al. 2017; Li et al. 2020a). The values are similar to those obtained by Mosser et al. (2012). For all models in this work, we calculated the modes within 5σ of ν_{\max} .

By comparing the red points in the two panels, we noticed that the differences are similar after the surface correction, independent of whether using the prescription or not. This is expected, since the corrected frequencies were constructed to

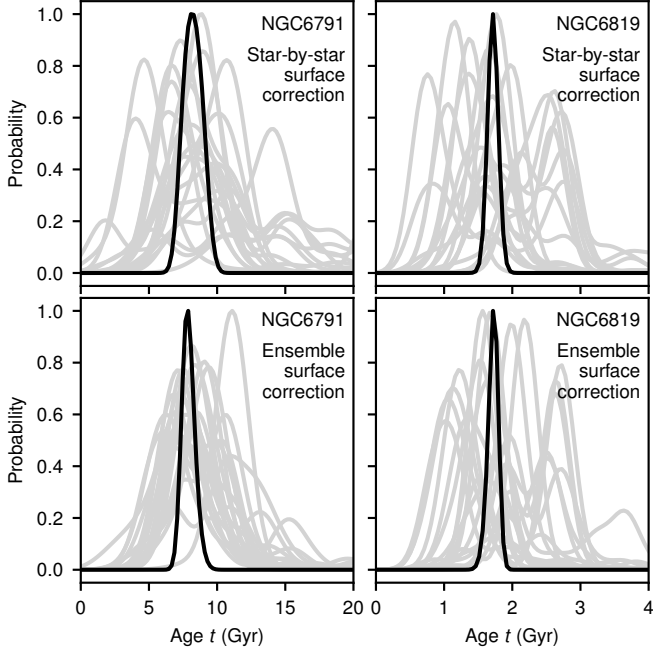


Figure 6. Probability distributions of stellar ages for the RGB stars within the *Kepler* open clusters NGC 6791 and NGC 6819. The age probability for each star are shown in grey, while the joint probability distribution is shown in black. Modelling with the prescription (lower panels) shows a reduction of the scatter in age, compared to modelling with a star-by-star surface correction (upper panels).

fit with the observed frequencies. However, when we compare the grey points in both panels, which represent $\Delta\nu$ calculated from the uncorrected frequencies, the outliers are only present in the case of star-by-star fit (top panel). These outliers are eliminated when the prescription was applied in the ensemble fit (bottom panel).

Secondly, we argue that adopting the prescriptions also reduces scatter in model-based parameters. This can be seen from modelling stars in open clusters, members of which are expected to have the same age. We examined the test sample introduced in Sec. 3.1, namely the RGB stars in NGC 6791 and NGC 6819. In Fig. 6, we show the probability distributions of ages for each star (in grey lines), and compare them with and without using our new prescription. It is evident that the probabilities with the prescriptions applied display smaller scatter overall. The root-mean-square values of individual model-based ages reduces from 2.11 Gyr to 1.60 Gyr for NGC 6791, and from 0.46 Gyr to 0.34 Gyr for NGC 6819.

On a side note, we compared our age estimates for the two open clusters against recent studies in Table 3. Our estimates occupy the lower end of the published ages. We attribute this to our adopted observational constraints: the relatively high metallicity for NGC 6791 ($[M/H] = 0.36$ dex), and the large extinction value for NGC 6819 (mean $E(B-V) = 0.17$). The effect of extinction and metallicity on age can be seen from Table 2 of Basu et al. (2011).

To allow easy-access to our stellar models and the surface-corrected frequencies, we published them in an online repository (see Data Availability).

Table 3. List of ages for the two open clusters.

Age (Gyr)	Methods	References
NGC 6791		
6.8 – 8.6	Seismology	Basu et al. (2011)
7.68 ± 1.60	Seismology	This work
8.2 ± 0.3	Seismology	McKeever et al. (2019)
8.3 ± 0.8	Isochrone fitting	Brogaard et al. (2012)
8.3	Binary	Brogaard et al. (2021)
10.1 ± 0.9	Seismology	Kallinger et al. (2018)
NGC 6819		
1.57 ± 0.34	Seismology	This work
2 – 2.4	Seismology	Basu et al. (2011)
2.4	Isochrone fitting	Jeffries et al. (2013)
2.4 ± 0.2	Eclipsing binary	Brewer et al. (2016)
2.5	Isochrone fitting	Balona et al. (2013)
2.62 ± 0.25	Eclipsing binary	Sandquist et al. (2013)
2.9 ± 0.3	Seismology	Kallinger et al. (2018)
3.1 ± 0.4	Eclipsing binary	Jeffries et al. (2013)

5 CORRECTION TO THE P-MODE LARGE SEPARATION FROM STELLAR MODELS

The scaling relation that relates the p-mode large separation $\Delta\nu$ to stellar mean density, $\Delta\nu \propto \sqrt{\rho}$ (Ulrich 1986), is broadly used (see Hekker 2020, for a review). This relation is only an approximation and stellar models have been used to correct it (White et al. 2011; Sharma et al. 2016; Guggenberger et al. 2016; Rodrigues et al. 2017; Serenelli et al. 2017; Pinsonneault et al. 2018). Sharma et al. (2016, hereafter S16) introduced a correction factor $f_{\Delta\nu}$ to the standard $\Delta\nu$ scaling relation:

$$\left(\frac{\Delta\nu}{\Delta\nu_{\odot}} \right) = f_{\Delta\nu} \left(\frac{\rho}{\rho_{\odot}} \right)^{0.5}, \quad (13)$$

where $\Delta\nu_{\odot} = 135.1 \mu\text{Hz}$ is the solar value of the large frequency separation (Huber et al. 2011).

The correction factor $f_{\Delta\nu}$ are used when estimating the mass and radius via the usual scaling relations (Stello et al. 2008; Kallinger et al. 2010):

$$\frac{M}{M_{\odot}} \approx \left(\frac{\nu_{\max}}{\nu_{\max,\odot}} \right)^3 \left(\frac{\Delta\nu}{f_{\Delta\nu}\Delta\nu_{\odot}} \right)^{-4} \left(\frac{T_{\text{eff}}}{T_{\text{eff},\odot}} \right)^{3/2}, \quad (14)$$

and

$$\frac{R}{R_{\odot}} \approx \left(\frac{\nu_{\max}}{\nu_{\max,\odot}} \right) \left(\frac{\Delta\nu}{f_{\Delta\nu}\Delta\nu_{\odot}} \right)^{-2} \left(\frac{T_{\text{eff}}}{T_{\text{eff},\odot}} \right)^{1/2}. \quad (15)$$

To use Eq. 13 to determine $f_{\Delta\nu}$ from models, we need to know the model-predicted density and $\Delta\nu$, the latter of which is usually calculated from radial oscillation frequencies. Since the surface correction is negative, we expect that the model $\Delta\nu$ value will decrease when the correction is applied (Kjeldsen et al. 2008). However, this correction was previously ignored. Here, we investigate this change and analyse its implication on stellar properties derived from the asteroseismic relations.

5.1 Results

Firstly, we present the correction factor, $f_{\Delta\nu}$, calculated from our stellar models and prescriptions. Fig. 7 shows $f_{\Delta\nu}$ as a function of T_{eff} (left panels) and $\Delta\nu$ (right panels), for three

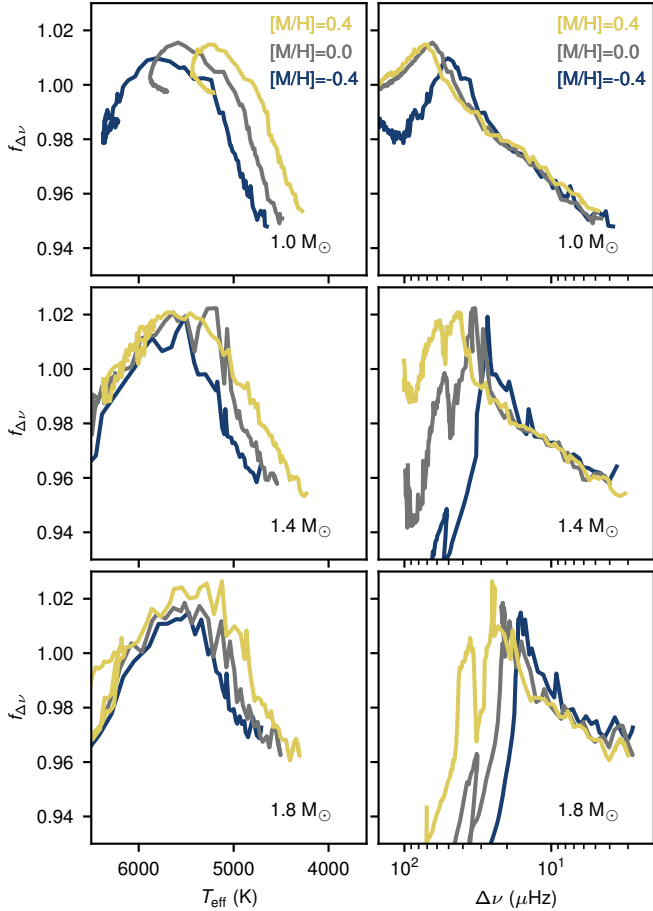


Figure 7. Correction factor for the $\Delta\nu$ scaling relation, $f_{\Delta\nu}$, as a function of T_{eff} (left panels) and $\Delta\nu$ (right panels) for three metallicities and three masses. The values for $f_{\Delta\nu}$ were derived using stellar models with the surface correction considered. The small fluctuations along the lines arise from the uncertainty in the helium abundance and the mixing length parameter.

masses and three metallicities. The overall variations of $f_{\Delta\nu}$ resemble those calculated from models by [White et al. \(2011, Fig. 4\)](#) and [S16 \(Fig. 4\)](#), neither of which included a surface correction. However, our values for $f_{\Delta\nu}$ are systematically smaller compared to the work from [S16](#), due to this correction. Fig. 8 shows the effect of surface correction on $f_{\Delta\nu}$. The change of $f_{\Delta\nu}$ is small for main-sequence stars, but is larger on the RGB, showing an $\sim 2\%$ reduction, where the surface correction is relatively significant (see also Fig. 3b).

The revised correction factors can be used to estimate the mass and radius via Eq. 14 and 15. Unlike the surface corrections done in Sec. 3.3, these do not require any additional model calculations by the user. They simply involve revising the standard scaling relation. We provide a Python routine to derive $f_{\Delta\nu}$ given user-specified observables, based on the models that are calibrated in this work. For a given star, the user specifies observational constraints and their associated uncertainties (e.g. L , T_{eff} , $[M/H]$ and ν_{max}). Each model is assigned with a χ^2 (using Eq. 7). Next, the correction factor $f_{\Delta\nu}$ of the star is estimated by taking the average of model $f_{\Delta\nu}$ values, weighted by $\exp(-\chi^2/2)$.

We can also provide a simple fitting formula of $f_{\Delta\nu}$ with

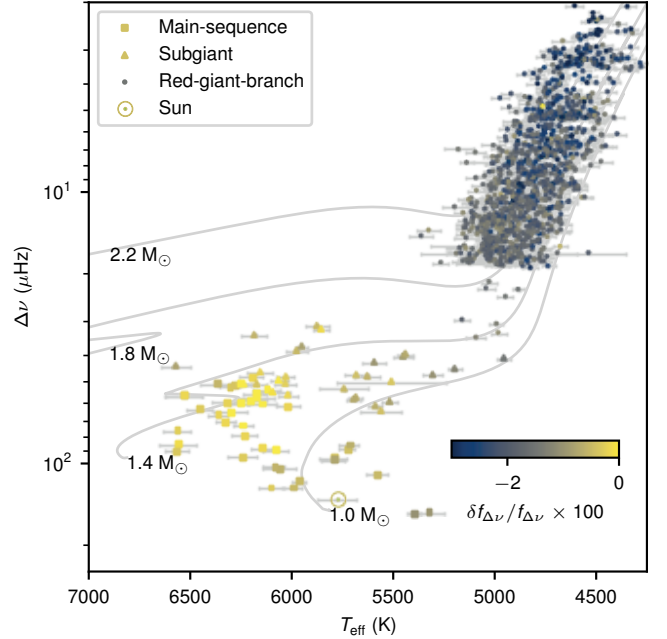


Figure 8. Fractional differences of $f_{\Delta\nu}$ between before and after the surface correction.

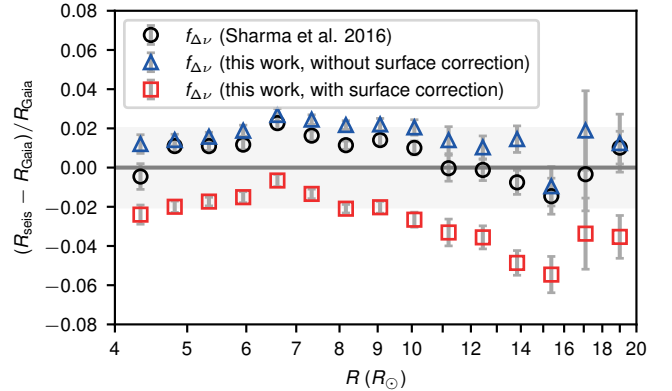


Figure 9. Comparison of *Gaia* radii and asteroseismic radii, using $f_{\Delta\nu}$ calculated in [S16](#) and this work. The data points are binned medians, and the error bars represent the standard errors of the medians. The grey band highlights the 2% systematic uncertainties (e.g. temperature scale) discussed by [Zinn et al. \(2019\)](#).

respect to stellar properties. We explored various functional forms (linear, log-linear and polynomial) and included the observed ν_{max} , $\Delta\nu$, T_{eff} and $[M/H]$ as independent variables to perform simple regressions. The following form obtains a reasonably good fit ($r^2 = 0.85$) and avoids over-fitting with

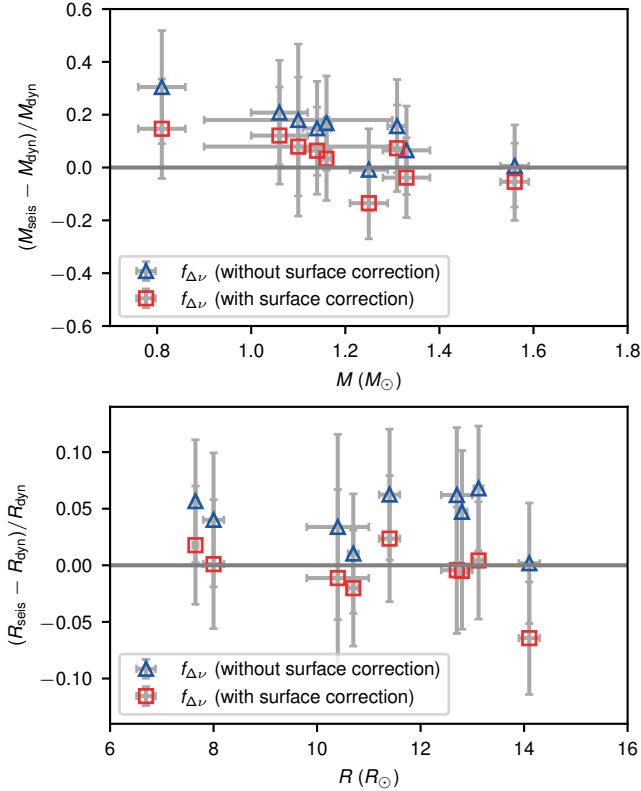


Figure 10. Comparison of the dynamical and the asteroseismic masses and radii using eclipsing binaries (Gaulme et al. 2016; Themeßl et al. 2018; Brogaard et al. 2018; Benbakoura et al. 2021). The asteroseismic properties were determined using $f_{\Delta\nu}$ with and without the surface correction, respectively.

higher orders (examined via cross-validation):

$$\begin{aligned}
 f_{\Delta\nu} = & \beta_0 + \beta_1 \log_{10}(\nu_{\max}/3090 \text{ } \mu\text{Hz}) \\
 & + \beta_2 \log_{10}(\Delta\nu/135.1 \text{ } \mu\text{Hz}) \\
 & + \beta_3 (T_{\text{eff}}/5777 \text{ K}) \\
 & + \beta_4 (T_{\text{eff}}/5777 \text{ K})^2 \\
 & + \beta_5 (T_{\text{eff}}/5777 \text{ K})^3 \\
 & + \beta_6 [\text{M}/\text{H}], \\
 & \text{for } 0.8 < M/M_{\odot} < 2.2, -0.8 < [\text{M}/\text{H}] < 0.5, \\
 & \text{and pre-RGB tip } (\Delta\nu > 2.0 \text{ } \mu\text{Hz}).
 \end{aligned} \tag{16}$$

The best-fitting parameters are $\beta = \{4.1027, 0.1706, -0.1863, -10.5526, 11.8359, -4.3733, 0.0015\}$. Note that the above formula does not predict $f_{\Delta\nu} = 1$ for solar properties, since we did not require the formula to pass through the solar reference point. To obtain the most accurate estimations on $f_{\Delta\nu}$, we suggest using the provided Python routine.

Naturally, fitting formula would need to be tested before applying outside the parameter ranges of our sample. Extending it to other ranges, such as metal-poor, high-mass, and red-clump stars, requires more data and will be the subject of future work.

5.2 Comparisons to Gaia radii

To show how the surface corrected $f_{\Delta\nu}$ affects stellar radii, we compared the asteroseismic radii with the Gaia radii calculated by Zinn (2021), using the APOKASC sample (Pinsonneault et al. 2018). The T_{eff} and $[\text{M}/\text{H}]$ from APOGEE (Abdurro'uf et al. 2022) were used to derive Gaia radii for bolometric corrections and converting from luminosities. We calculated the asteroseismic radii through Eq. 15, where we adopted the SYD pipeline values for $\Delta\nu$ and ν_{\max} (Serenelli et al. 2017; Yu et al. 2018), and T_{eff} from APOGEE.

Fig. 9 shows the result. Without the surface correction considered, the $f_{\Delta\nu}$ in this work (blue triangles) produce similar radii to S16 (black circles), despite the fact that the underlying stellar models are different. Christensen-Dalsgaard et al. (2020) reported a spread of only 0.2% in the values of $f_{\Delta\nu}$ from different stellar modelling code. In addition, we found that differences in the mixing length can change $f_{\Delta\nu}$ by $\sim 1\%$ (see Appendix B for more details). A larger discrepancy emerges when we applied the surface correction (red squares). Eq. 15 indicates that the seismic radius is proportional to $f_{\Delta\nu}^2$. Since correctly accounting for the surface effect reduces $f_{\Delta\nu}$ by $\sim 2\%$ for RGB stars (Fig. 8), this translates to a systematic $\sim 4\%$ decrease of the asteroseismic radius scale. This is exactly what we see in Fig. 9. As summarized by Zinn et al. (2019), the systematic uncertainties involved in this comparison, such as uncertainties in bolometric correction and extinction, the IRFM temperature scale, and asteroseismic reference points, can add up to 2%. It is not yet possible to conclude any disagreement between the asteroseismic and Gaia radii with this precision.

There is a significant excursion of red squares at $R > 10 R_{\odot}$ in Fig. 9 that cannot be explained by the causes discussed above. The dip associated with the excursion is also present when using the $f_{\Delta\nu}$ without surface correction. The red clump stars, which burn helium in the core, have radii around $10 R_{\odot}$ (see Fig. 6 of Li et al. 2021a). After exhausting core helium, they become asymptotic-giant-branch (AGB) stars and are difficult to be distinguished from RGB stars based on g-mode period spacings alone (Kallinger et al. 2012; Dréau et al. 2021). Hence, the dip is probably a result of the contamination from AGB stars in the sample. This is supported by the excess of very low-mass stars above $10 R_{\odot}$, due to AGB stars having lost more mass than RGB stars (see Fig. 2g of Li et al. 2021a). The impact of this contamination on Galactic population studies clearly deserves further investigation.

5.3 Comparisons to eclipsing binaries

Similarly, we can compare the asteroseismic radius and mass with the dynamical properties determined from eclipsing binaries. We used the eclipsing binary sample studied by Gaulme et al. (2016), Themeßl et al. (2018), Brogaard et al. (2018) and Benbakoura et al. (2021), who determined the dynamical masses and radii through radial-velocity and lightcurve modelling. We calculated their asteroseismic radii and masses through Eq. 14 and 15, using $\Delta\nu$, ν_{\max} , and T_{eff} reported in Benbakoura et al. (2021). Fig. 10 shows the resulting comparison. Using the corrected $f_{\Delta\nu}$ produces excellent agreement of those properties determined from the two independent means, while the $f_{\Delta\nu}$ without correction tends to systematically overestimate them. Although Benbakoura

et al. (2021) did not consider the surface corrected $f_{\Delta\nu}$, they also found agreement between the asteroseismic and dynamical properties, through modifying the solar reference values appearing in the scaling relations. Our results thus remove the need to shift the reference values when the surface correction is taken into account. Moreover, the impact of surface correction changes as a function of stellar properties (Fig. 8), so it would be difficult to reconcile all stars if the reference values are treated as a constant.

According to Eq. 14, the scaling mass is proportional to $f_{\Delta\nu}^4$ (e.g. Sharma et al. 2016). Hence, as a result of the change in $f_{\Delta\nu}$, the seismic mass scale decreases by $\sim 8\%$. This could have significant consequences for Galactic archaeology since the ages of low-mass stars are critically dependent on their masses.

6 CONCLUSIONS

We provide a prescription for the surface correction as a function of stellar properties, exploiting the fact that the correction should vary smoothly across the H–R diagram. Our main findings are summarised as follows:

- (i) The absolute values of the surface correction are larger in main-sequence stars and smaller in RGB stars. For the relative surface correction as a fraction of ν_{\max} , the trend is reversed (Sec. 3.4 and Fig. 3).
- (ii) Using the prescription, we were able to reduce scatter and the number of outliers in stellar properties estimated from stellar modelling (Sec. 4 and Figs. 5 and 6). This demonstrates the power of our ensemble-based parameterization of the surface correction.
- (iii) We present our stellar models in an online repository. The models include radial frequencies before and after applying the surface correction calibrated in this work.
- (iv) Taking into account the surface correction, we present a revised $\Delta\nu$ scaling relation (Sec. 5.1 and Fig. 7). We provided a fitting formula (Eq. 16) and a Python routine to determine $f_{\Delta\nu}$ given user-specified observables.
- (v) The values of $f_{\Delta\nu}$ are smaller by up to 2%, after taking into account the surface correction (Sec. 5.1 and Fig. 8). This results in decreases of up to 4% in radii and up to 8% in masses when using the asteroseismic scaling relations.
- (vi) We showed that the mass and radius determined with the revised $f_{\Delta\nu}$ improve the agreement with those determined from eclipsing binaries (Sec. 5.3 and Fig. 10).

For most readers, item (iv) will be the most useful. It describes a modification to the $\Delta\nu$ scaling relation that, for the first time, takes the surface correction into account and we encourage its use when deriving masses and radii from asteroseismic parameters.

ACKNOWLEDGEMENTS

We thank Warrick Ball, Sarbani Basu, Karsten Brogaard, Jørgen Christensen-Dalsgaard, and Günter Houdek for interesting comments and discussions. T.R.B acknowledges funding from the Australian Research Council (Discovery Project DP210103119 and Laureate Fellowship FL220100117). D.H.

acknowledges support from the Alfred P. Sloan Foundation and the National Aeronautics and Space Administration (80NSSC19K0597). M.J. acknowledges the Lasker Fellowship granted by the Space Telescope Science Institute. T.L. acknowledges the Joint Research Fund in Astronomy (U2031203) under cooperative agreement between the National Natural Science Foundation of China (NSFC) and Chinese Academy of Sciences (CAS) and the NSFC grants 12090040 and 12090042. H.K. acknowledges funding for the Stellar Astrophysics Centre provided by The Danish National Research Foundation (Grant agreement no.: DNR106).

We gratefully acknowledge the Kepler teams, whose efforts made these results possible. Funding for the Kepler mission is provided by the NASA Science Mission Directorate. This paper includes data collected by the Kepler mission and obtained from the MAST data archive at the Space Telescope Science Institute (STScI). STScI is operated by the Association of Universities for Research in Astronomy, Inc., under NASA contract NAS 5–26555.

This work presents results from the European Space Agency (ESA) space mission Gaia. Gaia data are being processed by the Gaia Data Processing and Analysis Consortium (DPAC). Funding for the DPAC is provided by national institutions, in particular the institutions participating in the Gaia MultiLateral Agreement (MLA). The Gaia mission website is <https://www.cosmos.esa.int/gaia>. The Gaia archive website is <https://archives.esac.esa.int/gaia>.

Funding for the Sloan Digital Sky Survey IV has been provided by the Alfred P. Sloan Foundation, the U.S. Department of Energy Office of Science, and the Participating Institutions.

We acknowledge the use of the National Computational Infrastructure (NCI) which is supported by the Australian Government, and accessed through the Sydney Informatics Hub HPC Allocation Scheme, which is supported by the Deputy Vice-Chancellor (Research), University of Sydney.

This work is made possible by the following open-source software: Numpy (van der Walt et al. 2011), Scipy (Virtanen et al. 2020), Matplotlib (Hunter 2007), Astropy (Astropy Collaboration et al. 2013, 2018), Pandas (Wes McKinney 2010), MESA (Paxton et al. 2011, 2013, 2015, 2018, 2019), GYRE (Townsend & Teitler 2013), ISOCCLASSIFY (Huber et al. 2017; Berger et al. 2020), JAX and OPTAX (Babuschkin et al. 2020).

DATA AVAILABILITY

The code and processed data used in this work are available on Github.¹ The calibrated stellar models including oscillation frequencies and the correction factors $f_{\Delta\nu}$ can be downloaded from zenodo.² All raw data (e.g. the Keck spectra) are available on request to the corresponding authors.

REFERENCES

- Abdurro’uf et al., 2022, *ApJS*, 259, 35
- Aguirre Børsen-Koch V., et al., 2022, *MNRAS*, 509, 4344
- Ahumada R., et al., 2020, *ApJS*, 249, 3

¹ <https://www.github.com/parallelpro/surface>

² <https://zenodo.org/record/7905521>

- Asplund M., Grevesse N., Sauval A. J., Scott P., 2009, *ARA&A*, **47**, 481
- Astropy Collaboration et al., 2013, *A&A*, **558**, A33
- Astropy Collaboration et al., 2018, *AJ*, **156**, 123
- Babuschkin I., et al., 2020, The DeepMind JAX Ecosystem, <http://github.com/deepmind>
- Ball W. H., Gizon L., 2014, *A&A*, **568**, A123
- Ball W. H., Gizon L., 2017, *A&A*, **600**, A128
- Balmforth N. J., 1992, *MNRAS*, **255**, 632
- Balona L. A., et al., 2013, *MNRAS*, **430**, 3472
- Basu S., et al., 2011, *ApJ*, **729**, L10
- Bedding T. R., et al., 2011, *Nature*, **471**, 608
- Belkacem K., Kupka F., Philidet J., Samadi R., 2021, *A&A*, **646**, L5
- Bellinger E. P., Angelou G. C., Hekker S., Basu S., Ball W. H., Guggenberger E., 2016, *ApJ*, **830**, 31
- Benbakoura M., et al., 2021, arXiv e-prints, p. [arXiv:2101.05351](https://arxiv.org/abs/2101.05351)
- Berger T. A., Huber D., van Saders J. L., Gaidos E., Tayar J., Kraus A. L., 2020, *AJ*, **159**, 280
- Brewer L. N., et al., 2016, *AJ*, **151**, 66
- Brogaard K., et al., 2012, *A&A*, **543**, A106
- Brogaard K., et al., 2018, *MNRAS*, **476**, 3729
- Brogaard K., Arentoft T., Jessen-Hansen J., Miglio A., 2021, *MNRAS*, **507**, 496
- Broomhall A. M., Chaplin W. J., Davies G. R., Elsworth Y., Fletcher S. T., Hale S. J., Miller B., New R., 2009, *MNRAS*, **396**, L100
- Brown T. M., Gilliland R. L., Noyes R. W., Ramsey L. W., 1991, *ApJ*, **368**, 599
- Buchhave L. A., Latham D. W., 2015, *ApJ*, **808**, 187
- Buchler J. R., Yueh W. R., 1976, *ApJ*, **210**, 440
- Casagrande L., et al., 2021, *MNRAS*, **507**, 2684
- Cassisi S., Potekhin A. Y., Pietrinferni A., Catelan M., Salaris M., 2007, *ApJ*, **661**, 1094
- Choi J., Dotter A., Conroy C., Cantiello M., Paxton B., Johnson B. D., 2016, *ApJ*, **823**, 102
- Christensen-Dalsgaard J., 2012, *Astronomische Nachrichten*, **333**, 914
- Christensen-Dalsgaard J., Dappen W., Lebreton Y., 1988, *Nature*, **336**, 634
- Christensen-Dalsgaard J., Thompson M. J., Gough D. O., 1989, *MNRAS*, **238**, 481
- Christensen-Dalsgaard J., et al., 1996, *Science*, **272**, 1286
- Christensen-Dalsgaard J., et al., 2020, *A&A*, **635**, A165
- Claret A., Torres G., 2018, *ApJ*, **859**, 100
- Compton D. L., Bedding T. R., Ball W. H., Stello D., Huber D., White T. R., Kjeldsen H., 2018, *MNRAS*, **479**, 4416
- Corsaro E., et al., 2012, *ApJ*, **757**, 190
- Cunha M. S., et al., 2021, *MNRAS*, **508**, 5864
- Dréau G., Mosser B., Lebreton Y., Gehan C., Kallinger T., 2021, *A&A*, **650**, A115
- Duan R. M., Zong W., Fu J. N., Chen Y. H., Hermes J. J., Vanderbosch Z. P., Ma X. Y., Charpinet S., 2021, *ApJ*, **922**, 2
- Dziembowski W. A., Paterno L., Ventura R., 1988, *A&A*, **200**, 213
- Eddington A. S., 1926, The Internal Constitution of the Stars. The University Press
- El-Badry K., Rix H.-W., Heintz T. M., 2021, *MNRAS*, **506**, 2269
- Elsworth Y., Hekker S., Basu S., Davies G. R., 2017, *MNRAS*, **466**, 3344
- Ferguson J. W., Alexander D. R., Allard F., Barman T., Bodnarik J. G., Hauschildt P. H., Heffner-Wong A., Tamanai A., 2005, *ApJ*, **623**, 585
- Furlan E., et al., 2018, *ApJ*, **861**, 149
- Gaia Collaboration et al., 2016, *A&A*, **595**, A1
- Gaia Collaboration et al., 2021, *A&A*, **649**, A1
- Gaulme P., et al., 2016, *ApJ*, **832**, 121
- Gough D. O., 1990, Comments on Helioseismic Inference. Springer-Verlag Berlin Heidelberg, p. 283, doi:10.1007/3-540-53091-6
- Green G. M., Schlafly E., Zucker C., Speagle J. S., Finkbeiner D., 2019, *ApJ*, **887**, 93
- Grigahcène A., Dupret M. A., Sousa S. G., Monteiro M. J. P. F. G., Garrido R., Scuflaire R., Gabriel M., 2012, *MNRAS*, **422**, L43
- Grundahl F., et al., 2017, *ApJ*, **836**, 142
- Guggenberger E., Hekker S., Basu S., Bellinger E., 2016, *MNRAS*, **460**, 4277
- Handberg R., Brogaard K., Miglio A., Bossini D., Elsworth Y., Slumstrup D., Davies G. R., Chaplin W. J., 2017, *MNRAS*, **472**, 979
- Hekker S., 2020, *Frontiers in Astronomy and Space Sciences*, **7**, 3
- Heney L., Vardya M. S., Bodenheimer P., 1965, *ApJ*, **142**, 841
- Herwig F., 2000, *A&A*, **360**, 952
- Hon M., Stello D., Yu J., 2017, *MNRAS*, **469**, 4578
- Houdek G., Trampedach R., Aarslev M. J., Christensen-Dalsgaard J., 2017, *MNRAS*, **464**, L124
- Houdek G., Lund M. N., Trampedach R., Christensen-Dalsgaard J., Handberg R., Appourchaux T., 2019, *MNRAS*, **487**, 595
- Howard A. W., et al., 2010, *ApJ*, **721**, 1467
- Huber D., et al., 2011, *ApJ*, **743**, 143
- Huber D., et al., 2017, *ApJ*, **844**, 102
- Hunter J. D., 2007, *Computing in Science & Engineering*, **9**, 90
- Iglesias C. A., Rogers F. J., 1993, *ApJ*, **412**, 752
- Iglesias C. A., Rogers F. J., 1996, *ApJ*, **464**, 943
- Jeffries Mark W. J., et al., 2013, *AJ*, **146**, 58
- Jiang C., Gizon L., 2021, *Research in Astronomy and Astrophysics*, **21**, 226
- Jofré E., Petrucci R., Saffe C., Saker L., Artur de la Villarmois E., Chavero C., Gómez M., Mauas P. J. D., 2015, *A&A*, **574**, A50
- Johnson J. A., et al., 2017, *AJ*, **154**, 108
- Jørgensen A. C. S., Weiss A., Mosumgaard J. R., Silva Aguirre V., Sahlholdt C. L., 2017, *MNRAS*, **472**, 3264
- Jørgensen A. C. S., Mosumgaard J. R., Weiss A., Silva Aguirre V., Christensen-Dalsgaard J., 2018, *MNRAS*, **481**, L35
- Jørgensen A. C. S., Weiss A., Angelou G., Silva Aguirre V., 2019, *MNRAS*, **484**, 5551
- Jørgensen A. C. S., et al., 2020, *MNRAS*, **495**, 4965
- Joyce M., Chaboyer B., 2018a, *ApJ*, **856**, 10
- Joyce M., Chaboyer B., 2018b, *ApJ*, **864**, 99
- Kallinger T., et al., 2010, *A&A*, **509**, A77
- Kallinger T., et al., 2012, *A&A*, **541**, A51
- Kallinger T., Beck P. G., Stello D., Garcia R. A., 2018, *A&A*, **616**, A104
- Kjeldsen H., Bedding T. R., 1995, *A&A*, **293**, 87
- Kjeldsen H., Bedding T. R., Christensen-Dalsgaard J., 2008, *ApJ*, **683**, L175
- Li Y., Bedding T. R., Li T., Bi S., Stello D., Zhou Y., White T. R., 2020a, *MNRAS*, **495**, 2363
- Li T., Bedding T. R., Christensen-Dalsgaard J., Stello D., Li Y., Keen M. A., 2020b, *MNRAS*, **495**, 3431
- Li Y., Bedding T. R., Stello D., Sharma S., Huber D., Murphy S. J., 2021a, *MNRAS*, **501**, 3162
- Li Y., Zhang Q.-s., Wu T., Su J., Chen X.-h., Lin G.-f., Guo J.-h., Liu J.-y., 2021b, *ApJ*, **916**, 107
- Li T., Li Y., Bi S., Bedding T. R., Davies G., Du M., 2022, *ApJ*, **927**, 167
- Lindgren L., et al., 2021, *A&A*, **649**, A4
- Lund M. N., et al., 2017, *ApJ*, **835**, 172
- Lyttle A. J., et al., 2021, *MNRAS*, **505**, 2427
- Magic Z., Weiss A., 2016, *A&A*, **592**, A24
- Maíz Apellániz J., Pantaleoni González M., Barbá R. H., 2021, *A&A*, **649**, A13
- Manchon L., Belkacem K., Samadi R., Sonoi T., Marques J. P. C., Ludwig H. G., Caffau E., 2018, *A&A*, **620**, A107
- McKeever J. M., Basu S., Corsaro E., 2019, *ApJ*, **874**, 180
- Mosser B., et al., 2012, *A&A*, **537**, A30
- Mosser B., et al., 2014, *A&A*, **572**, L5

Mosumgaard J. R., Jørgensen A. C. S., Weiss A., Silva Aguirre V., Christensen-Dalsgaard J., 2020, *MNRAS*, **491**, 1160

Nsamba B., Campante T. L., Monteiro M. J. P. F. G., Cunha M. S., Rendle B. M., Reese D. R., Verma K., 2018, *MNRAS*, **477**, 5052

Ong J. M. J., Basu S., Roxburgh I. W., 2021a, *ApJ*, **920**, 8

Ong J. M. J., Basu S., Lund M. N., Bieryla A., Viani L. S., Latham D. W., 2021b, *ApJ*, **922**, 18

Paxton B., Bildsten L., Dotter A., Herwig F., Lesaffre P., Timmes F., 2011, *ApJS*, **192**, 3

Paxton B., et al., 2013, *ApJS*, **208**, 4

Paxton B., et al., 2015, *ApJS*, **220**, 15

Paxton B., et al., 2018, *ApJS*, **234**, 34

Paxton B., et al., 2019, *ApJS*, **243**, 10

Petigura E. A., 2015, PhD thesis, University of California, Berkeley

Petigura E. A., et al., 2017, *AJ*, **154**, 107

Philidet J., Belkacem K., Goupil M. J., 2021, *A&A*, **656**, A95

Pinsonneault M. H., et al., 2018, *ApJS*, **239**, 32

Pols O. R., Tout C. A., Eggleton P. P., Han Z., 1995, *MNRAS*, **274**, 964

Potekhin A. Y., Chabrier G., 2010, *Contributions to Plasma Physics*, **50**, 82

Rodrigues T. S., et al., 2017, *MNRAS*, **467**, 1433

Rogers F. J., Nayfonov A., 2002, *ApJ*, **576**, 1064

Rosenthal C. S., Christensen-Dalsgaard J., Nordlund Å., Stein R. F., Trampedach R., 1999, *A&A*, **351**, 689

Sandquist E. L., et al., 2013, *ApJ*, **762**, 58

Saumon D., Chabrier G., van Horn H. M., 1995, *ApJS*, **99**, 713

Schmitt J. R., Basu S., 2015, *ApJ*, **808**, 123

Serenelli A., et al., 2017, *ApJS*, **233**, 23

Sharma S., Stello D., Bland-Hawthorn J., Huber D., Bedding T. R., 2016, *ApJ*, **822**, 15

Silva Aguirre V., et al., 2015, *MNRAS*, **452**, 2127

Sonoi T., Samadi R., Belkacem K., Ludwig H. G., Caffau E., Mosser B., 2015, *A&A*, **583**, A112

Sonoi T., Ludwig H. G., Dupret M. A., Montalbán J., Samadi R., Belkacem K., Caffau E., Goupil M. J., 2019, *A&A*, **621**, A84

Stello D., Bruntt H., Preston H., Buzasi D., 2008, *ApJ*, **674**, L53

Stello D., et al., 2010, *ApJ*, **713**, L182

Stello D., et al., 2013, *ApJ*, **765**, L14

Tayar J., et al., 2017, *ApJ*, **840**, 17

Tayar J., Claytor Z. R., Huber D., van Saders J., 2022, *ApJ*, **927**, 31

Thermon N., et al., 2018, *MNRAS*, **478**, 4669

Timmes F. X., Swesty F. D., 2000, *ApJS*, **126**, 501

Townsend R. H. D., Teitler S. A., 2013, *MNRAS*, **435**, 3406

Trampedach R., Aarslev M. J., Houdek G., Collet R., Christensen-Dalsgaard J., Stein R. F., Asplund M., 2017, *MNRAS*, **466**, L43

Ulrich R. K., 1986, *ApJ*, **306**, L37

Valle G., Dell'Omodarme M., Prada Moroni P. G., Degl'Innocenti S., 2015, *A&A*, **579**, A59

Vernazza J. E., Avrett E. H., Loeser R., 1981, *ApJS*, **45**, 635

Virtanen P., et al., 2020, *Nature Methods*, **17**, 261

Vogt S. S., et al., 1994, in Crawford D. L., Craine E. R., eds, *Society of Photo-Optical Instrumentation Engineers (SPIE) Conference Series Vol. 2198, Instrumentation in Astronomy VIII*. p. 362, doi:10.1117/12.176725

Vrard M., Mosser B., Samadi R., 2016, *A&A*, **588**, A87

Wes McKinney 2010, in Stéfan van der Walt Jarrod Millman eds, *Proceedings of the 9th Python in Science Conference*. pp 56 – 61, doi:10.25080/Majora-92bf1922-00a

White T. R., Bedding T. R., Stello D., Christensen-Dalsgaard J., Huber D., Kjeldsen H., 2011, *ApJ*, **743**, 161

Yu J., Huber D., Bedding T. R., Stello D., Hon M., Murphy S. J., Khanna S., 2018, *ApJS*, **236**, 42

Zinn J. C., 2021, *AJ*, **161**, 214

Zinn J. C., Pinsonneault M. H., Huber D., Stello D., Stassun K., Serenelli A., 2019, *ApJ*, **885**, 166

van der Walt S., Colbert S. C., Varoquaux G., 2011, *Computing in Science and Engineering*, **13**, 22

APPENDIX A: SURFACE CORRECTION WITH HOPF ATMOSPHERIC MODELS

We carried out an additional set of stellar model calculation using the solar-calibrated Hopf atmosphere (Paxton et al. 2013), which is equivalent to the fit provided by Sonoi et al. (2019) to the VAL-C model (Vernazza et al. 1981). The results are presented in Table A1. Notably, there is a significant discrepancy in the fitted coefficients between the pre-RGB and RGB samples — especially for a , which represents the amount of surface correction at ν_{\max} for a solar model. Considering the atmosphere is solar-calibrated, it may generalise poorly on RGB stars. Further studies are needed to understand its cause. To enhance the applicability of the surface correction prescription proposed in this paper, we recommend using the atmosphere calculated based on the Eddington $T-\tau$ relation rather the Hopf atmosphere.

APPENDIX B: SYSTEMATIC UNCERTAINTIES OF THE CORRECTION FACTORS

We can study two types of uncertainties arising from the calculation of the correction factor $f_{\Delta\nu}$. The first type of error is due to uncertain stellar physics. Using our surface-corrected stellar models, we can quantify the spread of $f_{\Delta\nu}$ due to the changes of Y_{init} and α_{MLT} , both of which are poorly constrained model parameters. We generated synthetic stars with the following stellar properties: L , ν_{\max} , T_{eff} , and $[M/H]$, along a $1 M_{\odot}$, solar metallicity, pre-RGB-tip evolutionary track from MIST. We assumed 2% observational uncertainties for L , 2% for ν_{\max} , 2.4% for T_{eff} , and 0.1 dex for $[M/H]$, according to their typical values (e.g. Tayar et al. 2022; Yu et al. 2018). Then we treated these properties as observational constraints and estimated $f_{\Delta\nu}$, using the fitting routine introduced in Sec. 5.1. In addition, we assigned Gaussian priors on each model based on its Y_{init} and α_{MLT} values, the results of which are shown in the top and middle panels of Fig. B1. Changing α_{MLT} clearly has a bigger impact than Y_{init} . The differences on the RGB and the main sequence are smaller than 0.5%, and in the subgiant phase ($\nu_{\max} \sim 1000 \mu\text{Hz}$) they can reach $\sim 1\%$. However, the $f_{\Delta\nu}$ itself presents a larger variation than these at most $\sim 1\%$ uncertainties (see also Fig. 7), indicating the necessity of making the correction to the $\Delta\nu$ scaling relation.

The second type of error concerns the range of modes that are used to calculate the theoretical $\Delta\nu$. We compared two approaches: one using the default range of modes involved in our work, which is $\nu_{\max} \pm 5\sigma$, and another only using the modes in the $\nu_{\max} \pm 3\Delta\nu$ range. From the bottom panel of Fig. B1, we see negligible differences, indicating that the range of modes considered (as long as larger than $3\Delta\nu$) is not a major source of uncertainty.

This paper has been typeset from a \LaTeX file prepared by the author.

Table A1. Best-fitting parameters in the surface correction prescriptions. The stellar models are calculated with $T - \tau$ integrated model atmospheres using the solar-calibrated Hopf relation.

Atmosphere Model	Sample	a	b	c	d	a'	b'	c'	d'
Hopf	Cubic All	-3.06 ± 0.10	0.96 ± 0.01	-7.14 ± 0.20	-0.88 ± 0.02	—	—	—	—
Hopf	Cubic Pre-RGB	-4.25 ± 0.28	0.50 ± 0.06	-0.98 ± 0.49	-0.49 ± 0.08	—	—	—	—
Hopf	Cubic RGB	-2.90 ± 0.10	0.97 ± 0.01	-7.68 ± 0.22	-0.91 ± 0.02	—	—	—	—
Hopf	Inverse-cubic All	-4.73 ± 0.40	0.45 ± 0.06	2.27 ± 0.43	0.66 ± 0.11	-6.01 ± 0.38	-6.01 ± 0.38	-6.01 ± 0.38	-6.01 ± 0.38
Hopf	Inverse-cubic Pre-RGB	-4.73 ± 0.40	0.45 ± 0.06	2.27 ± 0.43	0.66 ± 0.11	-6.01 ± 0.38	-6.01 ± 0.38	-6.01 ± 0.38	-6.01 ± 0.38
Hopf	Inverse-cubic RGB	-1.45 ± 0.03	0.88 ± 0.01	-10.16 ± 0.20	-0.31 ± 0.02	-2.31 ± 0.06	-2.31 ± 0.06	-2.31 ± 0.06	-2.31 ± 0.06

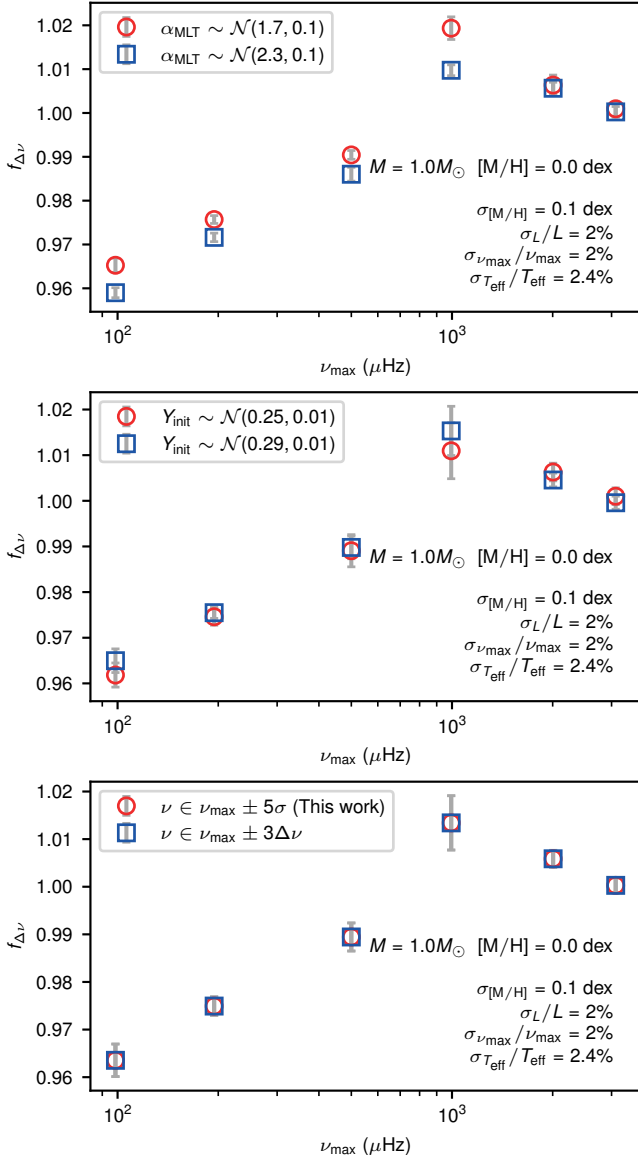


Figure B1. Changes of theoretical $f_{\Delta\nu}$ due to the choices of priors on α_{MLT} and Y_{init} (top and middle panels) and the ranges of modes to be included when calculating model $\Delta\nu$ (bottom panel).

6 Testing the ν_{\max} scaling relation with individual frequency modelling

The paper produced in this chapter is in the final stage of preparation and will be submitted to a peer-review journal. The work is a collaborative effort. I performed the observational data analysis and stellar modelling. I and Tim Bedding contributed to most experiments in this work. Dennis Stello and Daniel Huber interpreted the results. I wrote the manuscript, and the other authors have not yet commented on it.

Testing the ν_{\max} Scaling Relation with Individual Frequency Modelling

YAGUANG LI (李亚光) ^{1,*} TIMOTHY R. BEDDING ^{1,†} DENNIS STELLO ² AND DANIEL HUBER ³

¹*Sydney Institute for Astronomy (SIfA), School of Physics, University of Sydney, NSW 2006, Australia*

²*School of Physics, University of New South Wales, 2052, Australia*

³*Institute for Astronomy, University of Hawai‘i, 2680 Woodlawn Drive, Honolulu, HI 96822, USA*

ABSTRACT

The frequency of maximum power, ν_{\max} , in solar-like oscillations is thought to scale with the surface gravity and temperature as $\nu_{\max} \propto g/\sqrt{T_{\text{eff}}}$, though the basis for this relation is not well understood due to a lack of knowledge on the excitation mechanism. In this study, we used individual frequency modelling to homogeneously derive the scaling ν_{\max} and compared it to the actual ν_{\max} observed from oscillation spectra. We found that there is a strong degeneracy between the model-derived scaling ν_{\max} and the mixing length parameter, which can be lifted using calibrations with the dynamical properties of eclipsing binaries. Remarkably, we discovered that the ν_{\max} scaling relation holds very well after accounting for this correlation, and it shows no significant dependency on metallicity within the observational uncertainties. We also discussed the implication for estimating stellar properties. Both ν_{\max} and individual frequencies can provide strong constraints on stellar mass and radius, with precision of 2% and 1%, respectively. Yet, individual frequencies are better at constraining age, with precision of 10% compared to 35% from using ν_{\max} . When both sets of information are combined, we are able to achieve precision of 0.5% for mass, 0.1% for radius, and 5% for age. This is a regime where systematic uncertainties may dominate the error budget.

Keywords: stars: oscillations (including pulsations)

1. INTRODUCTION

Solar-like oscillations in solar-type stars and red giants are driven by near-surface convection. These oscillations manifest as peaks in the power spectrum of the star, with amplitudes that are modulated by a near-Gaussian envelope centred at a specific frequency known as the frequency of maximum power ν_{\max} .

Since ν_{\max} varies across the Hertzsprung–Russell (H–R) diagram, it carries important information about stellar properties. The ν_{\max} scaling relation was first proposed by Brown et al. (1991) as a roughly fixed fraction of the acoustic cutoff frequency, ν_{ac} , which in the stellar atmosphere, scales as $\nu_{\text{ac}} \propto g/\sqrt{T_{\text{eff}}}$, where g is the surface gravity and T_{eff} is the effective temperature. In the solar photosphere ν_{ac} is about 5500 μHz , whereas ν_{\max} is about 3090 μHz . Kjeldsen & Bedding (1995) further assumed that stars have similar structures as the Sun and scaled the relation using the solar values (see also

Belkacem et al. 2011):

$$\frac{\nu_{\max}}{\nu_{\max,\odot}} \approx \left(\frac{M}{M_{\odot}}\right) \left(\frac{R}{R_{\odot}}\right)^{-2} \left(\frac{T_{\text{eff}}}{T_{\text{eff},\odot}}\right)^{-1/2}, \quad (1)$$

where $\nu_{\max,\odot} = 3090 \mu\text{Hz}$, and $T_{\text{eff},\odot} = 5772 \text{ K}$.

One question that arises is whether the standard scaling relation holds true for all stars. In other words, does the ratio of the true frequency of maximum power, $\nu_{\max,\text{true}}$ to the frequency predicted by the scaling relation, $\nu_{\max,\text{scaling}}$ deviate from unity? This deviation can be quantified by the factor $f_{\nu_{\max}}$ (Sharma et al. 2011), which is determined by the equation:

$$\nu_{\max,\text{true}} = f_{\nu_{\max}} \nu_{\max,\text{scaling}}. \quad (2)$$

Examining this $f_{\nu_{\max}}$ is the aim of this work. We derive $\nu_{\max,\text{scaling}}$ by modelling individual frequencies, and compare it with $\nu_{\max,\text{true}}$, which is measured from observations.

2. DATA ANALYSIS

2.1. Observations

* e-mail: yaguang.li@sydney.edu.au

† e-mail: tim.bedding@sydney.edu.au

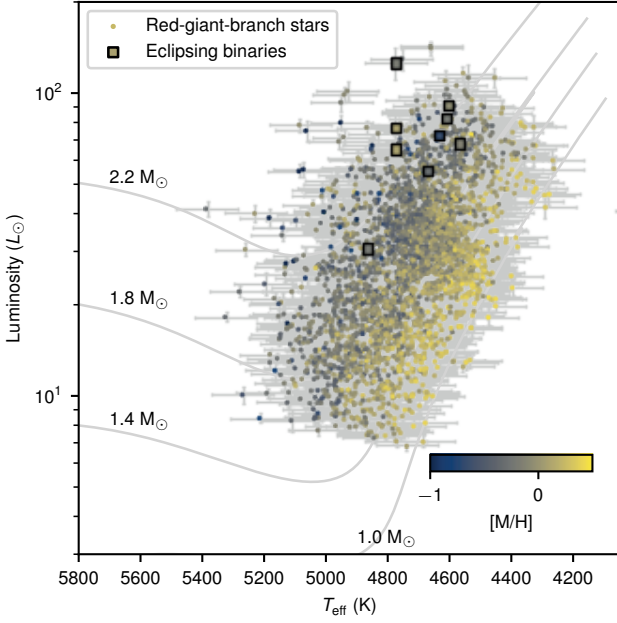


Figure 1. H–R diagram showing the sample used in this work, colour-coded by metallicity.

We used the RGB sample observed by *Kepler* and APOGEE (Pinsonneault et al. 2018). We collected ν_{\max} extracted by the SYD pipeline (Yu et al. 2018), oscillation frequencies ($l = 0, 2$) extracted by Kallinger (2019), $l = 1$ g-mode period spacings ($\Delta\Pi_1$) from Vrad et al. (2016), T_{eff} determined using the IRFM method calibrated by Casagrande et al. (2021), $[M/H]$ from APOGEE (Abdurro’uf et al. 2022), and luminosities determined with *J*-band magnitudes (Cutri et al. 2003), Green et al. (2019) extinctions, Choi et al. (2016) bolometric corrections and *Gaia* DR3 distances (Bailer-Jones et al. 2021).

2.2. Stellar models

We constructed a new grid of stellar models with MESA (version r15140; Paxton et al. 2011, 2013, 2015, 2018, 2019) and GRYE (version 6.0.1; Townsend & Teitler 2013), using the same input physics described in Li et al. (2022), except for two differences noted below. Firstly, the new models considered possible variations in the convective overshoot. We set an exponential overshooting scheme for all convective boundaries. Hence, in addition to stellar mass, metallicity, initial helium abundance, and mixing length parameter, the initial free parameters for the grid also include core overshoot $f_{\text{core}} \in (0., 0.02)$ and envelope overshoot $f_{\text{env}} \in (0., 0.008)$.

Secondly, the new models calculated radial modes and decomposed pure p modes for quadrupolar modes (the so-called π modes) using the method introduced by Ong

& Basu (2020). We considered the $l = 2$ modes because the spacing between $l = 0$ and $l = 2$ modes, or known as the small separation, correlates well with stellar mass and could provide crucial constraints on stellar properties (Kallinger et al. 2012; Montalbán et al. 2010).

2.3. Model fitting

We used the same framework described in Li et al. (2022) to perform model fitting. We corrected the surface effect in an ensemble approach, with benefits of eliminating unrealistic surface correction and reducing scatter in model-derived properties. This was done by parameterising the amount of surface correction at ν_{\max} , $\delta\nu_m$, and that at $1.1\nu_{\max}$, $\delta\nu'_m$, as functions of stellar surface properties:

$$\delta\nu_m = a \cdot (g/g_\odot)^b \cdot (T_{\text{eff}}/T_{\text{eff},\odot})^c \cdot (d \cdot [M/H] + 1), \quad (3)$$

and

$$\delta\nu'_m = a' \cdot (g/g_\odot)^{b'} \cdot (T_{\text{eff}}/T_{\text{eff},\odot})^{c'} \cdot (d' \cdot [M/H] + 1), \quad (4)$$

The free parameters $\{a, b, c, d, a', b', c', d'\}$ were fitted to the stellar models used in this work and the best fitting parameters are $\{-6.11, 0.79, -5.04, -0.79, -7.69, 0.79, -4.59, -0.87\}$. These two equations were then used to deduce the surface terms in the inverse-cubic formula (Ball & Gizon 2014).

We used both classical constraints (L) and seismic constraints ($l = 0$ and 2 oscillation frequencies) to constrain stellar models. The inferred parameters were determined from the marginalised probability functions.

3. RESULTS AND DISCUSSIONS

3.1. Degeneracies between the model-inferred scaling ν_{\max} and the mixing length

Our results suggest that the uncertainty in the mixing length parameter (α_{MLT}) limits the precision with which we can predict ν_{\max} . In Figure 2, we show the posterior probabilities for α_{MLT} and scaling ν_{\max} estimated for one example star, constrained by $[M/H]$, T_{eff} , L , $\nu_{l=0}$, and $\nu_{l=2}$. The figure illustrates that there is a strong correlation between α_{MLT} and ν_{\max} . Even when we added the constraint of the period spacing of dipole modes, $\Delta\Pi_1$, the correlation persisted. This leads us to conclude that the value of ν_{\max} cannot be accurately predicted from individual frequencies without knowing α_{MLT} . This is likely because individual frequencies are sensitive to the interior of the star, where α_{MLT} has less impact, compared to the surface.

It is not surprising that α_{MLT} is a challenge in stellar modelling. Previous studies have identified a correlation between α_{MLT} and metallicity (Tayar et al.

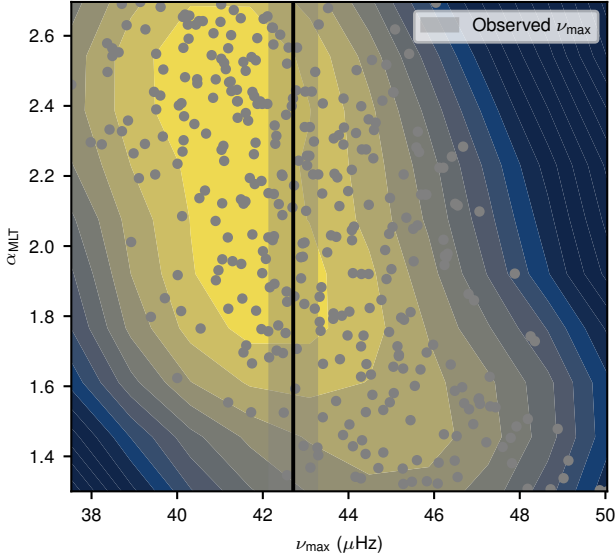


Figure 2. Correlation between the modelled ν_{max} (based on the scaling relation) and the mixing length parameter. The contours are the Gaussian kernel density estimate of the probability distributions with a bandwidth of 0.1 after a min-max normalization. The stellar models used for this estimate are shown in points. The star shown in this example is KIC 12735851.

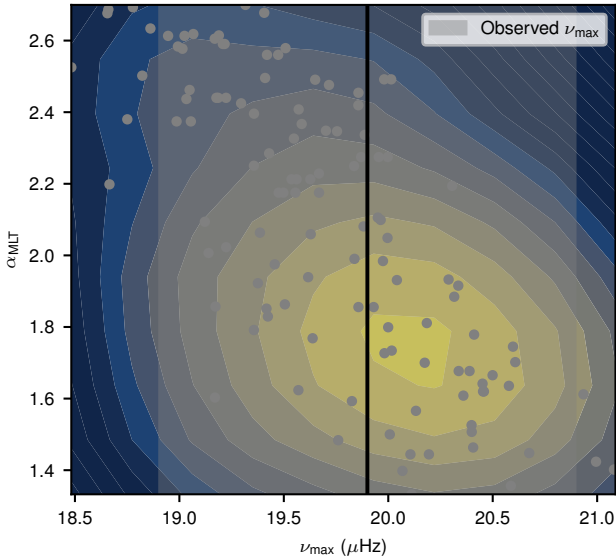


Figure 3. Same as Fig. 2, but for KIC 10001167, modelled using its dynamical properties from eclipsing binary modelling.

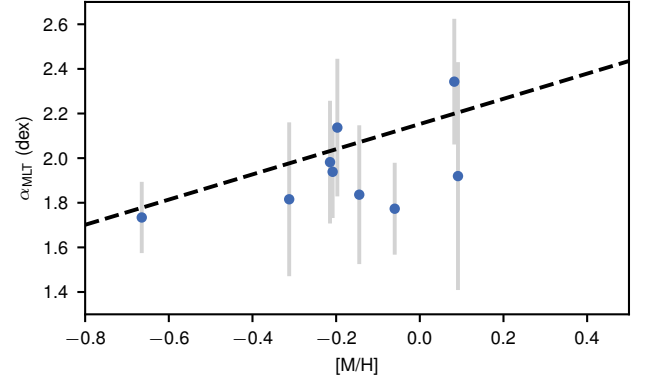


Figure 4. Mixing length parameter, α_{MLT} , vs. $[M/H]$ estimated for the eclipsing binaries.

ings highlight the need for adapting the value of α_{MLT} to different metallicities. Valle et al. (2019) suggested that the classical constraints (T_{eff} , $[M/H]$) and global oscillation parameters ($\Delta\nu$, ν_{max}) are not sufficient for accurately calibrating α_{MLT} . To complicate matters further, 3D hydrodynamic simulations of the stellar surface also indicate that α_{MLT} should be adjusted, but the magnitude of the adjustment inferred from these simulations differs significantly from that inferred from 1D models, suggesting that the values of α_{MLT} inferred from these two approaches could be fundamentally incompatible (Trampedach et al. 2014; Magic et al. 2015).

Here, we demonstrate that the dynamical properties of eclipsing binaries may provide a way to calibrate the mixing length parameter (α_{MLT}). In Figure 3, we show the probabilities estimated for an eclipsing binary in our sample, with additional constraints on the mass and radius obtained from its orbit. The strong correlation between α_{MLT} and ν_{max} seen in Figure 2 is largely eliminated, and the value of α_{MLT} is well constrained. In Figure 4, we show the estimated value of α_{MLT} as a function of $[M/H]$ for all asteroseismic eclipsing binaries in our sample. Although our sample size is limited, we observe a positive correlation between α_{MLT} and $[M/H]$, which is consistent with previous findings (Tayar et al. 2017; Viani et al. 2018). We provided a linear fit to this relation:

$$\alpha_{\text{MLT}} = 0.56 [M/H] + 2.15. \quad (5)$$

We encourage future studies to establish this relation when more asteroseismic binaries are discovered.

3.2. Testing the scaling relation

Given the limitations discussed earlier, what can we conclude about the ν_{max} scaling relation? In Figure 5, we show the revision factor of the ν_{max} scaling relation, $f_{\nu_{\text{max}}}$, as a function of mass, ν_{max} , $[M/H]$, and α_{MLT} .

2017), which, if left unaccounted for, can have significant implications for determining stellar ages. Joyce & Chaboyer (2018) also demonstrated that models with a solar-calibrated value of α_{MLT} are unable to reproduce the observed properties of metal-poor stars. These find-

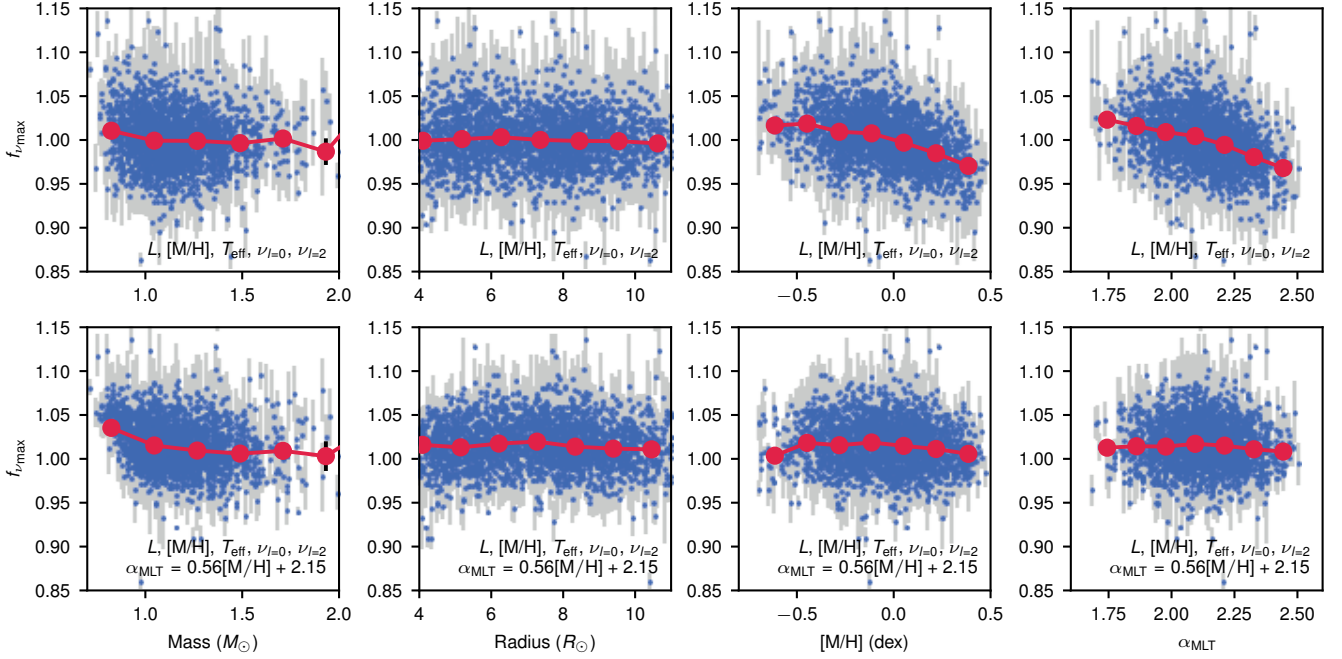


Figure 5. Deviation of the ν_{\max} scaling relation, $f_{\nu_{\max}}$, vs. mass, radius, $[M/H]$, and α_{MLT} . The top rows show the modelling results without imposing informative priors on α_{MLT} , and the bottom rows assuming the values of α_{MLT} calibrated from the eclipsing binaries.

The top row shows the relations using the directly returned $f_{\nu_{\max}}$ from the modelling. It appears that one might wrongly conclude that there is a dependency of ν_{\max} on $[M/H]$, which can be explained by the degeneracy with α_{MLT} shown in the rightmost panel. However, if we enforce the fitted relation from Equation 5, this dependence disappears, as shown in the bottom rows. Within the current observational uncertainties, the ν_{\max} scaling relation remains valid.

Our results, which show no departure from the standard scaling relation, are consistent with those of Coelho et al. (2015), who modelled stars using $\Delta\nu$, T_{eff} , and $[M/H]$ as input constraints. Zinn et al. (2019) also compared the radii derived from the scaling relation to Gaia radii and did not find any departure from the scaling relation at low metallicities. These studies suggest that the trend in metallicity reported in Epstein et al. (2014) may be due to an incorrect temperature scale in the metal-poor regime, potentially caused by a lack of T_{eff} calibrations.

However, our results are in some tension with theoretical studies that have suggested that the ν_{\max} scaling relation should include a term for $[M/H]$, based on the dependence of the acoustic cutoff frequency, ν_{ac} , on the first adiabatic exponent and the mean molecular weight (Jiménez et al. 2015; Yıldız et al. 2016; Viani et al. 2017). These quantities depend on $[M/H]$, leading to the prediction of a monotonic increase by more than 2% in ν_{\max}

when changing $[M/H]$ from -0.5 to 0.5 (Viani et al. 2017). This trend is not observed in our data. One possible explanation is that ν_{\max} may relate to ν_{ac} in a way that has not been considered in previous studies.

3.3. Implications on fundamental stellar properties

As we discussed in Section 3.1, it is not possible to predict ν_{\max} with sufficient precision using only the individual frequencies, due to the uncertainty in the mixing length parameter (α_{MLT}). This finding also suggests that ν_{\max} carries information that is distinct from that contained in the individual frequencies. The question we now explore is: what are the implications for estimating fundamental stellar properties?

In Figure 6, we show the median relative uncertainties obtained for mass, radius, and age using various combinations of seismic constraints. Firstly, it is evident that there is a natural decrease in uncertainties when adding $l = 2$ modes and the $l = 1$ period spacings, due to the increased information content. Secondly, comparing the combination of ($\nu_{l=0}$, $\nu_{l=2}$, $\Delta\Pi_1$) and the traditional grid-modelling method that is based on the $\Delta\nu$ and ν_{\max} scaling relation ($\Delta\nu$, ν_{\max}), we notice that the uncertainties obtained for mass and radius are similar (3% and 1%, respectively), but the scaling-relation-based age uncertainty is around 30% while the individual frequency-based age uncertainty is under 20%, and even reaches 10% when g-mode period spacing is con-

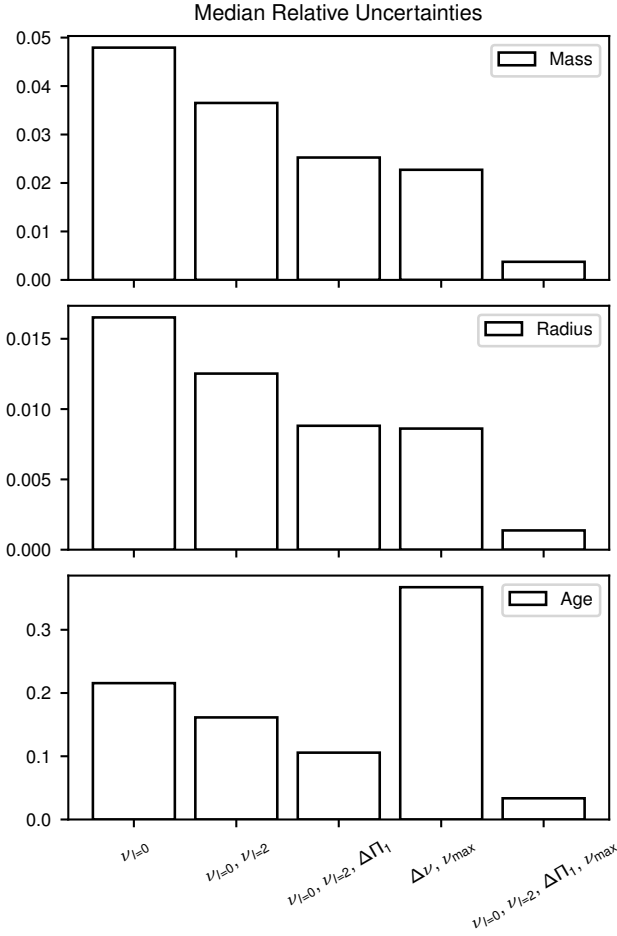


Figure 6. Median relative uncertainties of fundamental stellar properties, estimated from different combinations of seismic constraints indicated in the labels, in addition to the usual classical constraints T_{eff} , $[M/H]$ and L .

sidered. This indicates that while the scaling relation is sufficient to derive mass and radius, the individual frequencies are much more useful for determining ages. Finally, by combining all seismic information available, the precision for mass, radius, and age all reaches minimal levels, which likely exceeds the typical accuracy level that is dominated by systematic uncertainties arising from calculations of model physics (Silva Aguirre et al. 2017; Tayar et al. 2022; Huber et al. 2022). Future investigations are need to characterise the level of these uncertainties.

4. CONCLUSIONS

In this paper, we tested the ν_{\max} scaling relation, $\nu_{\max} \propto g/\sqrt{T_{\text{eff}}}$, using individual frequency modelling. Our main findings are summarised below:

1. The prediction of scaling ν_{\max} from individual frequencies is limited by uncertainties in the mixing length parameter, which can be calibrated using the dynamical properties of eclipsing binaries.
2. The value of ν_{\max} shows no departure beyond the standard scaling relation and no dependency on metallicity within the observational uncertainties.
3. Both ν_{\max} and individual frequencies can provide strong constraints on stellar mass and radius, but individual frequencies are able to provide age with three times better precision compared to using the $\Delta\nu$ and ν_{\max} scaling relations.
4. When both ν_{\max} and individual frequencies are used, we are able to achieve precision of 0.5% for mass, 0.1% for radius, and 5% for age.

Funding for the Kepler mission is provided by the NASA Science Mission Directorate. This paper includes data collected by the Kepler mission and obtained from the MAST data archive at the Space Telescope Science Institute (STScI). STScI is operated by the Association of Universities for Research in Astronomy, Inc., under NASA contract NAS 5-26555.

This work presents results from the European Space Agency (ESA) space mission Gaia. Gaia data are being processed by the Gaia Data Processing and Analysis Consortium (DPAC). Funding for the DPAC is provided by national institutions, in particular the institutions participating in the Gaia MultiLateral Agreement (MLA).

The APOGEE data is from the Sloan Digital Sky Survey IV, whose funding has been provided by the Alfred P. Sloan Foundation, the U.S. Department of Energy Office of Science, and the Participating Institutions.

We acknowledge the Sydney Informatics, the University of Sydney's high performance computing (HPC) cluster Artemis, and the School of Physics HPC cluster headnode for providing the HPC resources that have contributed to the research results reported within this paper.

Software: Numpy (van der Walt et al. 2011), Scipy (Virtanen et al. 2020), Matplotlib (Hunter 2007), Astropy (Astropy Collaboration et al. 2013, 2018), Pandas (Wes McKinney 2010), MESA (Paxton et al. 2011, 2013, 2015, 2018, 2019), MESASDK (Townsend 2020), GYRE (Townsend & Teitler 2013), pySYD (Chontos et al. 2021), Lightkurve (Lightkurve Collaboration et al. 2018), ISOCCLASSIFY (Huber et al. 2017; Berger et al. 2020), colte (Casagrande et al. 2021). The scripts and MESA inlists used in this work will be available at GitHub.

REFERENCES

- Abdurro'uf, Accetta, K., Aerts, C., et al. 2022, *ApJS*, 259, 35, doi: [10.3847/1538-4365/ac4414](https://doi.org/10.3847/1538-4365/ac4414)
- Astropy Collaboration, Robitaille, T. P., Tollerud, E. J., et al. 2013, *A&A*, 558, A33, doi: [10.1051/0004-6361/201322068](https://doi.org/10.1051/0004-6361/201322068)
- Astropy Collaboration, Price-Whelan, A. M., Sipőcz, B. M., et al. 2018, *AJ*, 156, 123, doi: [10.3847/1538-3881/aabc4f](https://doi.org/10.3847/1538-3881/aabc4f)
- Bailer-Jones, C. A. L., Rybizki, J., Fouesneau, M., Demleitner, M., & Andrae, R. 2021, *AJ*, 161, 147, doi: [10.3847/1538-3881/abd806](https://doi.org/10.3847/1538-3881/abd806)
- Ball, W. H., & Gizon, L. 2014, *A&A*, 568, A123, doi: [10.1051/0004-6361/201424325](https://doi.org/10.1051/0004-6361/201424325)
- Belkacem, K., Goupil, M. J., Dupret, M. A., et al. 2011, *A&A*, 530, A142, doi: [10.1051/0004-6361/201116490](https://doi.org/10.1051/0004-6361/201116490)
- Berger, T. A., Huber, D., van Saders, J. L., et al. 2020, *AJ*, 159, 280, doi: [10.3847/1538-3881/159/6/280](https://doi.org/10.3847/1538-3881/159/6/280)
- Brown, T. M., Gilliland, R. L., Noyes, R. W., & Ramsey, L. W. 1991, *ApJ*, 368, 599, doi: [10.1086/169725](https://doi.org/10.1086/169725)
- Casagrande, L., Lin, J., Rains, A. D., et al. 2021, *MNRAS*, 507, 2684, doi: [10.1093/mnras/stab2304](https://doi.org/10.1093/mnras/stab2304)
- Choi, J., Dotter, A., Conroy, C., et al. 2016, *ApJ*, 823, 102, doi: [10.3847/0004-637X/823/2/102](https://doi.org/10.3847/0004-637X/823/2/102)
- Chontos, A., Huber, D., Sayeed, M., & Yamsiri, P. 2021, arXiv e-prints, arXiv:2108.00582. <https://arxiv.org/abs/2108.00582>
- Coelho, H. R., Chaplin, W. J., Basu, S., et al. 2015, *MNRAS*, 451, 3011, doi: [10.1093/mnras/stv1175](https://doi.org/10.1093/mnras/stv1175)
- Cutri, R. M., Skrutskie, M. F., van Dyk, S., et al. 2003, 2MASS All Sky Catalog of point sources.
- Epstein, C. R., Elsworth, Y. P., Johnson, J. A., et al. 2014, *ApJL*, 785, L28, doi: [10.1088/2041-8205/785/2/L28](https://doi.org/10.1088/2041-8205/785/2/L28)
- Green, G. M., Schlafly, E., Zucker, C., Speagle, J. S., & Finkbeiner, D. 2019, *ApJ*, 887, 93, doi: [10.3847/1538-4357/ab5362](https://doi.org/10.3847/1538-4357/ab5362)
- Huber, D., Zinn, J., Bojsen-Hansen, M., et al. 2017, *ApJ*, 844, 102, doi: [10.3847/1538-4357/aa75ca](https://doi.org/10.3847/1538-4357/aa75ca)
- Huber, D., White, T. R., Metcalfe, T. S., et al. 2022, *AJ*, 163, 79, doi: [10.3847/1538-3881/ac3000](https://doi.org/10.3847/1538-3881/ac3000)
- Hunter, J. D. 2007, *Computing in Science & Engineering*, 9, 90, doi: [10.1109/MCSE.2007.55](https://doi.org/10.1109/MCSE.2007.55)
- Jiménez, A., García, R. A., Pérez Hernández, F., & Mathur, S. 2015, *A&A*, 583, A74, doi: [10.1051/0004-6361/201526469](https://doi.org/10.1051/0004-6361/201526469)
- Joyce, M., & Chaboyer, B. 2018, *ApJ*, 856, 10, doi: [10.3847/1538-4357/aab200](https://doi.org/10.3847/1538-4357/aab200)
- Kallinger, T. 2019, arXiv e-prints, arXiv:1906.09428. <https://arxiv.org/abs/1906.09428>
- Kallinger, T., Hekker, S., Mosser, B., et al. 2012, *A&A*, 541, A51, doi: [10.1051/0004-6361/201218854](https://doi.org/10.1051/0004-6361/201218854)
- Kjeldsen, H., & Bedding, T. R. 1995, *A&A*, 293, 87. <https://arxiv.org/abs/astro-ph/9403015>
- Li, Y., Bedding, T. R., Stello, D., et al. 2022, arXiv e-prints, arXiv:2208.01176. <https://arxiv.org/abs/2208.01176>
- Lightkurve Collaboration, Cardoso, J. V. d. M., Hedges, C., et al. 2018, Lightkurve: Kepler and TESS time series analysis in Python, Astrophysics Source Code Library. <http://ascl.net/1812.013>
- Magic, Z., Weiss, A., & Asplund, M. 2015, *A&A*, 573, A89, doi: [10.1051/0004-6361/201423760](https://doi.org/10.1051/0004-6361/201423760)
- Montalbán, J., Miglio, A., Noels, A., Scuflaire, R., & Ventura, P. 2010, *ApJL*, 721, L182, doi: [10.1088/2041-8205/721/2/L182](https://doi.org/10.1088/2041-8205/721/2/L182)
- Ong, J. M. J., & Basu, S. 2020, *ApJ*, 898, 127, doi: [10.3847/1538-4357/ab9ffb](https://doi.org/10.3847/1538-4357/ab9ffb)
- Paxton, B., Bildsten, L., Dotter, A., et al. 2011, *ApJS*, 192, 3, doi: [10.1088/0067-0049/192/1/3](https://doi.org/10.1088/0067-0049/192/1/3)
- Paxton, B., Cantiello, M., Arras, P., et al. 2013, *ApJS*, 208, 4, doi: [10.1088/0067-0049/208/1/4](https://doi.org/10.1088/0067-0049/208/1/4)
- Paxton, B., Marchant, P., Schwab, J., et al. 2015, *ApJS*, 220, 15, doi: [10.1088/0067-0049/220/1/15](https://doi.org/10.1088/0067-0049/220/1/15)
- Paxton, B., Schwab, J., Bauer, E. B., et al. 2018, *ApJS*, 234, 34, doi: [10.3847/1538-4365/aaa5a8](https://doi.org/10.3847/1538-4365/aaa5a8)
- Paxton, B., Smolec, R., Schwab, J., et al. 2019, *ApJS*, 243, 10, doi: [10.3847/1538-4365/ab2241](https://doi.org/10.3847/1538-4365/ab2241)
- Pinsonneault, M. H., Elsworth, Y. P., Tayar, J., et al. 2018, *ApJS*, 239, 32, doi: [10.3847/1538-4365/aaebfd](https://doi.org/10.3847/1538-4365/aaebfd)
- Sharma, S., Bland-Hawthorn, J., Johnston, K. V., & Binney, J. 2011, *ApJ*, 730, 3, doi: [10.1088/0004-637X/730/1/3](https://doi.org/10.1088/0004-637X/730/1/3)
- Silva Aguirre, V., Lund, M. N., Antia, H. M., et al. 2017, *ApJ*, 835, 173, doi: [10.3847/1538-4357/835/2/173](https://doi.org/10.3847/1538-4357/835/2/173)
- Tayar, J., Claytor, Z. R., Huber, D., & van Saders, J. 2022, *ApJ*, 927, 31, doi: [10.3847/1538-4357/ac4bbc](https://doi.org/10.3847/1538-4357/ac4bbc)
- Tayar, J., Somers, G., Pinsonneault, M. H., et al. 2017, *ApJ*, 840, 17, doi: [10.3847/1538-4357/aa6a1e](https://doi.org/10.3847/1538-4357/aa6a1e)
- Townsend, R. 2020, MESA SDK for Linux, 20.3.1, Zenodo, doi: [10.5281/zenodo.3706650](https://doi.org/10.5281/zenodo.3706650)
- Townsend, R. H. D., & Teitler, S. A. 2013, *MNRAS*, 435, 3406, doi: [10.1093/mnras/stt1533](https://doi.org/10.1093/mnras/stt1533)
- Trampedach, R., Stein, R. F., Christensen-Dalsgaard, J., Nordlund, Å., & Asplund, M. 2014, *MNRAS*, 445, 4366, doi: [10.1093/mnras/stu2084](https://doi.org/10.1093/mnras/stu2084)
- Valle, G., Dell'Omodarme, M., Prada Moroni, P. G., & Degl'Innocenti, S. 2019, *A&A*, 623, A59, doi: [10.1051/0004-6361/201834949](https://doi.org/10.1051/0004-6361/201834949)
- van der Walt, S., Colbert, S. C., & Varoquaux, G. 2011, *Computing in Science and Engineering*, 13, 22, doi: [10.1109/MCSE.2011.37](https://doi.org/10.1109/MCSE.2011.37)

- 391 Viani, L. S., Basu, S., Chaplin, W. J., Davies, G. R., &
392 Elsworth, Y. 2017, *ApJ*, 843, 11,
393 doi: [10.3847/1538-4357/aa729c](https://doi.org/10.3847/1538-4357/aa729c)
- 394 Viani, L. S., Basu, S., Ong J., M. J., Bonaca, A., & Chaplin,
395 W. J. 2018, *ApJ*, 858, 28, doi: [10.3847/1538-4357/aab7eb](https://doi.org/10.3847/1538-4357/aab7eb)
- 396 Virtanen, P., Gommers, R., Oliphant, T. E., et al. 2020,
397 *Nature Methods*, 17, 261,
398 doi: <https://doi.org/10.1038/s41592-019-0686-2>
- 399 Vrad, M., Mosser, B., & Samadi, R. 2016, *A&A*, 588, A87,
400 doi: [10.1051/0004-6361/201527259](https://doi.org/10.1051/0004-6361/201527259)
- 401 Wes McKinney. 2010, in *Proceedings of the 9th Python in*
402 *Science Conference*, ed. Stéfan van der Walt & Jarrod
403 Millman, 56 – 61, doi: [10.25080/Majora-92bf1922-00a](https://doi.org/10.25080/Majora-92bf1922-00a)
- 404 Yıldız, M., Çelik Orhan, Z., & Kayhan, C. 2016, *MNRAS*,
405 462, 1577, doi: [10.1093/mnras/stw1709](https://doi.org/10.1093/mnras/stw1709)
- 406 Yu, J., Huber, D., Bedding, T. R., et al. 2018, *ApJS*, 236,
407 42, doi: [10.3847/1538-4365/aaaf74](https://doi.org/10.3847/1538-4365/aaaf74)
- 408 Zinn, J. C., Pinsonneault, M. H., Huber, D., et al. 2019,
409 *ApJ*, 885, 166, doi: [10.3847/1538-4357/ab44a9](https://doi.org/10.3847/1538-4357/ab44a9)

7 Discovery of post-mass-transfer helium-burning red giant stars

The paper produced in this chapter is published as [Li, Yaguang et al. \(2022c\)](#). I performed the observational data analysis and stellar modelling. I, Tim Bedding, Simon Murphy, and Dennis Stello contributed to most experiments in this paper. Yifan Chen verified the $\Delta\nu$ and ν_{\max} calculations. Daniel Huber and Daniel R. Hey contributed to the statistical analysis of binaries. Meridith Joyce and Dion Marks helped construct stellar models. Xianfei Zhang and Shaolan Bi contributed to the theoretical analysis of binary evolution. Isabel Colman provided the light curves for stars in *Kepler* open clusters. Michael Hayden, Ben Montet, Sanjib Sharma and Yaqian Wu interpreted the chemical abundances. Sanjib Sharma also provided the *Galaxia* synthetic sample. Gang Li analysed the rotational splittings. I wrote the paper, and all authors (especially Tim Bedding, Simon Murphy and Dennis Stello) commented on the manuscript.



Discovery of post-mass-transfer helium-burning red giants using asteroseismology

Yaguang Li^{1,2}✉, Timothy R. Bedding^{1,2}✉, Simon J. Murphy^{1,2}, Dennis Stello^{2,3}, Yifan Chen¹, Daniel Huber⁴, Meridith Joyce⁵, Dion Marks¹, Xianfei Zhang⁶, Shaolan Bi⁶, Isabel L. Colman⁷, Michael R. Hayden¹, Daniel R. Hey^{1,2}, Gang Li⁸, Benjamin T. Montet^{3,9}, Sanjib Sharma¹ and Yaqian Wu¹⁰

A star expands to become a red giant when it has fused all the hydrogen in its core into helium. If the star is in a binary system, its envelope can overflow onto its companion or be ejected into space, leaving a hot core and potentially forming a subdwarf B star^{1–3}. However, most red giants that have partially transferred envelopes in this way remain cool on the surface and are almost indistinguishable from those that have not. Among ~7,000 helium-burning red giants observed by NASA's Kepler mission, we use asteroseismology to identify two classes of stars that must have undergone considerable mass loss, presumably due to stripping in binary interactions. The first class comprises about seven underluminous stars with smaller helium-burning cores than their single-star counterparts. Theoretical models show that these small cores imply the stars had much larger masses when ascending the red giant branch. The second class consists of 32 red giants with masses down to $0.5 M_{\odot}$, whose implied ages would exceed the age of the universe had no mass loss occurred. The numbers are consistent with binary statistics, and our results open up new possibilities to study the evolution of post-mass-transfer binary systems.

Mass loss in red giant stars remains one of the major uncertainties in stellar physics. A hydrogen-shell-burning red giant branch (RGB) star will reach its maximum luminosity at the tip of the RGB, where substantial mass loss occurs^{4,5}. It then starts the core-helium-burning (CHeB) phase at a much lower luminosity. Recent studies suggest that the accumulated mass loss driven by pulsation and radiation on the RGB can reduce the stellar mass by up to $0.1 M_{\odot}$, on the basis of asteroseismic observations of field stars^{6,7} and open clusters^{8–10}. In contrast, globular clusters tend to suggest a loss in mass of about $0.2 M_{\odot}$ on the RGB on the basis of the morphology of the horizontal branch on the Hertzsprung–Russell diagram^{11–13}, although the accuracy of photometric masses is still being debated¹⁴. Even greater changes in mass can occur during binary interactions, via stable Roche lobe overflow, common envelope ejection, or merging¹⁵.

The fate of an RGB star in a binary system can vary markedly, depending on the system's dynamical properties and hence the mass-transfer rate. If the star loses its entire hydrogen-rich envelope before reaching the RGB tip, it leaves a bare non-burning helium

core, forming a low-mass white dwarf^{16–18} ($M/M_{\odot} < 0.5$; M is the stellar mass). On the other hand, a stripped CHeB red giant could form a hot subluminous star of spectral type B (sdB) on the extreme horizontal branch^{2,3,19,20}. Indeed, most sdB stars are found to be in binary systems with short periods^{21–23}. Some stripped CHeB stars are found in binary systems with a Be star (B star with a circumstellar disk) as the companion^{24–26}, suggesting a mass-transfer history. However, there has been little success in finding CHeB red giant stars that have only partially transferred their envelopes, except in a few open clusters, where an anomaly in stellar mass is more easily identified^{10,27}.

To find these post-mass-transfer CHeB stars among the red giants observed by Kepler, we used asteroseismology to derive stellar parameters and evolutionary phases (Methods). According to the asteroseismic scaling relations^{28–30}, the so-called large frequency separation scales with the mean density, $\Delta\nu \propto M^{1/2} R^{-3/2}$ (R is the stellar radius), and the frequency of maximum oscillation power is proportional to the surface properties, $\nu_{\max} \propto g/\sqrt{T_{\text{eff}}} \propto MR^{-2} T_{\text{eff}}^{-1/2}$ (g is the surface gravity, T_{eff} the effective temperature). These two relations give stellar masses and radii to remarkable precision³¹. In addition, the non-radial oscillation modes of red giants (spherical degree $l \geq 1$) are mixed modes, which result from coupling between gravity (g) waves in the core and acoustic pressure (p) waves in the envelope^{32–35}. The period spacing of the $l=1$ modes, ΔP , is a reliable indicator to distinguish CHeB from RGB stars^{36,37}.

Figure 1 shows the parameters for 7,538 CHeB stars in our sample. Since both $\Delta\nu$ and ν_{\max} depend on radius, we examine the quantity $\nu_{\max}^{0.75}/\Delta\nu$ in Fig. 1a (both ν_{\max} and $\Delta\nu$ are in microhertz). According to the scaling relations, $\nu_{\max}^{0.75}/\Delta\nu$ is proportional to $M^{0.25} T_{\text{eff}}^{-0.375}$ and is approximately independent of radius^{37–39}. The most notable feature in Fig. 1a is a hook-like structure with almost all stars sitting on one side of a well defined edge, which corresponds to the zero-age helium-burning (ZAHeB) phase³¹. This ZAHeB edge is very sharp because almost all ZAHeB stars with $M \lesssim 1.8 M_{\odot}$ share a common helium core mass of $\sim 0.5 M_{\odot}$ (refs. 40,41), which was supported by electron degeneracy on the RGB (Extended Data Fig. 1). We calculated CHeB stellar models from $0.6 M_{\odot}$ to $2.0 M_{\odot}$ with solar metallicity and assuming single-star evolution (Methods), shown by the black lines. Overall, these models are consistent with the

¹Sydney Institute for Astronomy (SIfA), School of Physics, University of Sydney, Sydney, New South Wales, Australia. ²Stellar Astrophysics Centre, Department of Physics and Astronomy, Aarhus University, Aarhus, Denmark. ³School of Physics, University of New South Wales, Sydney, New South Wales, Australia. ⁴Institute for Astronomy, University of Hawai'i, 2680 Woodlawn Drive, Honolulu, HI 96822, USA. ⁵Space Telescope Science Institute, Baltimore, MD, USA. ⁶Department of Astronomy, Beijing Normal University, Beijing, China. ⁷Department of Astrophysics, American Museum of Natural History, Manhattan, NY, USA. ⁸IRAP, Université de Toulouse, CNRS, CNES, UPS, Toulouse, France. ⁹UNSW Data Science Hub, University of New South Wales, Sydney, New South Wales, Australia. ¹⁰Key Laboratory of Optical Astronomy, National Astronomical Observatories, Chinese Academy of Sciences, Beijing, China. ✉e-mail: yaguang.li@sydney.edu.au; tim.bedding@sydney.edu.au

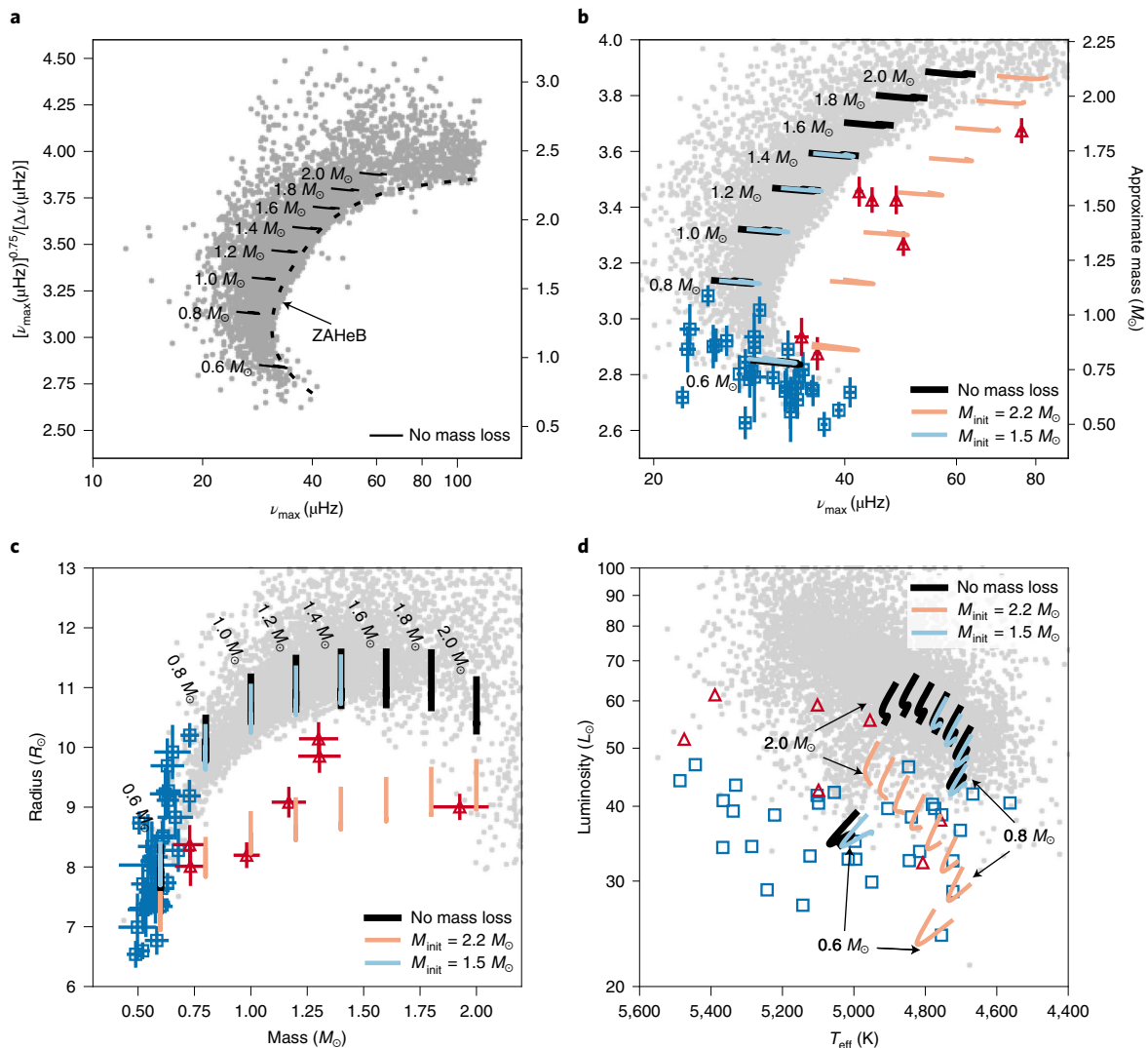


Fig. 1 | Fundamental parameters of CHeB stars in the Kepler red giant sample. a, b, The seismic quantity $\nu_{\max}^{0.75}/\Delta\nu$ versus ν_{\max} . **c,** The mass-radius diagram. **d,** The Hertzsprung–Russell diagram. The underluminous stars are shown by red triangles, the very low-mass stars by blue squares and the rest of the CHeB stars by grey dots. The final masses of stellar evolutionary tracks are indicated by numbers in M_{\odot} . The tracks were calculated without mass loss, with mass loss from an initial mass of $1.5 M_{\odot}$ and with mass loss from an initial mass of $2.2 M_{\odot}$. The underluminous stars were identified as stars lying $>1\sigma$ from the ZAHeb edge (a). Data points are median values. Error bars on the underluminous and very low-mass stars in b and c show 1σ uncertainties. Other data points are not shown with error bars to improve clarity.

majority of the CHeB population, especially considering the single metallicity and the neglect of convective overshoot⁴².

The group of stars in Fig. 1a that lie to the right of the ZAHeb edge cannot be explained by single-star evolution. They are smaller in radius, and hence lower in luminosity, than the main CHeB population with the same masses, implying that a smaller core is supplying their energy. We refer to them as underluminous stars (see Extended Data Figs. 2 and 3 for an example).

Figure 1a also reveals a set of stars with masses down to $0.5 M_{\odot}$. Modelling of the individual frequencies confirms the low mass (Methods and Extended Data Fig. 4). The age of the universe, 13.8 Gyr (ref. 43), puts a lower limit on the mass of a red giant without mass loss of approximately $0.8\text{--}1.0 M_{\odot}$. Specifically, in Fig. 2, we show this lower limit on mass as a function of $[M/H]$, determined by theoretical models (Methods). Since stellar winds driven by radiation and pulsation can only remove up to $0.2 M_{\odot}$ on the RGB, those stars below the threshold must have undergone much more extreme mass loss (Extended Data Fig. 1). We refer to

them as very low-mass stars (see Extended Data Figs. 2 and 3 for an example).

Figure 1b highlights the underluminous stars (red triangles) and the very low-mass stars (blue squares). We show the sample on the mass–radius diagram in Fig. 1c, calculated from T_{eff} , $\Delta\nu$ and ν_{\max} using the scaling relations, and on the Hertzsprung–Russell diagram in Fig. 1d (refs. 31,44–46). The ZAHeb edge is still evident in the mass–radius plane (Fig. 1c), though less sharp, due to observational uncertainties in T_{eff} . The ZAHeb edge is not visible in the luminosity– T_{eff} plane (Fig. 1d), presumably because T_{eff} depends strongly on both mass and metallicity on the RGB. This reasoning is supported by the fact that the solar-metallicity evolutionary models in Fig. 1d are unable to cover the whole observed T_{eff} range.

To understand the locations of the underluminous and very low-mass stars, we calculated stellar evolutionary models with various amounts of mass loss due to binary stripping (Methods). They are shown by the tracks in Fig. 1b–d. First, the models with a progenitor mass of $2.2 M_{\odot}$ that lose different fractions of their outer

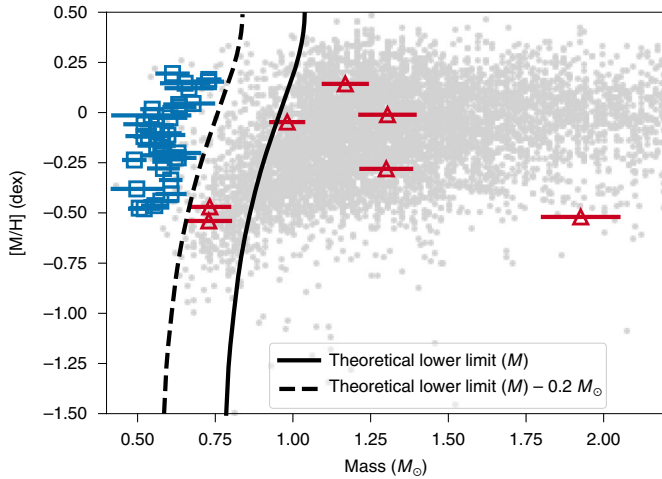


Fig. 2 | [M/H] versus mass for CHeB stars in the Kepler red giant sample.

The underluminous stars are shown as red triangles, the very low-mass stars as blue squares and the rest of the CHeB stars as grey dots. The theoretical lower limit on mass as a function of metallicity, as determined with stellar evolutionary models, is shown by the solid line, assuming no mass loss. The limit including a maximum possible mass loss of $0.2 M_{\odot}$ driven by radiation and pulsation on the RGB^{9–13,138} is shown by the dashed line. The very low-mass stars were identified as stars lying $>1\sigma$ to the left of the dashed line. Data points are median values. Error bars on the underluminous and very low-mass stars show 1σ uncertainties. Other data points are not shown with error bars to improve clarity.

envelopes (shown by orange lines) lie to the right of the ‘hook’ formed by the CHeB population, in the same location as the underluminous stars. This confirms that the underluminous stars were originally more massive on the RGB ($1.8 < M/M_{\odot} < 3.6$), where the central temperature rose quickly and the core started to collapse once it reached the Schönberg–Chandrasekhar limit⁴⁷. This limit does not apply to the lower-mass RGB stars ($M/M_{\odot} \lesssim 1.8$) because their dense cores are electron degenerate. Hence, at the end of the RGB, the higher-mass stars ($1.8 < M/M_{\odot} < 3.6$) initiated helium burning earlier and formed smaller helium cores than lower-mass stars ($M/M_{\odot} \lesssim 1.8$).

Second, we show models with a progenitor mass of $1.5 M_{\odot}$ that lost different amounts of mass due to binary stripping (light-blue lines). Their locations are almost the same as those without mass loss (black lines). This is because, after losing part of their envelope, their structure in the CHeB stage is essentially identical to that of a star that began its life with this lower mass. It is therefore impossible to decipher how much mass a star has lost on the basis of its current $\Delta\nu$, ν_{\max} , luminosity and T_{eff} if it was born with an initial mass below $1.8 M_{\odot}$. However, the $0.6 M_{\odot}$ models without mass loss are older than the universe, while the mass-loss models produce realistic ages for the very low-mass stars.

On the basis of known binary distributions, we can calculate the number of Kepler red giants expected to undergo mass loss after filling their Roche lobes (Methods). The resulting fraction of underluminous stars with progenitor masses between 1.8 and $3.6 M_{\odot}$ is predicted to be 0.13%. This is consistent with our observation, $0.09\% \pm 0.04\%$. The predicted fraction of post-mass-transfer stars with progenitor masses below $1.8 M_{\odot}$ is 2.01%—more than the $0.48\% \pm 0.09\%$ of very low-mass CHeB stars we observed. This is to be expected, because post-mass-transfer CHeB stars with $1.0 < M/M_{\odot} < 1.8$ hide in the overall CHeB population (grey dots in Fig. 1).

Although the post-mass-transfer stars that now appear as regular CHeB stars are difficult to identify, future studies of chemical

abundances may provide clues on mass transfer. One example is lithium (Li), an element that cannot survive in a high-temperature environment. In red giants, the expansion of the convective envelope dilutes Li on the surface by bringing Li-deficient layers from below. Hence, Li enhancement ($A(\text{Li}) = \log_{10}[n(\text{Li})/n(\text{H})] > 1.5$ dex, where $n(x)$ is the number density of atom x) in red giant stars is unusual^{48–51}. Among the underluminous stars (red triangles in Fig. 1), KIC 5000307 shows an unusually high abundance of Li⁵², with $A(\text{Li}) = 2.8$. Our result showing that this star has experienced considerable mass loss seems to suggest binarity as a Li production channel^{53,54}.

Another group of interest is the α -process elements, which trace the stellar populations in the Galaxy. In particular, the α -rich population is characterized by its old age⁵⁵, mainly consisting of low-mass stars, as shown in Fig. 3a by the $[\alpha/\text{M}] > 0.15$ sample. However, this population also contains the so-called young α -rich stars^{56,57}, which appear old chemically but have large masses. They are suggested to be in wide binary systems and to have been recipients of mass transfer^{58–61}. Studies of their companions may be a way to find more stripped CHeB stars.

The elemental abundances of individual stars depend on age and metallicity [M/H] (refs. ^{62,63}), which means that stars within a specific $[\alpha/\text{M}]$ range share a common age distribution. Figure 3b shows the mass distributions of RGB and CHeB stars with $[\alpha/\text{M}] < 0.03$. Almost all the RGB stars are more massive than $1 M_{\odot}$. Considering a maximum mass loss of $0.2 M_{\odot}$ on the RGB through radiation and pulsation, the $M < 0.8 M_{\odot}$ CHeB stars with $[\alpha/\text{M}] < 0.03$ must have transferred mass by other means. Chemical abundances allow us to identify more of these stars in this way.

Our discovery of the post-mass-transfer CHeB stars follows recent identifications of mergers on the RGB^{64,65} and demonstrates asteroseismology as a new way to find interesting binary systems in the red giant population. Expanding the current sample to brighter stars from the K2 and TESS missions will enable spectroscopic or astrometric measurements to solve the binary orbits, allowing detailed characterization of the systems and a better understanding of the mass-transfer channel¹⁹. This is critical to investigate whether some of these stars are still undergoing mass loss and whether they will ultimately become sdB stars. Asteroseismology also opens up other possibilities, since by modelling individual frequencies we can derive accurate masses and ages, thereby providing crucial constraints to the system’s history. Furthermore, analysing the rotational splitting of oscillation modes probes the core rotation and angular momentum transport surrounding these binary interactions, filling the gap between sdB stars and regular CHeB stars⁶⁶.

Methods

Sample selection and stellar parameters. We used the asteroseismic red giant catalogue by Yu et al.³⁹. This sample provides measurements of $\Delta\nu$ and ν_{\max} from the SYD pipeline⁶⁷, compilations of T_{eff} and [M/H], and masses and radii derived using the asteroseismic scaling relations^{68–73}. It also compiles classifications of the evolutionary stage (RGB/CHeB) from previous work^{74–78}. The CHeB stars and the low-luminosity RGB stars ($\nu_{\max} > 80 \mu\text{Hz}$) used in this work are all from this catalogue.

We cross-matched the sample with APOGEE DR17⁷⁹ and the Large Sky Area Multi-Object Fiber Spectroscopic Telescope (LAMOST) DR5⁸⁰ to obtain the elemental abundances ([M/H] and $[\alpha/\text{M}]$), replacing the values of [M/H] from Yu et al.³⁹ wherever possible. The elemental abundances are used in Figs. 2 and 3. We also obtained radial velocities (RVs) from APOGEE DR17⁷⁹ and the LAMOST Medium-Resolution Survey⁸¹.

We carefully remeasured the ν_{\max} values for the underluminous and very low-mass stars in our sample using the pySYD pipeline⁶⁸ and found good agreement with the catalogue values. In addition, we extracted the radial mode frequencies for these identified stars⁸³ and used them to redetermine their average $\Delta\nu$ by adopting the slope from fitting a straight line to the frequencies as a function of the radial orders⁸⁴. This allowed us to measure $\Delta\nu$ more accurately because it is less affected by one or more strong modes. We calculated the correction factors for the $\Delta\nu$ scaling relation according to Sharma et al.⁸⁵. The masses and radii (and associated uncertainties) were then redetermined using the rederived $\Delta\nu$ (with

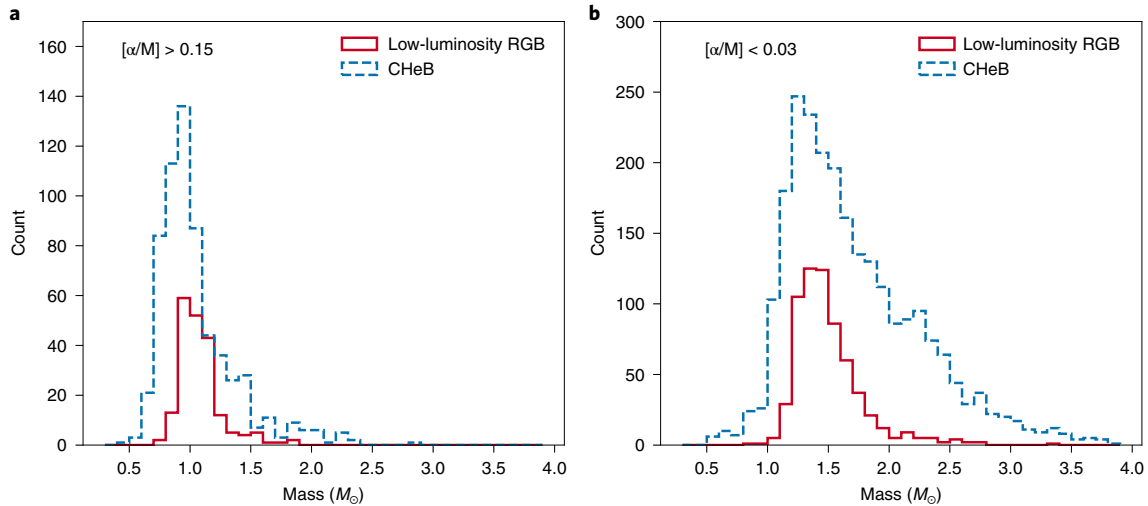


Fig. 3 | Mass distributions of low-luminosity RGB ($\nu_{\max} > 80 \mu\text{Hz}$) and CHeB stars in the Kepler red giant sample (Methods). **a, α -rich population ($[\alpha/M] > 0.15$). **b**, α -poor population ($[\alpha/M] < 0.03$).**

the associated correction factors) and the revised T_{eff} , while keeping all the other parameters the same as described by Yu et al.³⁹. We determined luminosities via the Stefan–Boltzmann law $L \propto R^2 T_{\text{eff}}^4$. We also examined the classification results based on the ΔP to confirm the evolutionary stages. To do this, the power spectrum in the period was sliced into segments of equal width and vertically stacked to construct the so-called period échelle diagram. By optimizing the width, ΔP could be obtained, such that $l=1$ modes align in a ‘zigzag’ pattern³⁷. We checked the period spacings directly (rather than fitting with functions⁸⁶) because the period spacings of CHeB and RGB populations (at similar ν_{\max}) differ by at least a factor of 4 and inspection of the échelle diagram is sufficient to assign the class of evolutionary stages^{86,87}. Extended Data Fig. 2 shows the power spectra for three representative stars, including a regular CHeB star (a), an underluminous star (b) and a very low-mass star (c). The spectra show clear detections of $l=1$ modes. Extended Data Fig. 3 shows the period échelle diagrams. Their period spacings are about 300 s, confirming them as CHeB stars. The main characteristics that set the post-mass-transfer stars apart are their values of ν_{\max} and $\Delta\nu$, and therefore their masses and radii.

Stellar evolutionary models. We calculated the stellar evolutionary models shown in Fig. 1 with MESA (Modules for Experiments in Stellar Astrophysics; version 15140)^{88–92} and GYRE (version 6.0.1)⁹³. We used the Henyey formalism⁹⁴ of the mixing-length theory to describe convection, with the mixing-length parameter α_{MLT} set to 2. Previous work in this mass regime suggests that fundamental parameters are not sensitive to the choice of α_{MLT} at this observational precision^{95,96}. We did not include convective overshoot. We adopted the current solar photospheric abundance measured by Asplund et al.⁹⁷ as the metal mixture for our calculation: $X_{\odot}=0.7381$, $Y_{\odot}=0.2485$, $Z_{\odot}=0.0134$. The opacity tables were accordingly set on the basis of the AGSS09 metal mixture. We used nuclear reaction rates from the JINA REACLIB database⁹⁸ and only considered a minimal set of elements adopted from basic.net in MESA. We adopted the grey model atmosphere with Eddington $T-\tau$ integration⁹⁹ as the surface boundary condition. MESA uses an equation of state blended from OPAL¹⁰⁰, SCVH¹⁰¹, PTEH¹⁰², HELM¹⁰³ and PC¹⁰⁴. MESA implements electron conduction opacities¹⁰⁵ and radiative opacities from OPAL^{106,107}, except for low-temperature data¹⁰⁸ and the high-temperature Compton-scattering regime¹⁰⁹.

We implemented an instant (compared with the evolutionary timescales) mass loss to model a quick binary stripping process. When the model evolved to the CHeB stage, mass loss from the surface was switched on (with the ‘mass_change’ option in MESA) at a rate of $2 M_{\odot} \text{Myr}^{-1}$. Because the helium burning lasts about 100 Myr for $M < 2.2 M_{\odot}$ stars^{42,76}, and the total amount of mass loss ranges from 0.2 to $1.6 M_{\odot}$, the implemented mass loss spanned less than 1% of the total CHeB stage. Mass loss was turned off once the desired final mass was reached, and the evolution was continued until the exhaustion of core helium. Using these settings, we calculated evolutionary models with initial masses 1.5 and $2.2 M_{\odot}$ and final masses ranging from 0.6 to $2.0 M_{\odot}$ in steps of $0.1 M_{\odot}$. We also computed models without any mass loss spanning this mass range, for comparison.

Identification of the underluminous stars. To set expectations of the sharpness of the ZAHHeB edge, we followed the previous method described by Li et al.³¹. This involved using a Galactic simulation sample generated by Galaxia^{110,111}, which has been tied to the Kepler target selection function. In Extended Data Fig. 1a,

we show the Galaxia CHeB population on the $\nu_{\max}^{0.75}/\Delta\nu-\Delta\nu$ diagram^{37–39}. Next, we identified the theoretical ZAHHeB edge using a spline (the black dashed line) interpolated between several anchor points (the green crosses). We focused on the vertical distances to the edge because the horizontal direction has negligible uncertainties (in Fig. 1b the error bars on the red triangles are smaller than the symbol size). In the inset of Extended Data Fig. 1a, we show the histogram of the vertical distances to the ZAHHeB edge. Although the simulated sample forms a very sharp edge, it is still broadened by scatter in T_{eff} and $[M/H]$. To determine the intrinsic broadening, we fitted the distribution with a half-Gaussian half-Lorentzian profile. The intrinsic broadening $\sigma_{\text{intrinsic}}$, measured by the standard deviation of the Gaussian profile, was 0.06.

We caution that the extremely metal-poor stars (e.g., $[M/H] = -2$ dex) could occupy the right-hand side of the edge, although they are very rare in our sample. As shown in Fig. 2, most Kepler CHeB stars have $[M/H] > -1.0$ dex. The identified underluminous stars (red triangles) have metallicities of > -0.5 dex. This means that the right-hand side of the edge is still a ‘forbidden’ zone for these stars.

Similarly, in Fig. 1b, we identified the observed ZAHHeB edge for the Kepler sample with a spline and collected all stars that lay on the right of the edge. The statistical uncertainty was combined with $\sigma_{\text{intrinsic}}$ in quadrature to represent the final uncertainty. The underluminous stars were selected as being at least 1σ away from the observed ZAHHeB edge in the vertical direction. We list the underluminous stars in Supplementary Information.

Identification of the very low-mass stars. The lowest possible mass of a CHeB star, limited by the age of the universe (13.8 Gyr; ref. 43), is critically dependent on the metallicity. Using stellar isochrones at 13.8 Gyr from MIST¹¹², we extracted the model masses at helium-burning stage for different values of $[M/H]$. In Extended Data Fig. 1b, we show the simulated Galaxia population on the $[M/H]$ –mass diagram. The simulated sample forms a very sharp edge that coincides with the theoretical limit on mass (denoted by the dashed line).

The theoretical limit on mass (the solid line) is also shown in Fig. 2, together with the observed Kepler sample. We assume that the mass loss driven by radiation and pulsation can at most lower this limit by $0.2 M_{\odot}$ (the dashed line). Hence, we identified the stars at least 1σ to the left of the dashed line as the very low-mass stars, which must experience enhanced mass loss, possibly due to a companion. We list the very low-mass stars in Supplementary Information.

Modelling of a very low-mass star. Since we rely on the scaling relations to derive stellar masses for the very low-mass stars, it is important to confirm the accuracy of the scaling relations in this regime. The $\Delta\nu$ scaling relation can be checked with stellar models by calculating the mode frequencies and comparing with the density^{84,85,113–116}. The models produce a correction factor, which is applied to observations. The problem lies in the ν_{\max} scaling relation, which does not have a solid theoretical basis. Zinn et al.¹¹⁷ found no obvious difference between the scaling-relation-based radii and the Gaia radii for stars smaller than $R = 30 R_{\odot}$ within observational uncertainties. Li et al.³¹ used the sharpness of the ZAHHeB edge to conclude that the ν_{\max} scaling relation has a very small intrinsic scatter of 1.1%. However, the ν_{\max} scaling relation could perhaps have a systematic offset that biases stellar masses in this very low-mass regime. To examine this, we used stellar modelling to show that one of the very low-mass stars is indeed very low mass, by constraining stellar models using luminosity, metallicity, T_{eff} and oscillation

mode frequencies. This does not use the information contained in the ν_{\max} scaling relation.

We chose the target KIC 8367834 because it has the best parallax among the very low-mass stars. We adopted the metallicity 0.19 ± 0.05 dex from APOGEE DR17⁷⁹. We determined T_{eff} to be $4,697 \pm 100$ K with the InfraRed Flux Method¹¹⁸. Using ISOCCLASSIFY^{119,120}, we derived trigonometric luminosities L , $32.87 \pm 1.22 L_{\odot}$, with the Gaia EDR3 parallax^{121,122}, 2MASS J-band magnitudes, and extinctions from the dust map¹²³. We extracted five radial frequencies⁸³. They are $21.07 \pm 0.03 \mu\text{Hz}$, $25.31 \pm 0.02 \mu\text{Hz}$, $29.40 \pm 0.02 \mu\text{Hz}$, $33.89 \pm 0.02 \mu\text{Hz}$ and $38.25 \pm 0.03 \mu\text{Hz}$.

We constructed a grid of stellar models by varying metallicities $[M/H]$ from 0.03 to 0.43 dex in steps of 0.05 dex (Z from 0.0152 to 0.0357), initial masses from 0.8 to $1.4 M_{\odot}$ in steps of $0.2 M_{\odot}$ and final masses from 0.5 to $0.8 M_{\odot}$ in steps of $0.02 M_{\odot}$. We first evolved models with various initial masses and metallicities until the onset of helium burning and saved these models. These models then lost their outer envelopes at a rate of $10 M_{\odot} \text{Myr}^{-1}$ until the desired final masses were reached. The total mass loss spans less than 1% of the helium-burning lifetime. The other model parameters were kept the same as the parameters we used to construct the models shown in Fig. 1. We calculated radial oscillation frequencies for all the models during the CHeB stage.

We optimized the stellar models using a maximum likelihood approach:

$$p \propto \exp(-\chi^2/2), \quad (1)$$

where

$$\chi^2 = \chi_{\text{classical}}^2 + \chi_{\text{seismic}}^2. \quad (2)$$

The classical constraints include three stellar properties, $q = \{L, T_{\text{eff}}, [M/H]\}$:

$$\chi_{\text{classical}}^2 = \sum_q \frac{[q_{\text{mod}} - q_{\text{obs}}]^2}{\sigma_q^2}. \quad (3)$$

The seismic constraints include the extracted radial modes:

$$\chi_{\text{seismic}}^2 = \sum_n \frac{[\nu_{\text{mod},n} - \nu_{\text{obs},n}]^2}{\sigma_{\nu_{\text{mod}}}^2 + \sigma_{\nu_{\text{obs},n}}^2}, \quad (4)$$

where $\sigma_{\nu_{\text{mod}}}$ is a systematic uncertainty due to the limited resolution of the model grid^{124,125}. To evaluate $\sigma_{\nu_{\text{mod}}}$, we first identified the best-fitting model (using equation (4) and treating $\sigma_{\nu_{\text{mod}}}$ as 0) and calculated its root-mean-square difference. We also corrected the theoretical frequencies due to the surface effect with the inverse-cubic formula¹²⁶.

Extended Data Fig. 4 shows the stellar models within 3σ of the classical constraints, colour-coded with the probability. First, the most likely mass lies in the 1.5σ region determined from the scaling relations, validating the accuracy of the scaling relations. Second, and unsurprisingly, the frequency modelling yields the stellar mass to a even greater precision, suggesting a more accurate method to determine masses.

Rates of binary interactions. We estimated the number of stars that would be expected to have lost mass due to binary interaction on the RGB. We used the observed masses and $[M/H]$ of Kepler CHeB stars as the mass (M_1) and metallicity distributions of the primary stars in binary systems and calculated the maximum radius on the RGB, $R_{\text{RGB,max}}$, with MIST stellar evolutionary tracks¹¹². Assuming circular orbits, we randomly sampled binary fractions f , orbital periods P and mass ratios $q = M_1/M_2$ from observations of binary statistics¹²⁷ and derived the radius of the L1 Lagrangian point¹²⁸ according to

$$R_{\text{L1}} = a \frac{0.49q^{2/3}}{0.6q^{2/3} + \ln(1 + q^{1/3})}, \quad (5)$$

where a is the semi-major axis, which links to the orbital period,

$$P = 2\pi \sqrt{\frac{a^3}{G(M_1 + M_2)}}. \quad (6)$$

The stars that expand their envelopes on the RGB beyond the L1 Lagrangian point, that is, $R_{\text{RGB,max}} > R_{\text{L1}}$, are subject to mass loss. The expected number of mass-loss stars is the sum of binary fractions f for the stars that satisfy the above condition.

Variations of RVs. Using multi-epoch RV data from APOGEE and LAMOST, we divided the maximal change $[RV_{\text{max}} - RV_{\text{min}}]$ by the median of statistical errors e_{RV} to represent RV variations¹²⁹ (Supplementary Information). Only a few of the identified post-mass-transfer stars show significant RV variations. To better understand the distributions, we generated RV time series RV_s at time t for the simulated binary sample with

$$RV_s(t) = 2\pi a/P \sin i^* \sin(2\pi t/P) + e_{\text{RV}}, \quad (7)$$

where i^* is the inclination angle drawn from an isotropic distribution, and e_{RV} is drawn from a normal distribution with standard deviation e_{RV} . Both t and e_{RV} used the observed RV measurements. Similarly, we generated RV time series for single stars with

$$RV_s(t) = e_{\text{RV}}. \quad (8)$$

Using the same method, we estimated the RV variations for the simulated samples. The comparison between the observed and the simulated samples suggests that a significant RV variation ($|RV_{\text{max}} - RV_{\text{min}}|/e_{\text{RV}} > 10$) may indicate a binary system, but a small RV variation does not necessarily exclude binarity. This explains the lack of RV variations in most stars identified in this work.

Data availability

We made use of publicly available data in this work. Kepler data are available from the MAST portal at <https://archive.stsci.edu/access-mast-data>, APOGEE data at <https://www.sdss.org/dr16/>, LAMOST data at <http://dr5.lamost.org/v3/doc/vac> and <https://github.com/hypergravity/paperdata> and Gaia data at <https://gea.esac.esa.int/archive/>. The data needed to reproduce this work are available at GitHub (https://github.com/parallelpro/Yaguang_stripped_rg_repo). All other data are available from the corresponding author upon reasonable request.

Code availability

This work is made possible by the following open-source software: NumPy¹³⁰, SciPy¹³¹, Matplotlib¹³², Astropy^{133,134}, Pandas¹³⁵, MESA^{88–92}, MESA SDK¹³⁶, GYRE⁹³, pySYD⁹², Lightkurve¹³⁷, EchellePlotter (<https://github.com/9yifanchen9/EchellePy>) and ISOCCLASSIFY^{119,120}. The scripts used in this work is available at a curated GitHub repository (https://github.com/parallelpro/Yaguang_stripped_rg_repo).

Received: 9 November 2021; Accepted: 4 March 2022;

Published online: 14 April 2022

References

- Heber, U. Hot subluminescent stars. *Publ. Astron. Soc. Pac.* **128**, 082001 (2016).
- Byrne, C. M., Stanway, E. R. & Eldridge, J. J. Binary evolution pathways of blue large-amplitude pulsators. *Mon. Not. R. Astron. Soc.* **507**, 621–631 (2021).
- Lynas-Gray, A. E. Asteroseismic observations of hot subdwarfs. *Front. Astron. Space Sci.* **8**, 576623 (2021).
- Reimers, D. Circumstellar absorption lines and mass loss from red giants. *Mem. Soc. R. Sci. Liege* **8**, 369–382 (1975).
- Schröder, K. P. & Cuntz, M. A new version of Reimers' law of mass loss based on a physical approach. *Astrophys. J.* **630**, L73–L76 (2005).
- Yu, J. et al. Asteroseismology of luminous red giants with Kepler—II. Dependence of mass-loss on pulsations and radiation. *Mon. Not. R. Astron. Soc.* **501**, 5135–5148 (2021).
- Miglio, A. et al. Age dissection of the Milky Way discs: red giants in the Kepler field. *Astron. Astrophys.* **645**, A85 (2021).
- Miglio, A. et al. Asteroseismology of old open clusters with Kepler: direct estimate of the integrated red giant branch mass-loss in NGC 6791 and 6819. *Mon. Not. R. Astron. Soc.* **419**, 2077–2088 (2012).
- Stello, D. et al. The K2 M67 Study: revisiting old friends with K2 reveals oscillating red giants in the open cluster M67. *Astrophys. J.* **832**, 133 (2016).
- Handberg, R. et al. NGC 6819: testing the asteroseismic mass scale, mass loss and evidence for products of non-standard evolution. *Mon. Not. R. Astron. Soc.* **472**, 979–997 (2017).
- McDonald, I. & Zijlstra, A. A. Mass-loss on the red giant branch: the value and metallicity dependence of Reimers' η in globular clusters. *Mon. Not. R. Astron. Soc.* **448**, 502–521 (2015).
- Lebzelter, T. & Wood, P. R. Long period variables and mass loss in the globular clusters NGC 362 and NGC 2808. *Astron. Astrophys.* **529**, A137 (2011).
- Salaris, M., Cassisi, S. & Pietrinferni, A. On the red giant branch mass loss in 47 Tucanae: constraints from the horizontal branch morphology. *Astron. Astrophys.* **590**, A64 (2016).
- An, D., Pinsonneault, M. H., Terndrup, D. M. & Chung, C. Comparison of the asteroseismic mass scale of red clump giants with photometric mass estimates. *Astrophys. J.* **879**, 81 (2019).
- Han, Z.-W., Ge, H.-W., Chen, X.-F. & Chen, H.-L. Binary population synthesis. *Res. Astron. Astrophys.* **20**, 161 (2020).
- Bergeron, P., Saffer, R. A. & Liebert, J. A spectroscopic determination of the mass distribution of DA white dwarfs. *Astrophys. J.* **394**, 228–247 (1992).
- Liebert, J., Bergeron, P. & Holberg, J. B. The formation rate and mass and luminosity functions of DA white dwarfs from the Palomar Green Survey. *Astrophys. J. Suppl. Ser.* **156**, 47–68 (2005).
- Brown, W. R., Kilic, M., Allende Prieto, C., Gianninas, A. & Kenyon, S. J. The ELM Survey. V. Merging massive white dwarf binaries. *Astrophys. J.* **769**, 66 (2013).

19. Han, Z., Podsiadlowski, P., Maxted, P. F. L., Marsh, T. R. & Ivanova, N. The origin of subdwarf B stars—I. The formation channels. *Mon. Not. R. Astron. Soc.* **336**, 449–466 (2002).
20. Hu, H. et al. A seismic approach to testing different formation channels of subdwarf B stars. *Astron. Astrophys.* **490**, 243–252 (2008).
21. Maxted, P. F. L., Heber, U., Marsh, T. R. & North, R. C. The binary fraction of extreme horizontal branch stars. *Mon. Not. R. Astron. Soc.* **326**, 1391–1402 (2001).
22. Napiwotzki, R. et al. Close binary EHB stars from SPY. *Astrophys. Space Sci.* **291**, 321–328 (2004).
23. Copperwheat, C. M., Morales-Rueda, L., Marsh, T. R., Maxted, P. F. L. & Heber, U. Radial-velocity measurements of subdwarf B stars. *Mon. Not. R. Astron. Soc.* **415**, 1381–1395 (2011).
24. El-Badry, K. & Quataert, E. A stripped-companion origin for Be stars: clues from the putative black holes HR 6819 and LB-1. *Mon. Not. R. Astron. Soc.* **502**, 3436–3455 (2021).
25. Shenar, T. et al. The ‘hidden’ companion in LB-1 unveiled by spectral disentangling. *Astron. Astrophys.* **639**, L6 (2020).
26. Irrgang, A., Geier, S., Kreuzer, S., Pelisoli, I. & Heber, U. A stripped helium star in the potential black hole binary LB-1. *Astron. Astrophys.* **633**, L5 (2020).
27. Brogaard, K., Arentoft, T., Jessen-Hansen, J. & Miglio, A. Asteroseismology of overmassive, undermassive, and potential past members of the open cluster NGC 6791. *Mon. Not. R. Astron. Soc.* **507**, 496–509 (2021).
28. Ulrich, R. K. Determination of stellar ages from asteroseismology. *Astrophys. J.* **306**, L37 (1986).
29. Brown, T. M., Gilliland, R. L., Noyes, R. W. & Ramsey, L. W. Detection of possible p-mode oscillations on Procyon. *Astrophys. J.* **368**, 599–609 (1991).
30. Kjeldsen, H. & Bedding, T. R. Amplitudes of stellar oscillations: the implications for asteroseismology. *Astron. Astrophys.* **293**, 87–106 (1995).
31. Li, Y. et al. Testing the intrinsic scatter of the asteroseismic scaling relations with Kepler red giants. *Mon. Not. R. Astron. Soc.* **501**, 3162–3172 (2021).
32. Aizenman, M., Smeyers, P. & Weigert, A. Avoided crossing of modes of non-radial stellar oscillations. *Astron. Astrophys.* **58**, 41–46 (1977).
33. Christensen-Dalsgaard, J., Bedding, T. R. & Kjeldsen, H. Modeling solar-like oscillations in η Bootis. *Astrophys. J.* **443**, L29 (1995).
34. Deheuvels, S. et al. Seismic and spectroscopic characterization of the solar-like pulsating CoRoT target HD 49385. *Astron. Astrophys.* **515**, A87 (2010).
35. Benomar, O. et al. Properties of oscillation modes in subgiant stars observed by Kepler. *Astrophys. J.* **767**, 158 (2013).
36. Dupret, M. A. et al. Theoretical amplitudes and lifetimes of non-radial solar-like oscillations in red giants. *Astron. Astrophys.* **506**, 57–67 (2009).
37. Bedding, T. R. et al. Gravity modes as a way to distinguish between hydrogen- and helium-burning red giant stars. *Nature* **471**, 608–611 (2011).
38. Huber, D. et al. Asteroseismology of red giants from the first four months of Kepler data: global oscillation parameters for 800 stars. *Astrophys. J.* **723**, 1607–1617 (2010).
39. Yu, J. et al. Asteroseismology of 16,000 Kepler red giants: global oscillation parameters, masses, and radii. *Astrophys. J. Suppl. Ser.* **236**, 42 (2018).
40. Sweigart, A. V., Greggio, L. & Renzini, A. The development of the red giant branch. II. Astrophysical properties. *Astrophys. J.* **364**, 527–539 (1990).
41. Montalbán, J. et al. Testing convective-core overshooting using period spacings of dipole modes in red giants. *Astrophys. J.* **766**, 118 (2013).
42. Girardi, L. Red clump stars. *Annu. Rev. Astron. Astrophys.* **54**, 95–133 (2016).
43. Planck Collaboration et al. Planck 2015 results. XIII. Cosmological parameters. *Astron. Astrophys.* **594**, A13 (2016).
44. Mosser, B. et al. Characterization of the power excess of solar-like oscillations in red giants with Kepler. *Astron. Astrophys.* **537**, A30 (2012).
45. Elsworth, Y. et al. Insights from the APOKASC determination of the evolutionary state of red-giant stars by consolidation of different methods. *Mon. Not. R. Astron. Soc.* **489**, 4641–4657 (2019).
46. Gaulme, P. et al. Active red giants: close binaries versus single rapid rotators. *Astron. Astrophys.* **639**, A63 (2020).
47. Schönberg, M. & Chandrasekhar, S. On the evolution of the main-sequence stars. *Astrophys. J.* **96**, 161–172 (1942).
48. Kumar, Y. B. et al. Discovery of ubiquitous lithium production in low-mass stars. *Nat. Astron.* **4**, 1059–1063 (2020).
49. Deepak & Lambert, D. L. Lithium abundances and asteroseismology of red giants: understanding the evolution of lithium in giants based on asteroseismic parameters. *Mon. Not. R. Astron. Soc.* **505**, 642–648 (2021).
50. Martell, S. L. et al. The GALAH survey: a census of lithium-rich giant stars. *Mon. Not. R. Astron. Soc.* **505**, 5340–5355 (2021).
51. Yan, H.-L. et al. Most lithium-rich low-mass evolved stars revealed as red clump stars by asteroseismology and spectroscopy. *Nat. Astron.* **5**, 86–93 (2021).
52. Silva Aguirre, V. et al. Old puzzle, new insights: a lithium-rich giant quietly burning helium in its core. *Astrophys. J.* **784**, L16 (2014).
53. Casey, A. R. et al. Tidal interactions between binary stars can drive lithium production in low-mass red giants. *Astrophys. J.* **880**, 125 (2019).
54. Zhang, X., Jeffery, C. S., Li, Y. & Bi, S. Population synthesis of helium white dwarf–red giant star mergers and the formation of lithium-rich giants and carbon stars. *Astrophys. J.* **889**, 33 (2020).
55. Bland-Hawthorn, J. & Gerhard, O. The Galaxy in context: structural, kinematic, and integrated properties. *Annu. Rev. Astron. Astrophys.* **54**, 529–596 (2016).
56. Chiappini, C. et al. Young $[\alpha/\text{Fe}]$ -enhanced stars discovered by CoRoT and APOGEE: what is their origin? *Astron. Astrophys.* **576**, L12 (2015).
57. Martig, M. et al. Young α -enriched giant stars in the solar neighbourhood. *Mon. Not. R. Astron. Soc.* **451**, 2230–2243 (2015).
58. Jofré, P. et al. Cannibals in the thick disk: the young α -rich stars as evolved blue stragglers. *Astron. Astrophys.* **595**, A60 (2016).
59. Yong, D. et al. GRACES observations of young $[\alpha/\text{Fe}]$ -rich stars. *Mon. Not. R. Astron. Soc.* **459**, 487–495 (2016).
60. Hekker, S. & Johnson, J. A. Origin of α -rich young stars: clues from C, N, and O. *Mon. Not. R. Astron. Soc.* **487**, 4343–4354 (2019).
61. Zhang, M. et al. Most “young” α -rich stars have high masses but are actually old. *Astrophys. J.* **922**, 145 (2021).
62. Sharma, S. et al. The GALAH Survey: dependence of elemental abundances on age and metallicity for stars in the Galactic disc. *Mon. Not. R. Astron. Soc.* **510**, 734–752 (2021).
63. Hayden, M. R. et al. The GALAH Survey: chemical clocks. Preprint at <https://arxiv.org/abs/2011.13745> (2020).
64. Rui, N. Z. & Fuller, J. Asteroseismic fingerprints of stellar mergers. *Mon. Not. R. Astron. Soc.* **508**, 1618–1631 (2021).
65. Deheuvels, S., Ballot, J., Gehan, C. & Mosser, B. Seismic signature of electron degeneracy in the core of red giants: hints for mass transfer between close red-giant companions. *Astron. Astrophys.* **659**, A106 (2022).
66. Aerts, C., Mathis, S. & Rogers, T. M. Angular momentum transport in stellar interiors. *Annu. Rev. Astron. Astrophys.* **57**, 35–78 (2019).
67. Huber, D. et al. Automated extraction of oscillation parameters for Kepler observations of solar-type stars. *Commun. Asteroseismol.* **160**, 74–91 (2009).
68. Stello, D., Bruntt, H., Preston, H. & Buzasi, D. Oscillating K giants with the WIRE satellite: determination of their asteroseismic masses. *Astrophys. J.* **674**, L53 (2008).
69. Kallinger, T. et al. Oscillating red giants in the CoRoT exofield: asteroseismic mass and radius determination. *Astron. Astrophys.* **509**, A77 (2010).
70. Chaplin, W. J. & Miglio, A. Asteroseismology of solar-type and red-giant stars. *Annu. Rev. Astron. Astrophys.* **51**, 353–392 (2013).
71. Hekker, S. & Christensen-Dalsgaard, J. Giant star seismology. *Astron. Astrophys. Rev.* **25**, 1 (2017).
72. Basu, S. & Hekker, S. Unveiling the structure and dynamics of red giants with asteroseismology. *Front. Astron. Space Sci.* **7**, 44 (2020).
73. Hekker, S. Scaling relations for solar-like oscillations: a review. *Front. Astron. Space Sci.* **7**, 3 (2020).
74. Hon, M., Stello, D. & Yu, J. Deep learning classification in asteroseismology. *Mon. Not. R. Astron. Soc.* **469**, 4578–4583 (2017).
75. Kallinger, T. et al. Evolutionary influences on the structure of red-giant acoustic oscillation spectra from 600 d of Kepler observations. *Astron. Astrophys.* **541**, A51 (2012).
76. Stello, D. et al. Asteroseismic classification of stellar populations among 13,000 red giants observed by Kepler. *Astrophys. J.* **765**, L41 (2013).
77. Mosser, B. et al. Mixed modes in red giants: a window on stellar evolution. *Astron. Astrophys.* **572**, L5 (2014).
78. Vrad, M., Mosser, B. & Samadi, R. Period spacings in red giants. II. Automated measurement. *Astron. Astrophys.* **588**, A87 (2016).
79. Abdurro’uf et al. The seventeenth data release of the Sloan Digital Sky Surveys: complete release of MaNGA, MaStar and APOGEE-2 data. *Astrophys. J. Suppl. Ser.* **259**, 35 (2022).
80. Xiang, M. et al. Abundance estimates for 16 elements in 6 million stars from LAMOST DR5 low-resolution spectra. *Astrophys. J. Suppl. Ser.* **245**, 34 (2019).
81. Zhang, B. et al. Self-consistent stellar radial velocities from LAMOST Medium-Resolution Survey DR7. *Astrophys. J. Suppl. Ser.* **256**, 14 (2021).
82. Chontos, A., Huber, D., Sayeed, M. & Yamsiri, P. pySYD: automated measurements of global asteroseismic parameters. Preprint at <https://arxiv.org/abs/2108.00582> (2021).
83. Li, Y. et al. Asteroseismology of 36 Kepler subgiants—I. Oscillation frequencies, linewidths, and amplitudes. *Mon. Not. R. Astron. Soc.* **495**, 2363–2386 (2020).
84. White, T. R. et al. Calculating asteroseismic diagrams for solar-like oscillations. *Astrophys. J.* **743**, 161 (2011).
85. Sharma, S., Stello, D., Bland-Hawthorn, J., Huber, D. & Bedding, T. R. Stellar population synthesis based modeling of the Milky Way using asteroseismology of 13,000 Kepler red giants. *Astrophys. J.* **822**, 15 (2016).

86. Vrad, M., Mosser, B. & Samadi, R. Period spacings in red giants. II. Automated measurement. *Astron. Astrophys.* **588**, A87 (2016).
87. Mosser, B. et al. Period spacings in red giants IV. Toward a complete description of the mixed-mode pattern. *Astron. Astrophys.* **618**, A109 (2018).
88. Paxton, B. et al. Modules for Experiments in Stellar Astrophysics (MESA). *Astrophys. J. Suppl. Ser.* **192**, 3 (2011).
89. Paxton, B. et al. Modules for Experiments in Stellar Astrophysics (MESA): planets, oscillations, rotation, and massive stars. *Astrophys. J. Suppl. Ser.* **208**, 4 (2013).
90. Paxton, B. et al. Modules for Experiments in Stellar Astrophysics (MESA): binaries, pulsations, and explosions. *Astrophys. J. Suppl. Ser.* **220**, 15 (2015).
91. Paxton, B. et al. Modules for Experiments in Stellar Astrophysics (MESA): convective boundaries, element diffusion, and massive star explosions. *Astrophys. J. Suppl. Ser.* **234**, 34 (2018).
92. Paxton, B. et al. Modules for Experiments in Stellar Astrophysics (MESA): pulsating variable stars, rotation, convective boundaries, and energy conservation. *Astrophys. J. Suppl. Ser.* **243**, 10 (2019).
93. Townsend, R. H. D. & Teitler, S. A. GYRE: an open-source stellar oscillation code based on a new Magnus Multiple Shooting scheme. *Mon. Not. R. Astron. Soc.* **435**, 3406–3418 (2013).
94. Henyey, L., Vardya, M. S. & Bodenheimer, P. Studies in stellar evolution. III. The calculation of model envelopes. *Astrophys. J.* **142**, 841–854 (1965).
95. Murphy, S. J., Joyce, M., Bedding, T. R., White, T. R. & Kama, M. A precise asteroseismic age and metallicity for HD 139614: a pre-main-sequence star with a protoplanetary disc in Upper Centaurus–Lupus. *Mon. Not. R. Astron. Soc.* **502**, 1633–1646 (2021).
96. Molnár, L., Joyce, M. & Kiss, L. L. Stellar evolution in real time: models consistent with the direct observation of a thermal pulse in T Ursae Minoris. *Astrophys. J.* **879**, 62 (2019).
97. Asplund, M., Grevesse, N., Sauval, A. J. & Scott, P. The chemical composition of the Sun. *Annu. Rev. Astron. Astrophys.* **47**, 481–522 (2009).
98. Cyburt, R. H. et al. The JINA REACLIB database: its recent updates and impact on type-I X-ray bursts. *Astrophys. J. Suppl. Ser.* **189**, 240–252 (2010).
99. Eddington, A. S. *The Internal Constitution of the Stars* (University Press, 1926).
100. Rogers, F. J. & Nayfonov, A. Updated and expanded OPAL equation-of-state tables: implications for helioseismology. *Astrophys. J.* **576**, 1064–1074 (2002).
101. Saumon, D., Chabrier, G. & van Horn, H. M. An equation of state for low-mass stars and giant planets. *Astrophys. J. Suppl. Ser.* **99**, 713–741 (1995).
102. Pols, O. R., Tout, C. A., Eggleton, P. P. & Han, Z. Approximate input physics for stellar modelling. *Mon. Not. R. Astron. Soc.* **274**, 964–974 (1995).
103. Timmes, F. X. & Swesty, F. D. The accuracy, consistency, and speed of an electron–positron equation of state based on table interpolation of the Helmholtz free energy. *Astrophys. J. Suppl. Ser.* **126**, 501–516 (2000).
104. Potekhin, A. Y. & Chabrier, G. Thermodynamic functions of dense plasmas: analytic approximations for astrophysical applications. *Contrib. Plasma Phys.* **50**, 82–87 (2010).
105. Cassisi, S., Potekhin, A. Y., Pietrinferni, A., Catelan, M. & Salaris, M. Updated electron–conduction opacities: the impact on low-mass stellar models. *Astrophys. J.* **661**, 1094–1104 (2007).
106. Iglesias, C. A. & Rogers, F. J. Radiative opacities for carbon- and oxygen-rich mixtures. *Astrophys. J.* **412**, 752–760 (1993).
107. Iglesias, C. A. & Rogers, F. J. Updated OPAL opacities. *Astrophys. J.* **464**, 943–953 (1996).
108. Ferguson, J. W. et al. Low-temperature opacities. *Astrophys. J.* **623**, 585–596 (2005).
109. Buchler, J. R. & Yueh, W. R. Compton scattering opacities in a partially degenerate electron plasma at high temperatures. *Astrophys. J.* **210**, 440–446 (1976).
110. Sharma, S., Bland-Hawthorn, J., Johnston, K. V. & Binney, J. Galaxia: a code to generate a synthetic survey of the Milky Way. *Astrophys. J.* **730**, 3 (2011).
111. Sharma, S. et al. The K2-HERMES Survey: age and metallicity of the thick disc. *Mon. Not. R. Astron. Soc.* **490**, 5335–5352 (2019).
112. Choi, J. et al. Mesa Isochrones and Stellar Tracks (MIST). I. Solar-scaled models. *Astrophys. J.* **823**, 102 (2016).
113. Guggenberger, E., Hekker, S., Basu, S. & Bellinger, E. Significantly improving stellar mass and radius estimates: a new reference function for the $\Delta\nu$ scaling relation. *Mon. Not. R. Astron. Soc.* **460**, 4277–4281 (2016).
114. Rodrigues, T. S. et al. Determining stellar parameters of asteroseismic targets: going beyond the use of scaling relations. *Mon. Not. R. Astron. Soc.* **467**, 1433–1448 (2017).
115. Serenelli, A. et al. The first APOKASC catalog of Kepler dwarf and subgiant stars. *Astrophys. J. Suppl. Ser.* **233**, 23 (2017).
116. Pinsonneault, M. H. et al. The second APOKASC catalog: the empirical approach. *Astrophys. J. Suppl. Ser.* **239**, 32 (2018).
117. Zinn, J. C. et al. Testing the radius scaling relation with Gaia DR2 in the Kepler field. *Astrophys. J.* **885**, 166 (2019).
118. Casagrande, L. et al. The GALAH survey: effective temperature calibration from the InfraRed Flux Method in the Gaia system. *Mon. Not. R. Astron. Soc.* **507**, 2684–2696 (2021).
119. Huber, D. et al. Asteroseismology and Gaia: testing scaling relations using 2200 Kepler stars with TGAS parallaxes. *Astrophys. J.* **844**, 102 (2017).
120. Berger, T. A. et al. The Gaia–Kepler Stellar Properties Catalog. I. Homogeneous fundamental properties for 186,301 Kepler stars. *Astron. J.* **159**, 280 (2020).
121. Gaia Collaboration et al. The Gaia mission. *Astron. Astrophys.* **595**, A1 (2016).
122. Gaia Collaboration et al. Gaia Early Data Release 3: summary of the contents and survey properties. *Astron. Astrophys.* **649**, A1 (2021).
123. Green, G. M., Schlafly, E., Zucker, C., Speagle, J. S. & Finkbeiner, D. A 3D dust map based on Gaia, Pan-STARRS 1, and 2MASS. *Astrophys. J.* **887**, 93 (2019).
124. Li, T. et al. Asteroseismology of 36 Kepler subgiants—II. Determining ages from detailed modelling. *Mon. Not. R. Astron. Soc.* **495**, 3431–3462 (2020).
125. Ong, J. M. J. et al. Mixed modes and asteroseismic surface effects. II. Subgiant systematics. *Astrophys. J.* **922**, 18 (2021).
126. Ball, W. H. & Gizon, L. A new correction of stellar oscillation frequencies for near-surface effects. *Astron. Astrophys.* **568**, A123 (2014).
127. Moe, M. & Di Stefano, R. Mind your Ps and Qs: the interrelation between period (P) and mass-ratio (Q) distributions of binary stars. *Astrophys. J. Suppl. Ser.* **230**, 15 (2017).
128. Eggleton, P. P. Approximations to the radii of Roche lobes. *Astrophys. J.* **268**, 368–369 (1983).
129. Mazzola Daher, C. et al. Stellar multiplicity and stellar rotation: insights from APOGEE. *Mon. Not. R. Astron. Soc.* **512**, 2051–2061 (2022).
130. van der Walt, S., Colbert, S. C. & Varoquaux, G. The NumPy array: a structure for efficient numerical computation. *Comput. Sci. Eng.* **13**, 22–30 (2011).
131. Virtanen, P. et al. SciPy 1.0: fundamental algorithms for scientific computing in Python. *Nat. Methods* **17**, 261–272 (2020).
132. Hunter, J. D. Matplotlib: a 2D graphics environment. *Comput. Sci. Eng.* **9**, 90–95 (2007).
133. Astropy Collaboration et al. Astropy: a community Python package for astronomy. *Astron. Astrophys.* **558**, A33 (2013).
134. Astropy Collaboration et al. The Astropy Project: building an open-science project and status of the v2.0 core package. *Astron. J.* **156**, 123 (2018).
135. McKinney, W. Data structures for statistical computing in Python. In *Proc. Ninth Python in Science Conference* (eds van der Walt, S. & Millman, J.) 56–61 (2010).
136. Townsend, R. *MESA SDK for Linux* (2020).
137. Lightkurve Collaboration et al. Lightkurve: Kepler and TESS time series analysis in Python. *Astrophysics Source Code Library* ascl:1812.013 (2018).
138. McDonald, I., Johnson, C. I. & Zijlstra, A. A. Empirical determination of the integrated red giant and horizontal branch stellar mass-loss in ω Centauri. *Mon. Not. R. Astron. Soc.* **416**, L6–L10 (2011).

Acknowledgements

We thank M. Hon, K. Brogaard and Y. Elsworth for their comments.

T.R.B. and D.H. acknowledge funding from the Australian Research Council (Discovery Project DP210103119). D.H. also acknowledges support from the Alfred P. Sloan Foundation and the National Aeronautics and Space Administration (80NSSC19K0597). M.J. acknowledges the Lasker Fellowship grant. S.B. acknowledges the Joint Research Fund in Astronomy (U2031203) under a cooperative agreement between the National Natural Science Foundation of China (NSFC) and Chinese Academy of Sciences (CAS) and the NSFC grants 12090040 and 12090042. G.L. acknowledges support from the project BEAMING ANR-18-CE31-0001 of the French National Research Agency (ANR) and from the Centre National d'Etudes Spatiales (CNES).

We gratefully acknowledge the Kepler teams, whose efforts made these results possible. Funding for the Kepler mission is provided by the NASA Science Mission Directorate. This paper includes data collected by the Kepler mission and obtained from the MAST data archive at the Space Telescope Science Institute (STScI). STScI is operated by the Association of Universities for Research in Astronomy, Inc., under NASA contract NAS 5–26555.

Guoshoujing Telescope (LAMOST) is a National Major Scientific Project built by the Chinese Academy of Sciences. Funding for the project has been provided by the National Development and Reform Commission. LAMOST is operated and managed by the National Astronomical Observatories, Chinese Academy of Sciences.

This work presents results from the European Space Agency (ESA) space mission Gaia. Gaia data are being processed by the Gaia Data Processing and Analysis Consortium (DPAC). Funding for the DPAC is provided by national institutions, in particular the institutions participating in the Gaia Multilateral Agreement (MLA). The Gaia mission website is <https://www.cosmos.esa.int/gaia>. The Gaia archive website is <https://archives.esac.esa.int/gaia>.

Funding for the Sloan Digital Sky Survey IV has been provided by the Alfred P. Sloan Foundation, the US Department of Energy Office of Science and the participating institutions.

We acknowledge Sydney Informatics (a core research facility of the University of Sydney), the high performance computing (HPC) cluster Artemis from the University of Sydney, the HPC cluster headnode from the School of Physics and the HPC cluster Gadi from the National Computational Infrastructure (NCI Australia, an NCRIS-enabled capability supported by the Australian Government) for providing the HPC resources that have contributed to the research results reported within this paper.

Author contributions

Y.L., T.R.B., D.S., Y.C., I.L.C. and G.L. analysed photometric data; S.J.M., D.H., X.Z., S.B. and D.R.H. contributed to binary confirmation; Y.L., M.J. and D.M. constructed theoretical models; B.T.M., M.R.H., S.S. and Y.W. interpreted spectroscopic data. All authors discussed the results and commented on the manuscript.

Competing interests

The authors declare no competing interests.

Additional information

Extended data is available for this paper at <https://doi.org/10.1038/s41550-022-01648-5>.

Supplementary information The online version contains supplementary material available at <https://doi.org/10.1038/s41550-022-01648-5>.

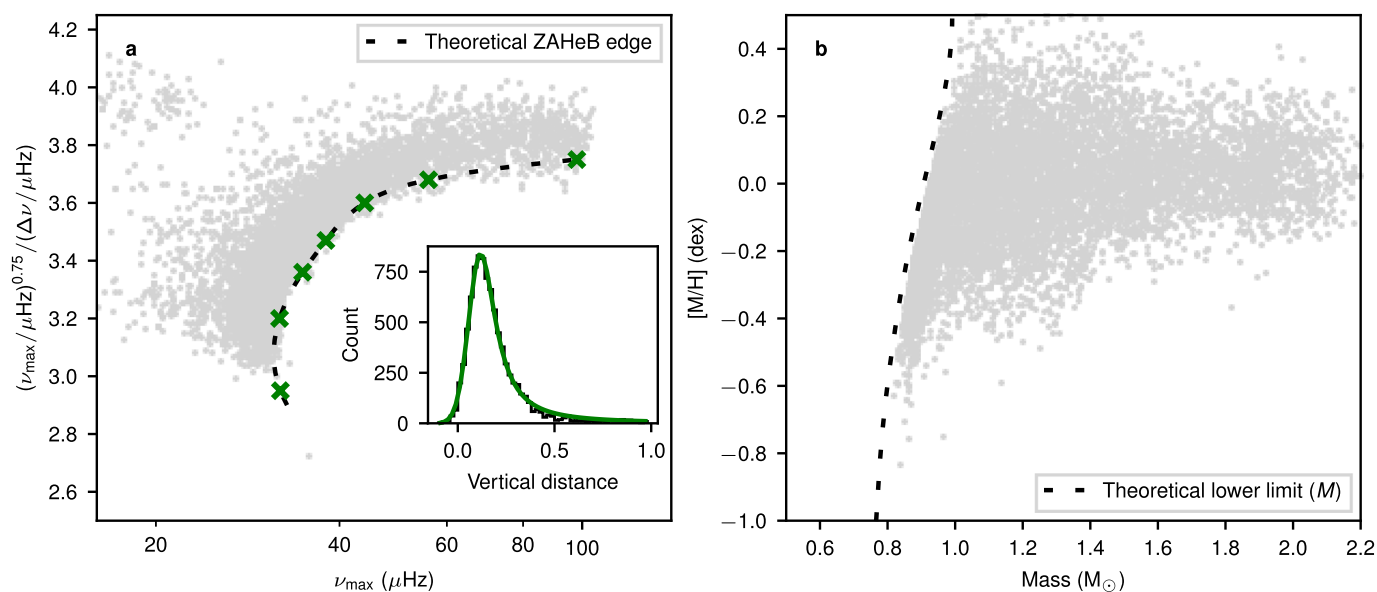
Correspondence and requests for materials should be addressed to Yaguang Li or Timothy R. Bedding.

Peer review information *Nature Astronomy* thanks Nicholas Rui, Oliver Hall and the other, anonymous, reviewer(s) for their contribution to the peer review of this work.

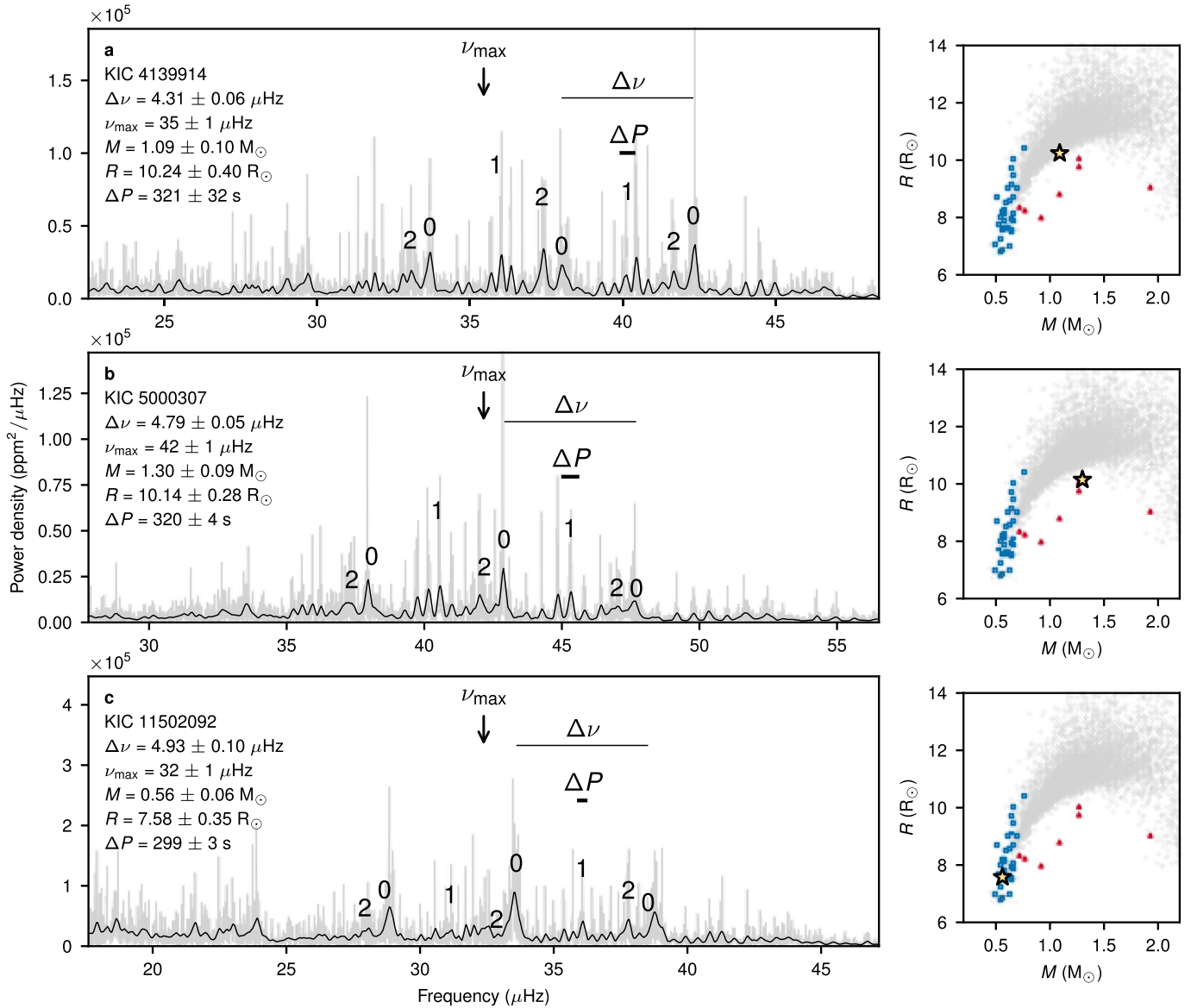
Reprints and permissions information is available at www.nature.com/reprints.

Publisher's note Springer Nature remains neutral with regard to jurisdictional claims in published maps and institutional affiliations.

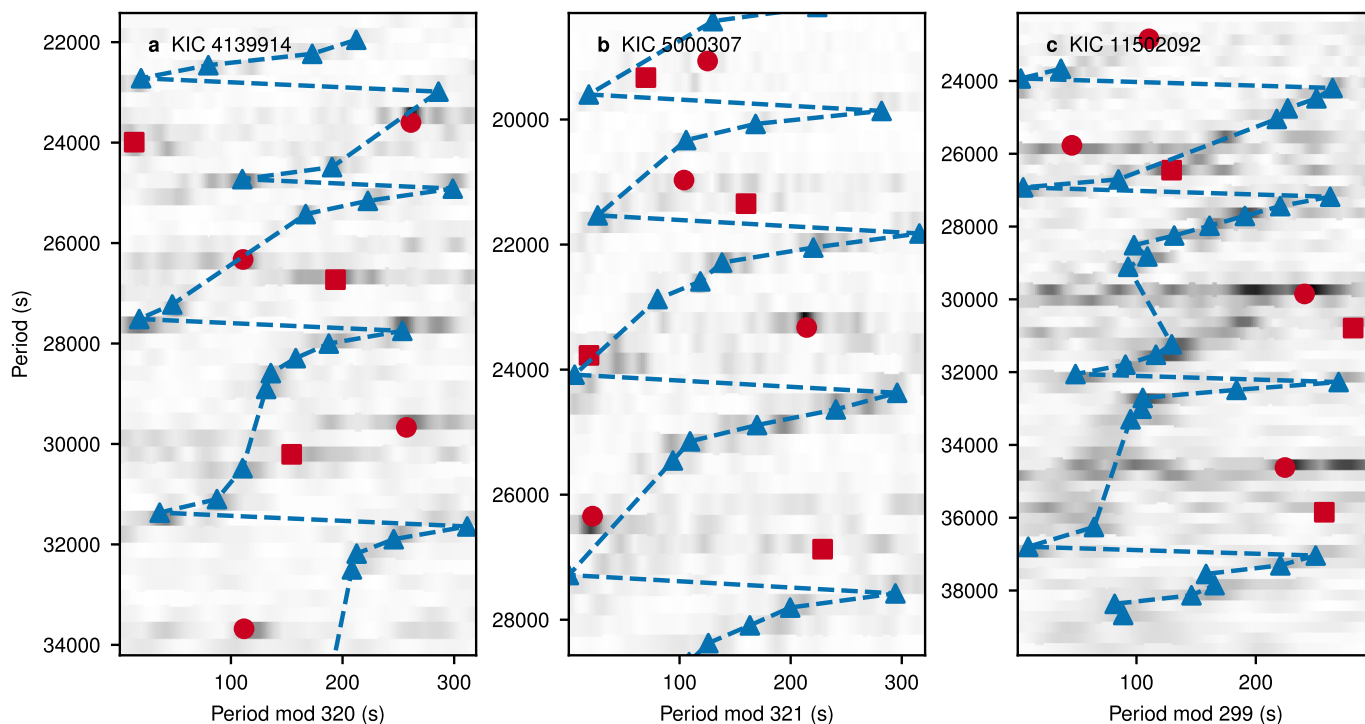
© The Author(s), under exclusive licence to Springer Nature Limited 2022



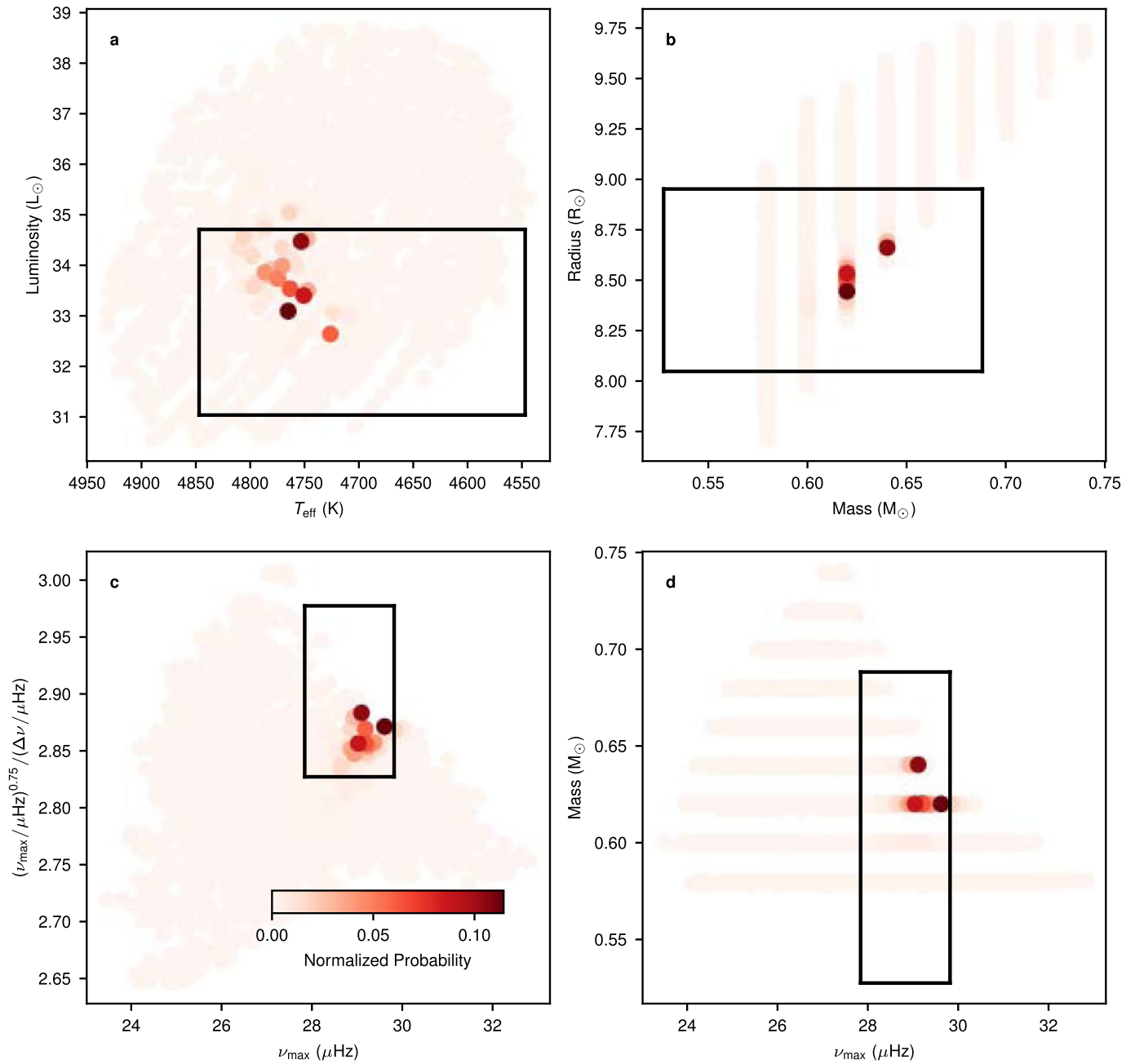
Extended Data Fig. 1 | Galaxia simulation of CHHe stars in the Kepler field. **a**, The seismic quantity $\nu_{\max}^{0.75}/\Delta\nu$ versus ν_{\max} . The ZAHeB edge (the black dashed line) is represented by a spline (defined by the crosses). The inset of **a** shows the distribution of the vertical distances to the edge. The distribution is fitted by a half-Gaussian half-Lorentzian profile, shown by the green line. The standard deviation of the half-Gaussian profile represents the intrinsic broadening of the ZAHeB edge. **b**, The metallicity-mass diagram. The dashed line is the lowest mass a star can be without mass loss given a metallicity, determined with MIST models (see Methods).



Extended Data Fig. 2 | Power spectra for three representative stars, including a regular CHB star (a), an underluminous star (b), and a very low-mass star (c). The right panels show their locations on the mass-radius diagram marked by the star symbols. The power spectra (grey lines) are smoothed by $0.06\Delta\nu$ (overlaid black lines). The integers 0–2 represent the angular-degree l . The locations of ν_{max} are indicated by the arrows. The observed values of $\Delta\nu$ and ΔP (see Extended Data Fig. 3) are represented by the lengths of the black line segments.



Extended Data Fig. 3 | Period échelle diagrams for the regular CHeB star (a), the under-luminous star (b), and the very-low-mass star (c) that are shown in Extended Fig. 2. The modes are marked by circles ($l=0$), triangles ($l=1$) and squares ($l=2$). Error bars are not shown. The blue dashed lines connect the $l=1$ modes in order. We adjusted the widths of the échelle diagrams such that the $l=1$ modes form a “zigzag” pattern³⁷. Those widths correspond to the period spacings of $l=1$ modes, which confirm them as CHeB stars.



Extended Data Fig. 4 | Stellar models for KIC 8367834 within 3σ of the classical constraints, colour-coded with probability using constraints from parallax, T_{eff} , metallicity, and oscillation frequencies. **a**, The Hertzsprung-Russell diagram. **b**, The mass-radius diagram. **c**, The seismic quantity $\nu_{\text{max}}^{0.75}/\Delta\nu$ versus ν_{max} . **d**, Mass versus ν_{max} . The black boxes show the 1.5σ confidence regions, either directly from observations (L , T_{eff} , ν_{max} , $\Delta\nu$) or from the scaling relations (M , R).

8 Conclusions and outlook

8.1 Conclusions

In this thesis, we have developed tools with *asteroseismology* to probe stellar interiors and to enable the characterisations of stellar properties. Our main conclusions are summarised as follows.

1. We extracted the oscillation parameters and the core and envelope rotation rates of *Kepler* subgiants, in Chapter 2 and Chapter 3, respectively. We showed that p-g mixed modes are potent probes of stellar ages. We found that the cores and envelopes of early subgiants rotate at similar speeds, suggesting near solid-body rotation on the main sequence and an efficient transport of angular momentum. Differential rotation emerges between 300 and 800 Myr after the main sequence, constraining the timescales of angular momentum transport.
2. We tested the validity of the asteroseismic scaling relations. In Chapter 4, we measured the intrinsic scatter of the scaling relations to be a few percent, which sets a fundamental floor for the precision. In Chapter 5, we showed the $\Delta\nu$ scaling relation has a 2% systematic bias if the surface effect is left uncorrected. In Chapter 6, we found no noticeable deviation of the ν_{\max} scaling relation compared to inferences from individual frequencies, providing a solid justification for its application.
3. We proposed a new prescription to correct the stellar surface effect in Chapter 5. This has been a troublesome problem in stellar modelling and involves using unconstrained free parameters. By parameterising the surface correction to relate with g , T_{eff} , and $[M/H]$, we were able to reduce the scatter of model-derived stellar properties.
4. We discovered new types of post-mass-transfer helium-burning red giants in Chapter 7. The first class comprises underluminous stars with smaller helium-burning cores than their single-star counterparts, and the second class consists of very low-mass stars, whose implied ages would exceed the age of the universe had no excessive mass loss occurred.

8.2 Outlook

Stars are fundamental building blocks of the universe, and determining basic properties such as age, luminosity, and mass can unlock critical insights spanning the Galaxy,

stars, and exoplanets. Despite recent advances, current techniques for determining these properties have not been fully optimised. However, the power of asteroseismology can be harnessed to take stellar characterisation to the next level. This can be supported by two methods: detailed characterisation of individual frequencies and ensemble modelling analysis. By further developing and utilising these methods, we can make significant strides in understanding the properties of stars and their role in shaping the cosmos.

Asteroseismology holds the potential for next-level accuracy due to its ability to provide more detailed information about stellar structure using individual frequencies, which can significantly reduce uncertainties in age determination. Current determinations of stellar properties often rely on the $\Delta\nu$ and ν_{\max} scaling relations, which reduce the asteroseismic information to only two parameters, resulting in typical age uncertainties of 30%. In contrast, by characterising and modelling individual frequencies, the age uncertainties can be reduced to 10%, dramatically increasing our ability to resolve critical events in time (Montalbán et al., 2021).

Another powerful approach that is often overlooked is ensemble modelling analysis. This method models many stars simultaneously, allowing for imposing correlations between parameters. For example, it can be used to describe poorly understood physical processes as a function of stellar parameters, such as the convective efficiency described by the mixing length α_{MLT} . Additionally, ensemble modelling analysis can be used to model all stars in a cluster or a binary system, taking advantage of the fact that the stars are coeval, which can unlock accurate knowledge on ages and helium abundances (McKee et al., 2019). By accounting for potential correlations, the use of ensemble modelling analysis can greatly improve the accuracy of inferred parameters. We suggest the following projects for future work.

Moving beyond solar calibration with more realistic stellar models

When constructing stellar models, assumptions on stellar physics must be made, and most of them are based on solar calibrations. However, differences in these assumptions can change mass by 5% and age by 20% for non-solar targets (Tayar et al., 2022a), imposing a fundamental limit on the accuracy of the inferred stellar properties. One can essentially move beyond solar calibration and use benchmark stars to calibrate the next generation of stellar models, bearing in mind that model physics can vary from star to star consistently.

Calibrating empirical age-dating methods with asteroseismology

Stellar ages can be determined using empirical relations, which are indispensable tools to access stellar ages where asteroseismology is not applicable. However, knowledge of these relations primarily relies on a few clusters, which have limited coverage in age and metallicity. These empirical age relations could be tied to the asteroseismic age scale, using *Gaia* wide binaries (El-Badry et al., 2021) or the kinematic velocity dispersion relation (Sharma et al., 2021) as the bridges.

Settling the fundamental parameter scales of metal-poor stars

Metal-poor stars are the living fossils of the early Galaxy, but their fundamental properties are poorly determined. Recent studies show that their T_{eff} could suffer from a large systematic offset (Grunblatt et al., 2021), stemming from a lack of metal-poor calibrators. The widely used ν_{max} scaling relation could also break in the very-low-metallicity environment (Epstein et al., 2014). One could use individual oscillation frequencies and *Gaia* luminosities, a combination that has seldom been explored, to infer the compatible T_{eff} scale and test our ability to derive accurate masses and ages for metal-poor stars.

Bibliography

- Aerts, C. 2021, *Reviews of Modern Physics*, 93, 015001, doi: [10.1103/RevModPhys.93.015001](https://doi.org/10.1103/RevModPhys.93.015001)
- Aerts, C., Christensen-Dalsgaard, J., & Kurtz, D. W. 2010, *Asteroseismology*, doi: [10.1007/978-1-4020-5803-5](https://doi.org/10.1007/978-1-4020-5803-5)
- Arentoft, T., Grundahl, F., White, T. R., et al. 2019, *A&A*, 622, A190, doi: [10.1051/0004-6361/201834690](https://doi.org/10.1051/0004-6361/201834690)
- Balmforth, N. J. 1992, *MNRAS*, 255, 603, doi: [10.1093/mnras/255.4.603](https://doi.org/10.1093/mnras/255.4.603)
- Basu, S., & Chaplin, W. J. 2017, *Asteroseismic Data Analysis: Foundations and Techniques*
- Basu, S., & Hekker, S. 2020, *Frontiers in Astronomy and Space Sciences*, 7, 44, doi: [10.3389/fspas.2020.00044](https://doi.org/10.3389/fspas.2020.00044)
- Basu, S., Mazumdar, A., Antia, H. M., & Demarque, P. 2004, *MNRAS*, 350, 277, doi: [10.1111/j.1365-2966.2004.07644.x](https://doi.org/10.1111/j.1365-2966.2004.07644.x)
- Beck, P. G., Montalbán, J., Kallinger, T., et al. 2012, *Nature*, 481, 55, doi: [10.1038/nature10612](https://doi.org/10.1038/nature10612)
- Bedding, T. R. 2014, in *Asteroseismology: 22nd Canary Islands Winter School of Astrophysics*, ed. P. L. Pallé & C. Esteban (Cambridge: Cambridge University Press), 60
- Bedding, T. R., Mosser, B., Huber, D., et al. 2011, *Nature*, 471, 608, doi: [10.1038/nature09935](https://doi.org/10.1038/nature09935)
- Bedding, T. R., Murphy, S. J., Hey, D. R., et al. 2020, *Nature*, 581, 147, doi: [10.1038/s41586-020-2226-8](https://doi.org/10.1038/s41586-020-2226-8)
- Belkacem, K., Marques, J. P., Goupil, M. J., et al. 2015a, *A&A*, 579, A30, doi: [10.1051/0004-6361/201526042](https://doi.org/10.1051/0004-6361/201526042)
- . 2015b, *A&A*, 579, A31, doi: [10.1051/0004-6361/201526043](https://doi.org/10.1051/0004-6361/201526043)
- Böhm-Vitense, E. 1958, *ZA*, 46, 108
- Brown, T. M., Gilliland, R. L., Noyes, R. W., & Ramsey, L. W. 1991, *ApJ*, 368, 599, doi: [10.1086/169725](https://doi.org/10.1086/169725)

- Byrne, C. M., Stanway, E. R., & Eldridge, J. J. 2021, MNRAS, 507, 621, doi: [10.1093/mnras/stab2115](https://doi.org/10.1093/mnras/stab2115)
- Cantiello, M., Mankovich, C., Bildsten, L., Christensen-Dalsgaard, J., & Paxton, B. 2014, ApJ, 788, 93, doi: [10.1088/0004-637X/788/1/93](https://doi.org/10.1088/0004-637X/788/1/93)
- Ceillier, T., Eggenberger, P., García, R. A., & Mathis, S. 2013, A&A, 555, A54, doi: [10.1051/0004-6361/201321473](https://doi.org/10.1051/0004-6361/201321473)
- Ceillier, T., Tayar, J., Mathur, S., et al. 2017, A&A, 605, A111, doi: [10.1051/0004-6361/201629884](https://doi.org/10.1051/0004-6361/201629884)
- Chaplin, W. J., & Miglio, A. 2013, ARA&A, 51, 353, doi: [10.1146/annurev-astro-082812-140938](https://doi.org/10.1146/annurev-astro-082812-140938)
- Chaplin, W. J., Basu, S., Huber, D., et al. 2014, ApJS, 210, 1, doi: [10.1088/0067-0049/210/1/1](https://doi.org/10.1088/0067-0049/210/1/1)
- Choi, J., Dotter, A., Conroy, C., et al. 2016, ApJ, 823, 102, doi: [10.3847/0004-637X/823/2/102](https://doi.org/10.3847/0004-637X/823/2/102)
- Christensen-Dalsgaard, J. 2015, MNRAS, 453, 666, doi: [10.1093/mnras/stv1656](https://doi.org/10.1093/mnras/stv1656)
- Christensen-Dalsgaard, J., Silva Aguirre, V., Cassisi, S., et al. 2020, A&A, 635, A165, doi: [10.1051/0004-6361/201936766](https://doi.org/10.1051/0004-6361/201936766)
- Colman, I. L., Bedding, T. R., Huber, D., & Kjeldsen, H. 2022, ApJS, 258, 39, doi: [10.3847/1538-4365/ac3a11](https://doi.org/10.3847/1538-4365/ac3a11)
- Corsaro, E., Stello, D., Huber, D., et al. 2012, ApJ, 757, 190, doi: [10.1088/0004-637X/757/2/190](https://doi.org/10.1088/0004-637X/757/2/190)
- Cox, J. P., & Giuli, R. T. 1968, Principles of stellar structure
- Cunha, M. S., Roxburgh, I. W., Aguirre Børsen-Koch, V., et al. 2021, MNRAS, 508, 5864, doi: [10.1093/mnras/stab2886](https://doi.org/10.1093/mnras/stab2886)
- De Ridder, J., Barban, C., Baudin, F., et al. 2009, Nature, 459, 398, doi: [10.1038/nature08022](https://doi.org/10.1038/nature08022)
- Deheuvels, S., Ballot, J., Beck, P. G., et al. 2015, A&A, 580, A96, doi: [10.1051/0004-6361/201526449](https://doi.org/10.1051/0004-6361/201526449)
- Deheuvels, S., Ballot, J., Eggenberger, P., et al. 2020, arXiv e-prints, arXiv:2007.02585. <https://arxiv.org/abs/2007.02585>
- Deheuvels, S., Ballot, J., Gehan, C., & Mosser, B. 2021, arXiv e-prints, arXiv:2108.11848. <https://arxiv.org/abs/2108.11848>
- Deheuvels, S., Doğan, G., Goupil, M. J., et al. 2014, A&A, 564, A27, doi: [10.1051/0004-6361/201322779](https://doi.org/10.1051/0004-6361/201322779)

- den Hartogh, J. W., Eggenberger, P., & Hirschi, R. 2019, *A&A*, 622, A187, doi: [10.1051/0004-6361/201834330](https://doi.org/10.1051/0004-6361/201834330)
- Dréau, G., Lebreton, Y., Mosser, B., Bossini, D., & Yu, J. 2022, *A&A*, 668, A115, doi: [10.1051/0004-6361/202243732](https://doi.org/10.1051/0004-6361/202243732)
- Dupret, M. A., Belkacem, K., Samadi, R., et al. 2009, *A&A*, 506, 57, doi: [10.1051/0004-6361/200911713](https://doi.org/10.1051/0004-6361/200911713)
- Eggenberger, P., den Hartogh, J. W., Buldgen, G., et al. 2019, *A&A*, 631, L6, doi: [10.1051/0004-6361/201936348](https://doi.org/10.1051/0004-6361/201936348)
- Eggenberger, P., Montalbán, J., & Miglio, A. 2012, *A&A*, 544, L4, doi: [10.1051/0004-6361/201219729](https://doi.org/10.1051/0004-6361/201219729)
- Eggenberger, P., Moyano, F. D., & den Hartogh, J. W. 2022, *A&A*, 664, L16, doi: [10.1051/0004-6361/202243781](https://doi.org/10.1051/0004-6361/202243781)
- El-Badry, K., Rix, H.-W., & Heintz, T. M. 2021, *MNRAS*, 506, 2269, doi: [10.1093/mnras/stab323](https://doi.org/10.1093/mnras/stab323)
- Epstein, C. R., Elsworth, Y. P., Johnson, J. A., et al. 2014, *ApJL*, 785, L28, doi: [10.1088/2041-8205/785/2/L28](https://doi.org/10.1088/2041-8205/785/2/L28)
- Farnir, M., Valentino, A., Dupret, M. A., & Broomhall, A. M. 2023, *MNRAS*, 521, 4131, doi: [10.1093/mnras/stad788](https://doi.org/10.1093/mnras/stad788)
- Fellay, L., Buldgen, G., Eggenberger, P., et al. 2021, *A&A*, 654, A133, doi: [10.1051/0004-6361/202140518](https://doi.org/10.1051/0004-6361/202140518)
- Foreman-Mackey, D., Agol, E., Ambikasaran, S., & Angus, R. 2017, *AJ*, 154, 220, doi: [10.3847/1538-3881/aa9332](https://doi.org/10.3847/1538-3881/aa9332)
- Frandsen, S., Fredslund Andersen, M., Brogaard, K., et al. 2018, *A&A*, 613, A53, doi: [10.1051/0004-6361/201730816](https://doi.org/10.1051/0004-6361/201730816)
- Fuller, J., Lecoanet, D., Cantiello, M., & Brown, B. 2014, *ApJ*, 796, 17, doi: [10.1088/0004-637X/796/1/17](https://doi.org/10.1088/0004-637X/796/1/17)
- Gaia Collaboration, Babusiaux, C., van Leeuwen, F., et al. 2018, *A&A*, 616, A10, doi: [10.1051/0004-6361/201832843](https://doi.org/10.1051/0004-6361/201832843)
- Gehan, C., Mosser, B., Michel, E., Samadi, R., & Kallinger, T. 2018, *A&A*, 616, A24, doi: [10.1051/0004-6361/201832822](https://doi.org/10.1051/0004-6361/201832822)
- Gilliland, R. L., Chaplin, W. J., Dunham, E. W., et al. 2011, *ApJS*, 197, 6, doi: [10.1088/0067-0049/197/1/6](https://doi.org/10.1088/0067-0049/197/1/6)
- Girardi, L. 2016, *ARA&A*, 54, 95, doi: [10.1146/annurev-astro-081915-023354](https://doi.org/10.1146/annurev-astro-081915-023354)
- Goldreich, P., Murray, N., & Kumar, P. 1994, *ApJ*, 424, 466, doi: [10.1086/173904](https://doi.org/10.1086/173904)

- Gough, D. O. 1986, in *Hydrodynamic and Magnetodynamic Problems in the Sun and Stars*, ed. Y. Osaki, 117
- Goupil, M. J., Mosser, B., Marques, J. P., et al. 2013, *A&A*, 549, A75, doi: [10.1051/0004-6361/201220266](https://doi.org/10.1051/0004-6361/201220266)
- Grunblatt, S. K., Zinn, J. C., Price-Whelan, A. M., et al. 2021, *ApJ*, 916, 88, doi: [10.3847/1538-4357/ac0532](https://doi.org/10.3847/1538-4357/ac0532)
- Grundahl, F., Arentoft, T., Christensen-Dalsgaard, J., et al. 2008, in *Journal of Physics Conference Series*, Vol. 118, *Journal of Physics Conference Series*, 012041, doi: [10.1088/1742-6596/118/1/012041](https://doi.org/10.1088/1742-6596/118/1/012041)
- Grundahl, F., Fredslund Andersen, M., Christensen-Dalsgaard, J., et al. 2017, *ApJ*, 836, 142, doi: [10.3847/1538-4357/836/1/142](https://doi.org/10.3847/1538-4357/836/1/142)
- Han, Z.-W., Ge, H.-W., Chen, X.-F., & Chen, H.-L. 2020, *Research in Astronomy and Astrophysics*, 20, 161, doi: [10.1088/1674-4527/20/10/161](https://doi.org/10.1088/1674-4527/20/10/161)
- Handberg, R., Brogaard, K., Miglio, A., et al. 2017, *MNRAS*, 472, 979, doi: [10.1093/mnras/stx1929](https://doi.org/10.1093/mnras/stx1929)
- Hatt, E., Nielsen, M. B., Chaplin, W. J., et al. 2023, *A&A*, 669, A67, doi: [10.1051/0004-6361/202244579](https://doi.org/10.1051/0004-6361/202244579)
- Heber, U. 2016, *PASP*, 128, 082001, doi: [10.1088/1538-3873/128/966/082001](https://doi.org/10.1088/1538-3873/128/966/082001)
- Hekker, S., & Christensen-Dalsgaard, J. 2017, *A&A Rv*, 25, 1, doi: [10.1007/s00159-017-0101-x](https://doi.org/10.1007/s00159-017-0101-x)
- Hekker, S., Elsworth, Y., De Ridder, J., et al. 2011a, *A&A*, 525, A131, doi: [10.1051/0004-6361/201015185](https://doi.org/10.1051/0004-6361/201015185)
- Hekker, S., Basu, S., Stello, D., et al. 2011b, *A&A*, 530, A100, doi: [10.1051/0004-6361/201016303](https://doi.org/10.1051/0004-6361/201016303)
- Heney, L., Vardya, M. S., & Bodenheimer, P. 1965, *ApJ*, 142, 841, doi: [10.1086/148357](https://doi.org/10.1086/148357)
- Hey, D. 2021, *Asteroseismology and pulsation timing of the A-type stars observed by Kepler*, The University of Sydney
- Houdek, G. 2006, in *ESA Special Publication*, Vol. 624, *Proceedings of SOHO 18/GONG 2006/HELAS I, Beyond the spherical Sun*, 28
- Houdek, G., & Dupret, M.-A. 2015, *Living Reviews in Solar Physics*, 12, 8, doi: [10.1007/lrsp-2015-8](https://doi.org/10.1007/lrsp-2015-8)
- Howell, M., Campbell, S. W., Stello, D., & De Silva, G. M. 2022, *MNRAS*, 515, 3184, doi: [10.1093/mnras/stac1918](https://doi.org/10.1093/mnras/stac1918)

- Huber, D., Bedding, T. R., Stello, D., et al. 2011, *ApJ*, 743, 143, doi: [10.1088/0004-637X/743/2/143](https://doi.org/10.1088/0004-637X/743/2/143)
- Huber, D., Chaplin, W. J., Christensen-Dalsgaard, J., et al. 2013, *ApJ*, 767, 127, doi: [10.1088/0004-637X/767/2/127](https://doi.org/10.1088/0004-637X/767/2/127)
- Huber, D., Silva Aguirre, V., Matthews, J. M., et al. 2014, *ApJS*, 211, 2, doi: [10.1088/0067-0049/211/1/2](https://doi.org/10.1088/0067-0049/211/1/2)
- Joyce, M., & Chaboyer, B. 2018, *ApJ*, 856, 10, doi: [10.3847/1538-4357/aab200](https://doi.org/10.3847/1538-4357/aab200)
- Joyce, M., & Tayar, J. 2023, arXiv e-prints, arXiv:2303.09596, doi: [10.48550/arXiv.2303.09596](https://doi.org/10.48550/arXiv.2303.09596)
- Khan, S., Hall, O. J., Miglio, A., et al. 2018, *ApJ*, 859, 156, doi: [10.3847/1538-4357/aabf90](https://doi.org/10.3847/1538-4357/aabf90)
- Kippenhahn, R., & Weigert, A. 1990, *Stellar Structure and Evolution*
- Kjeldsen, H., & Bedding, T. R. 1995, *A&A*, 293, 87. <https://arxiv.org/abs/astro-ph/9403015>
- Kjeldsen, H., Bedding, T. R., Viskum, M., & Frandsen, S. 1995, *AJ*, 109, 1313, doi: [10.1086/117363](https://doi.org/10.1086/117363)
- Kurtz, D. W. 2022, *ARA&A*, 60, 31, doi: [10.1146/annurev-astro-052920-094232](https://doi.org/10.1146/annurev-astro-052920-094232)
- Lebreton, Y., & Goupil, M. J. 2014, *A&A*, 569, A21, doi: [10.1051/0004-6361/201423797](https://doi.org/10.1051/0004-6361/201423797)
- Li, T., Bedding, T. R., Christensen-Dalsgaard, J., et al. 2020a, *MNRAS*, 495, 3431, doi: [10.1093/mnras/staa1350](https://doi.org/10.1093/mnras/staa1350)
- Li, T., Bedding, T. R., Huber, D., et al. 2018, *MNRAS*, 475, 981, doi: [10.1093/mnras/stx3079](https://doi.org/10.1093/mnras/stx3079)
- Li, T., Li, Y., Bi, S., et al. 2022a, *ApJ*, 927, 167, doi: [10.3847/1538-4357/ac4fbf](https://doi.org/10.3847/1538-4357/ac4fbf)
- Li, Y., Bedding, T. R., Li, T., et al. 2020b, *MNRAS*, 495, 2363, doi: [10.1093/mnras/staa1335](https://doi.org/10.1093/mnras/staa1335)
- Li, Y., Bedding, T. R., Stello, D., et al. 2021, *MNRAS*, 501, 3162, doi: [10.1093/mnras/staa3932](https://doi.org/10.1093/mnras/staa3932)
- . 2022b, arXiv e-prints, arXiv:2208.01176, doi: [10.48550/arXiv.2208.01176](https://doi.org/10.48550/arXiv.2208.01176)
- Li, Y., Bedding, T. R., Murphy, S. J., et al. 2022c, *Nature Astronomy*, 6, 673, doi: [10.1038/s41550-022-01648-5](https://doi.org/10.1038/s41550-022-01648-5)
- Lynas-Gray, A. E. 2021, *Frontiers in Astronomy and Space Sciences*, 8, 19, doi: [10.3389/fspas.2021.576623](https://doi.org/10.3389/fspas.2021.576623)

- Magic, Z., Weiss, A., & Asplund, M. 2015, *A&A*, 573, A89, doi: [10.1051/0004-6361/201423760](https://doi.org/10.1051/0004-6361/201423760)
- Marques, J. P., Goupil, M. J., Lebreton, Y., et al. 2013, *A&A*, 549, A74, doi: [10.1051/0004-6361/201220211](https://doi.org/10.1051/0004-6361/201220211)
- Mathur, S., García, R. A., Huber, D., et al. 2016, *ApJ*, 827, 50, doi: [10.3847/0004-637X/827/1/50](https://doi.org/10.3847/0004-637X/827/1/50)
- Mathur, S., García, R. A., Breton, S., et al. 2022, *A&A*, 657, A31, doi: [10.1051/0004-6361/202141168](https://doi.org/10.1051/0004-6361/202141168)
- Matteuzzi, M., Montalbán, J., Miglio, A., et al. 2023, *A&A*, 671, A53, doi: [10.1051/0004-6361/202245746](https://doi.org/10.1051/0004-6361/202245746)
- Mazumdar, A., Monteiro, M. J. P. F. G., Ballot, J., et al. 2014, *ApJ*, 782, 18, doi: [10.1088/0004-637X/782/1/18](https://doi.org/10.1088/0004-637X/782/1/18)
- McDonald, I., & Zijlstra, A. A. 2015, *MNRAS*, 448, 502, doi: [10.1093/mnras/stv007](https://doi.org/10.1093/mnras/stv007)
- McKeever, J. M., Basu, S., & Corsaro, E. 2019, *ApJ*, 874, 180, doi: [10.3847/1538-4357/ab0c04](https://doi.org/10.3847/1538-4357/ab0c04)
- Miglio, A., Brogaard, K., Stello, D., et al. 2012, *MNRAS*, 419, 2077, doi: [10.1111/j.1365-2966.2011.19859.x](https://doi.org/10.1111/j.1365-2966.2011.19859.x)
- Montalbán, J., Miglio, A., Noels, A., et al. 2013, *ApJ*, 766, 118, doi: [10.1088/0004-637X/766/2/118](https://doi.org/10.1088/0004-637X/766/2/118)
- Montalbán, J., Mackereth, J. T., Miglio, A., et al. 2021, *Nature Astronomy*, 5, 640, doi: [10.1038/s41550-021-01347-7](https://doi.org/10.1038/s41550-021-01347-7)
- Monteiro, M. J. P. F. G. 2009, *Evolution and Seismic Tools for Stellar Astrophysics*, Vol. 316
- Mosser, B., Gehan, C., Belkacem, K., et al. 2018, *A&A*, 618, A109, doi: [10.1051/0004-6361/201832777](https://doi.org/10.1051/0004-6361/201832777)
- Mosser, B., Vrad, M., Belkacem, K., Deheuvels, S., & Goupil, M. J. 2015, *A&A*, 584, A50, doi: [10.1051/0004-6361/201527075](https://doi.org/10.1051/0004-6361/201527075)
- Mosser, B., Belkacem, K., Goupil, M. J., et al. 2011, *A&A*, 525, L9, doi: [10.1051/0004-6361/201015440](https://doi.org/10.1051/0004-6361/201015440)
- Mosser, B., Goupil, M. J., Belkacem, K., et al. 2012a, *A&A*, 540, A143, doi: [10.1051/0004-6361/201118519](https://doi.org/10.1051/0004-6361/201118519)
- . 2012b, *A&A*, 548, A10, doi: [10.1051/0004-6361/201220106](https://doi.org/10.1051/0004-6361/201220106)
- Moyano, F. D., Eggenberger, P., Mosser, B., & Spada, F. 2023, arXiv e-prints, arXiv:2302.07811, doi: [10.48550/arXiv.2302.07811](https://doi.org/10.48550/arXiv.2302.07811)

- Murphy, S. J., Bedding, T. R., White, T. R., et al. 2022, MNRAS, 511, 5718, doi: [10.1093/mnras/stac240](https://doi.org/10.1093/mnras/stac240)
- Nsamba, B., Moedas, N., Campante, T. L., et al. 2021, MNRAS, 500, 54, doi: [10.1093/mnras/staa3228](https://doi.org/10.1093/mnras/staa3228)
- Paxton, B., Bildsten, L., Dotter, A., et al. 2011, ApJS, 192, 3, doi: [10.1088/0067-0049/192/1/3](https://doi.org/10.1088/0067-0049/192/1/3)
- Paxton, B., Cantiello, M., Arras, P., et al. 2013, ApJS, 208, 4, doi: [10.1088/0067-0049/208/1/4](https://doi.org/10.1088/0067-0049/208/1/4)
- Paxton, B., Marchant, P., Schwab, J., et al. 2015, ApJS, 220, 15, doi: [10.1088/0067-0049/220/1/15](https://doi.org/10.1088/0067-0049/220/1/15)
- Paxton, B., Schwab, J., Bauer, E. B., et al. 2018, ApJS, 234, 34, doi: [10.3847/1538-4365/aaa5a8](https://doi.org/10.3847/1538-4365/aaa5a8)
- Paxton, B., Smolec, R., Schwab, J., et al. 2019, ApJS, 243, 10, doi: [10.3847/1538-4365/ab2241](https://doi.org/10.3847/1538-4365/ab2241)
- Pinçon, C., Belkacem, K., & Goupil, M. J. 2016, A&A, 588, A122, doi: [10.1051/0004-6361/201527663](https://doi.org/10.1051/0004-6361/201527663)
- Pinsonneault, M. H., Elsworth, Y. P., Tayar, J., et al. 2018, ApJS, 239, 32, doi: [10.3847/1538-4365/aaebfd](https://doi.org/10.3847/1538-4365/aaebfd)
- Refsdal, S., & Weigert, A. 1970, A&A, 6, 426
- Reimers, D. 1975, Memoires of the Societe Royale des Sciences de Liege, 8, 369
- Rui, N. Z., & Fuller, J. 2021, MNRAS, doi: [10.1093/mnras/stab2528](https://doi.org/10.1093/mnras/stab2528)
- Samadi, R., Belkacem, K., & Sonoi, T. 2015, in EAS Publications Series, Vol. 73-74, EAS Publications Series, 111–191, doi: [10.1051/eas/1573003](https://doi.org/10.1051/eas/1573003)
- Schönberg, M., & Chandrasekhar, S. 1942, ApJ, 96, 161, doi: [10.1086/144444](https://doi.org/10.1086/144444)
- Schröder, K. P., & Cuntz, M. 2005, ApJL, 630, L73, doi: [10.1086/491579](https://doi.org/10.1086/491579)
- Sharma, S., Hayden, M. R., Bland-Hawthorn, J., et al. 2021, MNRAS, 506, 1761, doi: [10.1093/mnras/stab1086](https://doi.org/10.1093/mnras/stab1086)
- Silva Aguirre, V., Christensen-Dalsgaard, J., Cassisi, S., et al. 2020, A&A, 635, A164, doi: [10.1051/0004-6361/201935843](https://doi.org/10.1051/0004-6361/201935843)
- Stello, D., Huber, D., Kallinger, T., et al. 2011, ApJL, 737, L10, doi: [10.1088/2041-8205/737/1/L10](https://doi.org/10.1088/2041-8205/737/1/L10)
- Stello, D., Huber, D., Bedding, T. R., et al. 2013, ApJL, 765, L41, doi: [10.1088/2041-8205/765/2/L41](https://doi.org/10.1088/2041-8205/765/2/L41)

- Stello, D., Vanderburg, A., Casagrande, L., et al. 2016, *ApJ*, 832, 133, doi: [10.3847/0004-637X/832/2/133](https://doi.org/10.3847/0004-637X/832/2/133)
- Tassoul, M. 1980, *ApJS*, 43, 469, doi: [10.1086/190678](https://doi.org/10.1086/190678)
- Tayar, J., Beck, P. G., Pinsonneault, M. H., García, R. A., & Mathur, S. 2019, *ApJ*, 887, 203, doi: [10.3847/1538-4357/ab558a](https://doi.org/10.3847/1538-4357/ab558a)
- Tayar, J., Claytor, Z. R., Huber, D., & van Saders, J. 2022a, *ApJ*, 927, 31, doi: [10.3847/1538-4357/ac4bbc](https://doi.org/10.3847/1538-4357/ac4bbc)
- Tayar, J., Somers, G., Pinsonneault, M. H., et al. 2017, *ApJ*, 840, 17, doi: [10.3847/1538-4357/aa6a1e](https://doi.org/10.3847/1538-4357/aa6a1e)
- Tayar, J., Moyano, F. D., Soares-Furtado, M., et al. 2022b, *ApJ*, 940, 23, doi: [10.3847/1538-4357/ac9312](https://doi.org/10.3847/1538-4357/ac9312)
- Townsend, R. H. D., & Teitler, S. A. 2013, *MNRAS*, 435, 3406, doi: [10.1093/mnras/stt1533](https://doi.org/10.1093/mnras/stt1533)
- Trampedach, R., Stein, R. F., Christensen-Dalsgaard, J., Nordlund, Å., & Asplund, M. 2014, *MNRAS*, 445, 4366, doi: [10.1093/mnras/stu2084](https://doi.org/10.1093/mnras/stu2084)
- Triana, S. A., Corsaro, E., De Ridder, J., et al. 2017, *A&A*, 602, A62, doi: [10.1051/0004-6361/201629186](https://doi.org/10.1051/0004-6361/201629186)
- Ulrich, R. K. 1986, *ApJL*, 306, L37, doi: [10.1086/184700](https://doi.org/10.1086/184700)
- Unno, W., Osaki, Y., Ando, H., Saio, H., & Shibahashi, H. 1989, *Nonradial oscillations of stars*
- Valle, G., Dell'Omodarme, M., Prada Moroni, P. G., & Degl'Innocenti, S. 2019, *A&A*, 623, A59, doi: [10.1051/0004-6361/201834949](https://doi.org/10.1051/0004-6361/201834949)
- Verma, K., Rørsted, J. L., Serenelli, A. M., et al. 2022, *MNRAS*, 515, 1492, doi: [10.1093/mnras/stac1860](https://doi.org/10.1093/mnras/stac1860)
- Verma, K., & Silva Aguirre, V. 2019, *MNRAS*, 489, 1850, doi: [10.1093/mnras/stz2272](https://doi.org/10.1093/mnras/stz2272)
- Viani, L. S., Basu, S., Ong J., M. J., Bonaca, A., & Chaplin, W. J. 2018, *ApJ*, 858, 28, doi: [10.3847/1538-4357/aab7eb](https://doi.org/10.3847/1538-4357/aab7eb)
- Vrard, M., Mosser, B., & Samadi, R. 2016, *A&A*, 588, A87, doi: [10.1051/0004-6361/201527259](https://doi.org/10.1051/0004-6361/201527259)
- Vrard, M., Pinsonneault, M., Hon, M., et al. 2021, in *Posters from the TESS Science Conference II (TSC2)*, 141, doi: [10.5281/zenodo.5131114](https://doi.org/10.5281/zenodo.5131114)
- Yan, H.-L., Zhou, Y.-T., Zhang, X., et al. 2021, *Nature Astronomy*, 5, 86, doi: [10.1038/s41550-020-01217-8](https://doi.org/10.1038/s41550-020-01217-8)

- Yu, J., Huber, D., Bedding, T. R., et al. 2018, *ApJS*, 236, 42, doi: [10.3847/1538-4365/aaaf74](https://doi.org/10.3847/1538-4365/aaaf74)
- . 2016, *MNRAS*, 463, 1297, doi: [10.1093/mnras/stw2074](https://doi.org/10.1093/mnras/stw2074)
- Zhang, J., Bi, S., Li, Y., et al. 2020a, *ApJS*, 247, 9, doi: [10.3847/1538-4365/ab6165](https://doi.org/10.3847/1538-4365/ab6165)
- Zhang, J., Shi, J.-R., Yan, H.-L., et al. 2021, *ApJL*, 919, L3, doi: [10.3847/2041-8213/ac224c](https://doi.org/10.3847/2041-8213/ac224c)
- Zhang, X., Jeffery, C. S., Li, Y., & Bi, S. 2020b, *ApJ*, 889, 33, doi: [10.3847/1538-4357/ab5e89](https://doi.org/10.3847/1538-4357/ab5e89)
- Zhou, Y., Nordlander, T., Casagrande, L., et al. 2021a, *MNRAS*, 503, 13, doi: [10.1093/mnras/stab337](https://doi.org/10.1093/mnras/stab337)
- . 2021b, *MNRAS*, 503, 13, doi: [10.1093/mnras/stab337](https://doi.org/10.1093/mnras/stab337)